

Electron Paramagnetic Resonance Studies and Magnetic Field Effects on Porphyrin Nanostructures and Triad Systems

by

Sabine Richert

A thesis submitted in partial fulfillment of the requirements for the degree of Doctor of Philosophy

University of Oxford & New College

Trinity Term 2016

Abstract

Electron Paramagnetic Resonance Studies and Magnetic Field Effects on Porphyrin Nanostructures and Triad Systems

A thesis submitted for the degree of Doctor of Philosophy at the University of Oxford by

Sabine Richert, New College, Trinity 2016

The studies presented in this thesis deal with the investigation of inter- and intramolecular interactions in porphyrin nanostructures and molecular triad systems using a variety of different electron paramagnetic resonance (EPR) based techniques as well as optical spectroscopy.

Dipolar and exchange couplings were investigated in a range of linear and cyclic copper-containing porphyrin nanostructures by continuous wave (cw) and pulse EPR. The magnitude of the exchange interaction, J, and trends in this property could be determined by numerical simulations of the cw EPR spectra or pulse dipolar evolution data. Using double electron-electron resonance (DEER), through-bond exchange coupling in a bis-copper six-porphyrin nanoring could directly be measured over a distance of $\sim$4 nm. By comparison of the results with those obtained for a singly connected but otherwise identical system, the J-coupling in this ring structure containing two identical, parallel paths was further shown to be the result of constructive quantum interference.

In a ten-membered porphyrin nanoring containing two copper and eight zinc centres, the interaction between the central metals of the porphyrins and axial nitrogen ligands of different molecular templates was investigated by cw EPR, electron nuclear double resonance (ENDOR) and DEER. The weak coupling between copper and axial nitrogen ligands could be detected and it was found that the difference in binding affinity between copper and zinc to axial nitrogen ligands influences the structure of the formed complexes and preferred location of the copper centres. We were able to show that the template design allows control over the complex geometry on a molecular level.

Triplet state delocalisation was investigated in a series of ladder complexes, formed between linear zinc porphyrin oligomers and bidentate nitrogen ligands, by transient cw EPR and pulse ENDOR techniques. It was found that even though the porphyrin units are held in an approximately co-planar arrangement within the ladder complex, which should favour long-range electronic communication, complete delocalisation is restricted to two porphyrin units at low temperatures and no delocalisation across the bridging ligand was observed.

In a different project on symmetric and asymmetric zinc porphyrin oligomers with varying side and end groups, the influence of electronic symmetry on triplet state delocalisation was determined to be the major factor governing and limiting the extent of triplet state delocalisation in linear porphyrin oligomers.

Triplet states of zinc porphyrins with different side groups have also been investigated in liquid crystal solvents by EPR. The alignment of the porphyrins is observed to depend strongly on the side groups of the porphyrin core. The orientation and conformations of the porphyrins could be obtained by simulation of the transient cw EPR spectra and order parameters were determined.

The influence of small ($<$10 G) magnetic fields on the recombination kinetics of spin-correlated radical pairs formed upon photo-excitation of molecular triad systems was studied by transient absorption techniques. Molecular triads serve as model compounds for the study of anisotropic magnetic field effects, which could previously only be detected at comparatively high fields of $>$30 G. Here it is shown for the first time that hyperfine-driven magnetic field effect anisotropy is observable at magnetic fields comparable to that of the Earth ($\sim$0.5 G), underlining the feasibility of a chemical compass for avian magnetoreception.

Acknowledgements

First of all, I would like to thank my supervisor, Christiane Timmel, for accepting me in her group and allowing me to work on so many different and all truly captivating and exciting research projects. I particularly enjoyed the freedom I was given to follow my own ideas and the many opportunities I had to present my work at international conferences and seminars. I am extremely grateful for all her help, advice and support over the past years and for her being an amazing person to talk to in difficult moments.

Furthermore, I am grateful to Harry Anderson (University of Oxford, UK) for giving me the opportunity to explore the properties of a large collection of his fascinating porphyrin structures and for co-supervising most of the projects presented in this thesis. In this context I would also like to mention the names of two of my collaborators in the Anderson group, Martin Peeks and Jonathan Cremers, who were available for many valuable discussions.

I am deeply indebted to Ilya Kuprov (University of Southampton, UK) for his contributions to the analysis of the results presented in Chapters 2 and 4 of this work and for sharing his ideas and his vast knowledge on computer simulations of large spin systems with us.

Moreover, I would like to thank Michael Therien (Duke University, USA) for providing the porphyrin samples investigated in Chapter 7 and his student, George Bullard, for synthesising and sending those samples.

I am grateful to Michael Wasielewski (Northwestern University, USA) for inviting me to perform the fs to ms TA studies in his labs, which are presented in Chapter 10. I would also like to thank him for many helpful discussions and advice on science and beyond.

Various other people had a major influence on my scientific destiny and contributed indirectly to this thesis by providing guidance and support over many years. I cannot list all of them here, but would especially like to mention and thank the following people: Malcolm Forbes (Bowling Green State University, USA), Fred Brouwer (University of Amsterdam, NL), Xavier Allonas (ENSCMu/UHA Mulhouse, F), Eric Vauthey (Université de Genève, CH) and Stephan Landgraf (Graz University of Technology, A).

Finally, I am extremely grateful for the pleasant working atmosphere, the absolutely abnormal conversation topics in the group office, the food on **the** table and the enjoyable moments outside the lab, only made possible by the (maybe slightly crazy and definitely not boring) people who surrounded me during the last three years. Thank you to all the present and past members of the Timmel group who shared part of their time at Oxford with me. I shall not attempt to list all names here, but there are a couple of people who definitely deserve to be mentioned: Claudia Tait for patiently teaching me a lot about EPR and being a good friend, Will Myers for many insightful discussions and help with EPR instrumentation, Marcin Konowalczyk for low-pass filtering my thoughts in many late-night discussions and being a fantastic desk-neighbour, Christian Kerpal for the fruitful collaboration on the most amazing topic and the moments when it is just unbelievably enjoyable to be able to talk to somebody in your mother tongue, and Emrys Evans for keeping me company in the office on many weekends and 'early' mornings and generally being there whenever help was required.

Disclaimer

Some passages of text in this thesis, of which I am the sole author, have been quoted verbatim from the following sources issued from the research presented in this work (or the electronic supporting information thereof):

- **Chapter 2:** Richert, S.; Kuprov, I.; Peeks, M. D.; Suturina, E.; Cremers, J.; Anderson, H. L.; Timmel, C. R. Quantifying the Exchange Coupling in Linear Copper Porphyrin Oligomers. *in preparation.*

- **Chapter 3:** **(a)** Richert, S.; Cremers, J.; Anderson, H. L.; Timmel, C. R. Exploring Template-Bound Dinuclear Copper Porphyrin Nanorings by EPR Spectroscopy. *Chem. Sci.* **2016**, *7*, 6952−6960. **(b)** Cremers, J.; Richert, S.; Kondratuk, D. V.; Claridge, T. D. W.; Timmel, C. R.; Anderson, H. L. Nanorings with Copper(II) and Zinc(II) Centers: Forcing Copper Porphyrins to Bind Axial Ligands in Heterometallated Oligomers. *Chem. Sci.* **2016**, *7*, 6961−6968.

- **Chapter 4:** Richert, S.; Cremers, J.; Kuprov, I.; Peeks, M. D.; Anderson, H. L.; Timmel, C. R. Constructive Quantum Interference in a Bis-Copper Six-Porphyrin Nanoring. *Nat. Commun.*, *accepted.*

- **Chapter 5:** Richert, S.; Tait, C. E.; Timmel, C. R. Transient EPR and Hyperfine Spectroscopy for the Study of Triplet State Delocalisation. *J. Magn. Reson.* **2017**, *invited article, submitted.*

- **Chapter 6:** Richert, S.; Peeks, M. D.; Tait, C. E.; Anderson, H. L.; Timmel, C. R. Photogenerated Triplet States in Supramolecular Porphyrin Ladder Assemblies: An EPR Study. *Phys. Chem. Chem. Phys.* **2016**, *18*, 24171−24175.

- **Chapter 7:** Richert, S.; Bullard, G.; Rawson, J.; Angiolillo, P. J.; Therien, M. J.; Timmel, C. R. On the Importance of Electronic Symmetry for Triplet State Delocalization. *submitted for publication.*

- **Chapter 10:** Kerpal, C.; Richert, S.; Storey, J.; Liddell, P. A.; Gust, D.; Hore, P. J.; Timmel, C. R. *in preparation.*

It is not because things are difficult that we do not dare, it is because we do not dare that they are difficult.
– Seneca (4 BC – 65)

To my parents.

Table of Contents

1 Introduction to Electron Paramagnetic Resonance **1**

1.1 Magnetic Interactions . . . 2
1.1.1 Zeeman Interaction . . . 3
1.1.2 Hyperfine Interaction . . . 4
1.1.3 Nuclear Quadrupole Interaction . . . 5
1.1.4 Zero-Field Splitting . . . 5
1.1.5 Interactions Between Different Electron Spins . . . 6

1.2 EPR Instrumentation and Basic Experiments . . . 7
1.2.1 Continuous Wave EPR . . . 7
1.2.2 Pulse EPR Spectroscopy . . . 10

1.3 Hyperfine Spectroscopy . . . 19
1.3.1 ESEEM & HYSCORE . . . 20
1.3.2 Pulse ENDOR . . . 26

1.4 Dipolar Spectroscopy . . . 29
1.4.1 Manifestation of Dipolar Coupling in cw EPR . . . 31
1.4.2 Pulse Dipolar Spectroscopy . . . 33

2 Quantifying the Exchange Coupling in Linear Copper Porphyrin Oligomers **41**

2.1 Investigated Structures . . . 41

2.2 EPR of Linear Copper Porphyrin Oligomers . . . 42

2.3 Numerical Simulations of the cw EPR Spectra . . . 47
2.3.1 Simulation of the Frozen Solution Spectrum of the Dimer . . . 49
2.3.2 Simulations for the Longer Oligomers . . . 52

2.4 Conclusions . . . 54

3 Molecular Geometry and Metal-Ligand Interactions in *c*-P10$_{Cu2}$ Complexes **57**

3.1 Characterisation of the Metal-Ligand Interaction . . . 60
3.1.1 cw EPR . . . 60
3.1.2 Davies ENDOR . . . 61
3.1.3 DFT Calculations . . . 61
3.1.4 Spectral Simulations & HYSCORE . . . 65

3.2 Structure Determination by Dipolar Spectroscopy . . . 69

3.3 Conclusions . . . 75

4 Constructive Quantum Interference in *c*-P6$_{Cu2}$ **77**

4.1 UV-vis and EPR Characterisation . . . 78
4.2 Through-bond Exchange Coupling Detected by DEER . . . 81
4.3 Separation of the Effects of D and J on the DEER Data . . . 83
4.3.1 Determination of D . . . 84
4.3.2 Justification of the DEER Background . . . 85
4.3.3 Quantification of J . . . 87
4.3.4 Verification of the Sign of J . . . 88
4.4 Conclusions . . . 89

5 Introduction to Triplet State EPR 91

5.1 EPR of Porphyrin Triplets . . . 91
5.1.1 Origin of the Triplet Spectrum . . . 92
5.1.2 Interpretation of the Triplet Spectrum . . . 95
5.2 Probing Triplet State Delocalisation . . . 97
5.2.1 Transient cw EPR . . . 98
5.2.2 Triplet State ENDOR . . . 98

6 Triplet State Delocalisation in Zinc Porphyrin Ladders 101

6.1 Ladder Formation and Stability . . . 103
6.2 Transient cw EPR and Simulations . . . 106
6.2.1 Linear Oligomers . . . 106
6.2.2 DABCO Ladders . . . 109
6.3 Mims ENDOR & DFT . . . 110
6.4 Conclusions . . . 114

7 On the Importance of Electronic Symmetry for Triplet State Delocalisation 117

7.1 Investigated Oligomers . . . 118
7.2 Transient cw EPR and Simulations . . . 120
7.3 Mims ENDOR & DFT . . . 122
7.4 Conclusions . . . 126

8 Probing the Alignment of Porphyrins in Liquid Crystals 127

8.1 Liquid Crystal Order . . . 129
8.2 Alignment of Liquid Crystal Samples . . . 132
8.3 Experimental Results . . . 133
8.4 Data Analysis and Simulations . . . 138
8.4.1 Simulations Assuming Biaxiality . . . 141
8.4.2 Validation of the Simulations . . . 142
8.5 Conclusions . . . 144

9 Radical Pair Photophysics under the Influence of Magnetic Fields 147

9.1 Magnetoreception and the Radical Pair Mechanism . . . 149
9.1.1 Experimental Requirements and Considerations . . . 152
9.1.2 Magnetic Field Effect Anisotropy . . . 156
9.2 Radical Pair EPR . . . 158

10 Chemical Compass Behaviour of a Carotenoid–Porphyrin–Fullerene Triad 161

10.1 Characterisation by Optical Spectroscopy and Transient EPR . . . 163
10.1.1 Absorption and Fluorescence . . . 163
10.1.2 Transient Absorption Spectroscopy . . . 164
10.1.3 Transient cw EPR . . . 168
10.2 Magnetic Field Effects in the Low Field Region . . . 169
10.2.1 Earth's Field Effect . . . 170
10.2.2 Isotope Effect . . . 171
10.3 Orientation Dependent Magnetic Field Effects . . . 173
10.4 Conclusions . . . 177

A Experimental Details I

A.1 Sample Preparation . . . I
A.2 Continuous Wave EPR . . . II
A.3 Pulse EPR . . . II
A.3.1 Copper Porphyrin EPR . . . II
A.3.2 Triplet EPR Studies . . . IV
A.4 Transient EPR Laser Setup . . . V
A.5 DFT Calculations . . . VI
A.5.1 Geometry Optimisations . . . VI
A.5.2 Hyperfine Coupling Calculations . . . VI
A.6 Transient Absorption Setup and Data Analysis . . . VII

B Additional EPR Data on Copper Porphyrins IX

B.1 Pulse EPR Data of Linear Bis-Copper Porphyrin Oligomers . . . IX
B.2 Variable Temperature cw EPR of Linear Copper Porphyrin Oligomers . . . X
B.3 EPR Characterisation of ***c*-P6$_{Cu6}$** . . . XIV

C Details of the EPR Simulations using Spinach XXI

C.1 Simulation of the Exchange Coupling in **P2$_{Cu2}$** . . . XXI
C.2 Derivation of the Analytic Expression for DEER Including D and J . . . XXII

D Characterisation of the Metal-Ligand Interaction between P1$_{Cu}$ and Pyridine XXV

D.1 Experimental Results XXV
D.2 Numerical Simulations of the Spectra XXVI

E Orientation Selective DEER on *c*-P10$_{Cu2}$ **XXXI**

F Additional Triplet EPR Data on Zinc Porphyrin Oligomers **XXXIX**

F.1 Butadiyne-Linked Oligomers XXXIX
F.2 Ethyne-Linked Oligomers XL

References **XLIII**

Chapter 1

Introduction to Electron Paramagnetic Resonance

Electron Paramagnetic Resonance (EPR) is a spectroscopic technique which is employed for the characterisation of paramagnetic species, such as organic radicals, radical pairs, triplet states, or paramagnetic metal centres. In the experiment, a static magnetic field of the order of several tens to hundreds of milli-Tesla is typically applied on the sample and transitions between different spin states split by the magnetic field can then be induced by microwave irradiation. Various continuous wave and pulse EPR techniques are available at different microwave frequencies, and can be used to obtain specific information about the interactions of electron spins with the external magnetic field, interactions between different electron spins, or interactions between electron spins and nuclear spins.

In most cases, numerical simulations of the acquired data allow determination of the magnetic parameters of the system, which can then be related to specific molecular properties. In this way, valuable information about the electronic structure and molecular environment of the spin centres is obtained. EPR is therefore often applied, for instance, for the study of through-bond and through-space electronic communication between different subunits of complex molecular structures or for the study of structure and conformational dynamics in biological or synthetic molecular systems. In the absence of paramagnetic centres, spin labelling of the structures at specific sites can make an in-depth EPR investigation possible.

In the present work, various continuous wave and pulse EPR techniques as well as optical spectroscopy are used for the investigation of inter- and intramolecular interactions in porphyrin nanostructures and molecular triad systems. Dipolar, exchange, and metal-ligand interactions are probed in linear and cyclic copper porphyrin structures in Chapters 2 to 4 to investigate electronic communication and molecular structure. Chapter 5 introduces the characteristics of triplet state EPR as a basis for the following Chapters 6 to 8. In Chapters 6 and 7, triplet state delocalisation is studied in different linear zinc porphyrin oligomers and complexes thereof, whereas in Chapter 8, the alignment of porphyrin oligomers in liquid crystals is probed *via* analysis of the corresponding triplet EPR spectra. Finally, Chapters 9 and 10 deal with the investigation of anisotropic magnetic field effects on the recombination kinetics of spin-correlated organic donor-acceptor pairs generated by photoexcitation. Chapter 9 explains the underlying theory, whereas the experimental results obtained on a molecular triad model system using transient absorption spectroscopy are presented in Chapter 10.

In the following, an introduction to the basic concepts of EPR spectroscopy shall be given with the focus on introducing the EPR techniques and instrumentation relevant to the systems studied in this work.

1.1 Magnetic Interactions

EPR spectroscopy relies on the concept of spin. The existence of half-integer spin angular momentum for an electron was originally discovered in the 1920s by O. Stern and W. Gerlach in their famous experiment, where they found that a beam of silver atoms was split into two components by an inhomogeneous magnetic field. Later on, it was concluded that this finding can only be explained if the electron possesses an intrinsic angular momentum, referred to as its spin. The spin angular momentum is denoted $\mathbf{S}$ and has eigenvalues m_S running in integer steps from $-S$ to $+S$ [1]. For an electron, the spin angular momentum quantum number is equal to $\frac{1}{2}$ and therefore two different eigenstates, referred to as the α ($m_S = +\frac{1}{2}$) and β ($m_S = -\frac{1}{2}$) states, are obtained.

Every moving charge possesses a magnetic moment. The magnetic moment, $\boldsymbol{\mu}_\mathbf{e}$, of the electron is directly proportional to its angular momentum, and defined as follows

$$\boldsymbol{\mu}_\mathbf{e} = -g_e \beta_e \mathbf{S} \tag{1.1}$$

where

$$\beta_e = \frac{e\hbar}{2m_e} \tag{1.2}$$

is the Bohr magneton, e and m_e stand for the electron charge and mass, respectively, and g_e is the free electron g-factor (2.0023).

In this work, nuclear spins will be denoted $\mathbf{I}$ and the nuclear magnetic moment is analogously defined as

$$\boldsymbol{\mu}_\mathbf{n} = \gamma_n \mathbf{I} = g_n \beta_n \mathbf{I} \tag{1.3}$$

where γ_n is the gyromagnetic ratio and $\beta_n = \frac{e_n\hbar}{2m_n}$ the nuclear magneton.

In EPR spectroscopy, electron spins are exposed to applied magnetic fields. The acquired experimental EPR spectra are the result of various interactions between the electron spin and the external field as well as between the electron spin and other spins of electronic or nuclear nature. The interactions can be summarised in the so-called spin Hamiltonian, $\mathcal{H}$, which describes the investigated spin system and, for a single electron spin, is given by

$$\mathcal{H} = \mathcal{H}_{\mathrm{EZ}} + \mathcal{H}_{\mathrm{ZFS}} + \mathcal{H}_{\mathrm{HF}} + \mathcal{H}_{\mathrm{NZ}} + \mathcal{H}_{\mathrm{NQ}} \tag{1.4}$$

where the individual contributions are referred to as the electron Zeeman ($\mathcal{H}_{\mathrm{EZ}}$), zero-field splitting ($\mathcal{H}_{\mathrm{ZFS}}$), hyperfine ($\mathcal{H}_{\mathrm{HF}}$), nuclear Zeeman ($\mathcal{H}_{\mathrm{NZ}}$) and nuclear quadrupole ($\mathcal{H}_{\mathrm{NQ}}$) interactions. In the following, the individual contributions to the spin Hamiltonian shall be outlined in more detail. Unless otherwise stated, all Hamiltonians are expressed in energy units.*

*In some of the EPR literature, angular frequency units are used rather than energy units. To obtain the corresponding Hamiltonians in angular frequency units, division of the expressions by $\hbar$ is necessary.

1.1.1 Zeeman Interaction

The interaction of an electron spin with the external magnetic field, represented by the vector **B**, is referred to as the electron Zeeman interaction. The corresponding Hamiltonian is given by

$$\mathcal{H}_{\mathrm{EZ}} = \beta_e \, \mathbf{B} \, \mathbf{g} \, \mathbf{S} \tag{1.5}$$

where the molecule specific **g**-tensor accounts for deviations from the free electron g-value caused by the spin-orbit interaction and describes the orientation-dependent variation of the Zeeman splitting. In its principal axis system, the **g**-tensor

$$\mathbf{g} = \begin{pmatrix} g_x & & \\ & g_y & \\ & & g_z \end{pmatrix} \tag{1.6}$$

can be characterised by the principal values g_x, g_y, and g_z. If $g_x \neq g_y \neq g_z$ the **g**-matrix is orthorhombic. An axially symmetric **g**-tensor is characterised by only two unique principal values, referred to as $g_\perp = g_x = g_y$ and $g_{||} = g_z$, whereas if all principal g-values are identical, the **g**-tensor is said to be isotropic and is reduced to a scalar, the g-value.

Typically, the direction of the applied static magnetic field is taken to define the z-axis of the reference frame. Under these conditions, the electron Zeeman Hamiltonian simplifies to

$$\mathcal{H}_{\mathrm{EZ}} = \beta_e B_0 \, \mathbf{g} \, S_z \tag{1.7}$$

where the field vector is reduced to a scalar with magnitude B_0 and the eigenvalues of the Hamiltonian are proportional to the eigenvalues of S_z [1]. Assuming an isotropic g-factor ($g_x = g_y = g_z$), the energies of the system can consequently be expressed as

$$E = \beta_e B_0 \, g \, m_S \tag{1.8}$$

yielding two states, for $m_S = \pm\frac{1}{2}$, whose energy separation $\Delta E = h\nu = g\beta_e B_0 \, \Delta m_S = g\beta_e B_0$ is linearly proportional to the applied magnetic field strength B_0.

Analogous to the electron Zeeman interaction, a nuclear Zeeman interaction can be defined,

$$\mathcal{H}_{\mathrm{NZ}} = -\beta_n B_0 \, g_n \, I_z \tag{1.9}$$

accounting for the interaction of nuclear spins with an external magnetic field. However, due to their larger mass, the energy separation $\Delta E = \gamma_n B_0$ is about three orders of magnitude smaller for nuclei as compared to electrons. Consequently, while EPR transitions can be excited by microwave irradiation (GHz), radiowaves (MHz) are required for the excitation of nuclear transitions. The nuclear Zeeman effect is therefore often negligible in EPR experiments, unless nuclear couplings are probed explicitly.

Considering only the effect of the electron Zeeman interaction in an $S = \frac{1}{2}$ system, only one single EPR transition with $\Delta m_S = \pm 1$ should be expected, which might be broadened due to **g**-tensor anisotropy. However, a further splitting of the energy levels can be expected from interactions of the electron spin with surrounding nuclear spins of the molecule or interactions with other electron spins.

1.1.2 Hyperfine Interaction

The interaction between an electron spin and nuclear spins is referred to as the hyperfine interaction. It leads to a splitting of the electronic levels into $2I + 1$ sublevels, for a single nuclear spin I, and gives rise to the characteristic hyperfine structure of EPR spectra (if the hyperfine coupling is larger than the line width). The hyperfine interaction is composed of two contributions of different origin, a dipolar and a Fermi-contact term [1]. The Fermi-contact term is isotropic and arises from a finite electron spin-density at the nucleus, whereas the contribution of the dipolar interaction between electron and nuclear spins makes the hyperfine interaction, A, anisotropic. Analogous to the **g**-tensor, the **A**-tensor can be characterised by its principal components A_x, A_y, A_z for an orthorhombic system, or $A_\perp$ and $A_{||}$ for an axial system. In the most general way, the hyperfine interaction Hamiltonian is given by

$$\mathcal{H}_{\mathrm{HF}} = \mathcal{H}_{\mathrm{HF,\,dd}} + \mathcal{H}_{\mathrm{HF,\,contact}} = \mathbf{S}\,\mathbf{A}\,\mathbf{I} \tag{1.10}$$

and the individual contributions can be expressed as

$$\mathcal{H}_{\mathrm{HF,\,dd}} = \frac{\mu_0}{4\pi\, r^3}\, g\beta_e g_n \beta_n \left[\frac{3}{r^2}(\mathbf{S}\,\mathbf{r})(\mathbf{I}\,\mathbf{r}) - \mathbf{S}\,\mathbf{I}\right] \tag{1.11}$$

and

$$\mathcal{H}_{\mathrm{HF,\,contact}} = \frac{2\,\mu_0}{3}\, g\beta_e g_n \beta_n \left|\Psi_0(0)\right|^2 \mathbf{S}\,\mathbf{I} \tag{1.12}$$

with μ_0 being the vacuum permeability, r the distance between the spins connected by the vector **r** and $\left|\Psi_0(0)\right|^2$ the overlap integral corresponding to the electron spin density at the nucleus. In isotropic liquid solution, the anisotropic contribution to **A** ($\mathcal{H}_{\mathrm{HF,\,dd}}$) averages out due to rapid molecular tumbling and the hyperfine interaction can be characterised by a scalar, a_{iso}, and written as

$$\mathcal{H}_{\mathrm{HF,iso}} = \sum_i a_{\mathrm{iso},i}\, S_z\, I_{iz} \tag{1.13}$$

where the sum runs over all nuclei, i, of the system and a_{iso} is defined according to

$$a_{\mathrm{iso}} = \frac{2\,\mu_0}{3}\, g\beta_e g_n \beta_n \left|\Psi_0(0)\right|^2 \tag{1.14}$$

Hyperfine coupling constants can either be positive or negative depending on the product of the sign of the nuclear magnetogyric ratio and that of the spin density at the nucleus. By convention, the hyperfine coupling constant is positive if the electron and nuclear spins are antiparallel in the lowest energy state [1].

1.1.3 Nuclear Quadrupole Interaction

In systems with nuclear spins $I \geq 1$, an uneven charge distribution in the vicinity of the nucleus causes a local electric field gradient which interacts with the quadrupole moment Q of the nucleus. The resulting interaction is referred to as the nuclear quadrupole interaction and defined according to

$$\mathcal{H}_{\mathrm{NQ}} = \mathbf{I}\,\mathbf{Q}\,\mathbf{I} \tag{1.15}$$

The nuclear quadrupole interaction tensor $\mathbf{Q}$ is symmetric and traceless. It can be seen as a measure of the extent to which the charge distribution deviates from spherical symmetry [1]. Typically, the principal axis frame is chosen such that the principal values are ordered as follows $|Q_1| \leq |Q_2| \leq |Q_3|$ and the interaction is normally specified in terms of the nuclear quadrupole coupling constant e^2qQ and the asymmetry parameter η, which relate to the three principal values in the following way

$$\mathbf{Q} = \begin{pmatrix} Q_1 & & \\ & Q_2 & \\ & & Q_3 \end{pmatrix} = \frac{e^2qQ}{4I(2I-1)} \begin{pmatrix} \eta - 1 & & \\ & -\eta - 1 & \\ & & 2 \end{pmatrix} \tag{1.16}$$

where eq is the largest magnitude component of the electric field gradient. The term e^2qQ can either be positive or negative, depending whether the electric charge distribution is oblate ($Q < 0$) or prolate ($Q > 0$), and $0 \geq \eta \geq 1$. In most cases, the nuclear quadrupole interaction is small and its effect on the EPR spectrum can therefore often be neglected.

1.1.4 Zero-Field Splitting

For spin systems with an electron spin of $S > \frac{1}{2}$, a splitting of the electronic energy levels occurs also in the absence of any external magnetic field, due to dipole-dipole interactions and/or second-order effects of the spin-orbit coupling [1]. This energetic splitting is referred to as the zero-field splitting and can in most cases be expressed as

$$\mathcal{H}_{\mathrm{ZFS}} = \mathbf{S}\,\mathbf{D}\,\mathbf{S} \tag{1.17}$$

where $\mathbf{D}$ is the zero-field splitting tensor. By convention, the principal values of $\mathbf{D}$ are energetically ordered so that $|D_Y| \leq |D_X| < |D_Z|$. Typically, the zero-field splitting interaction is parameterised by the two zero-field splitting parameters D and E defined as $D = \frac{3}{2}\,D_Z$ and $E = \frac{1}{2}\,(D_X - D_Y)$. In the principal axis system, the Hamiltonian can therefore be expressed as

$$\mathcal{H}_{\mathrm{ZFS}} = D\left(S_z^2 - \frac{1}{3}S^2\right) + E\left(S_x^2 - S_y^2\right) \tag{1.18}$$

Further details on the zero-field splitting in the case of triplet states are given in Chapter 5.

1.1.5 Interactions Between Different Electron Spins

If the molecular system to be investigated is composed of multiple weakly coupled electron spins, dipolar and exchange interactions between those spin centres need to be considered and can have an important influence on the experimental spectra. The following discussion shall be limited to a two-electron spin system with $S_1 = S_2 = \frac{1}{2}$. The Hamiltonian of such a system is given as

$$\mathcal{H}(\mathbf{S_1}, \mathbf{S_2}) = \mathcal{H}(\mathbf{S_1}) + \mathcal{H}(\mathbf{S_2}) + \mathcal{H}_D + \mathcal{H}_J \tag{1.19}$$

where the subscripts D and J stand for the dipolar and exchange interactions, respectively.

Electron-Electron Dipole Interaction

The Hamiltonian describing the weak dipolar interaction between two electron spins $\mathbf{S_1}$, $\mathbf{S_2}$ each with $S = \frac{1}{2}$ can be expressed as follows

$$\mathcal{H}_\mathrm{D} = \mathbf{S_1}\,\mathbf{D}\,\mathbf{S_2} = \frac{\mu_0}{4\pi\, r^3}\,\mathbf{g_1}\,\mathbf{g_2}\,\beta_e^2\left[\mathbf{S_1}\,\mathbf{S_2} - \frac{3}{r^2}(\mathbf{S_1}\,\mathbf{r})(\mathbf{S_2}\,\mathbf{r})\right] \tag{1.20}$$

where the meanings of the different symbols are analogous to those in **Equation (1.11)**. In typical EPR experiments, the high-field approximation can be assumed to be valid, implying that the electron Zeeman interaction is much larger than the dipolar interaction. Under these circumstances, the Hamiltonian can be simplified to

$$\mathcal{H}_\mathrm{D} = \frac{\mu_0}{4\pi\, r^3}\, g_1 g_2\, \beta_e^2\, \left(1 - 3\cos^2\theta\right)\, S_{1z}\, S_{2z} \tag{1.21}$$

where, furthermore, isotropic **g**-tensors were assumed and θ defines the angle between the spin-spin vector, **r**, and the static magnetic field direction. Expressed in angular frequency units and defining

$$\omega_{dd} = 2\,\pi\nu_{dd} = \frac{\mu_0}{4\pi\hbar\, r^3}\, g_1\, g_2\, \beta_e^2 \tag{1.22}$$

this Hamiltonian becomes

$$\mathcal{H}_\mathrm{D} = \omega_{dd}\left(1 - 3\cos^2\theta\right)\, S_{1z}\, S_{2z} \tag{1.23}$$

which is the form commonly used in dipolar spectroscopy.

Exchange Interaction

The exchange interaction defines the energetic splitting between the singlet and corresponding triplet states in systems with more than one electron spin. In this work, it is defined as

$$\mathcal{H}_\mathrm{J} = J\,\mathbf{S_1}\,\mathbf{S_2} \tag{1.24}$$

where J is the isotropic exchange coupling constant. J-coupling can also be anisotropic owing to spin-orbit coupling contributions ($\mathcal{H}_\mathrm{J} = \mathbf{S_1}\,\mathbf{J}\,\mathbf{S_2}$), but it is usually safe to neglect any orientation dependence for spin-spin separation distances above 1 nm [2], which is the case for all systems

studied in this work. Based on the chosen definition of the exchange coupling Hamiltonian, a positive J-value indicates antiferromagnetic coupling ($E_S < E_T$), whereas a negative value implies ferromagnetic coupling and $E_S > E_T$.[†]

While the dipolar interaction is a through-space interaction and depends to a first approximation only on the distance between the two spin centres, J-coupling is mediated through chemical bonds. Orbital overlap is thus required for J-coupling to be effective. The effect of J-coupling on EPR spectra as well as the quantification of exchange coupling by EPR is detailed for the case of copper porphyrins in Chapters 2 and 4.

1.2 EPR Instrumentation and Basic Experiments

In this section some practical aspects of EPR spectroscopy shall be discussed. We will start with a short description of the instrumentation for both continuous wave and pulse EPR. The aim is not to describe any particular instrument, but rather to illustrate which components a typical EPR spectrometer is composed of and to explain the major functions of these components. After outlining the instrumentation used in pulse EPR, we shall discuss the effect of spin relaxation on EPR spectra and explain the most basic and frequently used pulse sequences before moving on to the description of more advanced pulse experiments in the following sections on hyperfine and dipolar spectroscopy.

1.2.1 Continuous Wave EPR

In a continuous wave (cw) EPR experiment, a spectrum of a paramagnetic sample is recorded under continuous microwave irradiation. For technical reasons and in contrast to most other forms of spectroscopy, the (microwave) frequency is kept constant during the experiment. Rather than the frequency, the magnetic field is swept to obtain the EPR spectrum. The available microwave technology limits EPR experiments to certain microwave frequencies and the spectrometers are therefore typically classified according to their operating frequency. The most commonly employed frequency bands are X-band ($\sim$9.5 GHz), Q-band ($\sim$34 GHz) and W-band ($\sim$95 GHz).

The sample prepared for an EPR experiment is contained in a cylindrical EPR tube, normally made of quartz glass. The outer diameter of the tube depends on the type of spectrometer used and would typically be equal to 3$-$4 mm for measurements at X-band and to 0.6 mm at Q-band. The Boltzmann population differences between the states involved in an EPR transition are very small, leading to weak signals. To enhance the sensitivity of the measurement, the sample is placed in an EPR resonator. These resonators are metal cavities which are designed such that they concentrate the microwave power at the sample. At the resonance frequency of the cavity, a standing wave is formed inside the cavity with the magnetic field maximum at the sample position. Microwaves are generated by a source, which is normally either a klystron or a Gunn diode, are transported through rectangular wave guides and are then coupled into the resonator cavity *via* a

[†] It shall be noted here that different authors often adopt different definitions for $\mathcal{H}_J$. In DFT calculations and in most of the chemistry literature, the Hamiltonian is for instance defined as $\mathcal{H}_J = -2\,J\,\mathbf{S_1}\,\mathbf{S_2}$. The opposite sign implies that antiferromagnetic coupling is in this case indicated by a negative J value.

hole, referred to as the iris. The dimensions of the iris control the amount of microwaves entering and exiting the cavity by changing the impedance matching of the waveguide and cavity, and can slightly be adapted with the help of a so-called iris screw. The iris screw can be adjusted to match the impedances so that no microwaves are reflected back from the cavity at the resonant frequency of the cavity. The quality or Q-factor of the resonator indicates how efficiently a particular cavity stores the microwave energy (i.e. how well the impedances are matched). This Q-factor of the resonator can be changed within a certain range *via* adjustment of the iris whereby three different coupling regimes are generally distinguished: The regime where no microwave power is reflected back from the cavity at the resonant frequency is referred to as 'critical coupling', while 'under-coupling' or 'over-coupling' of the resonator are achieved by slightly increasing or reducing the iris dimensions as compared to critical coupling [3].

When a sample is inserted into an EPR resonator, the resonance properties of the cavity will change depending on the dielectric properties of the sample. Cw EPR experiments are typically carried out under critical coupling conditions. The first step after inserting the sample into the resonator is therefore to adjust the iris at an off-resonance field position to reach critical coupling. In the experiment, when the magnetic field is swept and becomes resonant with an EPR transition, the sample will absorb microwave energy and these increased losses in the cavity will lead to an increase in the impedance of the resonator (under-coupling). As a consequence, microwave power is reflected back from the cavity to the detector. This reflected power constitutes the EPR signal.

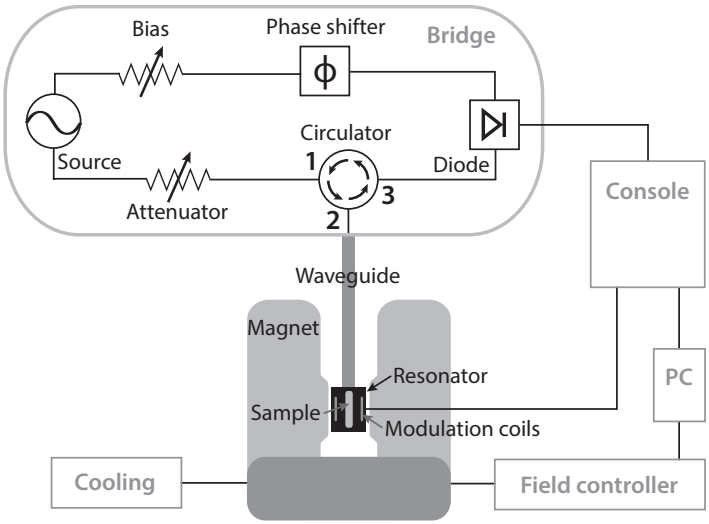


Figure 1.1: Overview of the major components of a continuous wave EPR spectrometer. For measurements at low temperatures further equipment is necessary, such as a vacuum turbo-pump, a temperature control unit and a cryostat connected *via* a transfer line to a liquid helium or nitrogen dewar.

Figure 1.1 shows a schematic drawing of the most important components of a cw EPR spectrometer. The resonator containing the sample is placed between the pole shoes of an electromagnet. Outside the sample compartment, modulation coils are mounted which serve to modulate the magnetic field as will be explained in more detail below. The microwave source and detector are contained in a unit referred to as the microwave bridge. A circulator assures that only the

microwave power reflected from the sample is transferred to the detector. Since the microwave power cannot easily be adjusted at the source, a variable attenuator is placed between the source and the circulator. The signal from the sample is typically detected by a Schottky barrier diode which converts microwave power into electric current. For optimal sensitivity and quantitative measurements, the diode needs to be operated in its linear regime, at microwave powers above 1 mW, where the output current is proportional to the square root of the incoming microwave power [3]. To be able to always operate the detector in its linear regime, a reference arm supplies the detector with some additional microwave power, the bias, which is typically adjusted to yield a detector current of roughly 200 μA. A phase shifter is used in the reference arm before combining the microwave power from the bias and the sample to ensure that the two signals are in phase.

To further increase the detection sensitivity, cw EPR makes use of field modulation. The external magnetic field at the site of the sample is sinusoidally modulated at a fixed frequency of typically 100 kHz. As a consequence, the microwaves reflected back from the cavity are amplitude modulated at the same frequency. When detecting this oscillating absorption signal with a phase-sensitive detector, a derivative line shape is obtained as is illustrated in **Figure 1.2**. Phase sensitive detection has the advantage that any noise from the detector diode and baseline instabilities due to electronic drifts can be considerably reduced. A disadvantage, however, is that signals much broader than the modulation amplitude are difficult to detect since the field modulation will only lead to very small signal oscillations in those cases [4]. In general, the sensitivity increases with the modulation amplitude, as long as the latter does not exceed the line width of the EPR transitions to be detected (i.e. a too large modulation amplitude distorts narrow signals).

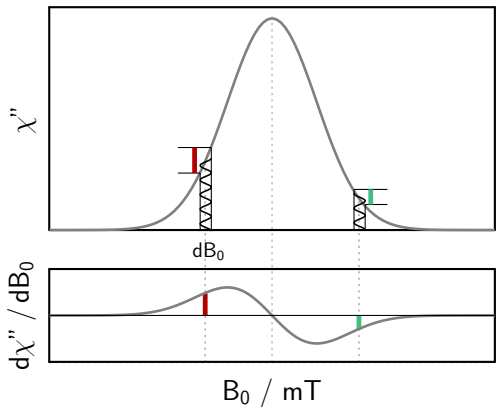


Figure 1.2: Illustration of the effect of B_0 field modulation on an absorptive EPR signal (*top*). A signal with a derivative line shape is obtained (*bottom*).

Finally, the detected derivative signal is processed in the console and acquired on a computer. In the actual experiment, various parameters related to the data acquisition (such as the time constant of the phase sensitive detector, the scan speed, microwave power, modulation amplitude and frequency) need to be optimised to obtain the best possible result. For a detailed discussion on tuning of the instrument and a description of the optimisation of the parameters, the interested reader is directed to references [3] and [4].

1.2.2 Pulse EPR Spectroscopy

In pulse EPR experiments, instead of being continuously irradiated with microwave power, the sample is exposed to a sequence of strong microwave pulses of nanosecond duration. Depending on the applied pulse sequence, different information on various interactions in the sample can be obtained as will become clear in the following sections. The principal components of a pulse EPR spectrometer are similar to those used in cw EPR. In addition, a pulse forming unit (PFU) and a high power traveling-wave tube amplifier (TWT) are required, for generation and amplification of the microwave pulses, and the signal is acquired without making use of field modulation. The PFU is normally equipped with several channels which allow for an individual adjustment of the pulse amplitudes and phases. The high-power microwave pulses can additionally be attenuated using the main attenuator which acts on all channels.

For most pulse EPR experiments, an excitation bandwidth of at least a few tens of MHz is required. The excitation bandwidth (for rectangular pulses), $\Delta\nu$, is inversely proportional to the pulse duration, t_p, which, in most standard experiments, ranges from roughly 4 to 200 ns. Assuming the validity of the empirical relationship $\Delta\nu \simeq \frac{1.2}{t_p}$ [4], this would correspond to bandwidths of about 300 to 6 MHz. In order to avoid a limitation of the excitation bandwidth of the pulses by the resonator bandwidth, defined as the frequency difference between the two frequency points where the power in the resonator is attenuated by a factor of two compared to the centre of the dip (3 dB points), the resonator has to be overcoupled [4].

Apart from bandwidth considerations, another reason for working with an overcoupled resonator is related to the recovery time of the spectrometer, the so-called dead-time. The dead-time depends on the resonator ring-down time[‡] and the receiver recovery time (preamplifier overload) [5]. Normally, ringing of the resonator is the limiting factor and depends on the operating frequency and the quality factor, Q, of the cavity. Overcoupling of the resonator is required in order to keep the spectrometer dead-time short, which is particularly important for fast-relaxing samples.

On the other hand, an overcoupled resonator leads to a lower quality factor of the cavity and consequently lower sensitivity, so the resonator should only be overcoupled as much as needed for a particular experiment. Working with an overcoupled resonator additionally implies that a large percentage of the applied microwave power is reflected back to the detector. Since the reflected power would readily damage the sensitive microwave detector, the latter is protected by a so-called defense pulse. The defense pulse is an additional pulse from the pattern generator which determines the time window during which the power reaching the detector is strongly attenuated by a power limiter or completely blocked using a switch. At X-band, the spectrometer dead-time for an overcoupled resonator typically amounts to about 100 ns. The signals from the sample are then detected by downconversion of the microwave signal to video frequencies making use of difference frequency mixing. At the mixer, the microwave signal coming from the sample is combined with that from the reference arm. In order not to introduce additional noise, none of the

[‡]During a microwave pulse, a significant amount of microwave power enters and is stored in the resonator. This power then radiates towards the receiver after the pulse and needs to be dissipated before data acquisition can start. The ring-down time of the resonator is given as the time it takes for the microwave power to decay to the noise level after application of the microwave pulse.

two components should have an amplitude below the noise-level of the mixer. The signal coming from the sample is therefore pre-amplified and the bias voltage in the reference arm is maximised. After the mixer, the final difference frequency signal can be further amplified by adjustment of the video gain.[§] Usually quadrature detection is employed, which allows detection of both transverse magnetisation components of the signal, referred to as the 'real' and 'imaginary' signals. The final signal phase can be adapted with a phase shifter located in the reference arm.

For more advanced experiments, additional equipment, such as a second microwave source or a radio-frequency (RF) source, amplifier and adapted probe head, may be necessary.

The Effect of Microwave Pulses

In the absence of a microwave pulse, assuming $S = \frac{1}{2}$, the alignment of the spins is either parallel (α) or anti-parallel (β) to the direction of the external magnetic field, which is defined to be the z-axis of the laboratory frame. The fraction of spins aligned anti-parallel to the field is slightly larger at Boltzmann equilibrium, resulting in a net stationary magnetisation along the $+z$ axis. The spins precess around the z-axis at the electron Larmor frequency ω_L corresponding to the applied magnetic field B_0

$$\omega_L = \omega_0 = g_e \, \beta_e \, B_0 \tag{1.25}$$

When a microwave pulse is applied, the z-magnetisation, M_z, is turned by a flip angle β,

$$\beta = \gamma_e \, B_1 \, t_p = \omega_1 \, t_p \tag{1.26}$$

where ω_1 is the amplitude of the B_1 field generated by the microwave pulse in angular frequency units and t_p is the pulse length. In many EPR experiments, the applied pulses need to have a flip angle of either $\frac{\pi}{2}$ or π. According to the above equation, this can be achieved either by adjusting the power of the microwave pulses or their length.

When applying a $\frac{\pi}{2}$ pulse along $+x$, the magnetisation vector is flipped onto the $-y$ axis, and subsequently rotates in the xy plane at the Larmor frequency. For the sake of convenience, we shall now introduce a new coordinate system, referred to as the rotating frame, which rotates at the Larmor frequency ω_0 of the on-resonance spins: In the rotating frame, the magnetisation after application of a $\frac{\pi}{2}$ pulse is now stationary in the xy plane along $-y$.

Since the excitation bandwidth of the available microwave pulses is normally not large enough as to excite the whole EPR spectrum uniformly, only a small fraction of the spins excited by the microwave pulse will exactly be on resonance with the microwave frequency ω_0. For spins which are slightly off-resonance, the microwave pulse will not be an ideal $\frac{\pi}{2}$ pulse and the Larmor precession frequency ω_L will have an offset $\Delta\omega = \omega_L - \omega_0$ with respect to the microwave frequency. In the rotating frame, the magnetisation vector corresponding to these off-resonance spin packets will rotate at the difference frequency $\Delta\omega$. Since this difference frequency corresponds to the signal detected in an EPR experiment, it is most convenient to describe the effect of microwave pulses on the magnetisation in the rotating frame. The experimentally detected EPR signal $V(t)$ can be

[§] A change of the gain by 6 dB corresponds to a change in signal intensity by a factor of two, since the signal intensity is proportional to the square of the microwave power.

expressed as [6]

$$V(t) \propto M_0 \sin\beta\big[\cos(\Delta\omega\, t) + i\, \sin(\Delta\omega\, t)\big] \tag{1.27}$$

where quadrature detection of the 'real' and 'imaginary' signals is assumed and M_0 is the thermal equilibrium magnetisation before the microwave pulse. In the most basic EPR experiments these signals are then recorded either as a function of time at a fixed field or as a function of field at a fixed time delay.

In most cases, EPR lines are inhomogeneous, meaning that the contributing spins exhibit different Larmor precession frequencies even in the case of uniform excitation. An ensemble of spins with a common Larmor precession frequency is referred to as a spin packet and the corresponding homogeneous EPR line is characterised by a line width Γ_{hom}. Inhomogeneous EPR lines arise from a superposition of homogeneous lines corresponding to several spin packets with slightly different centre frequencies.¶

Over time, the excitation of different spin packets with different Larmor frequencies will lead to a dephasing of the magnetisation in the xy plane. Apart from dephasing due to inhomogeneities in the sample, different relaxation mechanisms are operative, which will contribute to the gradual decay of the M_x and M_y magnetisation components and eventually restore the initial Boltzmann equilibrium. This decay of the M_x and M_y components of the magnetisation vector after the pulse is referred to as the free-induction decay (FID). **Figure 1.3** illustrates the effect of a $\frac{\pi}{2}$ pulse along x on the M_z magnetisation using the semi-classical vector picture in the rotating frame. The decay of the magnetisation is only shown schematically. In **Figure 1.4** the time behaviour of the different magnetisation components after the pulse is compared in the laboratory and rotating frames.

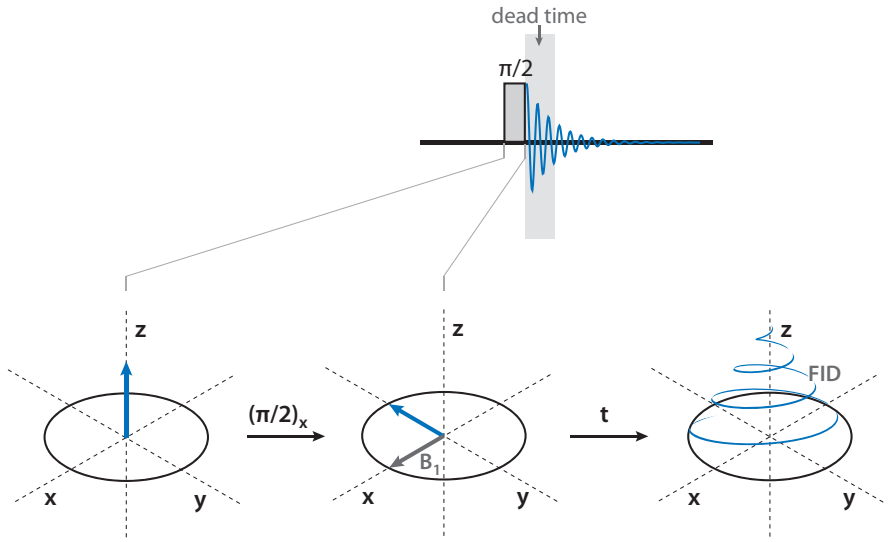


Figure 1.3: Illustration of the effect of a $\frac{\pi}{2}$ pulse applied along the x-axis on the magnetisation using the semi-classical vector model in the rotating frame. After being rotated onto the $-y$ axis, the magnetisation in the xy plane decays with time due to different relaxation mechanisms resulting in an FID signal.

¶While homogeneous lines are typically Lorentzian, inhomogeneous lines are approximately Gaussian in shape. The homogeneous line width of a spin packet is related to the phase memory time (transverse relaxation) of the spins.

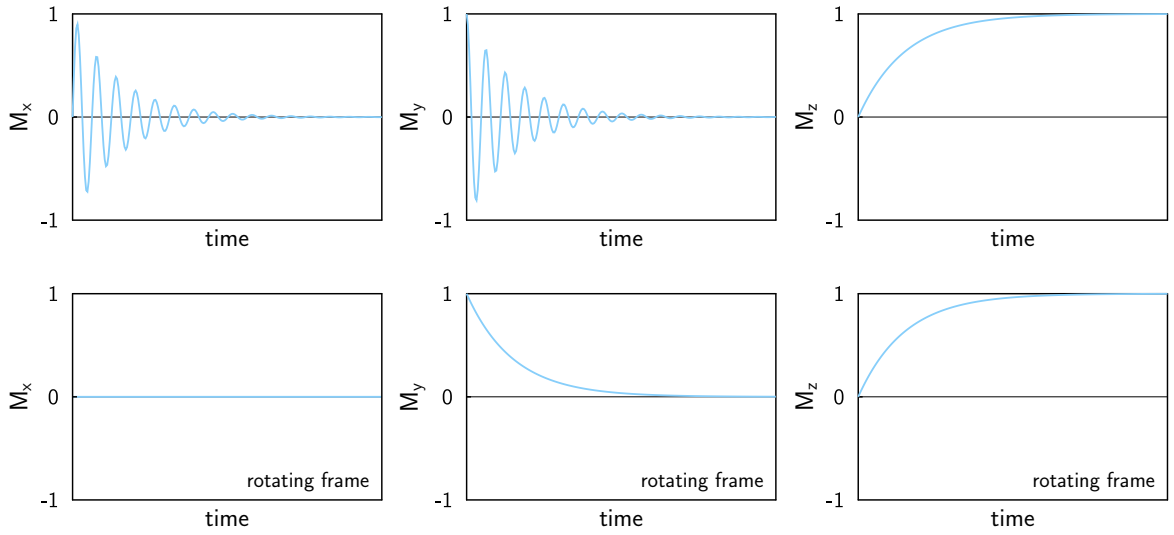


Figure 1.4: Illustration of the time behaviour of the different components of the magnetisation vector after application of a $\frac{\pi}{2}$ pulse along x in the laboratory (*top*) and the rotating (*bottom*) frames for a single spin packet.

Relaxation

Relaxation is caused by fluctuations of the local magnetic field in the vicinity of the electron spin, due to interactions with its environment, and is temperature and field dependent. Generally, two main relaxation mechanisms are distinguished. Any processes reducing the population difference between the two electronic spin states involved in the EPR transition, such as spin-flips caused by dynamic interactions (exchange of thermal energy) of the spins with their local sourroundings, can cause longitudinal relaxation [7]. This mechanism, also referred to as spin-lattice relaxation, is characterised by the relaxation time T_1 and is responsible for restoring the equilibrium M_z magnetisation after the microwave pulse. In systems containing transition metals, the modulation of spin-orbit coupling (i.e. $\mathbf{g}$) is often the main contribution to spin-lattice relaxation and is responsible for the short T_1 values often observed for these compounds [7].

Transverse relaxation, or spin-spin relaxation, described by the relaxation time T_2, is usually caused by energy-conserving spin flip-flops or any other events leading to random fluctuations in the electron precession frequencies and consequently a loss in phase coherence in the xy plane. For transverse relaxation, no exchange of energy with the environment is required. However spin-flips which lead to longitudinal relaxation also cause a loss in phase coherence and therefore contribute to transverse relaxation [6].

The effect of relaxation on the magnetisation can be incorporated into the so-called Bloch equations, which are the equations of motion for the individual components of the magnetisation. These macroscopic equations can only provide a phenomenological picture but are very helpful for understanding many of the basic EPR experiments. The time-behaviour of the individual

magnetisation components is given by

$$\begin{aligned}\frac{\mathrm{d}M_x}{\mathrm{d}t} &= \gamma\big(\mathbf{B}\times\mathbf{M}\big)_x - \frac{M_x}{T_2}\\ \frac{\mathrm{d}M_y}{\mathrm{d}t} &= \gamma\big(\mathbf{B}\times\mathbf{M}\big)_y - \frac{M_y}{T_2}\\ \frac{\mathrm{d}M_z}{\mathrm{d}t} &= \gamma\big(\mathbf{B}\times\mathbf{M}\big)_z + \frac{M_0 - M_z}{T_1}\end{aligned} \tag{1.28}$$

where $\mathbf{M}$ is the total magnetisation, the symbol $\times$ indicates the cross product and the gyromagnetic ratio γ can be replaced by $\beta_e g$ in the case of electron spins. In EPR experiments the total magnetic field $\mathbf{B}$ consists of a static field component, B_0, along z and a time-dependent component B_1, rotating in the xy plane at frequency ω. With

$$\mathbf{B} = \begin{pmatrix} B_1\cos(\omega t)\\ B_1\sin(\omega t)\\ B_0\end{pmatrix} \qquad \text{and} \qquad \mathbf{M} = \begin{pmatrix} M_x\\ M_y\\ M_z\end{pmatrix} \tag{1.29}$$

the above expressions yield

$$\begin{aligned}\frac{\mathrm{d}M_x}{\mathrm{d}t} &= \gamma\big(-M_yB_0 + M_zB_1\sin(\omega t)\big) - \frac{M_x}{T_2}\\ \frac{\mathrm{d}M_y}{\mathrm{d}t} &= \gamma\big(-M_zB_1\cos(\omega t) + M_xB_0\big) - \frac{M_y}{T_2}\\ \frac{\mathrm{d}M_z}{\mathrm{d}t} &= \gamma\big(-M_xB_1\sin(\omega t) + M_yB_1\cos(\omega t)\big) + \frac{M_0 - M_z}{T_1}\end{aligned} \tag{1.30}$$

In most cases (in solid matrices), T_2 is several orders of magnitude shorter than T_1. Furthermore, relaxation can be different for EPR transitions corresponding to different m_I sublevels (and therefore orientation dependent).[‖] Especially for systems containing transition metals, both relaxation times are strongly temperature dependent. In these cases, the measurement temperature is chosen such that the T_2 value is at least in the μs range, whenever possible, since T_2 limits the maximum length of many pulse sequences that can be applied. At the same time it is advisable to try to keep T_1 reasonably short, since it determines the repetition rate of the experiment and therefore the duration of the measurement.

Primary and Stimulated Echo

The detection of the FID after application of a single microwave pulse often proves difficult, especially for fast-relaxing samples, since a lot of information is lost during the spectrometer dead time (cf. **Figure 1.3**). This problem can be overcome by applying a second microwave pulse with flip angle π after a time interval τ as illustrated in **Figure 1.5**. This pulse sequence is referred to as the primary echo or Hahn echo sequence. When applying this sequence, differences in Larmor

[‖] This is usually the case if the modulation of an anisotropic hyperfine interaction contributes significantly to relaxation.

precession frequencies, which arise from excitation of different spin packets and lead to a loss of spin coherence, can be refocussed.

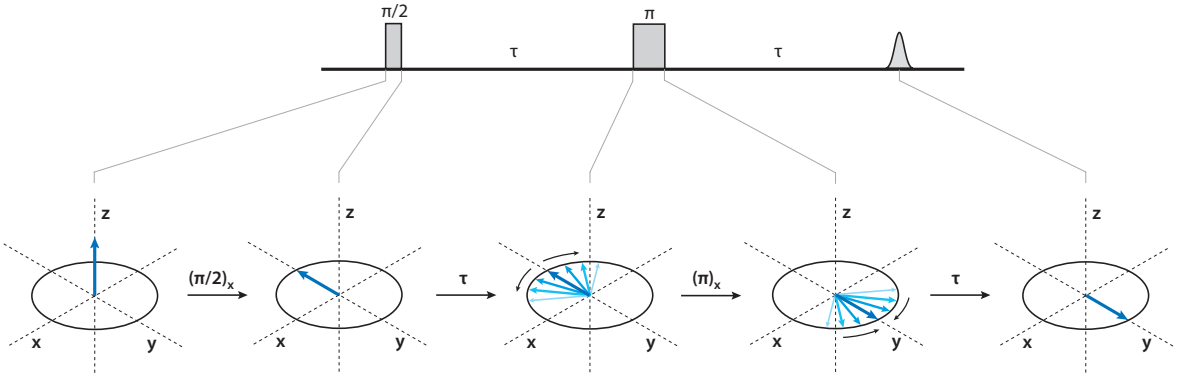


Figure 1.5: Illustration of the pulse sequence for the Hahn echo (*top*) and description of the behaviour of individual spin packets with different Larmor frequencies at selected time points during the sequence (*bottom*) by making use of the semi-classical vector model in the rotating frame. The different arrows in the *xy* plane represent different spin packets, rotating at their respective difference frequency $\Delta\omega$.

As shown in **Figure 1.5**, the initial M_z magnetisation is turned onto $-y$ by a $\frac{\pi}{2}$ pulse applied along $+x$. The magnetisation vectors corresponding to on-resonance spin packets stay along $-y$ in the rotating frame, while those of spin packets with different Larmor frequency start to rotate at different speeds, depending on the frequency offset $\Delta\omega$, which leads to dephasing of the magnetisation in the *xy* plane after a time interval τ. The π pulse which is then applied along $+x$ turns all magnetisation vectors by 180° around the *x*-axis without affecting their rotation sense and speed. After a further time interval τ, all magnetisation vectors will be refocussed along the $+y$ axis and the corresponding peak in signal intensity is referred to as the echo. The echo can be regarded as a pair of back-to-back FID's, so if we were able to excite the whole spectrum uniformly, a Fourier-transform of the second half of the echo should directly yield the EPR spectrum in the frequency domain [1].

Apart from the primary echo sequence, many other pulse sequences can be imagined which lead to the formation of an echo. Of particular use is the simulated echo pulse sequence shown in **Figure 1.6**. It consists of three $\frac{\pi}{2}$ pulses separated by inter-pulse delays of τ and T, respectively. The stimulated echo is then formed after a time τ following the third pulse.

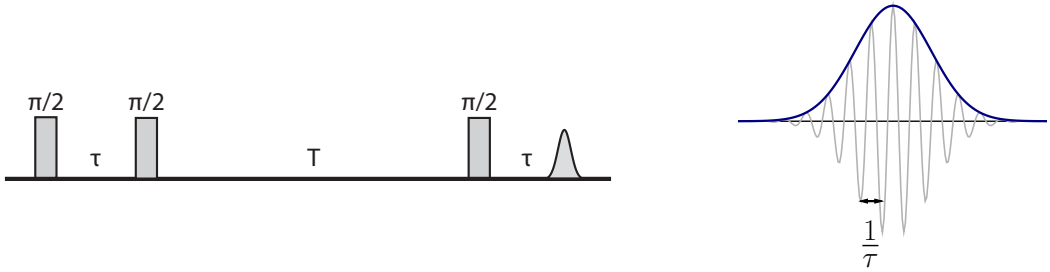


Figure 1.6: Illustration of the pulse sequence for the stimulated echo (*left*) and the polarisation grating across the inhomogeneous EPR line generated after the first two microwave pulses (*right*).

After the first $\frac{\pi}{2}$ pulse, the magnetisation fans out in the xy plane as we have seen before when considering the primary echo sequence. The effect of the second $\frac{\pi}{2}$ pulse applied after a time τ then depends on the offset frequency $\Delta\omega$ of the individual excited spin packets. The magnetisation vectors corresponding to on-resonance spins and spin packets with a rotating frame rotation frequency of $\Delta\omega = \frac{2n\pi}{\tau}$, where $n \in \mathbb{N}_0$, will be aligned along $-y$ after a time τ and the second $\frac{\pi}{2}$ pulse will turn these vectors onto the $-z$ axis. Any spin packets with rotation frequencies of $\Delta\omega = \frac{(2n-1)\pi}{\tau}$ will be aligned along $+y$ at the time $t = \tau$ and the corresponding magnetisation vectors will be rotated back onto the $+z$ axis, while the microwave pulse has no effect on spin packets with rotation frequencies of $\Delta\omega = \frac{(2n-1)\pi}{2\tau}$ which will be aligned along $\pm x$ [8].

Considering all spin packets, the two first $\frac{\pi}{2}$ pulses have the effect of generating an oscillating M_z magnetisation pattern (polarisation grating) with a period of $\frac{2\pi}{\tau}$ across the inhomogeneous EPR line in the frequency domain as shown in **Figure 1.6** (*right*). The transverse magnetisation remaining after the first two pulses then decays during T, while the longitudinal magnetisation pattern is transferred to transverse magnetisation by the third $\frac{\pi}{2}$ pulse and can be detected after a time τ in form of the stimulated echo, which can be regarded as an FID of the M_z magnetisation pattern. A major advantage of the simulated echo pulse sequence as compared to the primary echo sequence is that its maximum length is limited by T_1 rather than T_2.

Apart from the stimulated echo, four other echoes are generated in this three pulse sequence as can schematically be seen in **Figure 1.7**. In the experiment, it is possible to eliminate these additional unwanted echoes by making use of phase cycling. In addition, imbalances in the quadrature detection can be compensated this way. When a phase cycle is applied, the phases of the microwave pulses (and the detector) are changed in subsequent experiments in a predefined way and the resulting signals of the individual experiments are either added or subtracted so as to suppress all unwanted echoes. In the case of the stimulated echo sequence, a four-step phase cycle, composed of two two-step phase cycles $\pm x$ applied to the first two microwave pulses of the sequence, is sufficient to yield the desired result. For more details on coherence transfer pathways and phase cycling the following reviews are recommended [9–11].

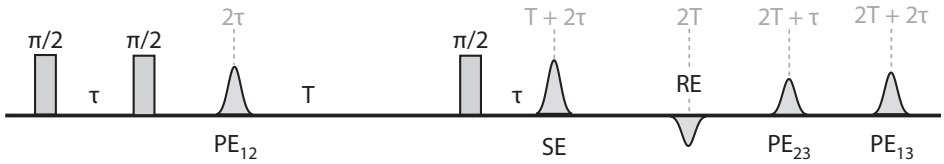


Figure 1.7: Illustration of the stimulated echo pulse sequence including all stimulated (SE), refocussed (RE) and primary (PE) echoes formed at different times in the experiment.

Measurement of Relaxation Times

Characterising the relaxation behaviour of a particular sample is not only important for pulse EPR experiments where relaxation determines the maximum length and repetition rate of a particular pulse sequence, but also for cw EPR where the knowledge of T_1 and T_2 can help to choose an appropriate measurement temperature and avoid power saturation effects. Furthermore, the relaxation rates determine the intrinsic line widths of the EPR transitions.

The determination of T_1 and T_2 often proves difficult in practice, since a variety of additional processes contribute to apparent relaxation other than the spin-flips and spin flip-flops generally thought to be responsible for spin-lattice and spin-spin relaxation, respectively. One complication arises, for instance, from the contribution of processes referred to as spectral diffusion.

The term spectral diffusion encompasses all processes that move spin magnetisation between different positions in the EPR spectrum [7] and the effect becomes apparent due to the limited bandwidth of the applied microwave pulses. Usually, the EPR lines are relatively broad so that not all spins can be excited (uniformly) and we consequently need to consider the presence of excited and non-excited spins. Although the non-excited spins do not, in principle, contribute to the EPR signal, spin flip-flops in the non-excited spin manifold, for instance, can cause changes in the local field at the position of the excited spins which can result in a transfer of magnetisation to parts of the spectrum outside the detection window. In general, spectral diffusion can be caused by many different processes such as electron-electron exchange, electron-nuclear cross relaxation or nuclear spin flip-flops [7]. Such or similar processes lead to a loss in spin coherence and appear as relaxation.

Due to the presence of various relaxation pathways, the relaxation curves measured in an EPR experiment are normally not mono-exponential and, depending on the sample and measurement conditions, it can therefore become difficult to extract the 'true' time constants for T_1 and T_2. The spin-lattice relaxation time T_1 is most often measured either by echo-detected saturation or inversion recovery methods [12]. In an inversion recovery experiment, a strong microwave π pulse initially inverts the magnetisation to the $-z$ axis. In the following, the delay T between the inversion pulse and an echo detection sequence is varied and the magnetisation is recorded as a function of T. A drawback of using the inversion recovery pulse sequence is that any spectral diffusion processes with time constants shorter than T_1 will contribute to the measured relaxation curve [12].

Making use of saturation recovery methods, the effects of spectral diffusion on the recorded relaxation curves can be limited. In a saturation recovery experiment, a long π pulse is initially applied to saturate the EPR transition and suppress the effects of spectral diffusion on the recovery. As it is also the case in an inversion recovery experiment, the magnetisation is then monitored as a function of the delay T between the initial pulse and an echo detection sequence. To separate the effects of spectral diffusion from the 'true' T_1 value, the length of the initial saturating microwave pulse is increased until a limiting value is obtained for the relaxation time, which should correspond to T_1 [12]. The application of this classical saturation recovery sequence with only one, long, saturation pulse can be hindered by technical limitations which do not allow one to make the pulse as long as required (length of the TWT gate). This limitation can partially be overcome by using the picket-fence method [12, 13] where the long π saturation pulse is replaced by a series of π-pulses. However, in this case, the time between the individual π pulses must be kept short relative to the spectral diffusion time to limit unwanted contributions to the measured relaxation curves.

The pulse sequence for the measurement of T_1 by saturation recovery using the Picket fence method is shown in **Figure 1.8**. To build up the relaxation curve, the magnetisation is probed as

a function of the delay T, between the Picket fence pulse train and the echo detection sequence, which is normally incremented logarithmically according to

$$T_{i+1} = T_i + i\,\Delta t_{\text{step}} \tag{1.31}$$

where Δt_{step} is the chosen non-linear time step.

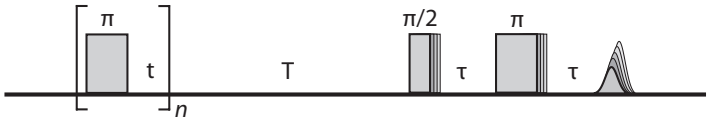


Figure 1.8: Illustration of the pulse sequence for the measurement of T_1 by echo-detected saturation recovery in combination with the Picket fence method.

The transverse relaxation time T_2 is usually approximated by measurement of the phase-memory time T_m. In a T_m measurement, the integrated Hahn echo intensity, I, is recorded as a function of the inter-pulse delay τ and the resulting curve can be fitted to obtain T_m using the following relationship

$$I(\tau) \propto \exp\left(-\frac{2\tau}{T_{\text{m}}}\right) \tag{1.32}$$

The relaxation rate obtained this way contains contributions from all different processes causing loss of electron spin coherence, which needs to be considered in the interpretation of the data if accurate values for T_2 are required.

FID and Echo-detected Field-swept EPR Spectra

The FID and echo pulse sequences discussed above can not only be used as detection sequences in more complicated EPR experiments but can also serve to record the EPR spectra of the compounds under investigation. In such experiments, the integrated FID or echo intensities are recorded as a function of the magnetic field. Compared to cw EPR, the spectra recorded with pulse EPR techniques can often provide complementary information. The use of cw EPR can, for instance, be unsatisfactory in cases where the EPR spectrum consists of both narrow and broad lines, since it may be difficult to find a good compromise regarding the modulation amplitude. A large modulation amplitude enhances the intensities of broad lines, but distorts the shape of narrow lines, whereas a small modulation amplitude might be needed to avoid line shape distortions but implies low sensitivity and the detection of broad features is hindered [6]. While in cw EPR the derivative of the EPR spectrum is detected with the use of field modulation, the application of pulse EPR techniques directly yields the absorption spectrum.

The shape of echo-detected field-swept EPR spectra is dependent on relaxation occurring during the free evolution period τ. If relaxation is strongly field-dependent, typically in the case of broad, anisotropic spectra (leading to orientation-dependent relaxation times), the spectral shape will be different depending on the chosen τ value. Additionally, nuclear modulation effects might lead to spectral shape distortions as they are likely to be orientation-dependent, if present. The contribution of nuclear modulations, which will be discussed in more detail in the next section,

arises from the excitation of forbidden EPR transitions and can therefore be limited by the use of long (i.e. spectrally narrow and thus selective) microwave pulses. In addition, the line width in echo-detected field-swept EPR also depends on the chosen integration window.

Due to these different causes of spectral distortion, it might in some cases be difficult to directly interpret the shape of the measured pulse EPR spectra, however the field-dependence of nuclear modulations and relaxation times can also be useful in some cases, for instance to separate spectra of different species [6]. A great advantage of recording spectra by pulse EPR as compared to cw EPR is the time resolution. The use of pulse EPR makes it possible to study short-lived transient species since the time resolution of the spectrum is solely determined by the time interval between the event creating the transient species (often a laser pulse) and the first microwave pulse. This time interval is generally referred to as the 'delay after flash' (DAF) and can be varied to study the lifetime of transient species.

FID detection of field-swept pulse EPR spectra has the disadvantage over echo-detection that it can only be used for slowly relaxing species. For short-lived species the most important information - or even all information - may be buried in the dead time. If FID detection is possible, it has the advantage that the shape of the spectrum is independent of relaxation and also nuclear modulations do not contribute. The shape of an FID integral detected EPR spectrum should theoretically be identical to the shape of the corresponding integrated cw EPR spectrum.

1.3 Hyperfine Spectroscopy

Having discussed the most basic pulse EPR experiments in the preceding section, this section shall be concerned with the principles of hyperfine spectroscopy including Electron Spin Echo Envelope Modulation (ESEEM) and Electron Nuclear DOuble Resonance (ENDOR) techniques. Both of these groups of techniques are commonly applied and provide complementary information about the coupling of the electron spin to nuclear spins in its vicinity. They measure hyperfine couplings and therefore probe the distribution of the electron spin density within the structure. Applications include the study of molecular structure, coordination effects and electron spin delocalisation.

The magnitude of the coupling to be detected and the available spectrometer frequency bands normally determine whether ESEEM or ENDOR techniques are more suitable for a particular application. In general, ESEEM techniques are more sensitive for small couplings. The strongest ESEEM modulations are observed when the nuclear Larmor frequency is of the same order of magnitude as the hyperfine coupling constant to be detected. This matching regime cannot always be achieved due to technical restrictions regarding the spectrometer frequencies. ENDOR is more sensitive for the measurement of hyperfine couplings larger than about 5 MHz. While the interpretation of ENDOR spectra is often more straightforward, the presence of combination frequencies, matrix signals and uncertainties in dead-time reconstruction can complicate the analysis of ESEEM time traces [6].

1.3.1 ESEEM & HYSCORE

The echo decay measured by variation of the time intervals τ or T in the primary or stimulated echo pulse sequences may be modulated by nuclear transition frequencies. If the hyperfine couplings of the system are evaluated from such an experiment, the corresponding two- or three-pulse sequence with varying inter-pulse delay, is referred to as the 2-pulse or 3-pulse ESEEM sequence.

2-pulse ESEEM

To explain the modulation of the primary echo decay by nuclear frequencies, we shall consider a model system with one electron and one nuclear spin, with $S = I = \frac{1}{2}$ and make use of the vector model. For a nuclear ESEEM effect to be observed, the quantisation axes of electron and nuclear spins must be different, which requires an anisotropic hyperfine interaction and a comparable magnitude of nuclear Zeeman and hyperfine interactions. Since anisotropic hyperfine interactions are required, ESEEM modulations are only observed in the solid state at a field position which does not correspond to one of the principal axes of the **A**-tensor [6].

Figure 1.9 gives an overview of the energy levels and transitions in the model system consisting of an electron and a nucleus. Splitting of the electron spin levels in a magnetic field due to the electronic Zeeman (EZ), nuclear Zeeman (NZ) and hyperfine (HF) interactions results in four energy levels, referred to as the $|\beta\alpha\rangle$, $|\beta\beta\rangle$, $|\alpha\alpha\rangle$ and $|\alpha\beta\rangle$ states, in the order of increasing energy, where the notation $|m_S m_I\rangle$ was adopted. The energetic order of the states shown in the figure applies for weak coupling to a nucleus with positive γ, such as a proton. Between the four states, six transitions are possible, corresponding to formally allowed EPR transitions with $\Delta m_S = \pm 1$ and $\Delta m_I = 0$, formally forbidden EPR transitions with $\Delta m_S = \pm 1$ and $\Delta m_I \pm 1$, and nuclear transitions with $\Delta m_I = \pm 1$ and $\Delta m_S = 0$.

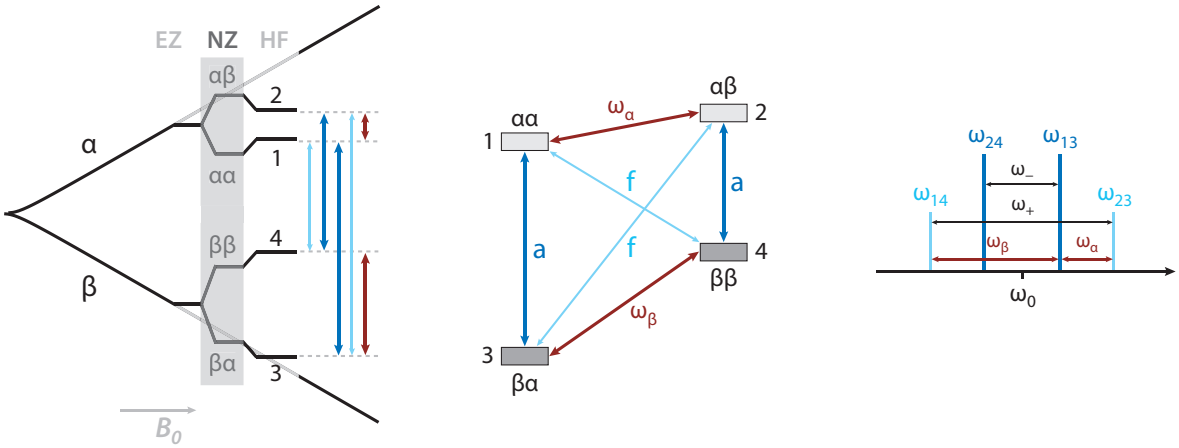


Figure 1.9: Schematic illustration of the energy levels and transitions in a four-level system consisting of an electron and a nucleus, with $S = I = \frac{1}{2}$. EPR transitions are indicated in blue, where the letters *a* and *f* stand for allowed and forbidden transitions, respectively, and nuclear transitions are marked in red.

In the figure, EPR transitions are indicated in blue, whereas nuclear transitions are marked in red. The EPR frequency spectrum of such a system consists of four lines (cf. **Figure 1.9**, *right*), where

the spacing of the lines depends on the nuclear transition frequencies $\omega_\alpha = |\omega_{12}|$ and $\omega_\beta = |\omega_{34}|$ and the relative intensity of the two formally forbidden EPR transitions is strongly dependent on the coupling regime. In **Figure 1.9** the situation is shown in the weak coupling regime where $|A| < 2\,\nu_I$.

In an ESEEM experiment, short (i.e. non-selective) microwave pulses are applied, which excite both the allowed and forbidden EPR transitions. For simplicity, we shall only consider the excitation of a pair of EPR transitions originating from a common energy level, namely the ω_{13} and ω_{23} transitions with a frequency offset of ω_α. We shall further assume that the microwave frequency is in resonance with ω_{13} [8].

Figure 1.10 shows the behaviour of the two magnetisation vectors in the xy plane at various time points in the 2-pulse ESEEM sequence. After the first microwave $\frac{\pi}{2}$ pulse applied along x, both components, a and f, corresponding to the allowed and forbidden EPR transitions with their respective frequencies ω_{13} and ω_{23}, are aligned along $-y$. During the first evolution period τ only the vector labelled f precesses in the rotating frame with frequency $\Delta\omega = \omega_{23} - \omega_{13} = \omega_\alpha$, while vector a precesses at ω_{13} and is therefore static in the rotating frame. The π pulse then rotates the magnetisation vectors by 180° around x and, at the same time, leads to a redistribution of electron coherence, which gives rise to the new components a' and f'. Since a and a' are on resonance, only f and f' precess in the following second evolution period at the frequency ω_α. After a time interval τ following the second pulse the vectors a and f will be aligned along y and give rise to an echo, however, the echo intensity will be reduced as compared to the case where only allowed transitions are excited, since the components a' and f' will in most cases refocus at an orientation other than y. The orientation of these two vectors at the end of the sequence ($t = 2\tau$), and therefore their contribution to the echo (i.e. projection onto the y-axis), depends on the inter-pulse delay τ.

Local intensity maxima are observed for $\tau = \frac{n\,2\pi}{\omega_\alpha}$, where $n \in \mathbb{N}_0$. The echo decay is thus modulated by $\cos(\omega_\alpha \tau)$ and the nuclear transition frequency ω_α can be obtained after subtraction of a decaying background function followed by Fourier transformation of the time trace.

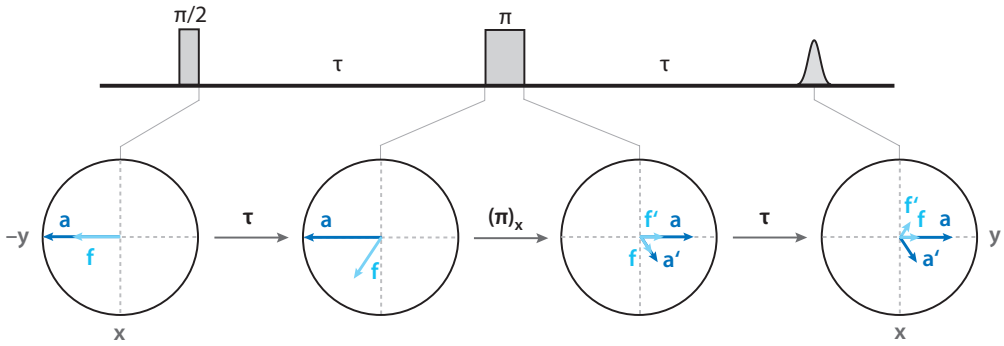


Figure 1.10: Schematic illustration of the redistribution of electron coherence after excitation of an allowed (ω_{13}) and a forbidden (ω_{23}) EPR transition sharing a common energy level in a 2-pulse ESEEM experiment. The behaviour is shown in the rotating frame and ω_{13} is assumed to coincide with the microwave frequency. The frequency offset of the magnetisation vectors f' and a' at the end of the sequence depends on τ and $\Delta\omega = \omega_{23} - \omega_{13}$. The echo decay as a function of τ is consequently modulated by the nuclear transition frequency ω_α.

In an actual 2-pulse ESEEM experiment, several pairs of (a/a, f/f, and) a/f-transitions are excited, which, in addition to ω_α and ω_β, also gives rise to modulations at the combination frequencies ω_+ and ω_- indicated in **Figure 1.9**. As can be inferred from **Figure 1.10**, the modulation depth in such an experiment depends on the relative intensities of the allowed and forbidden transitions. The nuclear modulation effect is maximised if the allowed and forbidden EPR transitions have equal intensities which is achieved in the so-called exact cancellation regime, where the hyperfine and nuclear Zeeman interactions become equal in magnitude, i.e. $|A| = 2|\nu_I|$. In this regime, m_I and m_S are no longer good quantum numbers, leading to a break-down of the EPR selection rules and to four transitions with equal transition probabilities.

Consequently, to maximise the nuclear ESEEM effect, the experiments should be performed at a microwave frequency where the magnitude of the nuclear Larmor frequency equals the magnitude of the hyperfine coupling to be detected. For reference, **Table 1.1** gives an overview of the Larmor frequencies of a range of nuclei at the most common spectrometer frequencies.

Table 1.1: Overview of the nuclear Larmor frequencies of several nuclei at different frequency bands assuming $g = g_e$ and microwave frequencies of 9.5, 34 and 95 GHz for X-, Q- and W-band, respectively. All Larmor frequencies are given in MHz.

Band	$\nu_L(^1H)$	$\nu_L(^2H)$	$\nu_L(^{13}C)$	$\nu_L(^{14}N)$	$\nu_L(^{15}N)$
X	14.5	2.2	3.6	1.0	1.5
Q	51.5	7.9	13.0	3.7	5.2
W	144	22.2	36.3	10.4	14.6

It can for example be seen that small nitrogen couplings of the order of 1 MHz are best detected at X-band, however since most nuclei have similar Larmor frequencies at X-band, making use of higher spectrometer frequencies might allow a better separation of the contributions originating from different nuclei.

So far, to illustrate the use of certain pulse sequences, we have explained the effect of microwave pulses on the magnetisation in terms of the semi-classical vector model. In the case of the excitation of allowed and forbidden transitions and to understand the details of more complicated pulse sequences, it can however be preferable to discuss the spin dynamics in the framework of quantum mechanics using the density matrix or product operator formalisms [1, 6]. Although a detailed discussion of these formalisms is beyond the scope of this introduction, we shall nevertheless outline the basic ideas in this section and review the 2-pulse ESEEM sequence using the density matrix terminology. For additional information, the interested reader is referred to the pertinent literature in the field [1, 6] and references therein.

Density Matrix Formalism

The state of any quantum mechanical system can be entirely described by a matrix ρ of dimension $n \times n$, referred to as its density matrix. The dimension, n, can be calculated for N electrons and

L nuclei of spin quantum number J, according to

$$n = 2^N \cdot \prod_{i=1}^{L} 2J_i + 1 \tag{1.33}$$

Consequently, for a two-spin system composed of an electron and a nuclear spin with $S = I = \frac{1}{2}$, we have $n = 4$. Let us first consider a single electron spin with $S = \frac{1}{2}$. This electron spin can either be in its $|\alpha\rangle$ or $|\beta\rangle$ state and the corresponding wavefunction $|\psi\rangle$ can be described as a linear combination of the two states

$$|\psi\rangle = c_1|\alpha\rangle + c_2|\beta\rangle = \begin{pmatrix} c_1 \\ c_2 \end{pmatrix} \tag{1.34}$$

where c_1 and c_2 are complex coefficients satisfying the normalisation condition $|c_1|^2 + |c_2|^2 = 1$. The density matrix is then defined as the outer product of the wavefunction

$$\rho = |\psi\rangle\langle\psi| = \begin{pmatrix} c_1 \\ c_2 \end{pmatrix} \begin{pmatrix} c_1^* & c_2^* \end{pmatrix} = \begin{pmatrix} |c_1|^2 & c_1 c_2^* \\ c_1^* c_2 & |c_2|^2 \end{pmatrix} \tag{1.35}$$

where the subscript * denotes the complex conjugate. The diagonal elements of the density matrix are real quantities and indicate the probabilities of finding the particle in the respective state as can be seen from the above equation. Diagonal elements are referred to as populations, P, and differences between population states are called polarisations and correspond to longitudinal magnetisation (M_z). Off-diagonal elements, which are superpositions of population states, are termed coherences. While populations are stationary, coherences are time-dependent. In an EPR experiment, coherences are detected, which correspond to magnetisation in the xy plane (M_x, M_y).

The time evolution of the density matrix is described by the Liouville-von-Neumann equation

$$\frac{\mathrm{d}\rho}{\mathrm{d}t} = \frac{i}{\hbar}[\rho, \mathcal{H}] \tag{1.36}$$

which, for a time-independent Hamiltonian, yields

$$\rho(t) = \exp(-i\mathcal{H}\Delta t/\hbar)\,\rho_0 \exp(i\mathcal{H}\Delta t/\hbar) \tag{1.37}$$

where the exponential operator, $\exp(i\mathcal{H}\Delta t/\hbar)$, is called a propagator [6]. Even the effect of complicated EPR pulse sequences on the magnetisation can conveniently be described using the density matrix formalism, where the pulse sequence is divided into several time intervals governed by different time-invariant Hamiltonians and the effect of pulses or free evolution periods on the initial density matrix, ρ_0, is simulated in analogy to **Equation (1.37)**. The state of the system can then be probed at any time and the result is obtained by calculating the expectation value of any

desired operator such as S_y according to

$$\langle S_y \rangle = \text{trace}\,(S_y\,\rho(t)) \tag{1.38}$$

Microwave pulses excite different transitions between population states and consequently generate coherences between them. In the course of an EPR experiment coherences can be transferred, resulting in the generation of polarisation, nuclear coherence or different electron coherence. Finally, at the end of the experiment, the remaining in-phase electron coherence is detected. In the 2-pulse ESEEM experiment described before, electron coherence generated by the first $\frac{\pi}{2}$ pulse is transferred between allowed and forbidden EPR transitions as an effect of the second microwave pulse. The 4×4 density matrix of the system can be visualised as shown in **Figure 1.11**. Allowed EPR transitions are always single-quantum (SQ) transitions, whereas forbidden EPR transitions can be divided into zero-quantum (ZQ) and double-quantum (DQ) transitions depending on the value of $\Delta m_S + \Delta m_I$.

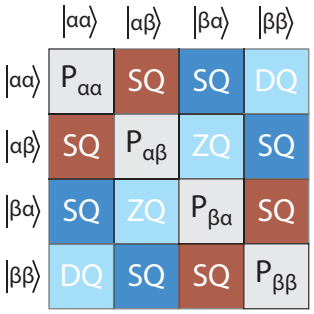


Figure 1.11: Schematic visualisation of the elements of a density matrix for a four-level system composed of an electron and nuclear spin with $S = I = \frac{1}{2}$. Populations are labelled with the letter P whereas electron and nuclear coherences are labelled according to their coherence order as zero-quantum (ZQ), single-quantum (SQ) and double-quantum (DQ) coherences. The adopted colour scheme coincides with that of the preceding figures.

3-pulse ESEEM

The 3-pulse ESEEM experiment relies on the stimulated echo pulse sequence shown in **Figure 1.6**. While in 2-pulse ESEEM only electron coherences are mixed, the second $\frac{\pi}{2}$ pulse in 3-pulse ESEEM transfers electron into nuclear coherence which subsequently evolves during T [8]. The third pulse then transfers the nuclear coherence back to electron coherence which is detected. In contrast to 2-pulse ESEEM, the modulations observed in 3-pulse ESEEM do not contain the sum- and difference frequencies, ω_+ and ω_-, which potentially simplifies the analysis. A complication however, arises from the fact that the amplitudes of the frequencies ω_α and ω_β do not only depend on T, but also on τ. In a standard 3-pulse ESEEM experiment only T is incremented, whereas the value for τ needs to be chosen and is kept constant. Depending on the chosen value of τ, the modulation amplitude for certain nuclear frequencies will be zero, leading to the suppression of the corresponding peaks in the ESEEM spectrum. Frequencies with zero modulation amplitude are referred to as 'blind spots' and occur for nuclear frequencies of $\omega_{\alpha/\beta} = \frac{n\,2\pi}{\tau}$, with $n \in \mathbb{N}_0$. To compensate for the blind spot behaviour, it is generally recommended either to use short τ values

which satisfy the condition $\tau < \frac{2\pi}{\omega_{\alpha/\beta,\,\mathrm{max}}}$ or to record 3-pulse ESEEM time traces for several τ values and combine the results.

An advantage of 3-pulse ESEEM over 2-pulse ESEEM is the narrower line width of the peaks and therefore better resolution generally observed. This is due to the fact that in 2-pulse ESEEM nuclear frequencies are measured as differences between electron transition frequencies [6]. Consequently, the experimental line width, which is inversely proportional to the relaxation time, is determined by the electron rather than the nuclear coherence decay. While electron coherence decays with T_m, the transverse nuclear relaxation time is rather of the order of T_1 of the electrons and so the lines observed in a 2-pulse ESEEM experiment are broader than would be expected. In 3-pulse ESEEM, nuclear coherences are created and decay with their characteristic time constant during T, resulting in narrower lines. Additionally, the maximum length of the time trace which can be recorded is increased significantly as compared to 2-pulse ESEEM.

HYSCORE

Correlation between the nuclear frequencies of different m_S manifolds can be achieved in a two-dimensional experiment referred to as HYSCORE for HYperfine Sublevel CORrElation spectroscopy [6], which has been proposed in the 1980s by Höfer et al. [14].

The pulse sequence used in HYSCORE, shown in **Figure 1.12**, is similar to the 3-pulse ESEEM sequence, only that the evolution period T is divided in two time intervals, t_1 and t_2, by a non-selective π pulse which mixes nuclear coherence between the different m_S manifolds. The intervals t_1 and t_2 are incremented separately to obtain a two-dimensional data set. After background correction and 2D-Fourier transformation a two-dimensional frequency correlation map is obtained. Nuclear coherence which has evolved with frequency ω_{12} during the time interval t_1 will evolve with frequency ω_{34} during t_2 and vice versa, leading to the observation of cross peaks at $(\omega_\alpha, \omega_\beta)$ and $(\omega_\beta, \omega_\alpha)$.



Figure 1.12: Illustration of the pulse sequence for HYSCORE.

Unwanted coherence transfers, due to the excitation of forbidden EPR transitions, additionally result in axial peaks at positions $(\omega_\alpha, 0)$, $(\omega_\beta, 0)$, $(0, \omega_\alpha)$, $(0, \omega_\beta)$ in the HYSCORE spectrum. Since the transfer of nuclear coherence by the mixing π pulse is rarely complete due to pulse non-ideality,** additional diagonal peaks are normally observed.

In the weak coupling case, $|A| < 2|\nu_I|$, the wanted cross-peaks appear in the $(+/+)$ quadrant of the spectrum, whereas they can be found in the $(-/+)$ quadrant in the case of strong coupling. Similar to 3-pulse ESEEM, blind spots also occur in HYSCORE experiments and need to be

**Since not all spin packets are on resonance with the π pulse, not all nuclear coherence is influenced by the pulse and continues to evolve at the same frequency during t_1 and t_2 leading to peaks at $(\omega_\alpha, \omega_\alpha)$ and $(\omega_\beta, \omega_\beta)$. It is therefore advisable to make the π mixing pulse as short as possible to achieve a large excitation bandwidth.

considered in the analysis. More details on the experiment and interpretation of the spectra can for example be found in [6].

1.3.2 Pulse ENDOR

Apart from ESEEM, the other type of spectroscopy which can be used for the measurement of hyperfine coupling constants by EPR is ENDOR. In contrast to ESEEM, ENDOR measurements require additional equipment such as a resonator equipped with RF coils as well as a radio-frequency source and amplifier connected to the probe head and interfaced with the spectrometer software.

Mainly two different pulse sequences are in use for pulse ENDOR experiments, which are referred to as Mims and Davies ENDOR, respectively, and are both based on the transfer of spin polarisation between electron and nuclear transitions. The use of Davies ENDOR should generally be preferred for large couplings, whereas Mims ENDOR performs better for smaller nuclear frequencies.

Depending on the relative magnitude of the hyperfine coupling to be detected as compared to the nuclear Larmor frequency, we distinguish a weak and a strong coupling regime. In the weak coupling regime, $|A| < 2|\nu_I|$, the two nuclear transitions are centred around the nuclear Larmor frequency ν_I and are separated by the hyperfine coupling constant A, whereas in the strong coupling regime, $|A| > 2|\nu_I|$, the transitions are centred around $\frac{A}{2}$ and separated by $2\nu_I$. Compared to ESEEM spectra, the interpretation of ENDOR data is normally more straightforward since only nuclear single quantum transitions are observed. In the following description of the pulse sequences, we shall again base our discussion on a model system composed of an electron and a nucleus with $S = I = \frac{1}{2}$ and assume an isotropic hyperfine coupling constant A.

Davies ENDOR

The pulse sequence applied in Davies ENDOR is shown in **Figure 1.13**. A long microwave π pulse selectively inverts the polarisation of one of the two allowed EPR transitions and is followed by a mixing period, T, during which a selective radio-frequency π pulse is applied. Finally, changes in polarisation induced by the RF pulse are measured using a two-pulse echo detection sequence.

In the experiment, the RF frequency is swept and the integrated EPR echo intensity is probed as a function of the radio-frequency. Whenever the RF pulse is in resonance with a nuclear transition of the system, a polarisation transfer occurs which has the effect of saturating both EPR transitions as schematically illustrated in **Figure 1.13**. As a consequence, the EPR echo intensity is reduced, resulting in a spectrum with peaks at the nuclear transition frequencies.

In most cases, non-selective microwave pulses are used to detect the changes in polarisation and the overall echo shape then results from two contributions: In the centre of the echo, an intense narrow echo signal is observed which arises from the contribution of all spin packets which were not inverted by the selective π microwave preparation pulse but excited by the nonselective microwave pulses of the detection sequence. This narrow signal is superimposed on a broad echo signal with opposite phase originating from the hole created by the first microwave and radio-frequency pulses. To obtain the ENDOR spectrum, the whole echo should be integrated [6].

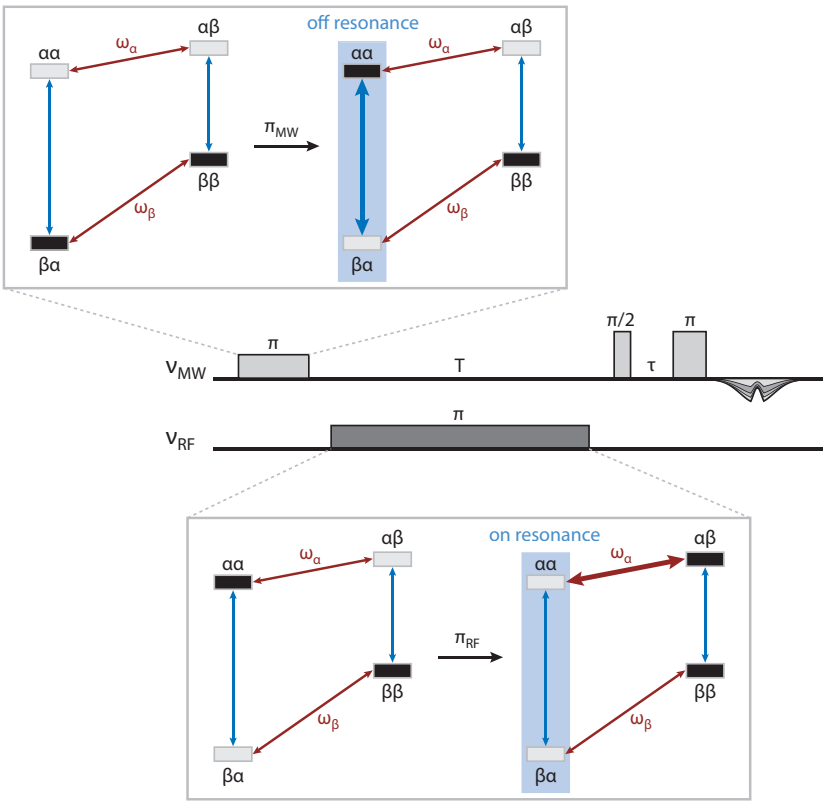


Figure 1.13: Illustration of the pulse sequence and the polarisation transfer induced by the pulses in Davies ENDOR.

Ideally, in order to avoid power saturation effects resulting in (power) broadening of the signals, the length of the RF π pulse should be longer than the nuclear phase memory time. In addition, longer RF pulses increase the selectivity. However, the length of the RF π pulse is limited by the maximum length of T and therefore by T_1. In many cases, it is thus advantageous to perform ENDOR experiments at low temperatures to increase not only T_1 but also the Boltzmann population differences between the energy levels and hence the sensitivity.

The detection of a Davies ENDOR signal can become difficult for small hyperfine couplings, owing to the excitation bandwidth of the microwave pulses. If the two EPR transitions can no longer be excited selectively, both EPR transitions are excited by the inversion pulse and the RF π pulse, even if on resonance, cannot have any effect on the populations. Generally, in the presence of small hyperfine couplings of only a couple of MHz, the use of Mims ENDOR should be preferred.

Mims ENDOR

The Mims ENDOR pulse sequence is based on the stimulated echo sequence and is shown in **Figure 1.14**. Non-selective microwave pulses are used and blind spots are observed as discussed before for 3-pulse ESEEM. The first two $\frac{\pi}{2}$ pulses prepare a polarisation grating and are followed by a mixing period T during which a selective RF π pulse is applied. The excitation of a nuclear transition by the RF pulse leads to a shift in the Larmor precession frequency of the electron spins, which is determined by the magnitude of the hyperfine coupling. As a consequence, the

magnetisation cannot be refocussed completely by the third microwave pulse and the echo intensity is reduced [6]. When plotting the integrated echo intensity as a function of the radio-frequency, we obtain a spectrum reflecting the frequencies of the nuclear transitions.

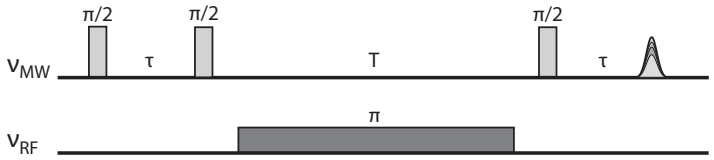


Figure 1.14: Illustration of the pulse sequence for Mims ENDOR.

Due to the presence of blind spots, the Mims ENDOR efficiency varies periodically as a function of the nuclear transition frequency according to

$$I_{\text{Mims}} \propto 1 - \cos(2\pi A\tau) \tag{1.39}$$

Consequently, depending on the chosen value for τ, selective frequencies in the ENDOR spectra are suppressed. For a given τ value, blind spots occur for nuclear frequencies of

$$\nu_{\text{blind}} = \frac{n}{\tau} \qquad n \in \mathbb{N}_0 \tag{1.40}$$

whereas intensity maxima are observed for

$$\nu_{\text{max}} = \frac{n + 0.5}{\tau} \qquad n \in \mathbb{N}_0 \tag{1.41}$$

To limit spectral distortions, it is therefore recommended to always repeat the experiment with a range of different τ values and to add the individual results. To illustrate the effect of blind spots, an example of the variation in the relative ENDOR intensity as a function of the nuclear transition frequency is shown in **Figure 1.15** for three different τ values and their (normalised) sum. The number of blind spots can be limited by the use of relatively short τ values, however the spectrometer dead time usually precludes the use of inter-pulse delays shorter than about 100 ns.

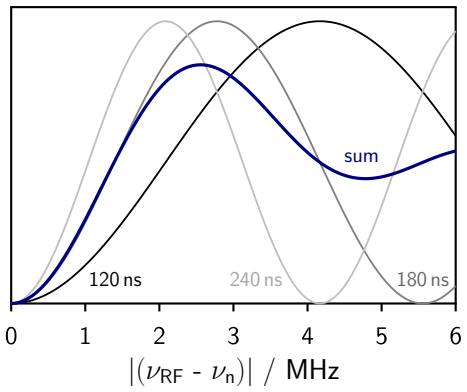


Figure 1.15: Illustration of the relative Mims ENDOR intensity as a function of the nuclear transition frequency for different τ values of 120, 180, and 240 ns and their sum.

Regarding the variation of the ENDOR intensity as a function of τ it is interesting to note that the choice of a large τ value can sometimes be advantageous for the detection of very small hyperfine couplings. For couplings of the order of 1 MHz, maximum efficiency is for example obtained for a value of $\tau = 500$ ns [6]. However such large τ values will result in an increased number of blind spots and should/can only be used if transverse relaxation is relatively slow.

Apart from hyperfine couplings between the electron spin and nuclear spins of the same molecule, also more distant nuclei can contribute to the ENDOR signal under some circumstances. Especially if the experiments are performed in frozen protonated matrices, distant (solvent) protons can give rise to small couplings which result in the observation of a matrix line at the ^{1}H Larmor frequency.

Due to the blind spot behaviour, it is generally difficult to compare peak intensities and line shapes for spectra measured using Mims and Davies ENDOR. In addition, the use of non-selective pulses in Mims and selective microwave pulses in Davies ENDOR can potentially lead to differences in the shape of the recorded spectra since different fractions of spins contribute to the signal in those two cases. Because more spin packets are excited in Mims ENDOR, the latter technique is inherently more sensitive.

1.4 Dipolar Spectroscopy

Information on the weak dipolar interaction, D, between two coupled electron spins in a nano-object can be obtained by a range of different spectroscopic techniques including cw as well as pulse EPR. We will base the following discussion on a system composed of just two (identical) coupled spin centres with spin $S = \frac{1}{2}$, which will be referred to as the A and B spins. Since the dipolar interaction is inversely proportional to the cube of the distance between the two spin centres, dipolar spectroscopy is often used for the determination of distances and distance distributions, yielding valuable information about molecular structure, conformations and flexibility.

The use of EPR has a couple of advantages over other techniques commonly applied for the investigation of (long-range) molecular structure, such as nuclear magnetic resonance (NMR) and X-ray crystallography. X-ray diffraction typically requires the availability of single crystals, which often cannot easily be obtained. Furthermore, X-ray experiments are performed in the solid state, where the investigated compounds might adopt a different conformation to that in solution or biological environments and no dynamic information can be extracted. In NMR experiments, the accessible distance range for molecular interactions is shorter and NMR is inherently less sensitive due to the larger magnetic moment of the electron spin as compared to nuclear spins [2]. In addition, NMR measurements typically become difficult to analyse for large structures or when paramagnetic centres are present.

Depending on the molecular structure and inter-spin distance, not only the dipolar interaction but also the exchange coupling interaction, J, between the two considered spin centres might be significant. The magnitude of J as compared to D defines the applicable coupling regime. In the weak coupling regime, we have

$$|\omega_A - \omega_B| \gg \left| J + \frac{\omega_{dd}}{2} \right| \tag{1.42}$$

whereas in the strong coupling regime the opposite holds true.

When introducing the electron dipole-dipole interaction in **Equations 1.23** and **1.22**, we have seen that its magnitude depends on the distance, r_{AB}, between the two spin centres as well as the angle, θ, between the spin-spin vector, **r**, and the direction of the external magnetic field according to

$$D = \frac{1}{r_{AB}^3}\frac{\mu_0}{4\pi\hbar} g_A g_B \beta_e^2 \left(1 - 3\cos^2\theta\right) = \omega_{dd}\left(1 - 3\cos^2\theta\right) \tag{1.43}$$

In a powder or isotropic frozen solution all molecular orientations are equally likely, however much fewer of these orientations correspond to an angle θ of 0° as compared to 90°. Considering all orientations, a $\sin\theta$ weighting needs to be applied and the resulting powder pattern for a single distance r_{AB} is referred to as a Pake pattern.

Figure 1.16 shows the Pake pattern for an inter-spin distance of 1.3 nm in the weak and strong coupling regimes. The points of maximum intensity correspond to orientations where $\theta = 90°$, whereas the outer edges of the Pake pattern indicate the dipolar coupling strength at $\theta = 0°$.

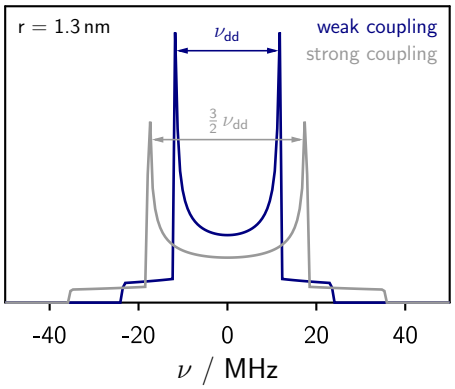


Figure 1.16: Pake pattern for a distance of 1.3 nm in the limits of weak and strong coupling.

In the weak coupling regime, the points of maximum intensity are separated by ν_{dd} and the edges of the Pake pattern by $2\nu_{dd}$ in the absence of exchange coupling. Small exchange couplings shift the turning points of the Pake pattern and the two distances become $\nu_{dd} - J$ and $2\nu_{dd} + J$, respectively [15]. For larger J values, the strong coupling regime might become applicable, where the points of maximum intensity are separated by $\frac{3}{2}\nu_{dd}$ and the outer edges by $3\nu_{dd}$. In the strong coupling regime, the Pake pattern does not contain any information on the magnitude of the exchange coupling.

In the following, we will discuss how distance information can be extracted from different types of EPR measurements based on the measurement of electron dipolar interactions. Short distances up to roughly 2 nm can be detected making use of cw EPR, whereas longer distances between roughly 1.5 and ~8 nm can be measured by pulse EPR techniques [16, 17]. Unless otherwise stated, we shall assume for most parts of the discussion that the influence of the exchange interaction J is negligible. In fact, it is very often assumed in the literature that J-couplings can be neglected for distances greater than 1 or 1.5 nm due to the approximately exponential dependence of the exchange coupling on distance. However, it has to be mentioned at this point, that the validity of this assumption always needs to be carefully verified in experiments, especially when dealing with

highly conjugated systems. Several cases are known, where significant exchange coupling was still observed for distances greater than 3 nm [18]. In this work, the manifestation of exchange coupling in cw EPR spectra and pulse dipolar spectroscopy is examined in Chapters 2 and 4.

1.4.1 Manifestation of Dipolar Coupling in cw EPR

If the distance between the two spin centres is shorter than about 1 nm, information on the dipolar coupling can often be inferred from the intensity of the so-called half-field transition [15, 16, 19, 20]. At those short distances, exchange coupling leads to mixing of the singlet and $|T_0\rangle$ states, whereas the $|T_+\rangle$ and $|T_-\rangle$ states are essentially unaffected and are shifted by the dipolar interaction D in the same way. The formally forbidden double quantum transition with $\Delta m_S = \pm 2$ becomes partially allowed and its intensity depends on D. At a given microwave frequency, this transition occurs at half the field strength as compared to the respective allowed single quantum transition, hence the name. It has been shown that the ratio of the integrated intensity of the half-field transition to the integrated intensity of the single-quantum transition can be related to the inter-spin distance, r_{AB}, and is independent of J as long as J is isotropic [15, 16].

If the inter-spin distance ranges between 1 and ∼1.8 nm and no half-field signals are observable, information on the distance can be obtained from an analysis of the cw EPR line shape [15]. Whether the effect of dipolar coupling on the line shape of the cw EPR spectrum is significant depends on the relative magnitude of the dipolar coupling as compared to the overall spectral width. In samples with large **g** or **A**-tensor anisotropies and therefore broad spectra, dipolar couplings above 1.5 nm might not have any discernible effect. The dependence of the magnitude of the dipolar coupling on the inter-spin distance, r_{AB}, is shown in **Figure 1.17** for $g = g_e$. It can be seen that the expected coupling for a distance of 1 nm is about 50 MHz, whereas this value drops rapidly to about 6 MHz for an inter-spin distance of 2 nm. If the g value of the system deviates significantly from the free electron g-factor, the following corrections may be applied

$$\nu_{dd,2} = \nu_{dd,1} \frac{g_2^2}{g_1^2} \qquad \text{and} \qquad r_2 = r_1 \left(\frac{g_2^2}{g_1^2} \right)^{1/3} \tag{1.44}$$

Since any fixed distance corresponds to a distribution of dipolar couplings described by a Pake pattern, the dipolar spectrum corresponding to a known distance distribution is a superposition of Pake patterns [2]. The presence of a dipolar interaction, D, between two spins should thus result in a broadening of the cw EPR spectrum, where the overall line shape of the coupled system is given as the convolution of the spectrum of the isolated spin with a distribution of Pake patterns corresponding to the expected distance distribution.

Although also other methods are in use, the described procedure referred to as dipolar convolution is probably the most commonly applied approach for the determination of dipolar interactions by cw EPR and will be described in the following paragraphs. For details on other methods the interested reader is referred to the literature [16, 17].

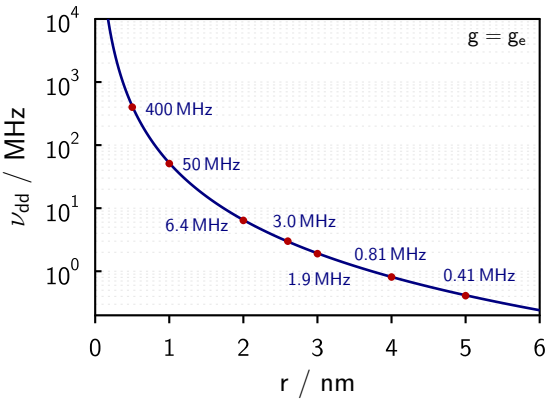


Figure 1.17: Dipolar coupling frequency as a function of the inter-spin distance for $g = g_e$.

Dipolar Convolution

The method of dipolar convolution can be used to measure distances in the range from approximately 0.4 to 2 nm. It relies on the dipolar broadening of the cw EPR spectrum in the presence of dipolar coupling between two spin centres. From the degree of broadening of the spectrum as compared to a reference spectrum, the strength of the dipolar coupling is deduced. Ideally, the reference compound needs to be almost identical to the one under study but only contain one of the two spin centres. To reproduce the spectrum of the compound containing two spin centres, the reference spectrum is convoluted with a Gaussian distribution of Pake patterns, resulting from a certain assumed distance distribution as is illustrated in **Figure 1.18**.

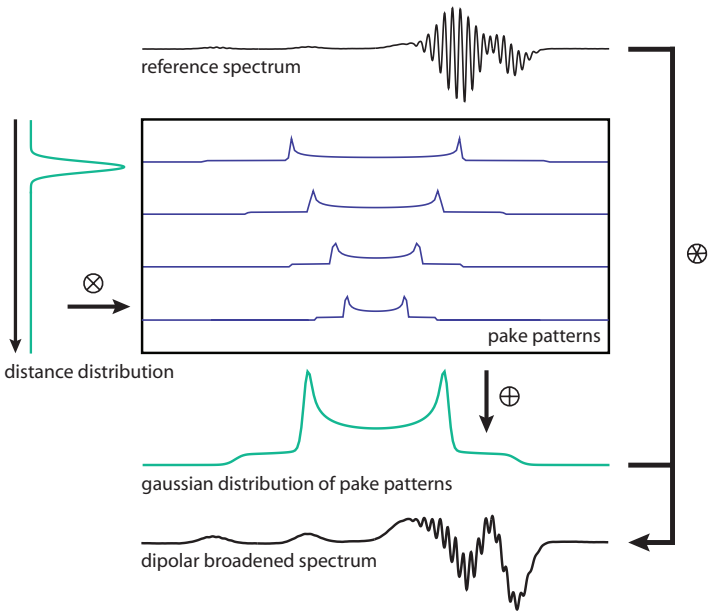


Figure 1.18: Schematic overview of the steps involved when applying the dipolar convolution method.

The distance distribution is then optimised, until a good agreement between the convolution result and the experimental spectrum containing two spin centres is obtained. Typically, a Gaussian distance distribution is assumed, parametrised by the centre of the distribution r_c and its width

σ_r. For the construction of the Pake patterns, knowledge of the coupling regime is required. If the coupling regime is unknown, large errors could potentially be introduced in the analysis due to the differences in the Pake patterns. In addition, dipolar convolution relies on a couple of assumptions which might not be justified in many cases: Most importantly, dipolar convolution in the weak coupling regime is only applicable if any significant contribution of exchange coupling to the experimental spectrum can be excluded, as it assumes that the entire spectral broadening is due to dipole-dipole interactions. Furthermore, it relies on the point dipole approximation and assumes an isotropic broadening of the spectrum, which can be problematic in cases of large **g**- or **A**-tensor anisotropies. Finally, high quality data are necessary for the analysis since the changes in spectral shape which need to be interpreted are typically very small. A significant amount of noise or background imperfections might therefore result in large errors, especially for distances close to 2 nm, where only minor spectral changes are expected due to dipolar coupling.

1.4.2 Pulse Dipolar Spectroscopy

Above 1.5 nm, when the method of dipolar convolution typically reaches its limits, pulse EPR techniques can be applied for the study of dipolar couplings between electrons. In this regime, the effect of pseudo-secular contributions mixing the $|\alpha\beta\rangle$ and $|\beta\alpha\rangle$ states and that of through-bond exchange couplings between electron spins can often be neglected [2]. We can assume localised spins (as compared to the separation distance), therefore the point-dipole approximation is valid and the dipolar interaction can be described according to **Equation (1.43)**.

A range of different pulse EPR techniques for the measurement of dipolar couplings are available such as Double-Quantum Coherence (DQC) [21–23], '2+1' [24–27], 3-pulse Double Electron-Electron Resonance (DEER or PELDOR for Pulsed ELectron DOuble Resonance) [28, 29] and its corresponding dead-time free 4-pulse variant [30, 31], and Relaxation-Induced Dipolar Modulation Enhancement (RIDME) [32, 33]. In very rare cases, for instance for spin-polarised radical pairs, information on dipolar (and exchange) couplings can also be obtained by observation of the out-of-phase electron spin echo (OOP-ESEEM) [34, 35].

Amongst the listed techniques, 4-pulse DEER is by far the most commonly applied method and has also been used for the characterisation of some of the systems studied in this work. In the following, we shall therefore only focus on 4-pulse DEER. Further details on the other methods are given in the relevant publications cited above.

4-Pulse DEER

The distance range which can be accessed by 4-pulse DEER extends from roughly 1.5 to 8 nm [36, 37]. The lower limit is determined by the excitation bandwidth of the microwave pulses, which needs to be wide enough to excite the entire dipolar spectrum (Pake pattern), while the upper limit is determined by the transverse relaxation properties of the sample.

Figure 1.19 shows the pulse sequence applied in 4-pulse DEER experiments. The measurements are performed at a specific magnetic field position by applying pulses at two different microwave frequencies. The spins in resonance with the detection frequency, ν_{det}, are referred to as the *A*

spins, whereas the spins in resonance with the pump frequency, ν_{pump}, are referred to as the B spins. At the detection frequency, a primary echo sequence with inter-pulse delay τ_1 is applied to generate transverse magnetisation which then evolves during a time interval $\tau_1 + \tau_2$ until a further π pulse is applied. The magnetisation is refocussed after a time delay τ_2 following the last microwave pulse at the detection frequency.

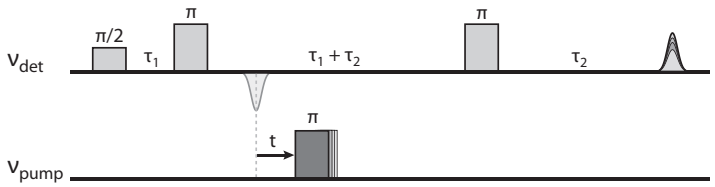


Figure 1.19: Illustration of the pulse sequence used in 4-pulse DEER.

The pump pulse applied to the B spins, inverts those spins and thus changes the local magnetic field at the position of the A spins as a consequence of the inter-spin coupling as is illustrated in **Figure 1.20**. It transfers coherence between the single-quantum transitions of the A spins which changes their precession frequency by ω_{dd} and leads to less magnetisation being refocussed at the end of the pulse sequence, resulting in a smaller echo intensity. The position of the pump π pulse within the pulse sequence is then varied and the (integrated) echo intensity is recorded as a function of the pump pulse displacement t to yield the DEER trace which is modulated by $\cos(\omega_{dd} t)$ [36]. Typically, a two-step phase cycle of $[(+x) - (-x)]$ is applied on the first observer pulse.

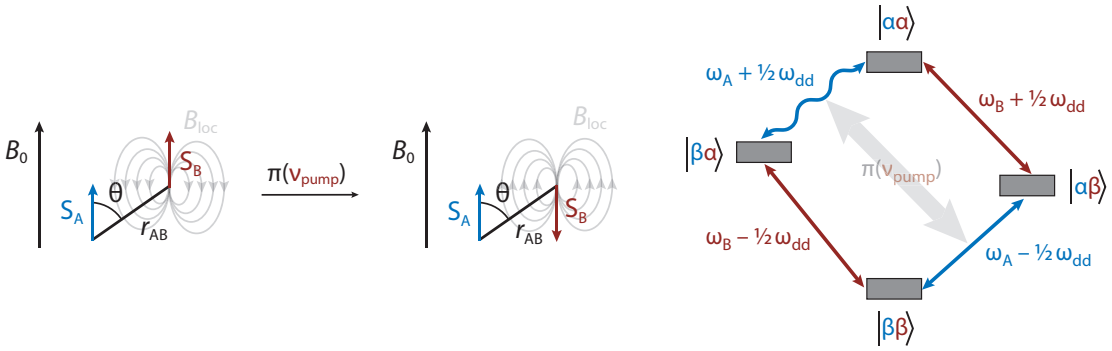


Figure 1.20: Illustration of the effect of the π pump pulse in DEER on an $S_A = S_B = \frac{1}{2}$ spin system.

Since the excitation bandwidth of the microwave pulses is often smaller than the EPR spectrum, this method can also be applied if the two spin centres have identical spectra [37]. If centres belonging to different nano-objects are excited, the corresponding fraction of the signal will not be modulated and will contribute to the time-dependent background signal $B(t)$ which can be approximated by an exponential function according to

$$B(t) = \exp\left(-kt^{d/3}\right) \tag{1.45}$$

where the constant k depends on the sample concentration and d characterises the background dimensionality typically equal (or close) to three for powder samples or isotropic frozen solutions.

The modulated part of the signal $F(t)$, also referred to as the form factor, is characterised by a certain modulation depth Δ defined as

$$\Delta = 1 - (1 - \lambda)^{n-1} \tag{1.46}$$

where n equals the number of spin centres in one nano-object. In the following we will assume that $n = 2$ and consequently the modulation depth Δ is equal to the pump inversion efficiency λ. The form factor can then be expressed as follows

$$F(t) = 1 - \lambda\Big[1 - \cos(\omega_{dd} t)\Big] \tag{1.47}$$

and the experimentally measured DEER signal $V(t)$ is given by the product of the form factor and the background signal

$$V(t) = F(t)\, B(t) \tag{1.48}$$

To separate the two contributions to $V(t)$, the background is usually fitted to the experimental data for long times $t > t_{\mathrm{bg}}$, where the form factor has largely decayed to zero. Division of $V(t)$ by the fitted background then yields $F(t)$. Additionally, for the analysis of the time traces, it will be helpful to define a so-called reduced form factor $f(t)$, only containing the information about the dipolar frequencies, according to

$$f(t) = \frac{F(t) - (1 - \lambda)}{\lambda} = \cos(\omega_{dd} t) \tag{1.49}$$

where the constant frequency part $f_0 = 1 - \lambda$ of the signal has been subtracted.

Since both microwave frequencies need to be accommodated in the EPR resonator in DEER experiments, the maximum frequency separation between detection and pump pulses is limited by the resonator bandwidth. The resonator bandwidth can be increased by overcoupling, however overcoupling also decreases the sensitivity and the available microwave strength at a given power. In a single-mode resonator, frequency separations of more than 100 MHz are therefore usually difficult depending on the resonator and the available power [6]. The frequency separation also puts a lower limit on the pulse lengths that can be used, since spectral overlap of the excitation profiles of the pump and detection pulses should be avoided. In general, short pulses have the advantage that a larger fraction of spins can be excited, which increases the sensitivity, while the selectivity of longer pulses might be desirable in other cases.

DEER time traces can be affected by artifacts arising from nuclear hyperfine couplings. To avoid nuclear ESEEM contributions, the τ_1 value can either be set to coincide with a blind spot of the corresponding nuclear modulation or be incremented in n steps over the course of successive experiments to cover the period of a nuclear modulation. The number of steps, n, is typically set to eight and the resulting DEER traces are averaged. For a deuterated matrix at X- and Q-band frequencies, $n = 8$ would for instance correspond to a time increment of 56 ns and 16 ns, for X- and Q-band, respectively. When τ_1 averaging is applied, the initial τ_1 value is often chosen as short as possible for maximum signal intensity.

The overall pulse sequence has a constant length, hence the effects of (transverse) relaxation do not vary with the pump pulse position and therefore do not contribute to the background decay. In order to determine the inter-spin distance and its distribution reliably from the modulations of the experimental data, the recorded DEER trace must have a certain minimal length. The maximum length of the DEER trace ($\sim\tau_2$) is determined by the decay rate of the transverse magnetisation and therefore by the phase memory time, T_m. In most cases, however, it might be advantageous not to push the length of the experimental trace to its limits, but rather to record a trace of just the length required to resolve the expected distance, with the aim to improve the signal-to-noise ratio of the data which scales with the echo intensity. For the sake of a reasonable sensitivity in the experiment, as a rule of thumb, the maximum dipolar evolution time, t_{max}, should be smaller than 1.5 T_m [38]. To calculate the optimum t_{max} required in order to determine a certain quantity reliably – such as the mean distance, the width of the distance distribution, or its shape – an empirical relationship has been derived [37] and is given as:

$$t_{\mathrm{max}} = 2\,\mu\mathrm{s}\left(\frac{r_{\mathrm{exp}}}{r_{\mathrm{ref}}}\right)^3 \tag{1.50}$$

where r_{exp} is the expected mean distance and the parameter r_{ref} adopts one of the following values depending on the quantity to be determined; $r_{\mathrm{ref}} = 3\,\mathrm{nm}$, 4 nm or 5 nm for a reliable determination of the shape, the width or the mean of the distribution, respectively. If the required t_{max} exceeds T_m, the latter can be increased by lowering the measurement temperature or by deuteration of the matrix [15].

Data Analysis and Interpretation

An idea about the distance of the dipolar coupling can be obtained from the time $t_{1/2}$, where the reduced form factor has decayed to half of its original value [37]. The empirical relationship

$$\langle r\rangle \sim 5\left(\frac{t_{1/2}}{0.48\,\mu\mathrm{s}}\right)^{1/3}\mathrm{nm} \tag{1.51}$$

is considered a good approximation.

The experimental data can also be subjected to a more quantitative model-free analysis which allows one to compute the distance distribution from the dipolar spectrum [39]. The mathematical problem to be solved is moderately ill-posed, implying that small variations in the input data (e.g. noise, different background correction) can have a large influence on the outcome of the analysis. The solution thus needs to be stabilised by imposing certain constraints to reduce distance artifacts. An algorithm often used for this purpose is Tikhonov regularisation, implemented for instance in the MATLAB [40] software package DeerAnalysis [41]. Smoothness criteria are imposed on the result and the distance distribution is constrained to include only positive values.

In this procedure, the mean square deviation ρ, between the simulated reduced form factor $KP(r)$ and the experimental one, $f(t)$, is minimised as well as the roughness, η, which is defined as the square norm of the second derivative of the distance distribution. Overall the following

function is minimised

$$G_\alpha = \|KP(r) - f(t)\|^2 + \alpha \left\| \frac{d^2}{dr^2} P(r) \right\|^2 = \rho + \alpha\eta \tag{1.52}$$

where K is a suitable kernel function [2, 41]. The roughness η is weighted by the regularisation parameter α, which determines the degree of smoothing. To optimise the value for α, the so-called 'L-curve criterion' is often applied which is based on a plot of $\log(\eta(\alpha))$ vs. $\log(\rho(\alpha))$. The value for α is typically varied on a logarithmic scale (for predefined values). A small α corresponds to under-smoothing and a strongly decaying branch in the plot, whereas a large α corresponds to over-smoothing and a branch with a slope close to zero. The optimum value for α then corresponds to the corner of the L-shaped curve.

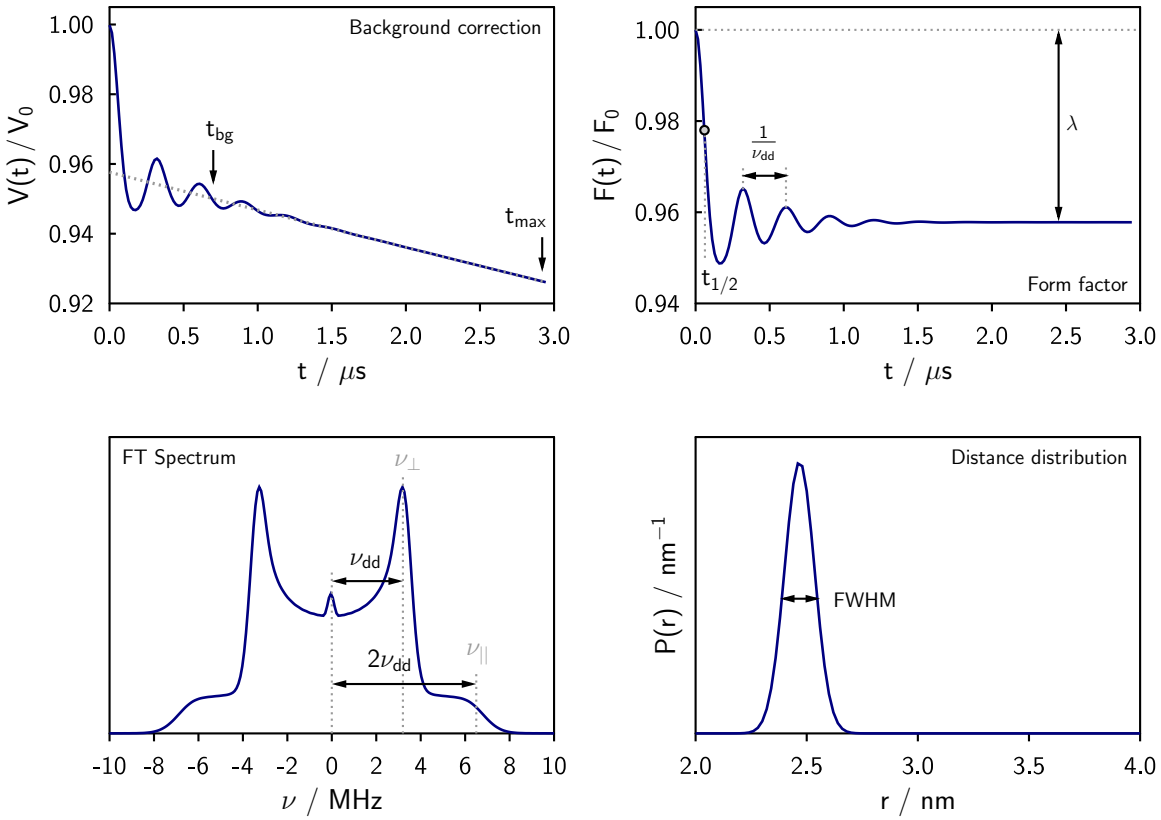


Figure 1.21: Illustration of the different steps involved in the DEER data treatment. An exponentially decaying background is fit to the time trace (*top left*) and subtracted to yield the form factor (*top right*) from which the modulation depth λ and $t_{1/2}$ can be determined. The dipolar modulation frequency can be obtained from a Fourier transformation of the time trace (*bottom left*) and an analysis of the form factor using Tikhonov regularisation eventually yields the corresponding distance distribution, where FWHM $= 2\sigma\sqrt{2\ln 2}$ (*bottom right*).

Any determination of distances from the dipolar evolution time trace depends on a reliable background correction. If the chosen background decays too fast (over-correction), long distances are suppressed, whereas if the background decay is too slow (under-correction) spurious contributions of long distances are introduced. To obtain reliable results, sufficiently long time traces with a

good signal-to-noise are thus required. A good error estimate can often be obtained by changing t_{bg}, the start time defining the range used for background correction, and comparing the variations in the distance distribution. This option is also implemented in DeerAnalysis and referred to as the 'validation' tool. **Figure 1.21** summarises the steps involved in the DEER data treatment and defines some of the variables mentioned in the text. When comparing the Pake pattern obtained from a Fourier transformation of the DEER time trace to the Pake patterns introduced in **Figure 1.16**, it has to be considered that DEER measures dipolar splittings directly, so compared to the normal Pake pattern the frequencies are doubled.

Orientation Selection

The classical model-free analysis of the DEER traces presented above is based on the assumption that all orientations are excited equally so that a regular Pake pattern with singularities at $-\nu_\perp$ and $\nu_\perp$ is obtained from an analysis of the dipolar evolution data. Especially for samples with a large **g** or **A**-tensor anisotropy and therefore broad spectra, this is very often not the case since the microwave pulses can only excite a very small part of the spectrum corresponding to a small subset of orientations. In those cases, effects of orientation selection need to be considered in the analysis of the DEER data. Orientation selection leads to a suppression of parts of the Pake pattern. Under certain conditions the singularities of the Pake pattern, which are used to compute the distances, may be suppressed. Hence trying to obtain a distance distribution from the data by Tikhonov regularisation might lead to large errors in the presence of orientation selection.

Often, however, orientation selection, although present, is not strong enough to lead to significant distortions of the Pake pattern. If the singularities of the Pake pattern are still visible and dominate the appearance of the Pake pattern, the errors in the mean distance made by applying Tikhonov regularisation to orientation selective data are typically not large [42]. Due to the r^{-3} dependence, the shift in frequency needs to be rather large in order to influence the distance estimate markedly. As a result, quite reliable results can often be obtained when analysing orientation selective data using model-free analysis procedures as is shown for instance in Chapter 3.

In some cases orientation selection can be advantageous as it offers the possibility to obtain additional information on the mutual orientation of the spin centres if it can properly be accounted for in the analysis. When wanting to include orientation selective effects in the analysis, a structural model needs to be found and DEER traces need to be calculated for all possible orientations within the boundaries of the model [43]. The orientations are characterised by the polar and azimuthal angles θ and φ, describing the location of the second spin centre in the **g**-tensor frame of the first, the inter-spin distance r, and the three Euler angles α, β, and γ indicating the orientation of the second **g**-tensor with respect to the reference frame. The weighted sum of the calculated DEER traces is then compared to the experimental data and the structural model is refined until a good agreement between the simulation and the experimental data is obtained. An overview of the parameters determining the relative orientations of the spin centres is given in **Figure 1.22**.

If orientation selection can be exploited, DEER traces recorded at different field positions (or frequency offsets) for one particular sample can contain complementary information. It is thus possible to obtain several constraints for the analysis with just one sample. For structure determi-

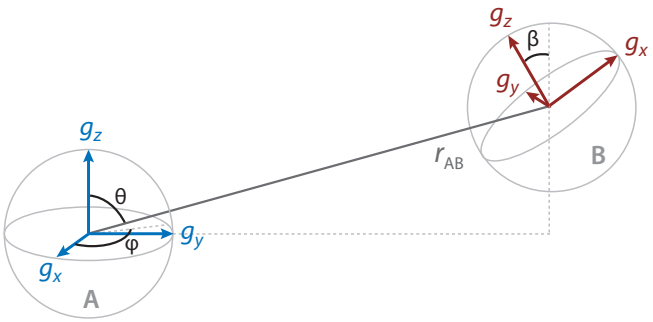


Figure 1.22: Overview of the definition of the parameters for the simulation of orientation selective effects in DEER.

nation in proteins, this might be a great advantage over using nitroxide spin labels with (almost) no orientation selection (at X- and Q-band). In the case of nitroxides, a new sample with a new spin labeling position (i.e. mutant) has to be prepared for every additional constraint needed to resolve the structure, while considerably fewer samples might be necessary when using spin labels showing orientation selection.

Chapter 2

Quantifying the Exchange Coupling in Linear Copper Porphyrin Oligomers

The through-bond exchange interaction, J, between two spin centres is a convenient measure of long-range electronic communication. Considering two spin centres with $S = \frac{1}{2}$, the exchange interaction characterises the energetic splitting between singlet and triplet states. If the singlet state lies below the triplet state, the interaction is said to be antiferromagnetic, whereas it is said to be ferromagnetic in case of a triplet ground state. If the two spin centres are more than about 1 nm apart, the effect of J can typically be assumed to be isotropic due to its approximately exponential dependence on distance. Since the exchange interaction relies on orbital overlap, it is a measure of the extent of electron spin delocalisation [44]. Its magnitude reflects the orbital structure of complex molecules as well as conformational changes. In molecules exhibiting extensive conjugation of the electronic π-system, significant exchange couplings have been detected for distances as large as 3.6 nm [18].

Depending on the magnitude of the exchange coupling interaction, different techniques can be applied for its characterisation, including measurements of the magnetic susceptibility and EPR spectroscopy. Compared to magnetic susceptibility measurements, EPR is considerably more sensitive. The lower detection limit for magnetic susceptibility measurements is generally of the order of $k_B T$, implying that the detected interaction cannot be smaller than about $1\,\mathrm{cm}^{-1}$ ($\sim 3 \cdot 10^4\,\mathrm{MHz} = 1.4\,\mathrm{K}$), unless the experiment is performed at very low temperatures [45]. On the contrary, by EPR, even very weak interactions of the order of $10^{-3}\,\mathrm{cm}^{-1}$ and lower can be probed.

Understanding the factors influencing electronic coupling, and therefore electronic communication, is of paramount importance for numerous applications in the fields of spintronics, molecular electronics and photovoltaics [46–50]. In this study, electronic communication in linear copper porphyrin oligomers designed as molecular wires [51, 52] is investigated by EPR *via* measurement of the exchange coupling between the copper centres.

2.1 Investigated Structures

The linear copper porphyrin oligomers with one, two, three or six porphyrin units are referred to as $\mathbf{P1_{Cu}}$, $\mathbf{P2_{Cu2}}$, $\mathbf{P3_{Cu3}}$, and $\mathbf{P6_{Cu6}}$, respectively, and are shown in **Figure 2.1**. The porphyrin units are linked by butadiyne groups, and aryl substituents are introduced at the two remaining *meso*-positions of the porphyrin core. In the present study, these aryl substituents are 3,5-di-

(tri(hexyl)silyl)phenyl groups, denoted **THS** throughout this work. The synthesis of the compounds was performed by Martin Peeks (Anderson group, University of Oxford, UK).

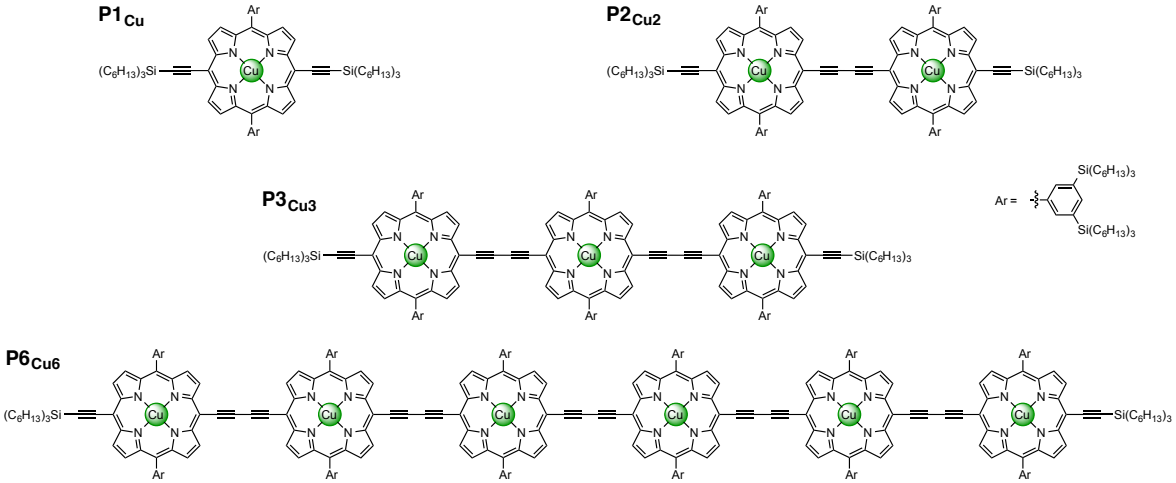


Figure 2.1: Chemical structures of the investigated copper porphyrin oligomers with **THS** side groups.

For an initial characterisation of the linear copper porphyrin oligomers, UV-vis spectra were recorded in toluene solution at room temperature. The corresponding data are shown in **Figure 2.2**. With increasing oligomer length, both the intense porphyrin Soret band ($S_0 \rightarrow S_2$) around 450 nm and the Q-bands at wavelengths above 500 nm ($S_0 \rightarrow S_1$) are found to shift to longer wavelengths, indicating an increase in the π-conjugation length. Furthermore, compared to the intensity of the porphyrin Soret bands, the relative intensity of the porphyrin Q-bands increases with increasing oligomer length, indicating that the corresponding transitions, which are forbidden in $\mathbf{P1_{Cu}}$, become gradually more allowed [53].

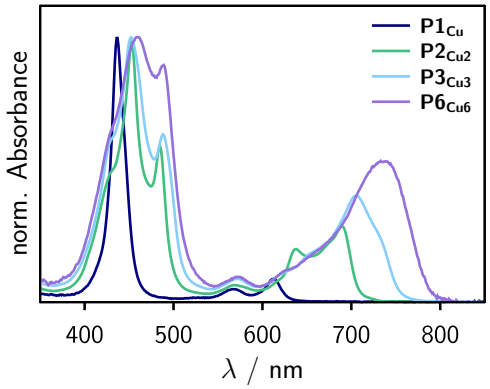


Figure 2.2: Normalised UV-vis spectra of the investigated compounds taken at room temperature in toluene solution.

2.2 EPR of Linear Copper Porphyrin Oligomers

For the EPR measurements, 0.2 mM solutions of the oligomers were prepared in either toluene-d_8 or regular toluene. Details on the sample preparation and experimental setup can be found in

Appendix A (cf. **Sections A.1** and **A.2**). **Figure 2.3** shows a comparison of the room temperature and frozen solution (100 K) cw EPR spectra of $\mathbf{P1_{Cu}}$ and $\mathbf{P2_{Cu2}}$ in toluene. The frozen solution spectrum of $\mathbf{P1_{Cu}}$ strongly resembles the spectrum of a typical copper porphyrin monomer as reported in the literature [54, 55]. The interaction of the unpaired electron of copper with its nuclear spin of $I = \frac{3}{2}$ results in four lines, two of which are clearly resolved at the low-field side of the spectrum and correspond to the out-of-plane or z orientation ($g_{||}$) of the electronic **g**-tensor. In the porphyrin plane (xy orientation, $g_{\perp}$), the interaction between the unpaired electron spin and the four in-plane nitrogen atoms with $I = 1$ leads to additional hyperfine structure. The pronounced **g**- and **A**-tensor anisotropy results in a fairly broad, axially symmetric, spectrum.

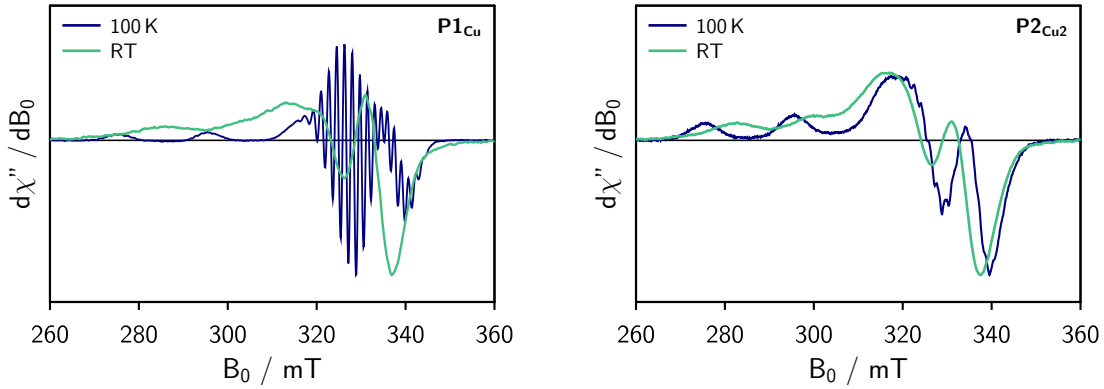


Figure 2.3: Comparison of the X-band cw EPR spectra recorded at 100 K and room temperature in toluene for $\mathbf{P1_{Cu}}$ (*left*) and $\mathbf{P2_{Cu2}}$ (*right*).

Compared to the frozen solution spectrum of $\mathbf{P1_{Cu}}$, that of $\mathbf{P2_{Cu2}}$ (**Figure 2.3**, *right*) is significantly broadened. In $\mathbf{P2_{Cu2}}$ the intensity of the two copper transitions, resolved at the low-field side of the spectrum, seems enhanced (relative to that of the intensity maximum) and much less hyperfine structure is visible. The observed broadening in the spectrum of $\mathbf{P2_{Cu2}}$, is most likely due to intramolecular interactions between the copper centres arising from both D and J.

If the isotropic tumbling limit can be reached in liquid solution, a separation of the individual contributions of D and J to the shape of the cw EPR spectrum may be feasible, since the anisotropic contribution (D) is averaged out [56–59]. Whenever the rate of rotational diffusion of the molecules is greater than the EPR transition frequency ($\sim 10^{10}$ Hz at X-band), isotropic values are obtained for g and A and any numerical simulation of the spectrum is greatly simplified.

However, comparing the room temperature cw EPR spectra of $\mathbf{P1_{Cu}}$ and $\mathbf{P2_{Cu2}}$, shown in **Figure 2.3**, with those recorded with 5,10,15,20-tetraphenyl-21H,23H-porphine copper(II) (**CuTPP**) at various temperatures, shown in Appendix B (**Figure B.3**), it is noted that the isotropic tumbling limit cannot be reached at room temperature with the compounds investigated here. In fact, the room temperature spectrum of $\mathbf{P1_{Cu}}$ strongly resembles the spectrum of **CuTPP** recorded at 200 K, where anisotropic interactions are clearly still present. These marked differences in the temperature behaviour of the cw EPR spectra are ascribed to the bulky side and end groups in $\mathbf{P1_{Cu}}$. The end groups seem to have the biggest impact, since similar spectra as for $\mathbf{P1_{Cu}}$ with **THS** side groups were obtained for $\mathbf{P1_{Cu}}$ with the smaller 3,5-di-*tert*-butylphenyl (**tBu**) aryl side

groups (data not shown). Since even at room temperature the tumbling of $\mathbf{P1_{Cu}}$ and $\mathbf{P2_{Cu2}}$ is still too slow for anisotropic contributions to average out, a straightforward separation of D and J based on the simulation of the EPR spectra does not seem to be possible.

The frozen solution (100 K) cw EPR spectra of all investigated compounds are compared in **Figure 2.4**. The direct comparison between the spectra of $\mathbf{P1_{Cu}}$ and $\mathbf{P2_{Cu2}}$ suggests that the hyperfine coupling constants and g-factors are similar in both compounds since the positions of the most prominent transitions are virtually identical.

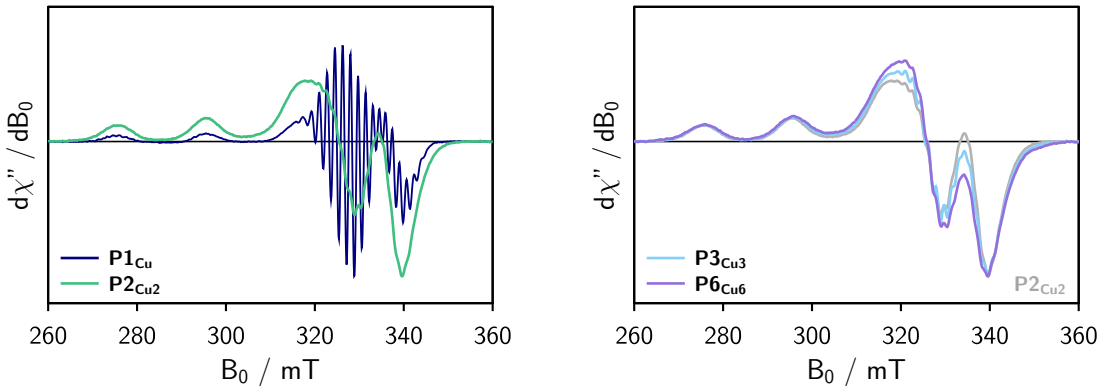


Figure 2.4: Comparison of the X-band cw EPR spectra of $\mathbf{P1_{Cu}}$ and $\mathbf{P2_{Cu2}}$ (*left*) and $\mathbf{P3_{Cu3}}$ and $\mathbf{P6_{Cu6}}$ (*right*) recorded at 100 K in toluene.

Compared to the spectrum of $\mathbf{P2_{Cu2}}$, only minor further broadening is observed in the spectra of the longer oligomers $\mathbf{P3_{Cu3}}$ and $\mathbf{P6_{Cu6}}$. Since the spectral broadening arising from the dipolar interaction between two copper centres separated by (at least) one porphyrin unit is negligible due to a separation of >2.7 nm (∼2.8 MHz = 1 G), the dipolar broadening is expected to be (almost) the same in all compounds with two or more copper units. The small additional broadening in the spectra of $\mathbf{P3_{Cu3}}$ and $\mathbf{P6_{Cu6}}$ is therefore likely to indicate a slight increase in J arising from increased π-conjugation. However, the small spectral differences between $\mathbf{P2_{Cu2}}$ and the longer oligomers suggest that also the J-coupling almost exclusively occurs between nearest neighbours.

It seems reasonable to assume that the difference between the spectra of $\mathbf{P1_{Cu}}$ and $\mathbf{P2_{Cu2}}$ is mainly caused by exchange coupling. To confirm that the hyperfine coupling constants of the system remain unchanged between $\mathbf{P1_{Cu}}$ and $\mathbf{P2_{Cu2}}$, ^{14}N Davies ENDOR experiments were carried out at Q-band frequencies. The spectra shown in **Figure 2.5** were acquired at 15 K. For every compound, ENDOR spectra were recorded at two different magnetic field positions corresponding to the xy and z orientations of the electronic **g**-tensor. The influence of orientation selection on the ENDOR spectra of $\mathbf{P1_{Cu}}$ is illustrated in Appendix D (**Figure D.3**). Details regarding the experimental setup and parameters used in the EPR experiments are given in Appendix A (**Subsection A.3.1**).

Since the nitrogen hyperfine coupling interaction is large compared to the nuclear Larmor frequency, the ENDOR spectra are in the strong coupling regime, where the ENDOR peaks are centred at $A/2$ and split by the nuclear Zeeman and nuclear quadrupole interactions. All information about the hyperfine coupling constants is thus contained in the peak positions with respect

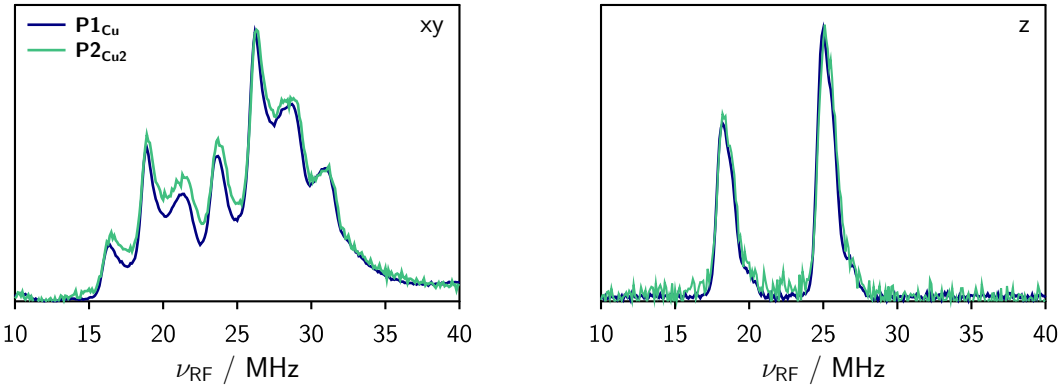


Figure 2.5: Comparison of the ^{14}N Davies ENDOR spectra of $\mathbf{P1_{Cu}}$ and $\mathbf{P2_{Cu2}}$ recorded at Q-band (15 K) in toluene-d_8 at magnetic field positions of about 1185 and 1102 mT corresponding to the *xy* (*left*) and *z* (*right*) orientations of the electronic **g**-tensor, respectively.

to the frequency axis (cf. also Appendix D, **Figure D.6**). Visual examination of the spectra in **Figure 2.5** indicates that the nitrogen hyperfine coupling constants are very similar in $\mathbf{P1_{Cu}}$ and $\mathbf{P2_{Cu2}}$. Based on the frozen solution cw EPR spectra also the copper out-of-plane hyperfine coupling constant, $A_{||}$, does not change markedly when increasing the oligomer length, as indicated by a similar spacing between the two outermost copper lines resolved at the low-field side of the spectrum. No direct conclusion can be drawn on the copper in-plane coupling, $A_{\perp}$, however a change in its magnitude seems unlikely, given that all other hyperfine couplings are found to be virtually identical between monomer and dimer.

To characterise the relaxation behaviour of the compounds, relevant for the simulations of the cw EPR spectra, the spin relaxation rates T_1 and T_2 were determined. The transverse relaxation curves measured by applying the 2-pulse echo decay pulse sequence at Q-band (15 K) are compared for $\mathbf{P1_{Cu}}$ and $\mathbf{P2_{Cu2}}$ in **Figure 2.6**. The measurements were taken at two different field positions corresponding to the *xy* and *z* orientations. The presence of any dipolar and exchange interactions is likely to lead to a shortening of the relaxation times. Relaxation is therefore expected to be faster in $\mathbf{P2_{Cu2}}$ as compared to $\mathbf{P1_{Cu}}$. The predictions are in line with the results shown in **Figure 2.6**. In addition, relaxation is observed to be faster when probing the *z* orientation, which might indicate different relaxation mechanisms. The shortening of the relaxation times in $\mathbf{P2_{Cu2}}$ as compared to $\mathbf{P1_{Cu}}$ seems more pronounced at *xy*.

The influence of temperature on the transverse relaxation behaviour can be inferred from **Figure 2.7**, where the 2-pulse echo decay time traces recorded at 100 K on *xy* are compared for $\mathbf{P1_{Cu}}$ and $\mathbf{P2_{Cu2}}$. The measurements were recorded at X-band frequencies for comparability with the cw EPR spectra to be simulated. Again it is observed that spin relaxation is considerably accelerated in $\mathbf{P2_{Cu2}}$. Compared to the measurements at 15 K, the phase memory time decreases by almost an order of magnitude.

In addition, the longitudinal spin relaxation times of $\mathbf{P1_{Cu}}$ and $\mathbf{P2_{Cu2}}$ were measured at 100 K by saturation recovery using the Picket fence method at X-band. From these measurement, an approximate value for T_1 of 2.6 μs could be determined for $\mathbf{P1_{Cu}}$ by fitting a bi-exponential recovery

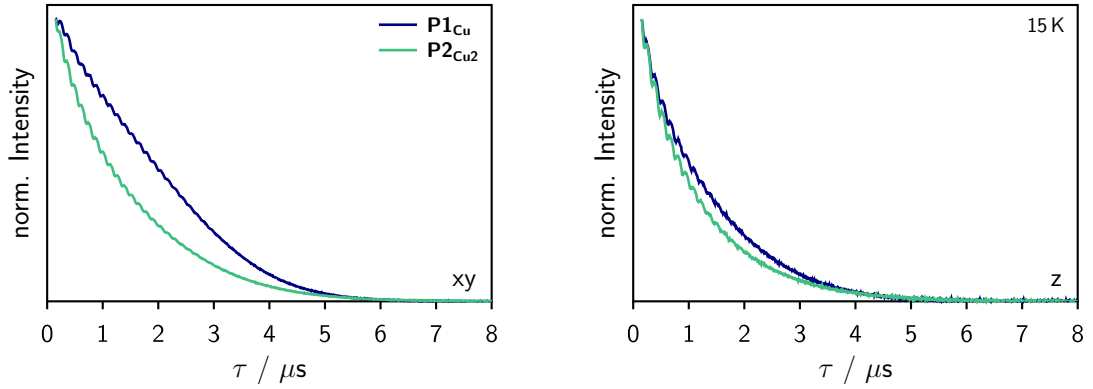


Figure 2.6: Comparison of the 2-pulse echo decay (T_m) of **P1$_{Cu}$** and **P2$_{Cu2}$** recorded at Q-band (15 K) in toluene-d_8 at magnetic field positions of about 1185 and 1102 mT corresponding to the *xy* (*left*) and *z* (*right*) orientations of the electronic **g**-tensor, respectively.

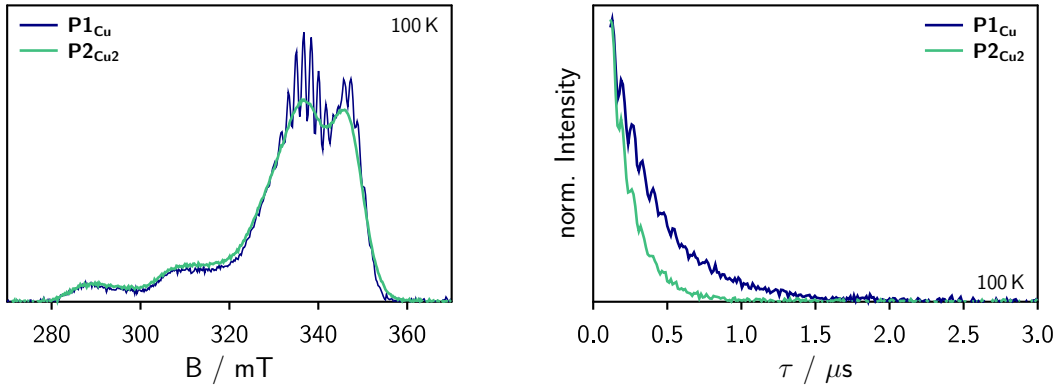


Figure 2.7: Comparison of the field-swept echo-detected EPR spectra using $\tau = 100$ ns (*left*) and 2-pulse echo decay (*right*) of **P1$_{Cu}$** and **P2$_{Cu2}$** recorded at X-band in frozen toluene-d_8 (100 K). The 2-pulse echo decay was recorded at a magnetic field position of about 336.5 mT corresponding to the *xy* orientation.

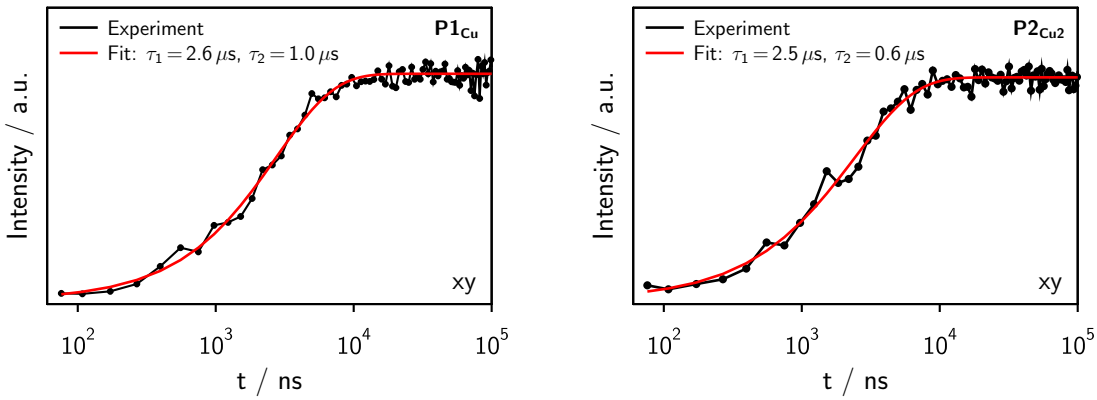


Figure 2.8: Saturation recovery measurement using the Picket fence method for **P1$_{Cu}$** (*left*) and **P2$_{Cu2}$** (*right*) recorded at X-band in frozen toluene-d_8 (100 K). The measurements were performed at a magnetic field corresponding to the *xy* orientation (~336.5 mT).

function with time constants τ_1 and τ_2 to the data. The longer time constant τ_1 is supposed to correspond to T_1, while spectral diffusion and other relaxation processes contribute to τ_2. For $\mathbf{P2_{Cu2}}$ a T_1 value of 2.5 μs was obtained applying the same treatment. Within experimental error, longitudinal relaxation thus seems to be identical for $\mathbf{P1_{Cu}}$ and $\mathbf{P2_{Cu2}}$.

2.3 Numerical Simulations of the cw EPR Spectra

In most previous studies, the magnitude of J was evaluated by an analysis of the cw EPR line shapes. If no coupling between the spin centres occurs, the cw EPR spectrum should coincide with that of the corresponding molecule possessing only one spin centre, while any type of intramolecular coupling will typically result in a broadening of the cw EPR spectrum [56, 59].

In rare cases, if the distance between the spin centres is well below 1 nm, the intensity of the half-field lines can be used to obtain information about J [20] as was shown, for instance, for copper centres separated by about 0.5 nm [60]. In the present study, however, the distance between the two copper centres in $\mathbf{P2_{Cu2}}$ amounts to 1.35 nm, as estimated by DFT calculations, and no half-field lines were observed.

Many examples have been reported where the magnitude of J was determined by numerical simulation of the isotropic liquid solution cw EPR spectrum. For copper compounds with inter-copper separations between 1.0 and 1.3 nm, J-couplings of the order of 10^{-4} to 10^{-3} cm^{-1} could for example be determined and a strong dependence of the magnitude of J on the nature of the linker and the relative orientation of the two copper centres was observed [57, 58].

In the absence of anisotropic interactions, such spectral simulations are relatively straightforward and computationally inexpensive. A number of different groups have made simulation programs available which could be used for this purpose [61–64]. However, as discussed above, the isotropic limit cannot be reached in toluene with the linear copper oligomers investigated in this work, preventing a straightforward separation of the contributions of D and J.

Many unknown parameters describing the restricted motion of the molecules would need to enter a simulation of the cw EPR spectra in the slow motion regime. It therefore appears that J can most reliably be obtained from a simulation of the spectra in the rigid limit (frozen solution). Based on the knowledge of the spin distribution in $\mathbf{P1_{Cu}}$, obtained from DFT calculations, and the distance between the two copper centres, it should be possible to determine D with quite high precision and use it as a fixed input rather than a variable simulation parameter.

To obtain an initial idea whether the contribution of J to the spectrum of $\mathbf{P2_{Cu2}}$ is significant, dipolar convolution was applied. When applying this method, J cannot be explicitly included in the simulations (nor quantified for that reason), but the influence of the exchange coupling to the spectrum can be assumed to be substantial if the spectral shape cannot be fully reproduced when only accounting for the dipolar interaction between the spin centres. In the procedure, the spectrum of $\mathbf{P1_{Cu}}$ was used as a reference spectrum and convoluted with a Gaussian distribution of Pake patterns corresponding to the expected distance distribution showing a single distance peak centred at 1.35 nm with a width of $\sigma_r = 0.04$ nm. Variations of the width of the distribution within reasonable limits were found not to have any marked impact on the final convolution result.

The simulations are shown in **Figure 2.9** for the weak and strong coupling regimes. Simulations in the weak coupling regime assume zero exchange coupling, while in the strong coupling regime $J \gg D$.

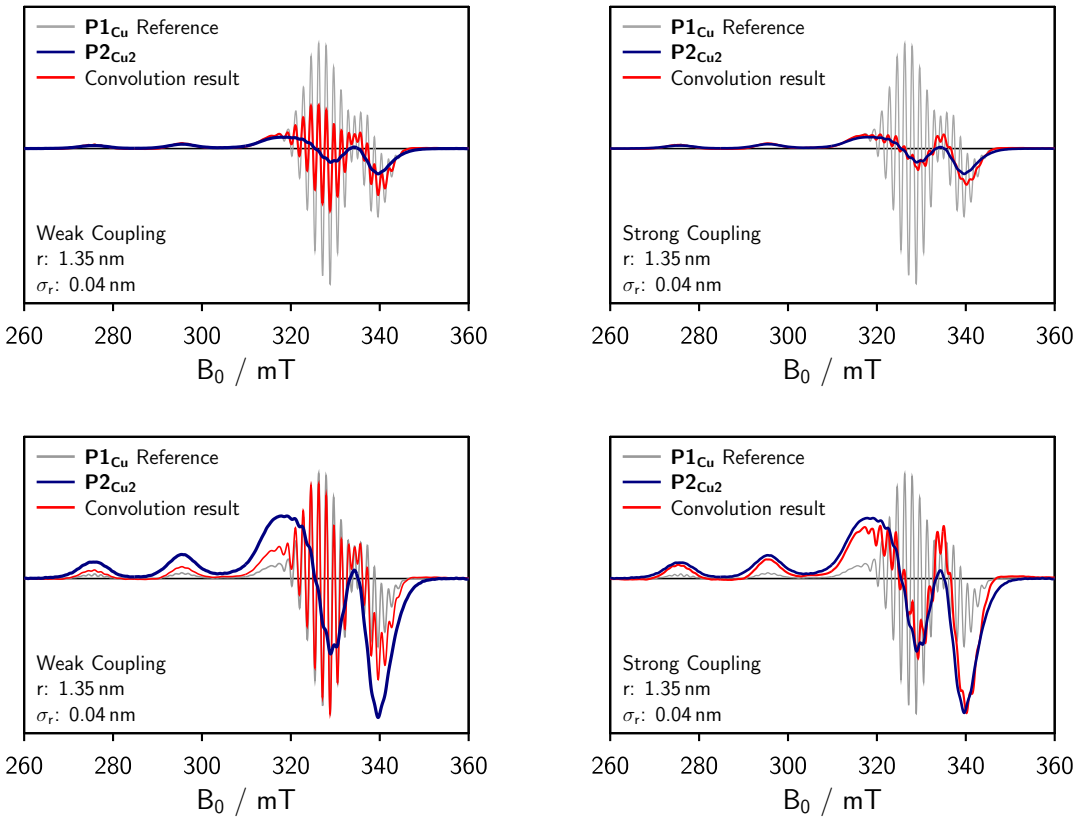


Figure 2.9: Convolution of the experimental spectrum of $\mathbf{P1_{Cu}}$ with a Gaussian distribution of Pake patterns corresponding to a distance distribution centred at 1.35 nm in the weak (*left*) or strong (*right*) coupling regime to account for the expected dipolar broadening of the spectrum in $\mathbf{P2_{Cu2}}$. The resulting dipolar broadened spectrum is normalised to either area (*top*) or intensity (*bottom*) and compared to the reference spectrum.

Although it may be questionable whether dipolar convolution yields an accurate result for $\mathbf{P2_{Cu2}}$, since the technique relies on the assumption of an isotropic broadening of the spectrum, which may be incorrect in the case of copper porphyrin oligomers, it provides a valid estimate of the expected spectral shape. A couple of conclusions can be drawn from the observations in **Figure 2.9**: In the weak coupling regime (*left*), negligible exchange coupling is assumed and only the influence of dipolar broadening on the spectrum is considered. As compared to the reference spectrum of $\mathbf{P1_{Cu}}$, the spectrum resulting from the convolution in the weak coupling regime is only slightly broadened and therefore far from reproducing the much broader spectrum observed experimentally for $\mathbf{P2_{Cu2}}$. We can thus conclude that a significant exchange coupling is most likely responsible for the majority of the spectral broadening observed for $\mathbf{P2_{Cu2}}$, i.e. $J > D$.

In agreement with the conclusions from the simulations in the weak coupling regime (i.e. that $J > D$), the convolution result obtained in the case of strong coupling (**Figure 2.9**, *right*) is much closer to reproducing the experimental spectrum of $\mathbf{P2_{Cu2}}$. However, minor spectral differences

are observed when comparing the simulation and the experimental spectrum of $\mathbf{P2_{Cu2}}$, which could indicate that the assumptions made when applying dipolar convolution for this system are not entirely valid.* Another reason for the apparent discrepancy could be that a smaller effective distance between the copper centres would need to be assumed due to partial delocalisation of the copper electron spin. In general, however, it can be concluded from this analysis that the through-bond coupling interaction, J, contributes markedly to the shape of the experimental cw EPR spectra.

2.3.1 Simulation of the Frozen Solution Spectrum of the Dimer

Dipolar convolution can only provide an estimate about the relative contribution of J to the spectral shape but does not allow for any type of quantification. A numerical simulation of the frozen solution spectrum based on an evaluation of the spin Hamiltonian, which takes the influence of D and J explicitly into account, was thus attempted. Since the experimental data presented in the preceding section suggest that the hyperfine parameters are the same between monomer and dimer, the hyperfine coupling constants and g-values to be used in the simulation of the spectrum of $\mathbf{P2_{Cu2}}$ were determined from a simulation of the spectrum of $\mathbf{P1_{Cu}}$ using the MATLAB [40] package EasySpin [64]. The result of the simulation is compared to the experimental data in **Figure 2.10** and the simulation parameters are indicated.

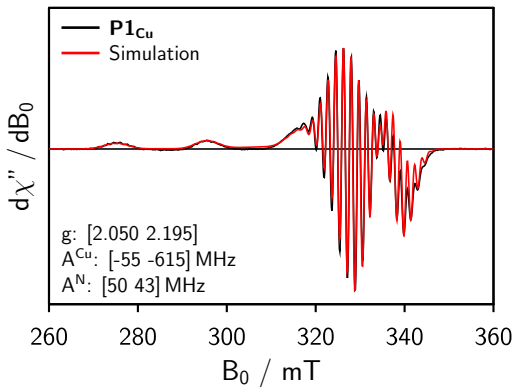


Figure 2.10: Numerical simulation of the cw EPR spectrum of $\mathbf{P1_{Cu}}$ using EasySpin to determine the hyperfine couplings and g-values.

To further reduce the number of variable input parameters for the simulation, the dipolar interaction, D, was estimated taking into account the distance between the spin centres and the spin density distribution. A visualisation of the calculated spin density distribution is shown for $\mathbf{P1_{Cu}}$ in **Figure 2.11**. It is observed that about 70 % of the spin density is located on copper, whereas the remaining 30 % is equally distributed between the four in-plane nitrogen atoms.

*If $J \gg D$, a perfect agreement between simulation and experiment would be expected (taken the validity of the assumptions for granted).

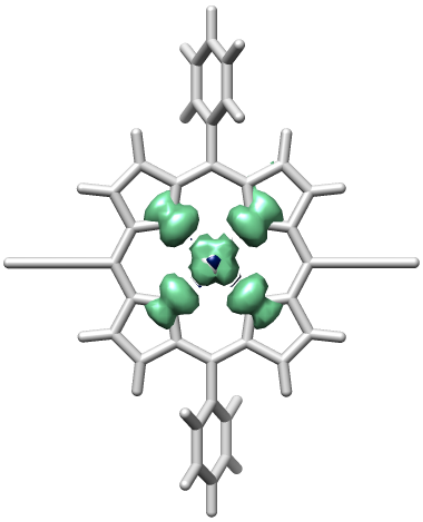


Figure 2.11: Visualisation of the spin density distribution in $\mathbf{P1_{Cu}}$ calculated in ORCA using DFT/B3LYP in combination with the EPRII basis set. In copper porphyrins the unpaired electron is expected to occupy the $d_{x^2-y^2}$ orbital [65], explaining the calculated spin density distribution.

In the simulations, an effective distance of 1.3 nm was adopted, corresponding to a coupling of about 24 MHz. The value of D was kept fixed so that the only variable parameters are the magnitude of the exchange interaction J and its distribution.[†]

As shown above, the hyperfine couplings of both nitrogen and copper contribute significantly to the shape of the cw EPR spectrum, so that they cannot be neglected in the simulations. The spin-space of a porphyrin dimer therefore becomes so large[‡] that most available and commonly used EPR simulation packages cannot handle the Hamiltonian dimensions any more due to memory limitations. These simulation packages typically simulate the EPR spectrum in the frequency domain, but for large spin systems this approach can become impractical. The best current algorithms either involve matrix factorisation in Hilbert space or matrix inverse-times-vector operations in Liouville space [64, 66]. The use of these procedures can become too expensive to compute the EPR spectra of very large spin systems in a reasonable time.

In the time-domain, however, considerable improvements in the simulation methods have recently been made [67], offering an alternative approach. Making use of the similarity between field-swept and frequency-swept EPR spectra, the simulation (and even fitting) of large spin systems becomes computationally feasible. The simulations presented below have been carried out by Prof. Ilya Kuprov (University of Southampton, UK) using the MATLAB package Spinach [68]. The simulation strategies employed to make the computation of large spin systems manageable are outlined in Appendix C (see **Section C.1**).

[†]Of course, also the dipolar interaction, D, has a certain distribution (due to variations in g, molecular motion and a distribution of the spin density) which would need to be considered. However, the variations in D are small as compared to the expected variations in J and are therefore neglected in the analysis to restrict the number of variable parameters. At maximum, a variation of D between roughly 1.1 nm (∼40 MHz) and 1.35 nm (∼22 MHz) is expected, when considering the spin density on the nitrogen atoms and possible bending of the structure.

[‡]A system with two electrons, two copper nuclei and eight nitrogen nuclei has a Hamiltonian dimension of 26244×26244 in Hilbert space and 688747536 in Liouville space.

When simulating the spectra in the time-domain using Spinach, the simulation parameters (**g**, **A**) determined for the porphyrin monomer from a simulation of the field-swept spectrum in **Figure 2.10** had to be adapted slightly to obtain a satisfactory fit due to the differences in the simulation approach. Taking the parameters indicated in **Figure 2.10** as an initial guess, the hyperfine couplings of copper and nitrogen as well as the g-factors were thus fitted until a good agreement between the Spinach simulation and the integrated experimental cw EPR spectrum was reached. The best fit obtained for adapted parameters of g = [2.051 2.180], A^{Cu} = [-71 -575] MHz and A^{N} = 46 MHz is shown in **Figure 2.12** (*left*). The deviations in the simulation parameters are minor and inconsequential for the purpose of evaluating J. The nitrogen hyperfine couplings were assumed to be isotropic since the experimentally observed anisotropy is not very pronounced and the calculations could be sped up considerably. Furthermore, for the simulations in the time domain, a knowledge of the relaxation rates of the systems is required. An initial guess for those values was obtained from the relaxation measurements shown in **Figures 2.7** and **2.8**, but also these values were optimised to reproduce the experimental spectrum of $\mathbf{P1_{Cu}}$ in the best possible way. Since it was shown that the relaxation behaviour is sufficiently similar for $\mathbf{P1_{Cu}}$ and $\mathbf{P2_{Cu2}}$, the relaxation parameters were kept constant for all further simulations after their initial optimisation to reduce the parameter space.

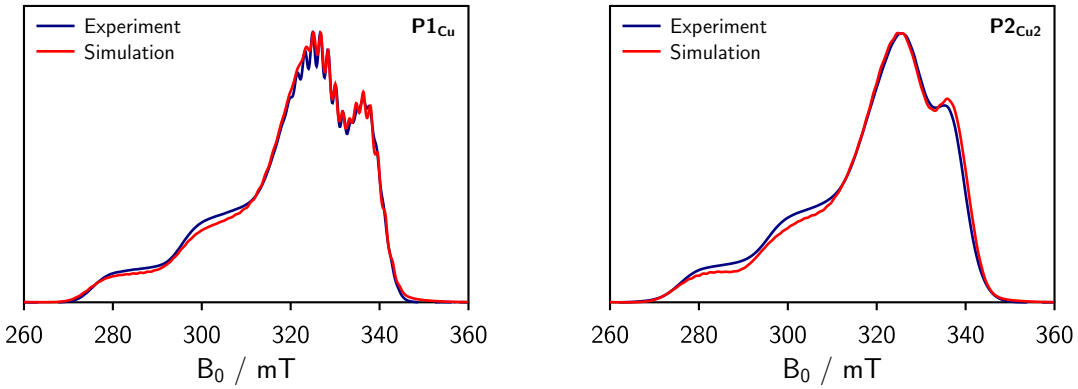


Figure 2.12: Simulations using Spinach as described in the text for $\mathbf{P1_{Cu}}$ (*left*) and $\mathbf{P2_{Cu2}}$ (*right*) in comparison with the respective experimental integrated cw EPR spectra.

For the simulation of the spectrum of $\mathbf{P2_{Cu2}}$, the hyperfine coupling parameters and g-values were taken from the fit of the monomer spectrum and D was set to correspond to an effective distance of 1.3 nm as mentioned before. Since the barrier for rotation of the two porphyrin planes in the dimer about the butadiyne linker is below 1 kcal mol^{-1} [69], several conformations of the molecule are expected to be populated at the freezing point of the solvent ($\sim$ 180 K) and thus to contribute to the frozen solution spectrum. To a first approximation it can be assumed that all dihedral angles between the porphyrin planes contribute equally. To reduce the number of free variables in the simulations, all rotational angles are thus considered with equal weight. The J-coupling was assumed to have the following angular dependence on the dihedral angle ϕ between the two porphyrin planes

$$J = C_1 \cos(2\,\phi) + C_2 \tag{2.1}$$

where $\phi = 0$ corresponds to a co-planar geometry. This dependence on ϕ simply corresponds to the first two terms of the harmonic series for any periodic function of ϕ, but is also suggested by the fact that the dominant part of the exchange interaction comes from orbital overlap, which, for a dimer composed of two identical monomers, should have a constant contribution and a cosine as the leading terms in the harmonic expansion of its dihedral angle dependence.

The constant parameters C_1 and C_2, determining the value of the exchange coupling, J, at every angle, ϕ, were then fitted together with an intensity scaling factor to simulate the experimental integrated cw EPR spectrum of $\mathbf{P2_{Cu2}}$. In the simulations using Spinach, the exchange coupling Hamiltonian is defined as $\mathcal{H}_J = J\,\mathbf{S_1}\,\mathbf{S_2}$. The best fit obtained for values of $C_1 = \pm 90$ MHz and $C_2 = \pm 90$ MHz is shown in **Figure 2.12** (*right*). It is insensitive to the overall sign of J, but C_1 and C_2 are found to have the same sign. Although minor differences in the intensities are observed, the fit to the experimental data can be considered satisfactory. Judging by the robustness of the fit, the standard deviation is expected to be of the order of 20 MHz. The comparatively large error stems from (i) the physical and algebraic assumptions made as well as (ii) the rather featureless character of the experimental spectrum of $\mathbf{P2_{Cu2}}$ which precludes a more precise quantification.

For comparison, the simulated spectra for $\mathbf{P1_{Cu}}$ and $\mathbf{P2_{Cu2}}$ are superimposed in **Figure 2.13** and contrasted to a superposition of the corresponding integrated experimental cw EPR spectra.

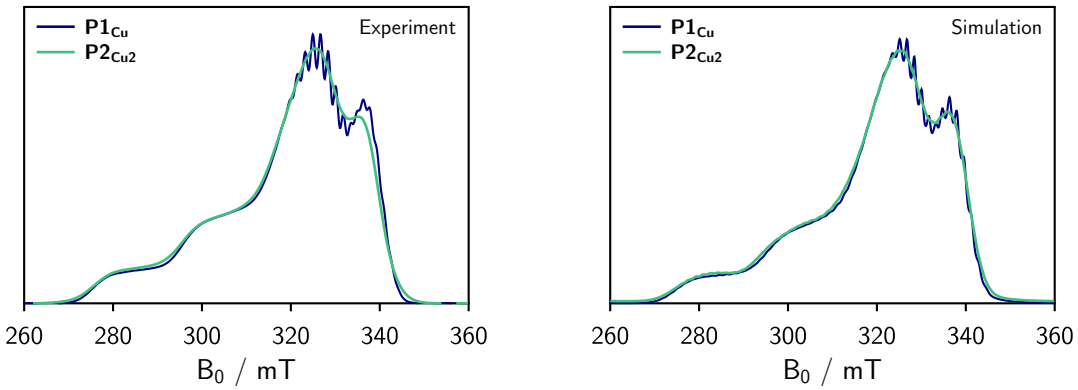


Figure 2.13: Comparison of the experimental integrated cw EPR spectra (*left*) and simulated EPR spectra using Spinach (*right*) of $\mathbf{P1_{Cu}}$ and $\mathbf{P2_{Cu2}}$.

Apart from rotation of the two porphyrin units about the triple bonds, also other motions, such as bending of the molecule, are expected to modulate the observed exchange coupling. Although only a variation of J due to rotation was explicitly considered in the simulations, since it would be impossible to identify and separate contributions to J of different origin, a significant contribution from other energetically low-lying twisting and bending modes cannot be excluded.

2.3.2 Simulations for the Longer Oligomers

For the simulation of the spectrum of $\mathbf{P3_{Cu3}}$, the hyperfine coupling parameters and g-values were fixed as well as D, and the parameters C_1 and C_2 were taken from the simulation of the dimer spectrum. The same angular dependence of J as for $\mathbf{P2_{Cu2}}$ was assumed, but considering an independent rotation about both butadiyne linkers. The J-coupling between the outer two

porphyrin units was assumed to be negligible. This assumption can be justified on the basis of the cw EPR spectrum of a porphyrin trimer with two terminal copper centres and a central zinc centre. The cw EPR spectrum of this molecule, referred to as **P3$_{Cu2}$**, is shown in **Figure 2.14** and is virtually identical to the spectrum of a copper porphyrin monomer. This suggests that the *J*-coupling between the two outer porphyrin units in a linear trimer is indeed negligible (compared to the width of its spectral features). More details on the EPR properties of **P3$_{Cu2}$** and longer linear porphyrin oligomers with two terminal copper units, as well as the structures of these molecules are given in Appendix B (cf. **Section B.1**).

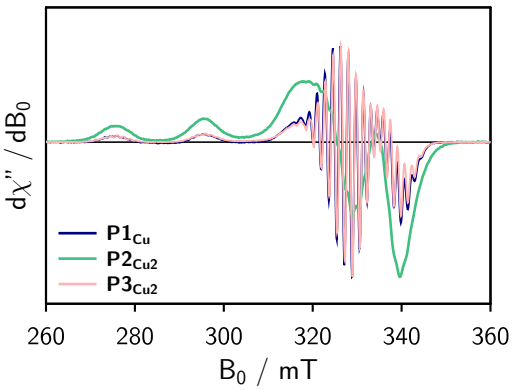


Figure 2.14: Comparison of the cw EPR spectra of **P1$_{Cu}$**, **P2$_{Cu2}$** and **P3$_{Cu2}$** recorded in frozen toluene at 100 K.

In **Figure 2.15**, the simulation for **P3$_{Cu3}$** is compared to the corresponding integrated experimental cw EPR spectrum. The good agreement between experiment and simulation confirms that *J*-coupling indeed only seems to be significant between nearest neighbours.

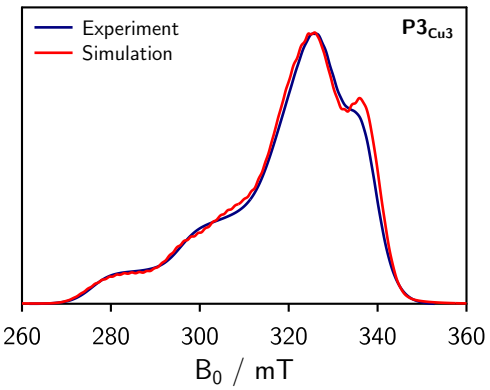


Figure 2.15: Comparison of the experimental integrated cw EPR spectrum of **P3$_{Cu3}$** with the result of the simulation using Spinach. Details on the simulation are given in the text.

The numerical simulation of the cw EPR spectrum of the linear hexamer **P6$_{Cu6}$** was not attempted, since the computational effort was not considered to be in relation to the small further insight that could potentially be gained, especially in view of the large number of assumptions on geometry, flexibility and interaction strengths which would need to be made.

Validation of the Results

To supply further confirmation that the influence of J in $\mathbf{P2_{Cu2}}$ is substantial, its spectrum was also simulated for $J = 0$. In **Figure 2.16** the simulated spectra of $\mathbf{P1_{Cu}}$, $\mathbf{P2_{Cu2}}$ considering only the influence of the dipolar interaction, and $\mathbf{P2_{Cu2}}$ assuming both dipolar and exchange interactions, are contrasted. It is observed that, compared to the spectrum of $\mathbf{P1_{Cu}}$, the shape of the simulated spectrum of $\mathbf{P2_{Cu2}}$ only changes slightly when only D is taken into account. These slight changes cannot account for the entire experimentally observed broadening (i.e. the almost missing hyperfine structure), showing that the influence of J is non-negligible.

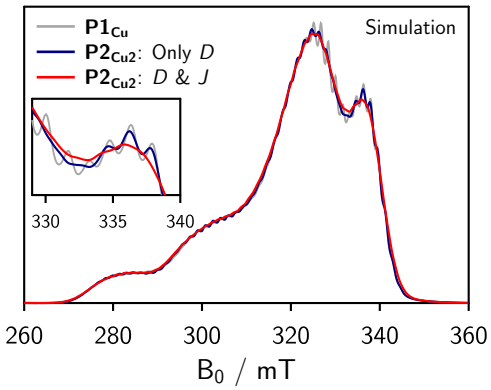


Figure 2.16: Comparison of the simulations using Spinach for $\mathbf{P1_{Cu}}$, $\mathbf{P2_{Cu2}}$ considering only the influence of D, and $\mathbf{P2_{Cu2}}$ assuming both D and J.

2.4 Conclusions

In the present study, the magnitude of the exchange interaction between two copper centres in linear copper porphyrin oligomers was evaluated by numerical simulation of the cw EPR spectra. Since the isotropic limit could not be reached at room temperature, due to the presence of bulky side and end groups in the structures preventing rapid molecular tumbling, a straightforward separation of the contributions of D and J to the EPR spectra was not possible. Consequently, the analysis needed to be performed on the frozen solution spectra.

A general characterisation of the investigated compounds by pulse EPR methods allowed the determination of the nitrogen hyperfine coupling constants and relaxation rates. It was found that the hyperfine coupling constants are virtually identical for $\mathbf{P1_{Cu}}$ and $\mathbf{P2_{Cu2}}$, within experimental accuracy. The nitrogen hyperfine coupling constants are of the order of 50 MHz. If the exchange coupling in the dimer was significantly larger than the hyperfine coupling interaction, one should theoretically expect the hyperfine couplings to be halved in the dimer since, due to the coupling between the two spin centres, the spin density should be evenly spread over both units. The fact that the hyperfine couplings remain unchanged despite the presence of J with a magnitude greater than 50 MHz, might be explained by the large copper hyperfine coupling $A_{||}$ of the order of 600 MHz present in these systems.

Dipolar convolution was applied to reproduce the dimer spectrum considering the known distance between the copper centres of 1.35 nm. From the analysis it could be concluded that the influence of J to the frozen solution cw EPR spectrum of $\mathbf{P2_{Cu2}}$ must be substantial.

To quantify the magnitude of J, the spectra of the dimer, $\mathbf{P2_{Cu2}}$, and trimer, $\mathbf{P3_{Cu3}}$, were simulated using a spin Hamiltonian approach, including the influence of D and J explicitly. Since also the hyperfine coupling constants of copper and nitrogen needed to be included in the simulation due to their significant contribution to the spectral shape, the spin Hamiltonian dimensions were beyond the limits of feasibility of commonly used simulation programs for EPR spectra. The simulations were thus performed in the time-domain using the software package Spinach, employing the strategies outlined in Appendix C.

For the simulation of the dimer spectrum, the spin Hamiltonian parameters of the monomer were taken as a reference and only J and its distribution were adapted. The best fit was obtained for a broad distribution in J centred at about 100 MHz.

Based on the results from cw EPR and numerical simulations, it was concluded that the J-coupling in the longer porphyrin oligomers with more than two units is not increased markedly with reference to $\mathbf{P2_{Cu2}}$, suggesting that, to a first approximation, the intra-molecular coupling in these systems is only effective between nearest neighbours. This result could also be confirmed by measuring the EPR spectrum of a linear porphyrin trimer with two copper units separated by a central zinc unit. The spectrum of this compound resembles that of a porphyrin monomer, indicating negligible exchange coupling between the two copper centres separated by $\sim$2.7 nm. Electronic communication thus seems to be restricted to about two porphyrin units in the investigated linear systems.

The broad width of the distribution in J found for $\mathbf{P2_{Cu2}}$ was suggested to arise from contributions of many different conformers. Many energetically low-lying molecular motions, including twisting and bending of the porphyrin chain are likely to be feasible and to modulate the exchange coupling significantly. This work demonstrates for the first time that a complete numerical simulation of the frozen solution spectrum of an unusually large spin system with a Hilbert dimension of 26244×26244 can be made feasible to an extent that even parameter fitting can readily be performed. Up-scaling of the calculations seems straightforward at the expense of computation time.

A considerably larger exchange coupling than observed in the linear systems is expected for a cyclic copper porphyrin hexamer, $\mathbf{\textit{c}\text{-}P6_{Cu6}}$, based on a visual inspection of the corresponding cw EPR spectra presented in Appendix B (**Section B.3**). A numerical simulation of the frozen solution spectrum taking all dipolar and exchange interactions into account, however, proves exceptionally difficult for this compound since many possibly invalid assumptions (regarding the coupling strengths, geometry and geometric flexibility in such a multi-spin system) would need to be made in order to keep the number of variable parameters within reasonable limits and thus the results physically meaningful. Additionally, due to the large size of the spin system, parameter fitting might not be easily feasible and the analysis might be complicated by the presence of quantum interference effects as shown in Chapter 4. No simulations were therefore performed on this system, but a complete EPR characterisation can be found in the Appendix.

Chapter 3

Molecular Geometry and Metal-Ligand Interactions in *c*-P10$_{Cu2}$ Complexes

Metal-ligand interactions and the molecular geometry of template-bound complexes of a ten-membered bis-copper porphyrin nanoring (***c*-P10$_{Cu2}$**) were investigated by hyperfine and dipolar spectroscopies. The hetero-metallated nanoring was synthesised by Jonathan Cremers (Anderson group, University of Oxford, UK) and contains two copper and eight zinc centres. The structure is shown together with that of the two molecular templates with either four (**T4**) or five (**T5**) binding sites in **Figure 3.1**. The aryl side groups on the porphyrin core are 3,5-di-*tert*-butylphenyl groups, referred to as **tBu** in this work.

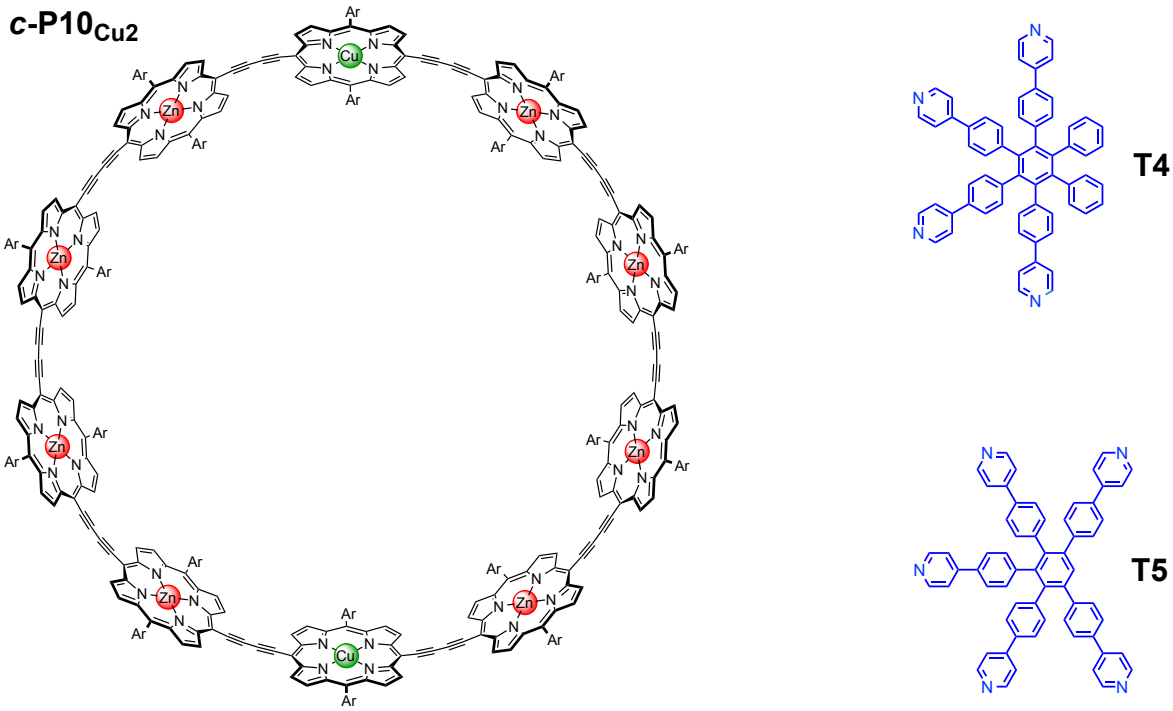


Figure 3.1: Chemical structures of ***c*-P10$_{Cu2}$** and the two molecular templates **T4** and **T5** (Ar = 3,5-di-*tert*-butylphenyl, **tBu**).

The metal centres in the porphyrin structure can bind axial nitrogen ligands of the molecular **T4** or **T5** templates to form supramolecular complexes by self-assembly, where two templates are bound per nanoring [70, 71]. While the interaction between axial nitrogen ligands and zinc centres is well

characterised [72], much less information is available on the corresponding interaction with copper. The coordination of the metal centres to axial nitrogen ligands is also exploited in the synthesis of the ten-membered nanoring as is illustrated in **Figure 3.2**. Since the nanoring is synthesised from two linear porphyrin pentamers with one central copper unit, the copper porphyrin units in the structure will necessarily be sitting opposite each other, separated by four zinc porphyrin units on either side. The **T5** template used in the synthesis of *c*-**P10$_{Cu2}$** can be removed by addition of pyridine to obtain the template-free ten-membered ring which is used as a comparison in this study. The template-bound structures are then obtained by adding either **T4** or **T5** template in stoichiometric equivalents to a solution of *c*-**P10$_{Cu2}$**.

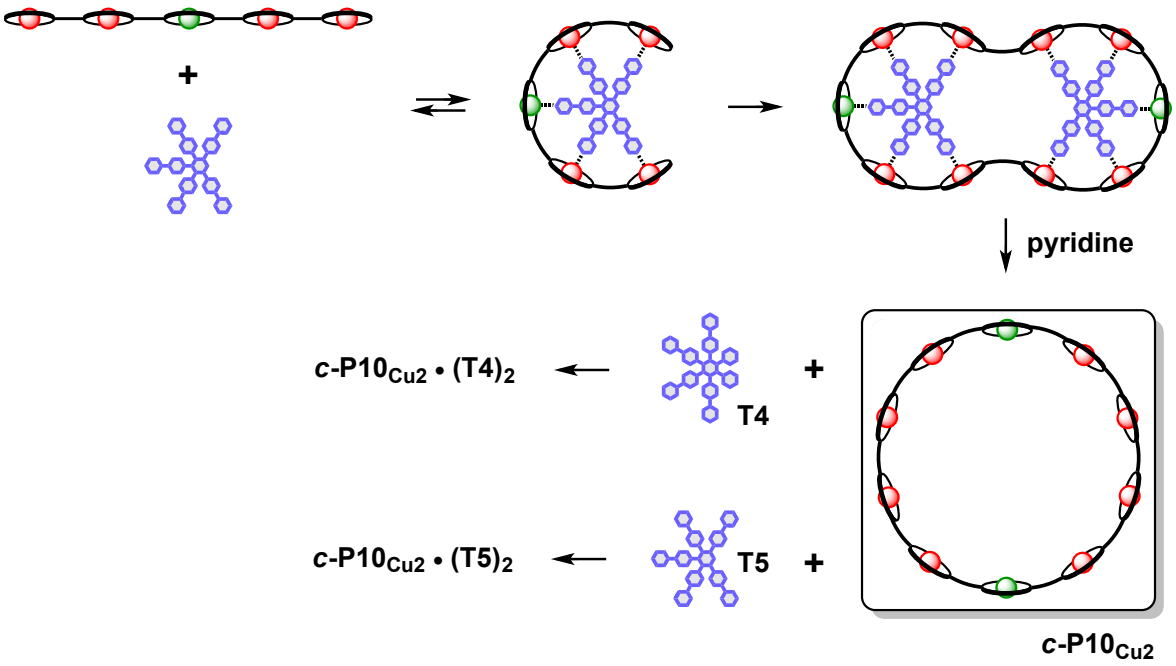


Figure 3.2: Overview of the synthetic strategy employed in the synthesis of the ten-membered bis-copper porphyrin nanoring *c*-**P10$_{Cu2}$**. Copper centres are shown in green, whereas zinc centres are indicated in red.

The formation of 1:2 complexes between *c*-**P10$_{Cu2}$** and the molecular templates can be confirmed by UV-vis titrations. Upon binding of the template to the porphyrin ring, the porphyrin Q-bands shift towards longer wavelengths and become considerably more structured as compared to the spectrum of the free ring. The spectral changes can be attributed to an increased rigidity (i.e. reduced dihedral angle spread) of the structures as a result of template coordination. UV-vis spectra at different points of a room temperature titration of a 0.96 μM chloroform solution of *c*-**P10$_{Cu2}$** with the molecular templates **T4** and **T5** are shown in **Figure 3.3** and were recorded by Jonathan Cremers (Anderson group, University of Oxford, UK). The porphyrin concentration was kept constant during the titration. In all cases a clear endpoint of the titration was observed after addition of two equivalents of template, confirming the binding of two templates per nanoring. The formed 1:2 complexes will henceforth be referred to as *c*-**P10$_{Cu2}$ · (T4)$_2$** and *c*-**P10$_{Cu2}$ · (T5)$_2$**. No marked differences are observed between the UV-vis spectra of *c*-**P10$_{Cu2}$ · (T4)$_2$** and *c*-**P10$_{Cu2}$ · (T5)$_2$**.

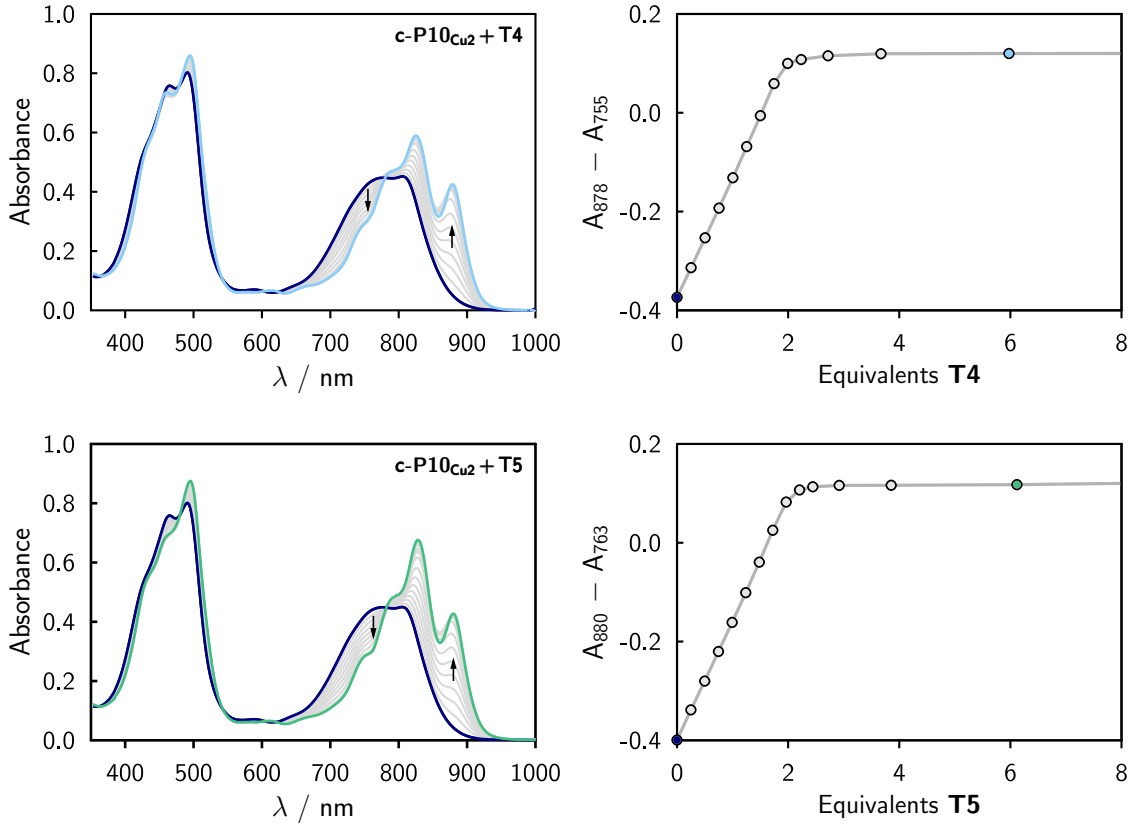


Figure 3.3: Room temperature UV-vis spectra (*left*) at different points of a titration of ***c*-P10$_{Cu2}$** with **T4** (*top*) or **T5** (*bottom*) in chloroform and corresponding plots of the change in absorbance at particular wavelengths (as indicated) as a function of template concentration (*right*).

While the stoichiometry of the complexes can be determined in a rather straightforward way by UV-vis titrations, more advanced experiments are necessary to determine the location of the two copper centres within the supramolecular complexes. In principle, three different positions of the copper units could be imagined, leading to three different Cu···Cu separation distances as illustrated in **Figure 3.4**. The indicated distances of 2.5 nm, 4.3 nm, and 5.0 nm have been estimated based on published values for a six-membered template-bound zinc porphyrin nanoring [73] and agree well with those obtained by molecular modelling of the structure using HyperChem [74] with the MM + force field and parameters adapted for porphyrins [75–78].

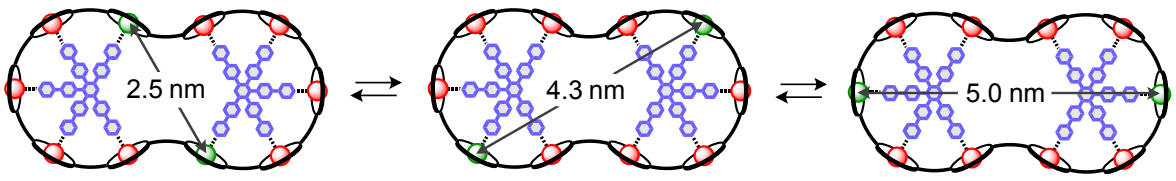


Figure 3.4: Cartoon illustrating the three conceivable conformations of ***c*-P10$_{Cu2}$ · (T5)$_2$** leading to three different separation distances between the copper centres of 2.5 nm, 4.3 nm and 5.0 nm. Similar structures are expected to form for ***c*-P10$_{Cu2}$ · (T4)$_2$**.

In this study, the relative populations of the three different conformations in the template-bound complexes are determined with the aim to explore how the presence of two metal ions with different

binding affinities to axial nitrogen ligands influences the geometry of the supramolecular assemblies. In the following, the interaction of copper with axial nitrogen ligands will be characterised by hyperfine techniques, before making use of pulse dipolar spectroscopy to determine inter-copper distances and distance distributions, and consequently obtain information about the structures and flexibility of the investigated compounds.

3.1 Characterisation of the Metal-Ligand Interaction

All EPR measurements were carried out on 0.2 mM samples in toluene-d_8, unless otherwise stated. Details on the sample preparation and experimental parameters are given in Appendix A (**Section A.1** and **Subsection A.3.1**). A slight excess of template was employed in the preparation of the ***c*-P10$_{Cu2}$ · (T4)$_2$** and ***c*-P10$_{Cu2}$ · (T5)$_2$** samples and complex formation was confirmed by UV-vis spectroscopy.

3.1.1 cw EPR

To characterise the electronic and nuclear environment in the vicinity of the copper centres in the ***c*-P10$_{Cu2}$** structures, cw EPR spectroscopy was used at X-band. In **Figure 3.5** (*left*) the frozen solution (100 K) cw EPR spectrum of ***c*-P10$_{Cu2}$** is compared to that of a copper porphyrin monomer **P1$_{Cu}$**. It can be seen that the two spectra are very similar, suggesting that the two copper centres in ***c*-P10$_{Cu2}$** are sufficiently far apart so that any intramolecular interactions between them, which could lead to line broadening, are small compared to the width of the spectral features. The spectrum of ***c*-P10$_{Cu2}$ · (T4)$_2$** also resembles that of **P1$_{Cu}$** as can be seen from **Figure 3.5** (*right*). Based on a visual comparison of the spectra, the g-values and hyperfine coupling constants seem to be virtually identical for ***c*-P10$_{Cu2}$** and ***c*-P10$_{Cu2}$ · (T4)$_2$**, which indicates that the local nuclear and electronic structure at the copper centres is very similar in both cases.

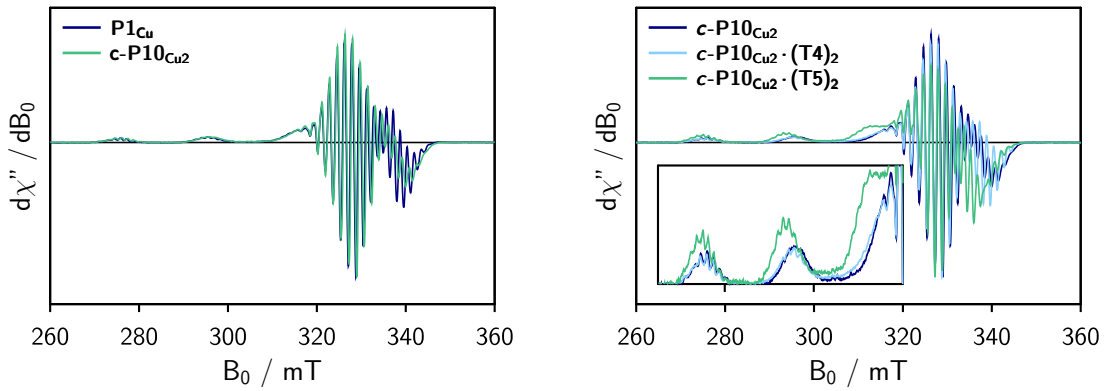


Figure 3.5: Comparison of the baseline and frequency corrected (9.39 GHz) X-band frozen solution cw EPR spectrum of ***c*-P10$_{Cu2}$** with the spectrum of **P1$_{Cu}$** (*left*) and the spectra of ***c*-P10$_{Cu2}$ · (T4)$_2$** and ***c*-P10$_{Cu2}$ · (T5)$_2$** (*right*) recorded in toluene-d_8 at 100 K.

Compared to those of ***c*-P10$_{Cu2}$** and ***c*-P10$_{Cu2}$ · (T4)$_2$**, clear differences are observed in the cw EPR spectrum of ***c*-P10$_{Cu2}$ · (T5)$_2$**. The whole spectrum is shifted to lower fields, indicating an

increase in the g-values, in particular $g_{||}$. In addition, the out-of-plane copper hyperfine coupling constant $A_{||}$ is reduced with respect to ***c*-P10$_{Cu2}$** and ***c*-P10$_{Cu2}$ · (T4)$_2$** as shown by the reduced splitting between the two outmost copper transitions which are resolved at the low-field side of the spectrum.

In the ***c*-P10$_{Cu2}$ · (T5)$_2$** sample, all metal centres are expected to be bound to a template leg in contrast to the other two samples. Consequently, the spectral differences could arise from coordination of copper to the fifth template leg in **T5**, while in **T4** the four template legs might preferentially bind to the zinc centres, leaving the two copper centres unbound. More information on this metal-ligand interaction should be accessible *via* measurement of the ^{14}N hyperfine coupling constants. Since small variations in the nitrogen couplings cannot be determined with high precision by cw EPR, Davies ENDOR spectroscopy was employed at Q-band frequencies.

3.1.2 Davies ENDOR

The ^{14}N Davies ENDOR spectra were recorded in frozen toluene-d_8 at 15 K. To obtain information on all principal components of the tensors, two spectra were recorded for every sample at field positions corresponding to the xy and z orientations as indicated in **Figure 3.6** for the case of ***c*-P10$_{Cu2}$**. Analogous positions were chosen for the other two samples.

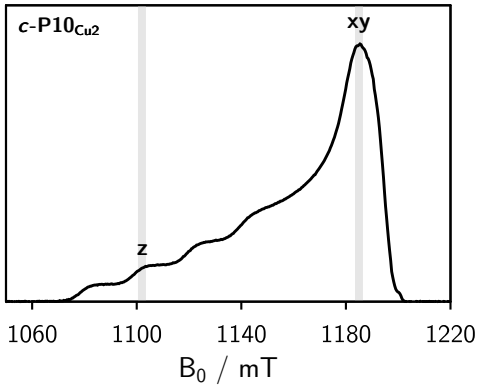


Figure 3.6: Field-swept echo-detected Q-band EPR spectrum of ***c*-P10$_{Cu2}$** recorded in frozen toluene-d_8 at 15 K. The field positions where the ENDOR spectra were taken are indicated.

The Davies ENDOR spectra of the three structures are compared in **Figure 3.7**. It can again be seen that the spectra of ***c*-P10$_{Cu2}$** and ***c*-P10$_{Cu2}$ · (T4)$_2$** are very similar, while pronounced additional peaks are observed in the spectrum of ***c*-P10$_{Cu2}$ · (T5)$_2$**. These additional peaks indicate a minor contribution of a species with slightly reduced nitrogen hyperfine coupling constants. To confirm the origin of the second contribution to the spectrum of ***c*-P10$_{Cu2}$ · (T5)$_2$**, density functional theory (DFT) calculations were performed.

3.1.3 DFT Calculations

Density functional theory calculations were carried out to characterise the metal-ligand interaction between copper or zinc ions and axial nitrogen ligands in porphyrin structures. Differences in molec-

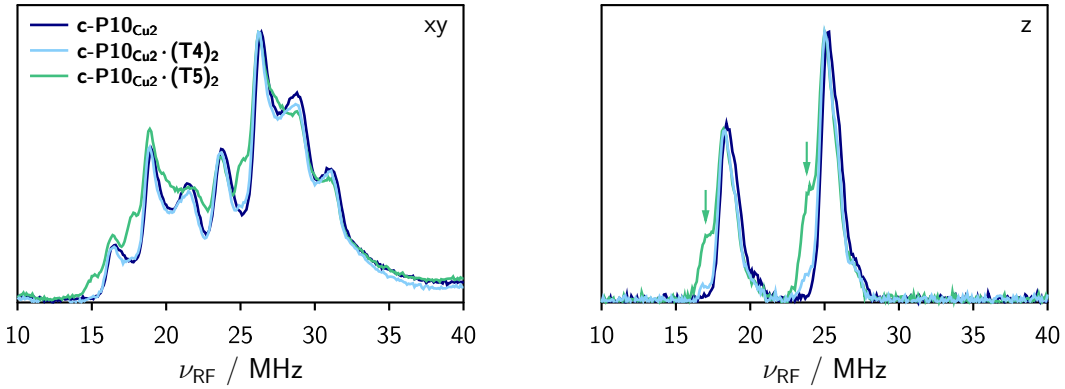


Figure 3.7: Comparison of the ^{14}N Davies ENDOR spectra of ***c*-P10$_{Cu2}$**, ***c*-P10$_{Cu2}$ · (T4)$_2$** and ***c*-P10$_{Cu2}$ · (T5)$_2$** recorded at Q-band frequencies (15 K) at a field position corresponding to the *xy* (*left*) and *z* (*right*) orientations. In the case of ***c*-P10$_{Cu2}$** the field was set to 1187 mT and 1107 mT for *xy* and *z*, respectively, while the corresponding field positions for the template-bound structures were 1184 mT and 1105 mT. The green arrow in the spectrum for the *z* orientation indicates the additional contribution observed for ***c*-P10$_{Cu2}$ · (T5)$_2$**.

ular geometry and binding strength are explored by constrained geometry optimisations and the calculation of the EPR parameters on the optimised structures allows interpretation of the trends observed in the experimental cw EPR and ENDOR spectra. Vibrational frequency calculations were carried out to confirm that the optimised structures corresponded to local minima.

Constrained geometry optimisations on a copper (**P1$_{Cu}$**) and a zinc (**P1**) porphyrin monomer were carried out for several fixed separations between the pyridine nitrogen and the central metal of the porphyrin unit. Details on the calculations are given in Appendix A (cf. **Subsection A.5.2**). In the calculations, the porphyrin side groups were truncated to phenyls and the **THS** end groups were replaced by a proton. The SCF energy differences with respect to the minimum structure were plotted as a function of the metal-pyridine separation and the results are shown in **Figure 3.8** for **P1· py** and **P1$_{Cu}$· py**.

From these calculations, the following conclusions can be drawn: The metal-pyridine nitrogen equilibrium separation is calculated to be 2.18 Å for **P1· py**, whereas it is found to be 2.35 Å for **P1$_{Cu}$· py**. The potential energy gain upon binding is considerably lower for **P1$_{Cu}$· py** as compared to **P1· py**, indicating that the binding of pyridine is weaker in the case of copper as the central metal. Without dispersion correction, equilibrium M$\cdots$N^{py} separation distances of 2.25 Å and 2.59 Å are obtained for **P1· py** and **P1$_{Cu}$· py**, respectively.

Regarding the geometry of **P1· py**, experimental data are available from X-ray crystallography in the CSD database. A statistical analysis of all available experimental data was found to yield a value of 2.16±0.03 Å as the mean Zn$\cdots$N^{py} separation distance [73], which is in very good agreement with the presented DFT results. A similar analysis based on X-ray data for the distance between the zinc atom and the porphyrin plane results in a mean value of 0.37±0.06 Å for **P1· py**, whereas in a template-bound six-membered zinc porphyrin ring a distance of 0.24±0.06 Å was found experimentally [73]. This result compares favourably with the distance of 0.28 Å obtained here by DFT for **P1· py**. In the equilibrium geometry, the zinc atom is thus markedly pulled out

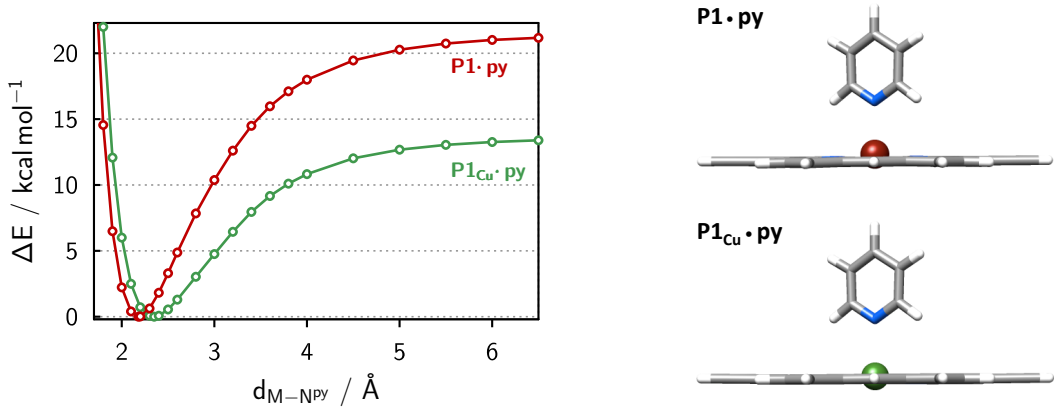


Figure 3.8: Total SCF energy differences with respect to the respective minimum structures as a function of the metal-pyridine nitrogen separation for **P1· py** and **P1$_{Cu}$· py** obtained from a constrained geometry optimisation in Turbomole using B3LYP in combination with the TZVP basis set and dispersion correction to the energies (*left*) and side view of the optimised minimum geometries of **P1· py** and **P1$_{Cu}$· py** (*right*). A slight out-of-plane distortion of the porphyrin plane is possible, but cannot be discerned in this representation.

of the porphyrin plane as is also shown in **Figure 3.8**. In the case of **P1$_{Cu}$· py**, a distance of only 0.12 Å between the copper ion and the porphyrin plane is found by DFT, indicating that the copper atom roughly remains in the centre of the porphyrin plane even when binding a pyridine ligand.

Regarding the interaction of copper and axial nitrogen ligands, much less information is available in the database. By X-ray crystallography of a copper porphyrin with two axial pyridine ligands, a Cu$\cdots$N^{py} distance of 2.58 Å was found experimentally [79], whereas a Cu$\cdots$N^{py} distance of 2.47 Å was reported for a copper porphyrin with one axial pyridine ligand [80].

To interpret the observed changes in the EPR spectra of the copper-containing complexes and assign the measured couplings to the different nuclei within the porphyrin core, the EPR properties were calculated by DFT for the equilibrium structures of **P1$_{Cu}$** and **P1$_{Cu}$· py**. Moreover, the orientations of the hyperfine and **g**-tensors are obtained by DFT, which are required for a numerical simulation of the experimental data. The calculated hyperfine and nuclear quadrupole tensors as well as the orientation of the **g**- and **A**-tensors are visualised for both structures in **Figure 3.9**. The relative size of the tensors reflects the magnitude of the coupling, however, for some tensors, scaling factors were applied as detailed in the figure caption. Nitrogen couplings are shown in blue, ^{13}C couplings in dark grey, and copper couplings in yellow. The **g**-tensor axes are indicated by dark blue arrows, while the light grey arrows represent the orientation of the hyperfine or nuclear quadrupole coupling tensors. By projection of the interaction tensors onto the **g**-tensor axes, scalar values are obtained which can directly be compared to the experiment. If the **A**- and **g**-tensors are collinear, these values correspond to the principal values of the hyperfine coupling tensors.

Table 3.1 gives an overview of the calculated nitrogen hyperfine coupling constants for the two structures which can be compared to the experiment. The couplings labelled N$^{1-4}$ refer to the in-plane nitrogens, whereas the coupling labelled N^5 corresponds to the coupling of the electron spin of copper to the axial pyridine ligand in **P1$_{Cu}$· py**.

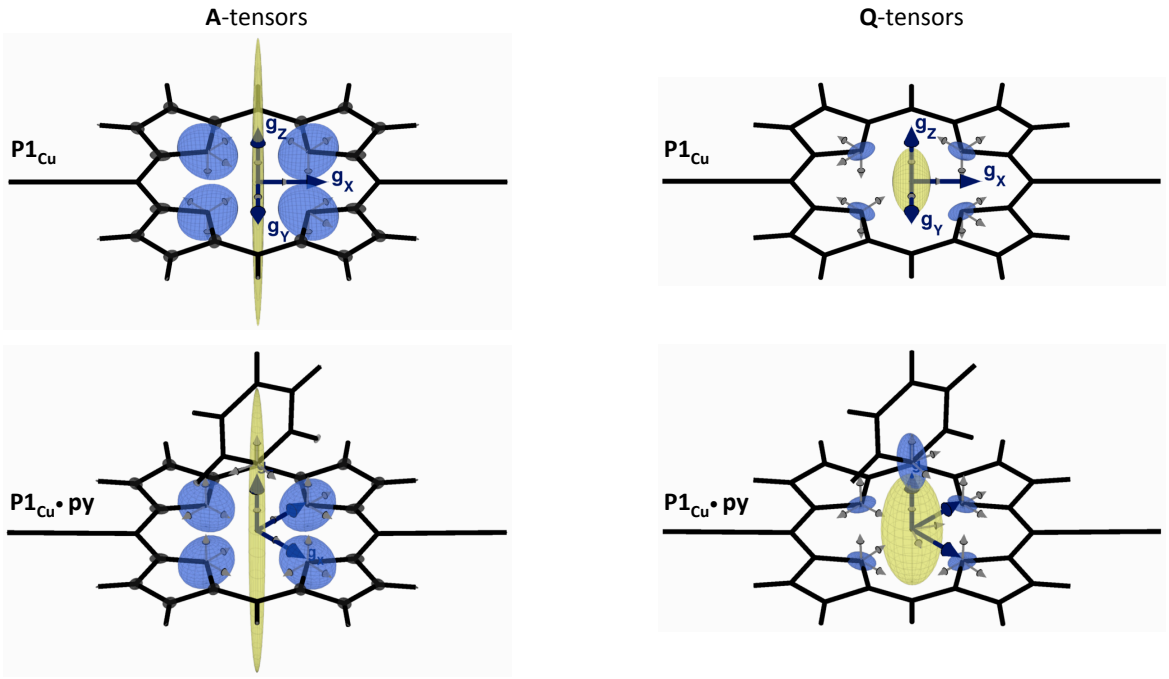


Figure 3.9: Illustration of the calculated hyperfine (*left*) and nuclear quadrupole (*right*) coupling tensors and **g**-tensor orientations in the molecular frame for **P1$_{Cu}$** (*top*) and **P1$_{Cu}$· py** (*bottom*). The relative sizes of the tensors reflect the magnitude of the coupling. However, for better visualisation, the hyperfine coupling tensors for nitrogen and copper were scaled down by a factor of two and four, respectively, compared to the proton and carbon hyperfine tensors. For visualisation of the nuclear quadrupole tensors, the **Q**-tensors were all scaled up equally by a factor of 30 as compared to the proton hyperfine tensors.

Table 3.1: Nitrogen hyperfine coupling constants calculated for **P1$_{Cu}$** and **P1$_{Cu}$· py** with ORCA V 3.0 using DFT/B3LYP in combination with the EPRII basis set.

	$A^{N^{1-4}}_{[x,y,z]}$ / MHz	$A^{N^{5}}_{[x,y,z]}$ / MHz
P1$_{Cu}$	[58, 46, 47]	-
P1$_{Cu}$· py	[55, 43, 44]	[-1.15, -1.14, -0.29]

Several observations can be made from the calculated nitrogen hyperfine couplings. First of all, it is noted that the hyperfine coupling constants of the pyridine nitrogen itself are only of the order of 1 MHz and therefore do not contribute to the experimental ^{14}N Davies ENDOR spectra shown above. The small size of the coupling to an axial ligand may be explained considering that the unpaired electron spin is occupying the $d_{x^2-y^2}$ orbital. Furthermore, it is observed that the in-plane nitrogen couplings are reduced by about 3 MHz in all directions upon binding of a pyridine ligand. This reduction in the in-plane hyperfine couplings explains the additional peaks observed in the ENDOR spectra of ***c*-P10$_{Cu2}$ · (T5)$_2$**: The experimentally observed spectrum seems to be a linear combination of two spectra. The peaks also observed in the spectra of ***c*-P10$_{Cu2}$** and ***c*-P10$_{Cu2}$ · (T4)$_2$** result from unbound copper porphyrin units, whereas the additional minor contribution to the spectrum of ***c*-P10$_{Cu2}$ · (T5)$_2$** is a result of the axial coordination to a nitrogen

ligand. The coupling to the pyridine ligand is not probed directly by ENDOR, but the interaction is detected *via* a reduction of the in-plane nitrogen hyperfine couplings.

Furthermore, upon binding of a pyridine ligand, DFT predicts an increase in $g_{\perp}$ and $g_{||}$ and a decrease in the out-of-plane copper hyperfine coupling constant $A_{||}$ of **P1$_{Cu}$**.* These trends are in very good agreement with the differences in the EPR parameters observed experimentally between **P1$_{Cu}$** and **P1$_{Cu}$·py**. The corresponding experimental data and simulations are presented in Appendix D (cf. **Figure D.7** and **Figure D.9**).

3.1.4 Spectral Simulations & HYSCORE

The experimental EPR parameters obtained for **P1$_{Cu}$** and **P1$_{Cu}$·py** (Appendix D) were also used in the numerical simulation of the spectra of ***c*-P10$_{Cu2}$**, ***c*-P10$_{Cu2}$·(T4)$_2$** and ***c*-P10$_{Cu2}$·(T5)$_2$**. Based on the results from DFT, in combination with the observations from ENDOR and cw EPR, it can be concluded that two species contribute to the spectra of ***c*-P10$_{Cu2}$·(T5)$_2$** (and to a lesser extent also to those of ***c*-P10$_{Cu2}$·(T4)$_2$**), corresponding to unligated and ligated copper porphyrin units, respectively. Consequently, the respective ENDOR and cw EPR spectra were simulated as a linear combination of two contributions. The hyperfine, nuclear quadrupole, and *g*-values were taken from simulations of the EPR and ENDOR spectra of **P1$_{Cu}$** and **P1$_{Cu}$·py** shown in Appendix D (cf. **Table D.1**) and only the relative weights of the two contributions were adapted to fit the spectra of the template-bound ***c*-P10$_{Cu2}$** structures. The numerical simulations were performed using the MATLAB package EasySpin. From the experiment only the absolute value of the hyperfine coupling constants can be determined. The signs of the couplings were consequently chosen in agreement with DFT calculations.

ENDOR Simulations

Figure 3.10 shows the experimental ^{14}N Davies ENDOR spectra of the three ***c*-P10$_{Cu2}$** structures together with the corresponding simulations. The two spectra for the *xy* and *z* orientations were fitted simultaneously for each compound. Even though only the relative percentage of the two spectral contributions was varied, the agreement between experiment and simulation is reasonable. The peak positions are well reproduced, while larger differences are observed regarding the relative peak intensities. However, as also discussed in Appendix D (cf. **Section D.2**), since all the relevant information for our purposes is contained in the peak positions, discrepancies in the relative intensities are not crucial for the interpretation of the spectra. To satisfactorily reproduce the spectra of ***c*-P10$_{Cu2}$·(T4)$_2$** and ***c*-P10$_{Cu2}$·(T5)$_2$** using the parameters from **P1$_{Cu}$** and **P1$_{Cu}$·py**, relative contributions of the second component of ≈5 % and ≈30 % needed to be invoked.

*For reasons outlined in Appendix A (cf. **Subsection A.5.2**), the values calculated for the in-plane copper hyperfine coupling constants $A_{\perp}$ of the copper structures are much smaller than experimentally observed. The coupling is close to zero and changes sign depending on the used basis set so that predictions of a trend in this parameter based on DFT results are error-prone and shall therefore not be attempted here.

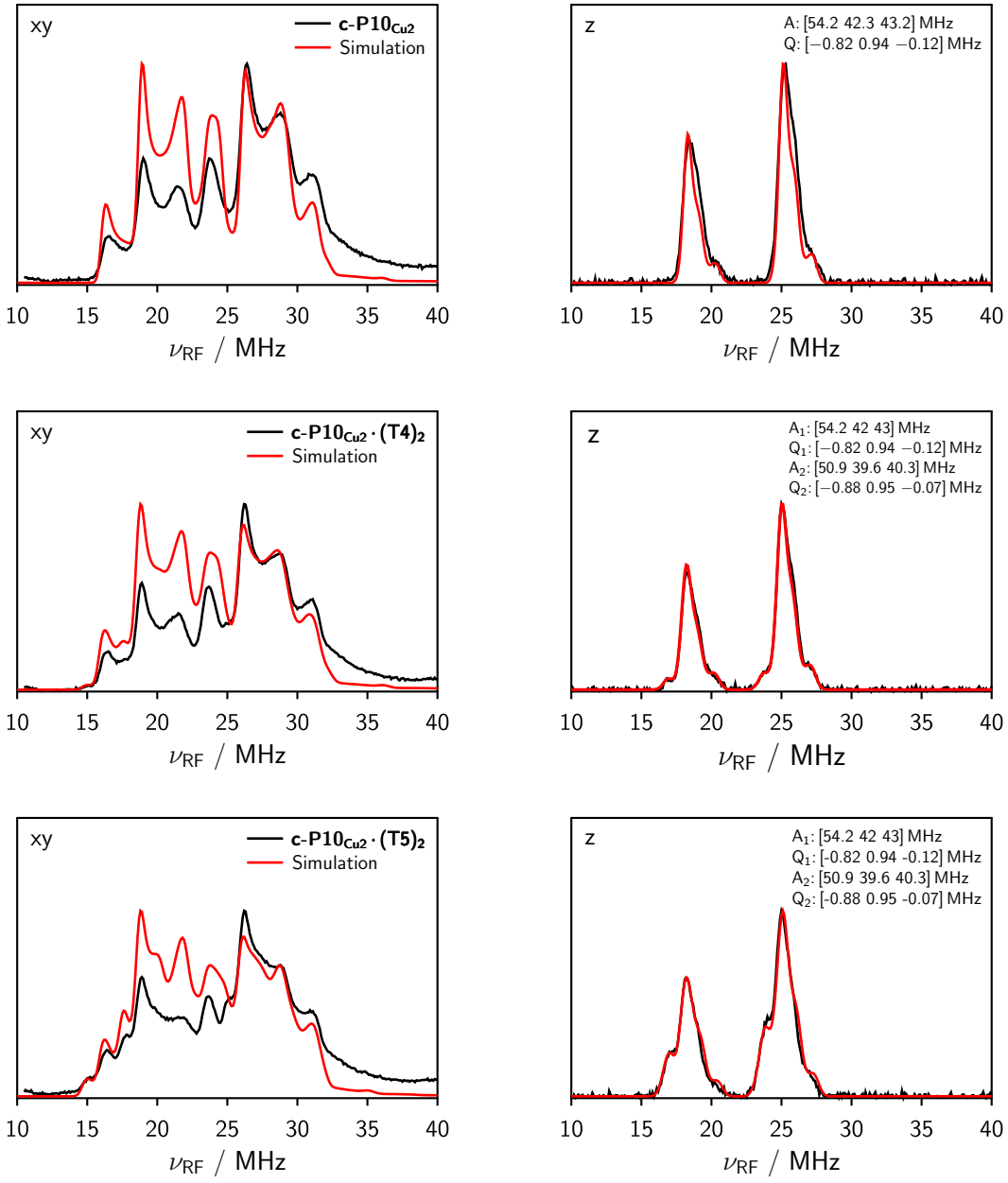


Figure 3.10: Experimental ^{14}N Davies ENDOR spectra of ***c*-P10$_{Cu2}$** (*top*), ***c*-P10$_{Cu2}$ · (T4)$_2$** (*centre*) and ***c*-P10$_{Cu2}$ · (T5)$_2$** (*bottom*) recorded at Q-band frequencies in frozen toluene-d_8 (15 K) at field positions corresponding to the respective *xy* (*left*) and *z* (*right*) orientations together with the corresponding simulations carried out using EasySpin. The simulation parameters are indicated in the figure. The spectra for ***c*-P10$_{Cu2}$ · (T4)$_2$** and ***c*-P10$_{Cu2}$ · (T5)$_2$** were simulated invoking two components, where the relative contribution of the second component amounts to ≈5 % and ≈30 %, respectively.

Simulations of the cw EPR Spectra

In **Figures 3.11** and **3.12** the experimental frozen solution cw EPR spectra of the three structures are shown together with their simulations. The nitrogen hyperfine coupling constants were taken from the simulations of the ENDOR spectra of **P1$_{Cu}$** and **P1$_{Cu}$· py**, and kept fixed during the

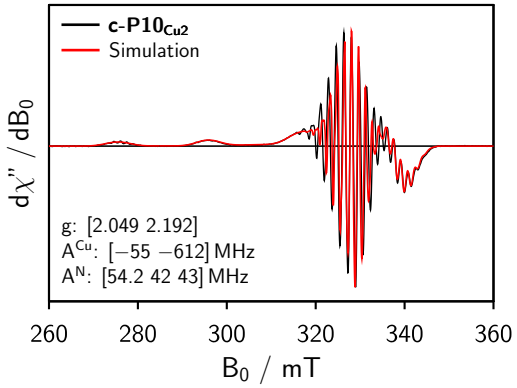


Figure 3.11: Experimental cw EPR spectrum of ***c*-P10$_{Cu2}$** recorded in frozen toluene-d_8 at 100 K together with a simulation carried out using EasySpin. The simulation parameters are indicated in the figure.

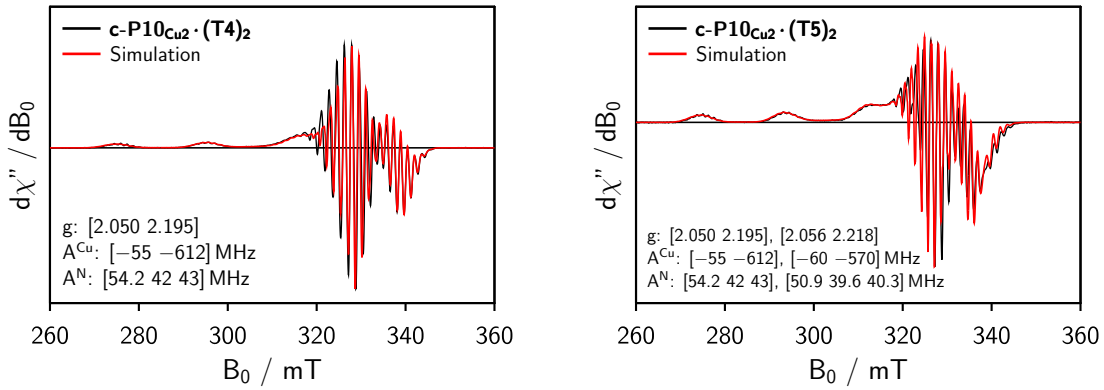


Figure 3.12: Experimental cw EPR spectra for ***c*-P10$_{Cu2}$ · (T4)$_2$** (*left*) and ***c*-P10$_{Cu2}$ · (T5)$_2$** (*right*) recorded in frozen toluene-d_8 at 100 K together with the corresponding simulations. The simulation parameters are indicated in the figure. To satisfactorily reproduce the experimental spectrum of ***c*-P10$_{Cu2}$ · (T5)$_2$**, a second contribution with a relative weight of ≈40 % needed to be invoked.

simulations. To simulate the spectrum of ***c*-P10$_{Cu2}$**, the copper hyperfine coupling constants and g-factors determined for **P1$_{Cu}$** were taken as an initial guess but were left to vary freely when applying a least-squares fitting routine. Compared to the parameters obtained for **P1$_{Cu}$**, the best fit is obtained for identical copper hyperfine couplings but slightly decreased g-values (<1 %).

The spectra of the template-bound structures were then simulated varying only the relative contributions of the two components with parameters adopted from the corresponding simulations for **P1$_{Cu}$** and **P1$_{Cu}$· py**. While the spectrum of ***c*-P10$_{Cu2}$ · (T4)$_2$** could be satisfactorily reproduced involving just one component, a second component with a relative contribution of ≈40 % was needed to reproduce the cw EPR spectrum of ***c*-P10$_{Cu2}$ · (T5)$_2$**.[†]

Overall, the spectral simulations thus confirm that more than one species is present in the sample of ***c*-P10$_{Cu2}$ · (T5)$_2$** with a contribution of about 30–40 %. The second species can be attributed

[†]In addition, the value of the out-of-plane copper hyperfine coupling constant, $A_\perp$, of the second component needed to be left as a fitting parameter to obtain a satisfactory result.

to a conformation of the nanoring where all five legs of the **T5** template are bound to porphyrin units, forcing copper to bind an axial nitrogen ligand. Judging by the relative percentages of this second component, it seems, however, that the fifth template leg in *c*-**P10$_{Cu2}$ · (T5)$_2$** is not bound to copper in the majority of all cases.

HYSCORE

In order to confirm the presence of the small coupling between the copper centre and the axial pyridine ligand predicted by DFT, X-band HYSCORE measurements were carried out on *c*-**P10$_{Cu2}$** and *c*-**P10$_{Cu2}$ · (T5)$_2$** in regular toluene at 15 K. Protonated toluene needed to be used since the use of deuterated toluene as a solvent resulted in strong deuterium modulations which completely dominated the ESEEM time traces and prevented the detection of small nitrogen couplings.

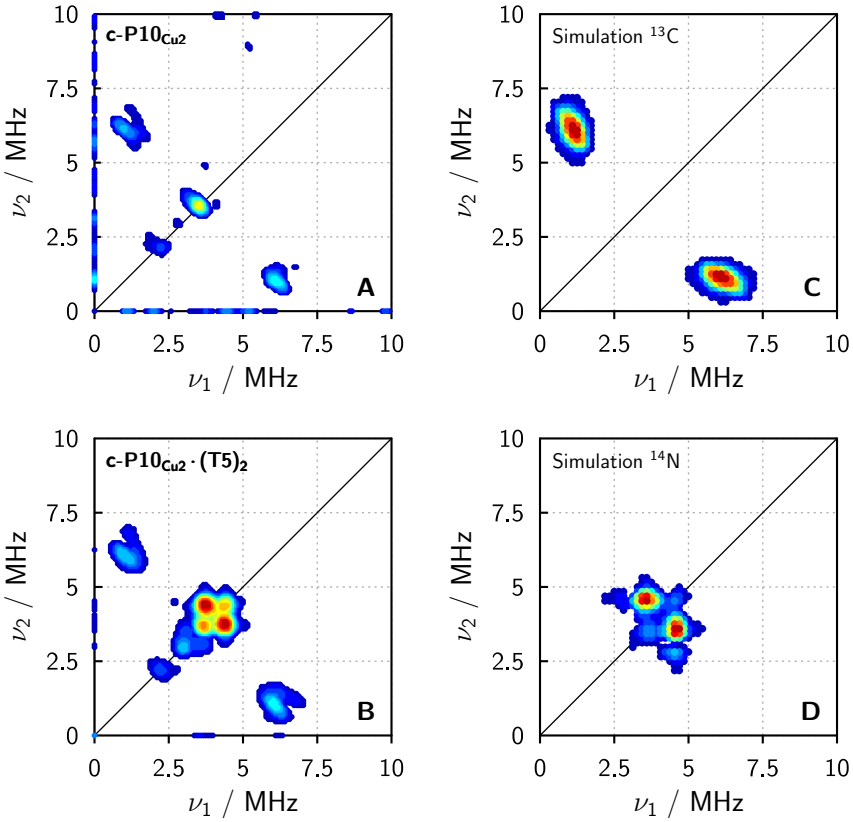


Figure 3.13: Experimental HYSCORE spectra for *c*-**P10$_{Cu2}$** (**A**) and *c*-**P10$_{Cu2}$ · (T5)$_2$** (**B**) recorded in toluene at 15 K and simulations of individual contributions to the experimental spectra using EasySpin for a ^{13}C nucleus with hyperfine coupling constants of [4.0 5.0 7.2] MHz for A_x, A_y, and A_z (**C**) and a ^{14}N nucleus with hyperfine couplings of [−1.15 −1.14 −0.29] MHz and nuclear quadrupole couplings of [0.80 1.30 −2.10] MHz (**D**).

Figure 3.13 shows the (+/+) quadrant of the experimental HYSCORE spectra of *c*-**P10$_{Cu2}$** (*top left*, **A**) and *c*-**P10$_{Cu2}$ · (T5)$_2$** (*bottom left*, **B**). No relevant signals were observed in the (−/+) quadrant. Strong ^{1}H signals were detected on the diagonal close to 14 MHz in both spectra but are not shown in the figure for clarity. A comparison of the two experimental HYSCORE spectra shows that all signals present in the spectrum of *c*-**P10$_{Cu2}$** are also observed for *c*-**P10$_{Cu2}$ · (T5)$_2$**.

However, in addition, two prominent cross peaks at (4.4, 3.8) and (3.8, 4.4) MHz are detected in the latter spectrum, which could be indicative for weak coupling to a nitrogen ligand.

To confirm the assignment of the cross peaks at (4.4, 3.8) and (3.8, 4.4) MHz in the spectrum of ***c*-P10$_{Cu2}$ · (T5)$_2$** and to identify the nature of the cross peaks at (1,6) and (6,1) MHz observed for both samples, numerical simulations were performed using EasySpin. The cross peaks observed in the spectrum of ***c*-P10$_{Cu2}$ · (T5)$_2$** could be reproduced convincingly using the hyperfine and nuclear quadrupole couplings obtained from DFT calculations for the pyridine nitrogen of **P1$_{Cu}$· py** (N^5 in **Table 3.1** with $Q^{N^5}_{[x,y,z]} = [0.80\ 1.30\ -2.10]$ MHz) as is shown in **Figure 3.13** (*bottom right*, **D**). The simulation parameters can be found in the figure caption. The good agreement between simulation and experiment allows assignment of the cross peaks at (4.4, 3.8) and (3.8, 4.4) MHz to the double-quantum peaks arising from the coupling of copper to the ^{14}N nucleus of an axial pyridine ligand in ***c*-P10$_{Cu2}$ · (T5)$_2$**.

Further simulations were performed to identify the nature of the rather intense cross peaks at (1,6) and (6,1) MHz. Judging from the magnitude of the coupling corresponding to these cross peaks, the latter could arise from the presence of ^{13}C nuclei within the structures. DFT calculations on **P1$_{Cu}$** reveal that a total of 16 carbon atoms within the porphyrin core exhibit almost equal ^{13}C couplings with an average hyperfine interaction of $A = [4.0\ 5.0\ 7.2]$ MHz (cf. **Figure 3.9**). The natural abundance of ^{13}C is low, but the large number of contributing atoms allow the coupling to be detected as is confirmed by simulation of the corresponding HYSCORE spectrum in **Figure 3.13** (*top right*, **C**).

3.2 Structure Determination by Dipolar Spectroscopy

Having characterised the metal-ligand interactions in the template-bound ***c*-P10$_{Cu2}$** structures by hyperfine techniques, dipolar spectroscopy was applied to obtain further information about the geometry and flexibility of the structures.

To begin with, the relaxation behaviour of the three compounds was studied in frozen toluene-d_8 solution at 15 K, since differences in the relaxation rates between the compounds could give a first indication about important structural differences or differences in the magnitude of intramolecular interactions. In addition, the knowledge of the approximate phase-memory time is required for the following DEER experiments. **Figure 3.14** shows the two-pulse echo decay (T_m) as a function of the inter-pulse delay τ for all three samples at X- and Q-band frequencies. Within experimental error, no differences in the signal decay are observed between the different ***c*-P10$_{Cu2}$** structures. At X-band, the echo decay is strongly modulated by weak coupling to ^{2}H nuclei of the solvent. At Q-band, these couplings are also present, but are much less pronounced and occur at a higher frequency of 7.9 as compared to 2.2 MHz.

The longitudinal relaxation ($\sim T_1$) of the investigated structures was also measured using saturation recovery in combination with the Picket fence method. The results for ***c*-P10$_{Cu2}$** and ***c*-P10$_{Cu2}$ · (T5)$_2$** are shown in **Figure 3.15**. Fitting of the experimental data using a bi-exponential model with parameters τ_1 and τ_2 results in a T_1 value (τ_1) of about 2 ms at 15 K. An analysis of the data recorded for the template-bound structures yields very similar results.

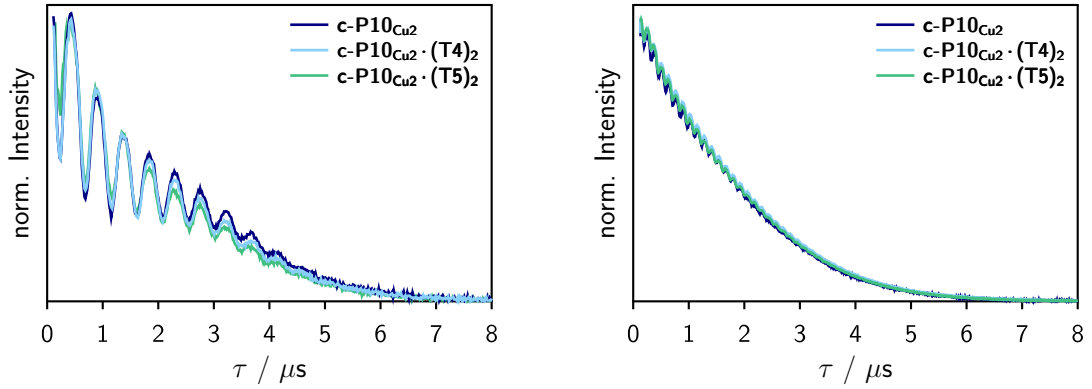


Figure 3.14: Comparison of the two-pulse echo decay (T_m) as a function of the inter-pulse delay τ for ***c*-P10$_{Cu2}$**, ***c*-P10$_{Cu2}$ · (T4)$_2$**, and ***c*-P10$_{Cu2}$ · (T5)$_2$** recorded in frozen toluene-d_8 at 15 K at X-band (*left*) and Q-band (*right*) frequencies using pulse lengths of 16 and 32 ns for $\pi/2$ and π pulses, respectively.

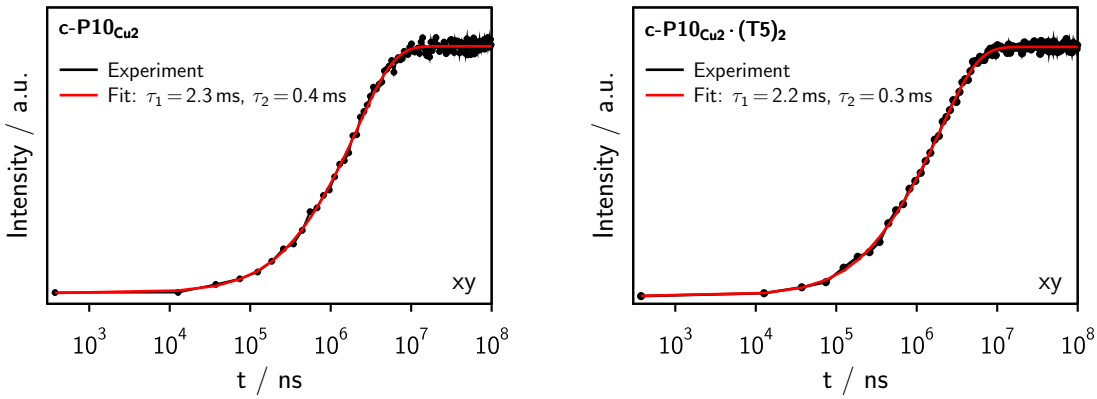


Figure 3.15: Saturation recovery experiment using the Picket fence method for the measurement of T_1 for ***c*-P10$_{Cu2}$** (*left*) and ***c*-P10$_{Cu2}$ · (T5)$_2$** (*right*) recorded at X-band in frozen toluene-d_8 (15 K).

To obtain information about the geometry and flexibility of the compounds and the location of the copper centres in the template-bound structures (cf. **Figure 3.4**), 4-pulse DEER experiments were performed at Q-band. The pump and observer pulses had a length of 12 and 16 ns, respectively. Further experimental details can be found in Appendix A (cf. **Subsection A.3.1**). The pump pulse frequency was chosen to coincide with the maximum of the field-swept echo-detected EPR spectrum, and a detection pulse frequency offset of +100 MHz was applied as is illustrated in **Figure 3.16**, taking the spectrum of ***c*-P10$_{Cu2}$** as an example.

Figure 3.17 (*left*) shows the experimental background-corrected DEER traces obtained for the three ***c*-P10$_{Cu2}$** structures. Well-defined dipolar modulations can be discerned in all traces, pointing towards Cu···Cu separations of roughly 2.5 nm in the template-bound structures and 4.3 nm in ***c*-P10$_{Cu2}$**. Since the dampening of the modulations is rather slow, it can be concluded that the distance distributions are rather narrow and the structures consequently fairly rigid.

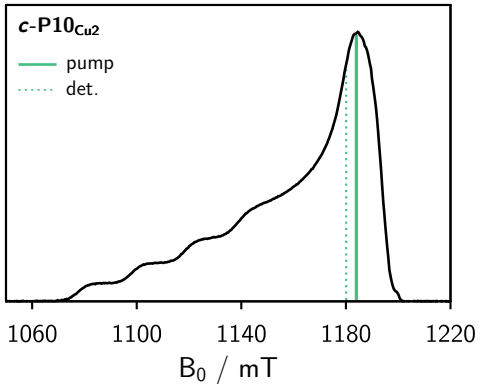


Figure 3.16: Field-swept echo-detected Q-band EPR spectrum of ***c*-P10$_{Cu2}$** recorded in frozen toluene-d_8 at 15 K. The positions of the pump and detection pulses within the spectrum, as used in the DEER experiments, are indicated. The frequency offset amounts to 100 MHz.

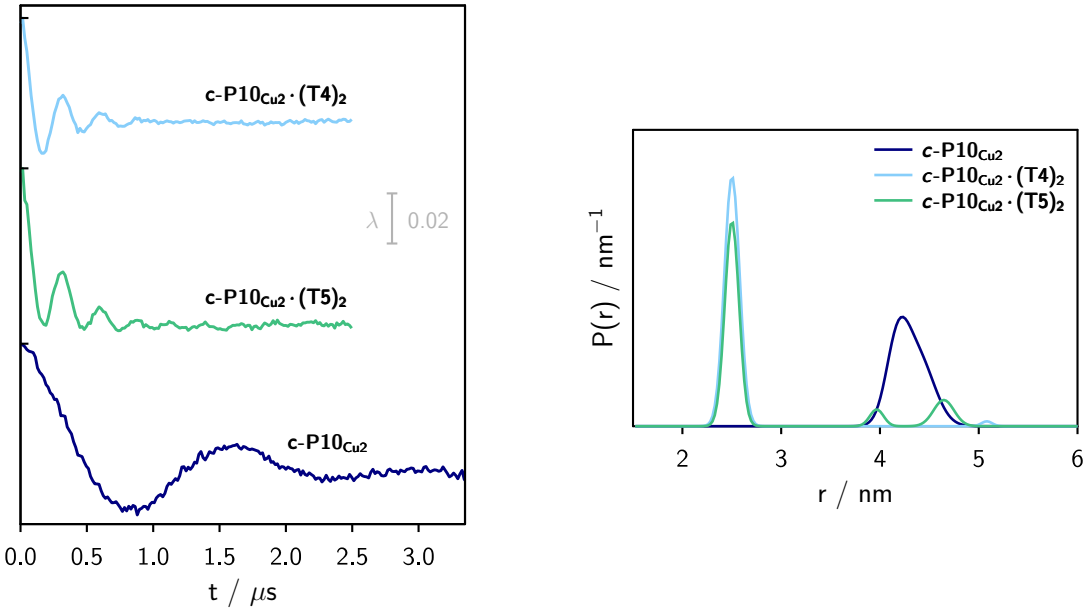


Figure 3.17: Experimental background-corrected DEER traces of ***c*-P10$_{Cu2}$ · (T4)$_2$** , ***c*-P10$_{Cu2}$ · (T5)$_2$** and ***c*-P10$_{Cu2}$** (*left*, from *top* to *bottom*) recorded at Q-band frequencies and corresponding *g*-factor corrected distance distributions obtained from a model-free analysis based on the Tikhonov regularisation algorithm as implemented in DeerAnalysis (*right*). The modulation depth scale is indicated in the figure.

The differences between the traces of ***c*-P10$_{Cu2}$ · (T4)$_2$** and ***c*-P10$_{Cu2}$ · (T5)$_2$** presumably arise from a larger contribution of longer inter-copper distances in ***c*-P10$_{Cu2}$ · (T5)$_2$** causing the observed 'up-lift' of the dipolar evolution trace at early times. In any case, it can be concluded that the shortest of the three possible Cu···Cu distances dominates the appearance of the DEER trace for both template-bound complexes.

To obtain the distance distributions corresponding to the DEER time traces, a model-free analysis was applied. The results are shown for all structures in **Figure 3.17** (*right*).

When exciting at the intensity maximum of the Q-band EPR spectrum of copper porphyrins with pulses of a length of 12 ns, orientation selection is expected [43, 81–84]. However, since

the **g**-tensor of the investigated structures is strongly axial and pump and observer pulses were chosen to excite spins in the $g_\perp$ part of the spectrum, inter-spin distances may nevertheless be obtained from the traces using Tikhonov regularisation as implemented in DeerAnalysis [41]. Under these conditions, the Pake pattern will always contain a contribution from the perpendicular component of the dipolar coupling yielding a distance peak at the 'true' inter-copper distance [42]. Additional peaks in the distance distribution might appear at shorter distances as a consequence of orientation selection, but were not observed in the analysis of the data shown here, suggesting that the effects of orientation selection on the obtained distance distributions are negligible. The effect of orientation selection on the DEER time traces and the analysis of it was investigated in detail for the ***c*-P10$_{Cu2}$** sample without templates and is discussed in Appendix E.

The distance distributions shown in **Figure 3.17** were corrected to account for g-factor differences.[‡] For ***c*-P10$_{Cu2}$**, a distance distribution centred at 4.28 nm is obtained. Available crystal structures [53] and DFT calculations performed for a zinc porphyrin dimer, point towards a Zn$\cdots$Zn distance of 1.35 nm, resulting in a diameter of 4.3 nm for a perfectly circular 10-membered porphyrin ring. The experimentally obtained distance is thus in excellent agreement with this value, confirming that the ring without template is fairly shape persistent in solution. Compared to the template-bound structures, however, the width of the distance peak obtained for ***c*-P10$_{Cu2}$** is larger, which indicates a larger flexibility of the free porphyrin ring.

The distance distributions for the template-bound structures both show a major peak centred at a distance of 2.50 nm with a width of $\sigma_r = 0.08$ nm. This distance clearly corresponds to the shortest of the three possible ones in **Figure 3.4** where the two copper porphyrin units are located in the centre of the structure. By X-ray crystallography of a template-bound six-membered zinc porphyrin nanoring [73], a distance of 1.22 nm was measured between two opposite zinc centres. Imagining the template-bound ten-membered porphyrin structures as being approximately composed of two of such six-membered rings, a Cu$\cdots$Cu distance of approximately 2.5 nm would be expected, which agrees well with the results from DEER spectroscopy.

For ***c*-P10$_{Cu2}$ · (T4)$_2$**, the distance of 2.50 nm is clearly the major contribution with a relative importance of $>$98 %, whereas further contributions at longer distances are present in the case of ***c*-P10$_{Cu2}$ · (T5)$_2$**. The contribution of the shortest distance is reduced to about 80 % in ***c*-P10$_{Cu2}$ · (T5)$_2$** and additional peaks in the region from 3.8 to 5 nm are observed. Apart from the peak at 2.5 nm, no other distances shorter that 4.3 nm are expected for a 'planar' structure. It might therefore be speculated that any contributions to the distance distribution in the range from 3.8 nm to 4.3 nm could arise from bending of the structure as proposed in [85], which would shorten the longer distances while not affecting the shortest one significantly. Twisting of the structure by large angles, however, appears unlikely, given that the shortest distance of 2.50 nm is in very good agreement with the expected value for a 'planar' structure and would be expected to be markedly shorter for a twisted conformation.

However, the minor contributions to the distance distribution of ***c*-P10$_{Cu2}$ · (T5)$_2$** should not be over-interpreted, since the errors on these relatively long distances are expected to be large due

[‡] DeerAnalysis uses the free electron g-factor of 2.0023, whereas the copper DEER traces were acquired at $g_\perp = 2.050$.

to (i) their small relative contribution to the time evolution, (ii) the limited length of the DEER trace and (iii) uncertainties in the applied background correction. We shall therefore not attempt to analyse the differences between the DEER traces of *c*-**P10$_{Cu2}$ · (T4)$_2$** and *c*-**P10$_{Cu2}$ · (T5)$_2$** in any more detail beyond noting that, essentially, only the shortest distance of 2.50 nm is observed for *c*-**P10$_{Cu2}$ · (T4)$_2$**, while also longer distances are contributing to the dipolar evolution of *c*-**P10$_{Cu2}$ · (T5)$_2$**.

Since only the shortest of the three conceivable Cu···Cu distances is obtained for the complex with **T4** and no coupling of the copper centres to the axial nitrogen ligands of the template is observed experimentally, it may be concluded that the preferred conformation of the template-bound complexes is governed by the difference in binding affinity for axial nitrogen ligands between zinc and copper. Given that axial nitrogen ligands preferentially bind to zinc centres, the particular geometry of the employed **T4** template selectively directs the two copper centres towards the centre of the structure, resulting in the shortest possible separation distance of 2.5 nm.

This result suggests that it should be possible to influence the preferred conformation of the template-bound structures by modification of the template geometry. To verify this hypothesis, we performed a further DEER experiment on a sample with a different, X-shaped, molecular template with four binding sites, referred to as **T4$_x$** and compared the results with those obtained for *c*-**P10$_{Cu2}$ · (T4)$_2$**. The hypothesised chemical structures of the two complexes are shown for comparison in **Figure 3.18**. If the preferred conformation of the *c*-**P10$_{Cu2}$** structures is indeed guided by differences in binding affinities, the two copper centres should be separated by the longest of the three distances of 5.0 nm in *c*-**P10$_{Cu2}$ · (T4$_x$)$_2$**.

c-**P10$_{Cu2}$ · (T4)$_2$** *c*-**P10$_{Cu2}$ · (T4$_x$)$_2$**

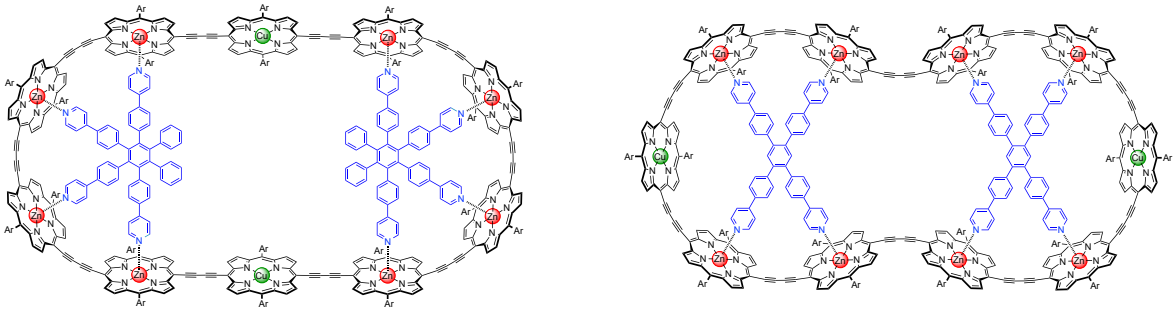


Figure 3.18: Chemical structures of the two complexes *c*-**P10$_{Cu2}$ · (T4)$_2$** (*left*) and *c*-**P10$_{Cu2}$ · (T4$_x$)$_2$** (*right*) containing two molecular templates with four binding sites each but different overall geometry.

Figure 3.19 shows a comparison of the DEER time traces and distance distributions obtained from Tikhonov regularisation for the two complexes *c*-**P10$_{Cu2}$ · (T4)$_2$** and *c*-**P10$_{Cu2}$ · (T4$_x$)$_2$**. Only one contribution corresponding to a distance distribution centred at 5.0 nm is obtained for *c*-**P10$_{Cu2}$ · (T4$_x$)$_2$**, in very good agreement with the predictions. The observation confirms that the preferred location of the copper porphyrin units is indeed governed by the differences in binding strength between zinc and copper to axial nitrogen ligands and opens up the possibility to control specific distances and thus geometries in supramolecular complexes at a molecular level.

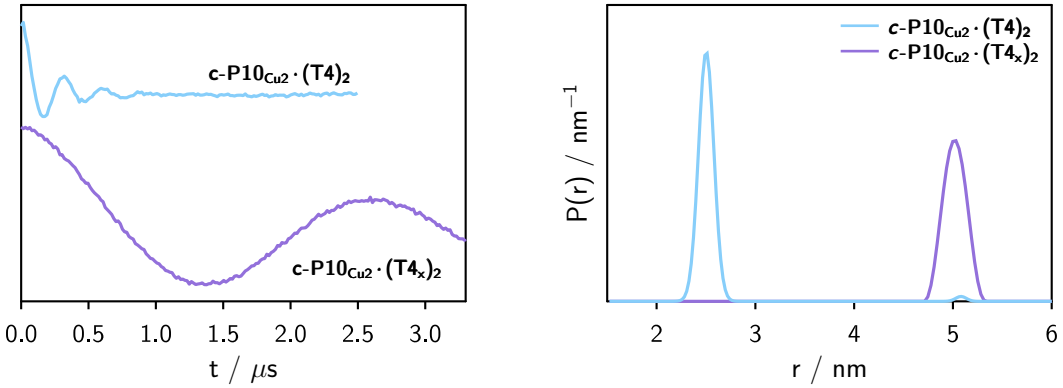


Figure 3.19: Comparison of the experimental DEER traces of ***c*-P10$_{Cu2}$ · (T4)$_2$** and ***c*-P10$_{Cu2}$ · (T4$_x$)$_2$** recorded at Q-band frequencies and 15 K in frozen toluene-d_8 (*left*) and corresponding distance distributions obtained from DeerAnalysis (*right*).

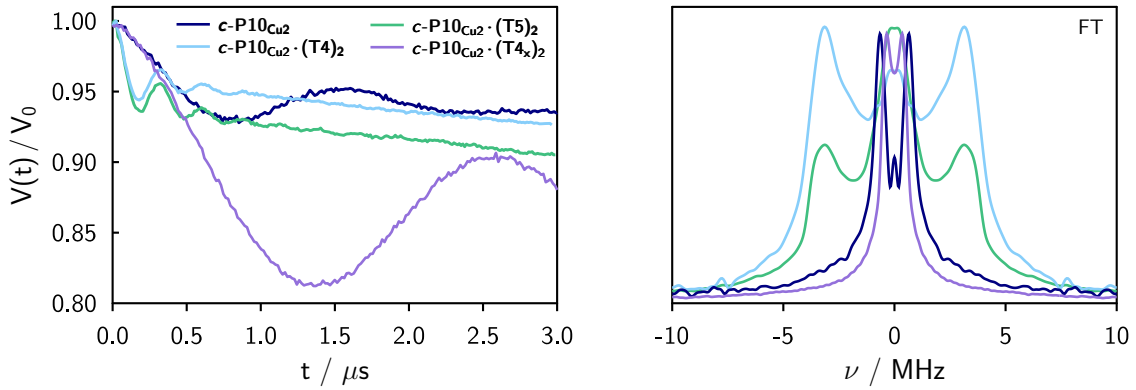


Figure 3.20: Experimental DEER data prior to background correction by an exponential background function with dimensionality $d = 3$ (*left*) and comparison of the Fourier transform of the background-corrected DEER time-traces (*right*) for all four investigated samples.

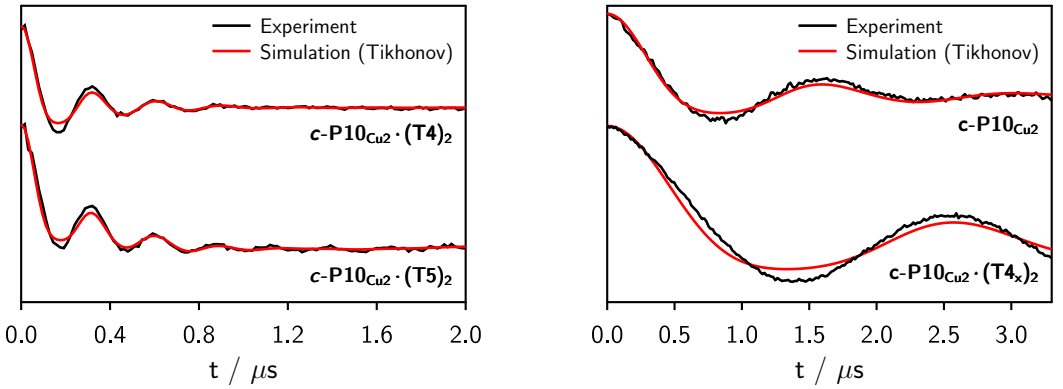


Figure 3.21: Experimental DEER traces for ***c*-P10$_{Cu2}$ · (T4)$_2$** and ***c*-P10$_{Cu2}$ · (T5)$_2$** (*left*) and ***c*-P10$_{Cu2}$** and ***c*-P10$_{Cu2}$ · (T4$_x$)$_2$** (*right*) together with the corresponding fit obtained as a result from the model-free analysis employing Tikhonov regularisation as implemented in DeerAnalysis.

For reference, the experimental DEER data prior to background correction, the Fourier transform of all background-corrected DEER traces and the simulations corresponding to the distance distributions obtained from DeerAnalysis are shown in **Figures 3.20** and **3.21**.

3.3 Conclusions

In this study, a variety of cw and pulse EPR techniques were used in combination with DFT calculations to investigate weak metal-ligand interactions and the preferred molecular conformations in template-bound complexes of a ten-membered bis-copper porphyrin nanoring. EPR is very sensitive to small changes in the local environment of the paramagnetic centres, allowing even weak metal-ligand interactions to be characterised, which cannot easily be detected by other techniques.

Davies ^{14}N ENDOR experiments combined with DFT calculations showed that copper centres do interact with axial nitrogen ligands of molecular templates. Upon binding of the ligand to copper, the hyperfine coupling constants of the in-plane nitrogen atoms are reduced by about 3 MHz. DFT calculations revealed that the coupling of the copper electron spin to the ^{14}N nucleus of a pyridine ligand is only of the order of 1 MHz and can therefore not be detected by Davies ENDOR. The coupling to pyridine could however be observed using HYSCORE at X-band frequencies.

Results from cw EPR showed that also the g-values and copper hyperfine coupling constants are altered upon ligand coordination. The observed relative increase in the g-values and decrease of $A_{||}$ of copper were also in agreement with predictions from DFT.

By measurement of the inter-copper distances, the populations of the three different conceivable conformers of the template-bound structures, ***c*-P10$_{Cu2}$ · (T4)$_2$** and ***c*-P10$_{Cu2}$ · (T5)$_2$**, were analysed. Additionally, information about the flexibility of the structures could be obtained from the width of the distance distributions. The shortest of the three Cu···Cu distances of 2.5 nm is found to dominate in both template-bound complexes. In ***c*-P10$_{Cu2}$ · (T5)$_2$**, additional contributions are observed at longer distances, whereas the distance peak at 2.5 nm is found to be virtually the only contribution to the distance distribution of ***c*-P10$_{Cu2}$ · (T4)$_2$**.

An analysis of the widths of the distance distributions suggests that all investigated structures are fairly rigid, but that the unbound nanoring is slightly more flexible than the template-bound structures. For ***c*-P10$_{Cu2}$**, an inter-copper separation distance of 4.3 nm was determined, in excellent agreement with expectations from molecular modelling for a perfectly circular 10-membered porphyrin ring.

The high preference for the conformation with the shortest possible inter-copper separation distance of 2.5 nm in ***c*-P10$_{Cu2}$ · (T4)$_2$** and ***c*-P10$_{Cu2}$ · (T5)$_2$** was shown to arise from the weaker binding affinity of axial pyridine ligands to copper centres as compared to zinc centres. Virtually no coupling of the copper electron spin to pyridine was observed for ***c*-P10$_{Cu2}$ · (T4)$_2$**, suggesting that the eight template legs of the two **T4** templates in the structure are all bound to zinc centres, therefore leaving the central positions, corresponding to the shortest separation distance, for the copper units.

In ***c*-P10$_{Cu2}$ · (T5)$_2$**, coupling of copper to the nitrogen of the pyridine ligand was observed directly by HYSCORE and indirectly by ENDOR. However, simulations of the cw and ENDOR

spectra suggest that only roughly 30−40 % of all copper units are bound to a template leg. The analysis of the DEER trace of *c*-**P10**$_{Cu2}$ · **(T5)**$_2$ further indicates that the contribution of the shortest distance amounts to >80 %. Although the uncertainty on these values is certainly high, it can be concluded that in most cases where the copper centres are located in the centre of the structure, the fifth pyridine template leg is not bound to a copper centre but rather extends towards the centre of the structure.

To demonstrate that the preferred geometry of the hetero-metallated nanorings is indeed governed by the difference in binding strength between copper and zinc, additional experiments were carried out on a complex between *c*-**P10**$_{Cu2}$ and an X-shaped isomer of **T4**. As predicted from the geometry of the template, only the largest Cu···Cu separation distance of 5.0 nm was observed in this case. **Figure 3.22** shows cartoons of the most likely geometries of all investigated samples and thus summarises the findings of this study.

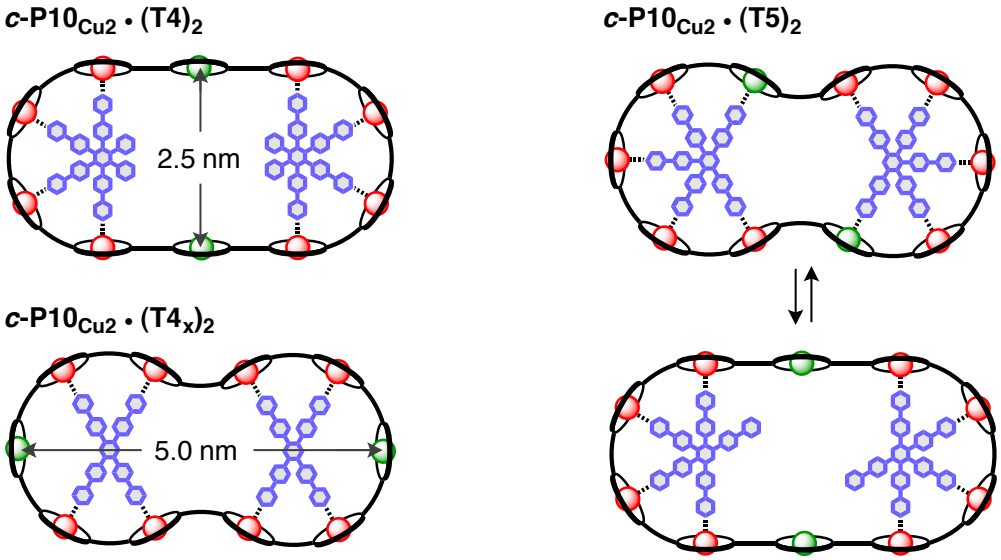


Figure 3.22: Cartoon illustrating the most likely geometries of the template-bound structures as judged by the results from hyperfine and dipolar spectroscopy. The Cu···Cu distance in the two most likely geometries for *c*-**P10**$_{Cu2}$ · **(T5)**$_2$ amounts to ∼2.5 nm in both structures.

The demonstration that the preferred conformation of the complexes can be switched by only changing the stereochemistry of the template is particularly remarkable, because it illustrates an indirect control of the separation between two active sites in a supramolecular assembly. Even if the template does not directly bind to the copper porphyrin units, it can change their positions within the complex by moving the zinc sites.

Chapter 4

Constructive Quantum Interference in *c*-P6$_{Cu2}$

In the present study, dipolar and exchange interactions are investigated in a six-membered bis-copper porphyrin nanoring (***c*-P6$_{Cu2}$ · T6**) bound to a rigid molecular template with six binding sites, referred to as **T6**. The structure of the molecule is shown in **Figure 4.1** (*left*). In Chapter 2 it was shown that the exchange interaction between two copper centres separated by a zinc porphyrin unit in linear conjugated porphyrin oligomers (**P3$_{Cu2}$**) is negligible at a distance of ∼2.7 nm. However the much higher rigidity and the bent geometry can significantly alter the orbital overlap in the cyclic template-bound system, ***c*-P6$_{Cu2}$ · T6**, which results in a measurable exchange interaction as will be demonstrated below.

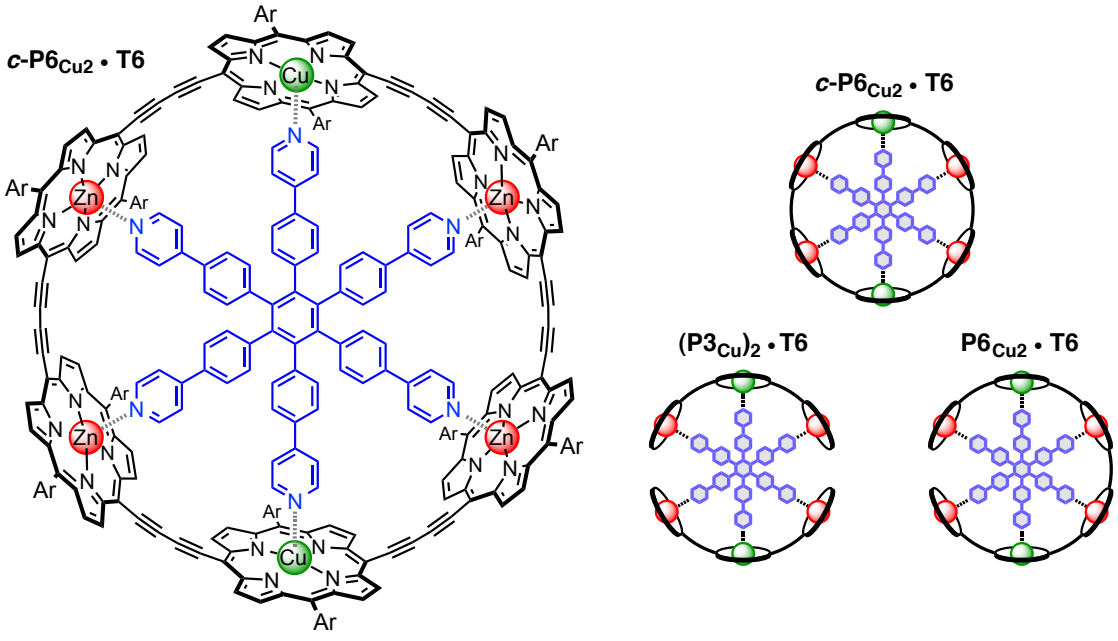


Figure 4.1: Chemical structure of ***c*-P6$_{Cu2}$ · T6** with **tBu** side groups (*left*) and cartoon showing the structures of all three investigated samples (*right*).

In addition, since the copper centres in the cyclic system are connected *via* two pathways, quantum interference effects on electronic coupling might be observable [86]. Several examples in the literature have shown Kirchhoff's circuit law, implying that the conductance through N parallel wires equals N times the conductance of a single wire, not being applicable on a molecular scale due to quantum interference effects [87–94]. It was proposed that the electron conductance in

an idealised system comprising two identical coupling paths connected in parallel should be four times that of the corresponding singly connected structure [88, 90]. But accurate predictions of the effects of quantum interference are difficult and the measured conductance crucially depends on the dimensions of the nano-object, notably the distance between the individual coupling paths [94]. In principle, electronic quantum interference on a molecular scale can either be constructive or destructive and is due to the breakdown of the assumptions made in the derivation of Kirchhoff's laws, i.e. that the individual resistances are not affected by the presence of others and that the connecting wires are resistance free [92].

Experimental evidence for such quantum interference effects remains scarce up to date since the corresponding measurements are complex and suitable model compounds are required to develop a more detailed understanding of the underlying phenomena. One of the key experiments so far was performed on single-molecule circuits containing one and two conducting backbones connected in parallel using the STM based break-junction technique [91]. In this study, an enhancement of the conductance by a factor of three was found for the structure comprising two coupling paths instead of one. However, a disadvantage of employing an open circuit arrangement as used in STM is that the effect of the connection of the molecules to the electrodes needs to be considered and accounted for in the analysis.

In the present study we present a 'non-invasive' way of measuring electronic communication in ***c*-P6$_{Cu2}$ · T6** – a model system comprising two identical coupling paths connected in parallel. Electronic communication in this molecular ring system is probed *via* the evaluation of the magnitude of the through-bond exchange coupling constant J.

To be able to evaluate the effects of quantum interference in ***c*-P6$_{Cu2}$ · T6**, two additional compounds are investigated in this study, in which one or both of the connections between the copper centres are broken. The compounds are referred to as **P6$_{Cu2}$ · T6** and **(P3$_{Cu}$)$_2$ · T6**, respectively, and their structures are illustrated in **Figure 4.1** (*right*). In contrast to the six-membered ring with **tBu** side groups, the linear compounds **P6$_{Cu2}$** and **P3$_{Cu}$** were synthesised with **THS** side groups. **P6$_{Cu2}$** and **P3$_{Cu}$** have terminal ethyne groups. The synthesis of all three compounds, the preparation of the EPR samples, as well as the UV-vis titrations presented below have been carried out by Jonathan Cremers (Anderson group, University of Oxford, UK).

4.1 UV-vis and EPR Characterisation

The formation of the molecular complexes **P6$_{Cu2}$ · T6** and **(P3$_{Cu}$)$_2$ · T6** in toluene was analysed by UV-vis titrations. In Chapter 3 it was shown that the interaction between axial nitrogen ligands and copper is much weaker than the corresponding interaction with zinc, so incomplete complex formation might be expected, especially in the case of **(P3$_{Cu}$)$_2$ · T6**. In addition, the formation of **(P3$_{Cu}$)$_2$ · T6**, and to a lesser extent also that of **P6$_{Cu2}$ · T6**, might be sterically hindered due to the terminal ethyne groups on **P3$_{Cu}$** and **P6$_{Cu2}$**. The data of a room temperature UV-vis titration of toluene solutions of **P6$_{Cu2}$** ($7.8 \cdot 10^{-7}$ M) and **P3$_{Cu}$** ($1.7 \cdot 10^{-6}$ M) with **T6** are shown in **Figure 4.2** and **Figure 4.3**, respectively. If complex formation were complete, sharp end points of the titration should be observed after addition of 1 (**P6$_{Cu2}$**) and 0.5 (**P3$_{Cu}$**) equivalents of **T6**.

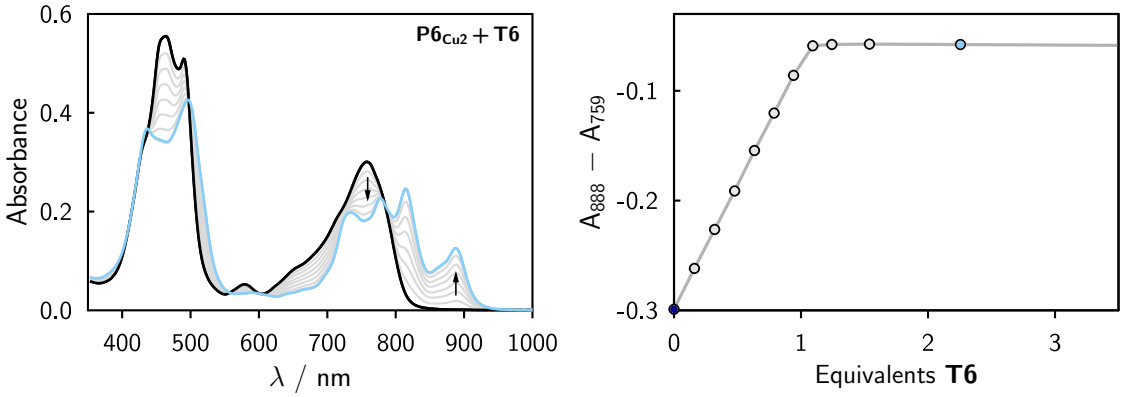


Figure 4.2: UV-vis titration of **P6$_{Cu2}$** with **T6** in toluene at 298 K (*left*) and corresponding change in absorbance at specific wavelengths as a function of the equivalents of **T6** added (*right*).

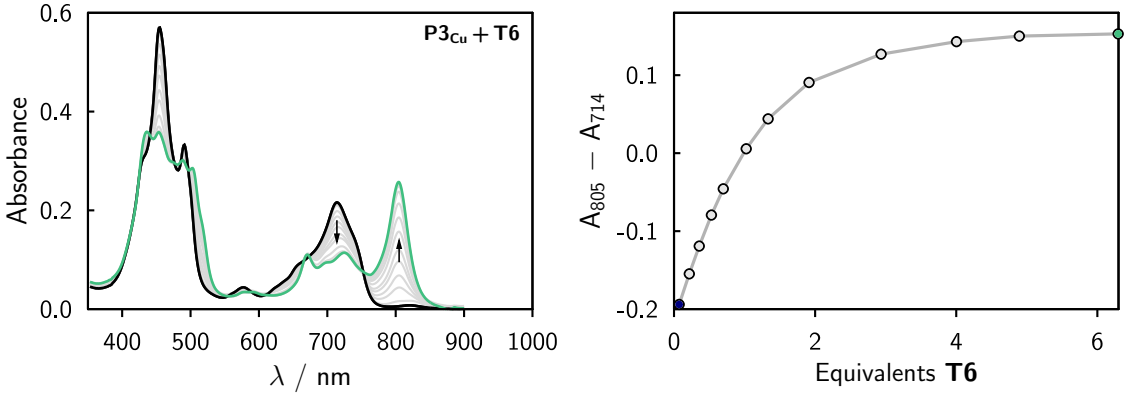


Figure 4.3: UV-vis titration of **P3$_{Cu}$** with **T6** in toluene at 298 K (*left*) and corresponding change in absorbance at specific wavelengths as a function of the equivalents of **T6** added (*right*).

In the case of **P6$_{Cu2}$** the formation of the expected 1:1 complex is indeed observed. After addition of about 1 equivalent of **T6**, no further changes are observed in the UV-vis absorption spectra. Upon complex formation, the intensity of the central peak of the porphyrin Soret band at $\sim$ 460 nm is considerably reduced and the porphyrin Q-bands shift towards the red and become more structured.

Also in the case of **P3$_{Cu}$** a red-shift of the Q-bands and a reduction of the central peak of the Soret band are observed upon complex formation. However, an end point of the titration could only be observed after addition of about 6 equivalents of **T6**, instead of the expected value of 0.5. Steric hindrance in combination with the lower binding affinity of copper to axial nitrogen ligands seem to prevent complete 2:1 complex formation. The end point of the UV-vis titration presumably corresponds to a situation where, in the majority of all cases, only one **P3$_{Cu}$** is bound per **T6**. Yet, at every point of the titration, a contribution of all four possible species, i.e. **(P3$_{Cu}$)$_2$ · T6**, **P3$_{Cu}$ · T6**, as well as free **P3$_{Cu}$** and **T6**, has to be expected. If **T6** is added in excess, the formation of **P3$_{Cu}$ · T6** should be preferred over **(P3$_{Cu}$)$_2$ · T6**, whereas the opposite should be the case if the concentration of **P3$_{Cu}$** is more than twice as high as that of **T6**. For the preparation of the EPR sample of **(P3$_{Cu}$)$_2$ · T6**, the stoichiometric ratio of 2:1 was chosen.

In this study, DEER spectroscopy will be used for the determination of D and J in the three investigated samples. All EPR samples were prepared at a porphyrin concentration of roughly 0.2 mM in deuterated toluene. Further details on the sample preparation and settings applied in the EPR experiments are given in Appendix A (**Section A.1** and **Subsection A.3.1**).

The normalised UV-vis spectra of the EPR samples recorded at room temperature in toluene are shown in **Figure 4.4**. Comparing the spectra to those in **Figures 4.2** and **4.3**, it is apparent that 2:1 complex formation is not complete in the case of **(P3$_{Cu}$)$_2$ · T6** under these conditions. However, using pulse dipolar spectroscopy, we are able to isolate the contributions of species exhibiting intramolecular spin-spin couplings from background contributions of molecules with only one spin centre, so that the presence of **P3$_{Cu}$ · T6** or free **P3$_{Cu}$** in the sample is unproblematic.

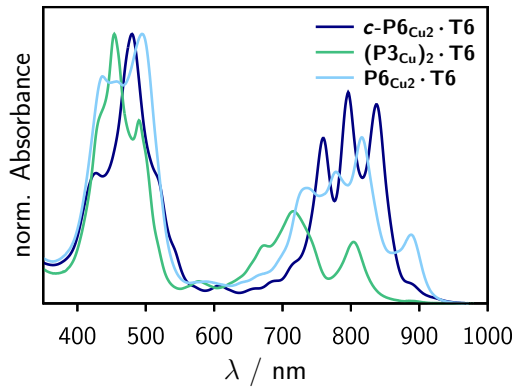


Figure 4.4: Normalised room temperature UV-vis spectra of the EPR samples in toluene at 298 K.

Figure 4.5 shows the echo-detected field-swept EPR spectra for all three investigated samples recorded in toluene-d_8 at 15 K together with measurements of the phase memory time T_m acquired at field positions corresponding to the maximum of the field-swept EPR spectrum ($g_\perp$). It is interesting to note that, compared to the template-bound oligomers, relaxation is considerably slowed down in ***c*-P6$_{Cu2}$ · T6**. This observation may be related to the higher rigidity of the ***c*-P6$_{Cu2}$ · T6** ring structure.

In Chapter 3 it was shown that ^{14}N Davies ENDOR measurements can be used to identify whether or not the copper centres in the sample are bound to axial nitrogen ligands. Binding of an axial ligand to copper leads to a decrease in the probed hyperfine coupling constants of the in-plane nitrogens of the porphyrin units and therefore a shift of the ENDOR spectrum to lower frequencies. ENDOR measurements on the studied samples demonstrate that, in frozen solution, i.e. under the same conditions as the DEER measurements will be performed, complex formation is not complete in either **(P3$_{Cu}$)$_2$ · T6** or **P6$_{Cu2}$ · T6**. The data are shown in **Figure 4.6** for the $g_\perp$ and $g_{||}$ orientations and are compared to the corresponding spectra acquired for ***c*-P6$_{Cu2}$ · T6** and **P6$_{Cu2}$** in toluene-d_8. The latter are shown in the background in grey. In ***c*-P6$_{Cu2}$ · T6** all copper centres are bound to an axial ligand, whereas in **P6$_{Cu2}$** no ligand coordination can occur. In the spectra of **(P3$_{Cu}$)$_2$ · T6** and **P6$_{Cu2}$ · T6**, contributions of both, bound and unbound copper centres, seem to be present, judged by the position of the ENDOR spectra with respect to those of ***c*-P6$_{Cu2}$ · T6** and **P6$_{Cu2}$**.

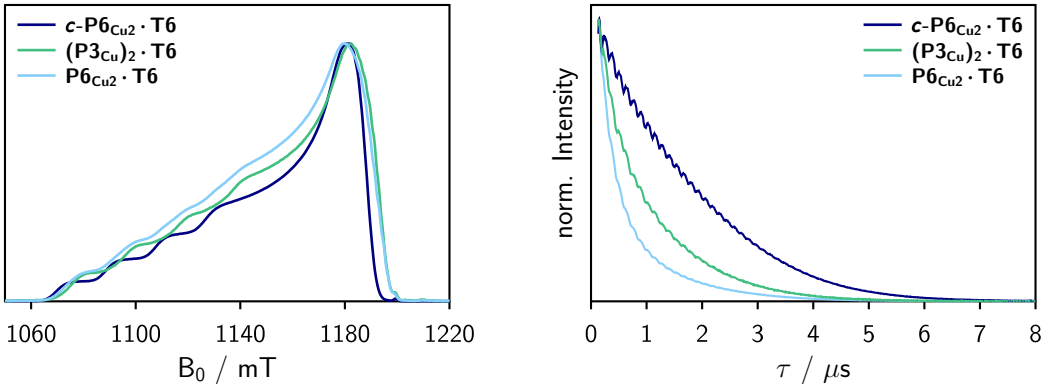


Figure 4.5: Field-swept echo-detected EPR spectra (τ = 400 ns) (*left*) and 2-pulse echo decay curves (T_m) recorded at a field position corresponding to the maximum of the respective field-swept EPR spectra (*right*). The data were acquired at Q-band in frozen toluene-d_8 at 15 K.

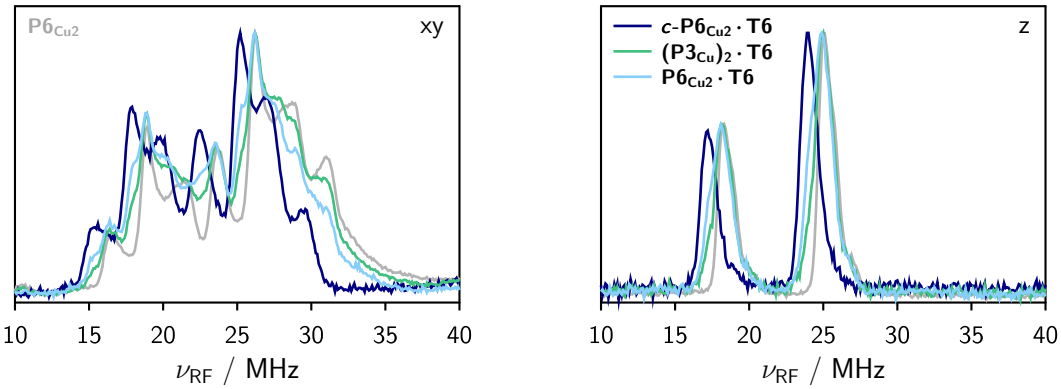


Figure 4.6: Davies ^{14}N ENDOR spectra of the three samples recorded at Q-band (15 K) at field positions corresponding to the *xy* (*left*) and *z* (*right*) orientations of the electronic **g**-tensor. For comparison, the spectrum of the linear hexamer without template, **P6$_{Cu2}$**, is shown in the background in grey.

4.2 Through-bond Exchange Coupling Detected by DEER

DEER measurements were first performed on ***c*-P6$_{Cu2}$ · T6**. In all experiments, the pump pulse was placed on the intensity maximum of the field-swept EPR spectrum (cf. **Figure 4.5**) and a detection pulse frequency offset of +100 MHz was applied. Unless otherwise stated, the measurements were performed at 15 K at Q-band frequencies. All further experimental details are given in Appendix A (**Subsection A.3.1**).

In the experimental Q-band DEER trace of ***c*-P6$_{Cu2}$ · T6** a high frequency modulation was observed corresponding to a frequency of ∼13 MHz. This frequency being too high as to be solely caused by the dipolar interaction between the two copper centres separated by a distance of roughly 2.4 nm (∼3.9 MHz at g = 2.05), it was speculated that it could result from exchange coupling. Additional measurements as outlined in the following were performed to rule out any alternative causes.

If the modulation was due to intermolecular interactions, the frequency should be affected by the sample concentration. To this end, a sample of ***c*-P6$_{Cu2}$ · T6** was prepared at only half of the original concentration in toluene-d_8. The data acquired at concentrations of 0.1 mM and 0.2 mM are compared in **Figure 4.7** (*left*). Since no difference in the modulation frequency is observed, coupling between spin centres on different ***c*-P6$_{Cu2}$ · T6** molecules can be ruled out as a cause for the observed modulation.

If the modulation was due to nuclear ESEEM effects, the modulation frequency would change when the measurements are performed at a different spectrometer frequency. **Figure 4.7** (*right*) shows a comparison of the traces recorded at X- and Q-band frequencies. Again, no differences in the modulation frequency of the DEER trace were observable, demonstrating that the modulation indeed results from intramolecular coupling between the two copper centres.

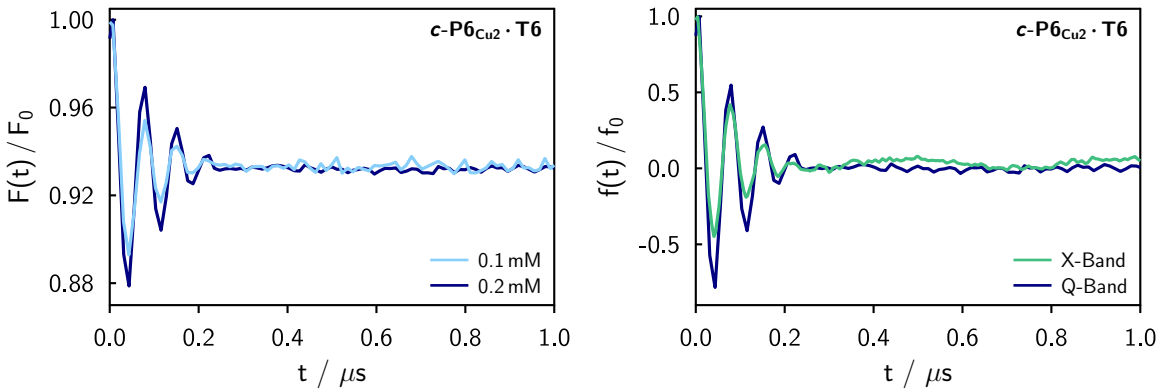


Figure 4.7: Comparison of the background-corrected DEER traces for ***c*-P6$_{Cu2}$ · T6** recorded at Q-band at two different concentrations of 0.1 and 0.2 mM (*left*) and comparison of the traces measured at X- and Q-band frequencies using a detection pulse frequency offset of +100 MHz (*right*).

It follows that the observed high-frequency modulation is likely to be a combination of D and J. Since the exchange interaction is mediated through bonds, it should be possible to isolate the influence of D by breaking the conjugation on both sides. The sample with two broken conjugations, **(P3$_{Cu}$)$_2$ · T6**, thus serves as a reference compound to characterise the dipolar interaction, which should be the same in all investigated complexes, whereas the sample with one broken conjugation, **P6$_{Cu2}$ · T6**, is expected to yield valuable information on the contribution of quantum interference effects.

Figure 4.8 shows a comparison of the experimental DEER traces of all three samples. Indeed, a much lower modulation frequency of about 3.5 MHz is observed for **(P3$_{Cu}$)$_2$ · T6**, in agreement with the expected distance of about 2.4 nm (at $g = 2.050$). As can also be seen from a comparison of the Fourier transforms of the three time traces shown in **Figure 4.9**, the main frequency component dominating the time trace of **P6$_{Cu2}$ · T6**, is larger compared to **(P3$_{Cu}$)$_2$ · T6**, but considerably smaller compared to ***c*-P6$_{Cu2}$ · T6**. The maxima of the dominant frequency peaks correspond to 3.5 MHz, 5.2 MHz and 13.1 MHz, for **(P3$_{Cu}$)$_2$ · T6**, **P6$_{Cu2}$ · T6**, and ***c*-P6$_{Cu2}$ · T6**, respectively.

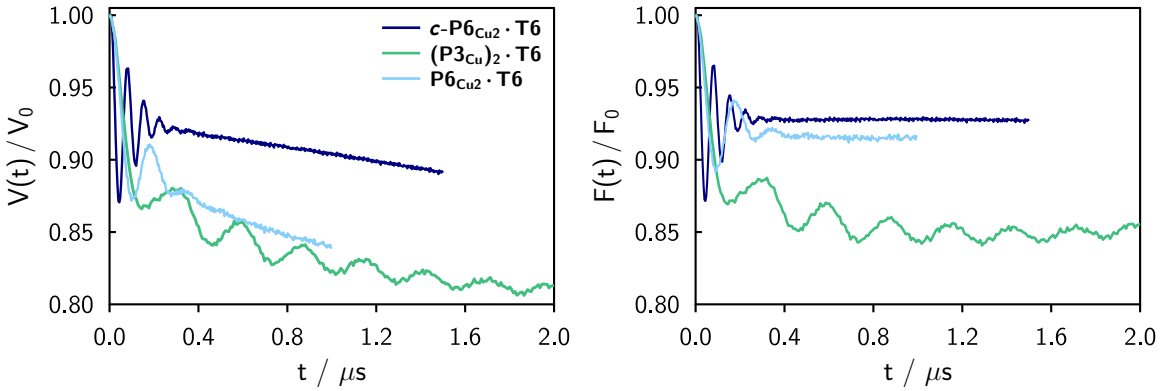


Figure 4.8: Comparison of the phase-corrected (*left*), and phase- and background-corrected (*right*) DEER traces of all three investigated samples measured in toluene-d_8 at Q-band (15 K).

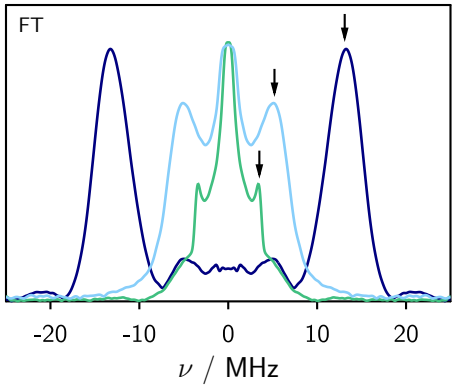


Figure 4.9: Fourier transforms of the background-corrected DEER traces of the three samples. The colour-code is the same as in previous figures.

4.3 Separation of the Effects of *D* and *J* on the DEER Data

By X-ray crystallography of a template-bound six-membered zinc porphyrin nanoring, a diameter of 2.44 nm has been determined between two opposite metal centres [73]. This distance might be slightly altered in the presence of two copper centres in the structure since it has for example been shown in Chapter 3 by DFT calculations that the equilibrium metal$\cdots$N distance between the nitrogen of an axial nitrogen ligand and copper is larger as compared to zinc. The strategy for the simulations outlined below is therefore as follows: To determine the exact value for D in the investigated copper-containing complexes, the DEER trace of **(P3$_{Cu}$)$_2$ · T6** will be simulated considering the g-factor at $g_\perp$ of 2.050. The value determined for D will then be assumed to be the same for all three samples, since D solely depends on the distance between the copper centres which are separated by the same rigid template in all cases.

In the analysis of the DEER data of ***c*-P6$_{Cu2}$ · T6** and **P6$_{Cu2}$ · T6**, the influence of J needs to be accounted for. Furthermore, in order to be able to determine J with high precision, the analysis should also allow for a separation of the contributions of D and J. For conjugated nitroxide biradicals such a separation was successfully demonstrated for cases where both singularities of the

Pake pattern could be detected after Fourier transformation of the DEER time traces [82, 95–97]. However, generally, the separation of the two contributions is not straightforward, especially if D and J are of the same order of magnitude.

To determine J from the experimental DEER data, the following analytic expression was derived by Prof. Ilya Kuprov (University of Southampton, UK), which describes the dependence of the reduced form factor $f(t)$ of the dipolar evolution time trace on D and J in the limit where the difference between the resonance frequencies of the two spins in the absence of coupling is much larger than the pseudo-secular part of the coupling Hamiltonian (weak coupling approximation).

$$f(t) = \sqrt{\frac{\pi}{6\,D\,t}}\left[\cos\Big((D+J)\,t\Big)\,\mathrm{FrC}\left(\sqrt{\frac{6\,D\,t}{\pi}}\right) + \sin\Big((D+J)\,t\Big)\,\mathrm{FrS}\left(\sqrt{\frac{6\,D\,t}{\pi}}\right)\right] \tag{4.1}$$

FrS and FrC are the Fresnel sine and cosine integrals, respectively. The parameters D and J in this expression are given in units of rad/s. The complete derivation of the equation is given in Appendix C (**Section C.2**).

As can be seen from the analytic result, the DEER time trace in the presence of through-bond exchange coupling has a complicated dependence on D and J. To a first approximation, however, the experimental signal is expected to oscillate with a frequency roughly corresponding to $D + J$. The expression was derived for an exchange coupling Hamiltonian of $\mathcal{H}_J = J\,\mathbf{S_1}\,\mathbf{S_2}$. The results of the simulations using this analytic expression were cross-checked against numerical simulations, based on a spin Hamiltonian approach, implemented in the MATLAB package Spinach [68] and found to be consistent.

To quantify the magnitude of J, all experimental data were background-corrected and the reduced form factors of the DEER traces were then simulated using **Equation (4.1)** assuming Gaussian distributions in the frequency domain for D and J.*

4.3.1 Determination of D

The result of the simulation for the sample with two broken conjugations, $\mathbf{(P3_{Cu})_2 \cdot T6}$, is shown in **Figure 4.10**. Since no through-bond coupling is possible in this case, J was set to zero in the simulations and only a Gaussian distribution in D, characterised by the centre frequency, D_c, and the width of the distribution, σ_D, was assumed.

Although the relative modulation amplitudes cannot be reproduced exactly, partially due to uncertainties in the DEER background correction, the simulations can be considered satisfactory since the modulation frequencies and the dampening of the oscillations, which contain all the relevant information for our purposes, can be well reproduced and determined with high precision. It is found that the distribution in D is relatively narrow with a width of only $\sigma_D = 0.12\,\mathrm{MHz}$. The determined centre frequency of 3.6 MHz corresponds to a Cu$\cdots$Cu distance of 2.47 nm at $g =$

*Obviously, the above equation can only be used in the absence of strong orientation selective effects on the detected modulation frequencies. In the present case, both detection and pump pulses where placed on $g_\perp$ when acquiring the DEER data, which should minimise the observation of any such effects on the modulation frequencies [42] as also discussed before in Chapter 3.

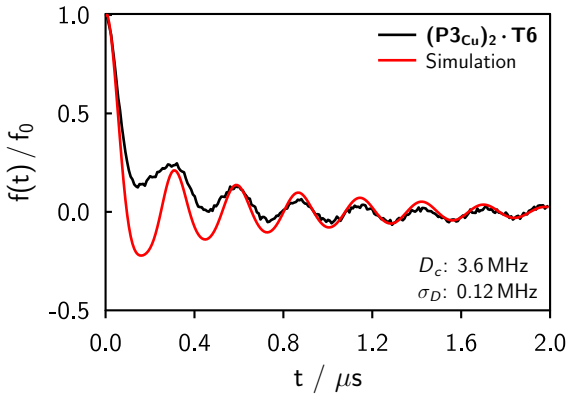


Figure 4.10: Simulation of the experimental DEER data for $\mathbf{(P3_{Cu})_2 \cdot T6}$ using the analytic expression given in the text and including a Gaussian distribution in D with parameters as indicated in the figure.

2.050 and is therefore in excellent agreement with expectations from available experimental data on a template-bound six-membered zinc porphyrin nanoring (2.44 nm) [73] and DFT calculations.

4.3.2 Justification of the DEER Background

As was already mentioned briefly when discussing the UV-vis and ENDOR data of the EPR samples, the complex formation in the $\mathbf{(P3_{Cu})_2 \cdot T6}$ and $\mathbf{P6_{Cu2} \cdot T6}$ samples is incomplete. In addition to the wanted 2:1 ($\mathbf{P3_{Cu}}$) and 1:1 ($\mathbf{P6_{Cu2}}$) complexes, we therefore expect the presence of different species arising from incomplete complex formation, which might contribute to the background of the experimental DEER traces. Such additional contributions to the signal are only expected for species/complexes with two copper centres at distances shorter than ~8 nm and could, at least partially, account for the observed (small) mismatch in the relative modulation amplitudes (i.e. intensities) between the experimental DEER data and the simulations shown above. Since the amplitudes are not considered in the interpretation of the data, these contributions do not affect our conclusions. However, it is desirable to understand the origin of the discrepancies.

Regarding the $\mathbf{(P3_{Cu})_2 \cdot T6}$ sample, we do not expect any DEER signal from unbound $\mathbf{P3_{Cu}}$, **T6** or the 1:1 complex $\mathbf{P3_{Cu} \cdot T6}$, but since it is known that zinc has a much higher affinity to bind to axial nitrogen ligands than copper, more complicated complexes involving two **T6** templates and at least two $\mathbf{P3_{Cu}}$ molecules could be imagined and could lead to the presence of various longer separation distances.

To demonstrate that a satisfactory simulation of the experimental data can be achieved by including a minor contribution accounting for different arrangements of **T6** and $\mathbf{P3_{Cu}}$, a second component with a broad contribution centred at a longer distance was included in the simulation of the DEER data of $\mathbf{(P3_{Cu})_2 \cdot T6}$. The centre and width of this second component were allowed to vary until the best possible fit was obtained. The result of this simulation is shown in **Figure 4.11** and the corresponding distributions in the distance and frequency domain are depicted in **Figure 4.12**.

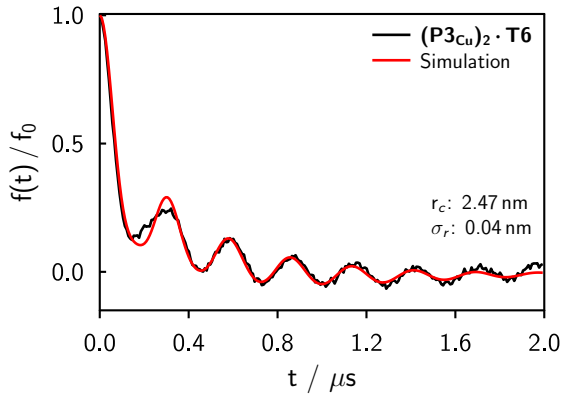


Figure 4.11: Simulation of the form factor of the background-corrected DEER trace of **(P3$_{Cu}$)$_2$ · T6** assuming a distance distribution consisting of two peaks with Gaussian distribution as shown in the figure below.

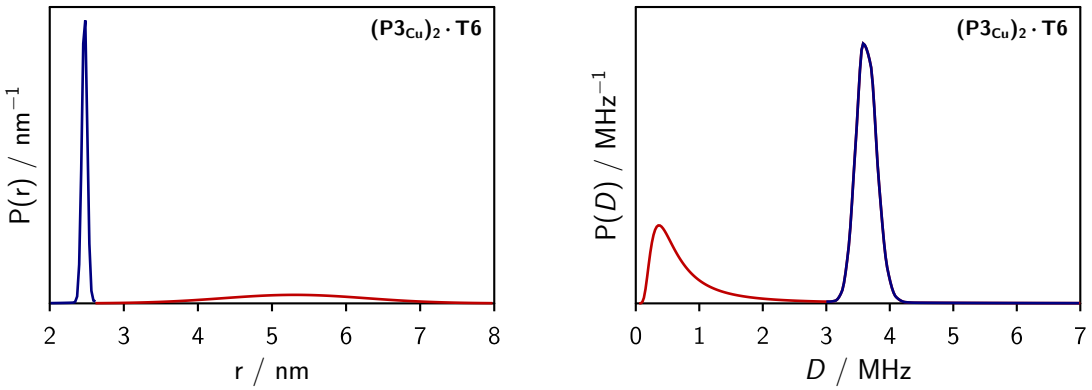


Figure 4.12: Distance distribution at $g = 2.050$ (*left*) and corresponding frequency distribution (*right*) resulting from a least-squares fit of the simulation to the experimental DEER data of **(P3$_{Cu}$)$_2$ · T6** when allowing the centre and width of a second Gaussian distance peak to vary.

It is found that the DEER trace of the **(P3$_{Cu}$)$_2$ · T6** sample can be well reproduced by including longer distances in the range between about 3.5 and 7 nm in addition to the dominating distance of about 2.5 nm with a main modulation frequency of 3.6 MHz. The presence of longer distances causes an 'uplift' of the dipolar evolution trace at early times which cannot be reproduced by the simulation with just one component shown in **Figure 4.10**. The remaining small differences between experiment and simulation in **Figure 4.11** might be a consequence of orientation selection.

Concerning **P6$_{Cu2}$ · T6**, complex formation seems more complete based on the UV-vis behaviour and ENDOR results. However, the ENDOR measurements revealed the presence of a minor contribution of unbound **P6$_{Cu2}$**, which is expected to contribute to the experimental DEER time trace. This contribution might cause minor amplitude differences between experiment and simulation for this sample. For reference, the DEER data (before background correction) recorded for **P6$_{Cu2}$** without template in toluene-d_8 is shown in **Figure 4.13** and compared to the data for **P6$_{Cu2}$ · T6**. Inspection of **Figure 4.13** further reveals that the rigidity of the structure is crucial for the obser-

vation of any *J*-coupling effects in DEER data. In the absence of the template imposing a rigid, circular geometry, no distinct modulations are discernible in the DEER trace of **P6$_{Cu2}$**.

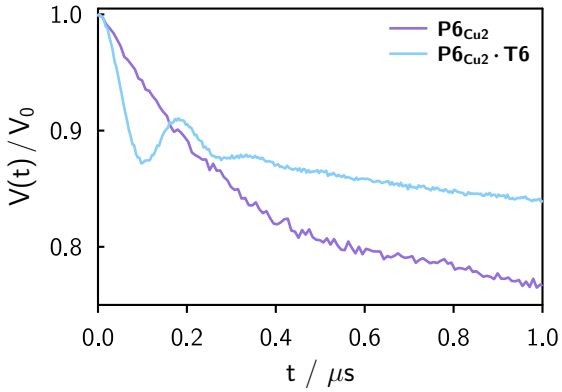


Figure 4.13: Comparison of the phase-corrected DEER traces of **P6$_{Cu2}$** and **P6$_{Cu2}$ · T6**.

4.3.3 Quantification of *J*

The distribution in *D*, determined by simulation of the data of **(P3$_{Cu}$)$_2$ · T6**, was used in the simulations of the DEER traces of ***c*-P6$_{Cu2}$ · T6** and **P6$_{Cu2}$ · T6** for the purpose of quantifying the through-bond coupling *J*. In the simulations including both *D* and *J*, consequently only the centre and width of the distribution in *J* were adapted. The results of the simulations for the two samples with one or two through-bond coupling paths are compared to the respective experimental data in **Figure 4.14**. The centres and widths of the frequency distributions in *J* and *D* used in the simulations are indicated in the figures. Compared to the distribution in *D*, the distributions in *J* were found to be much wider.

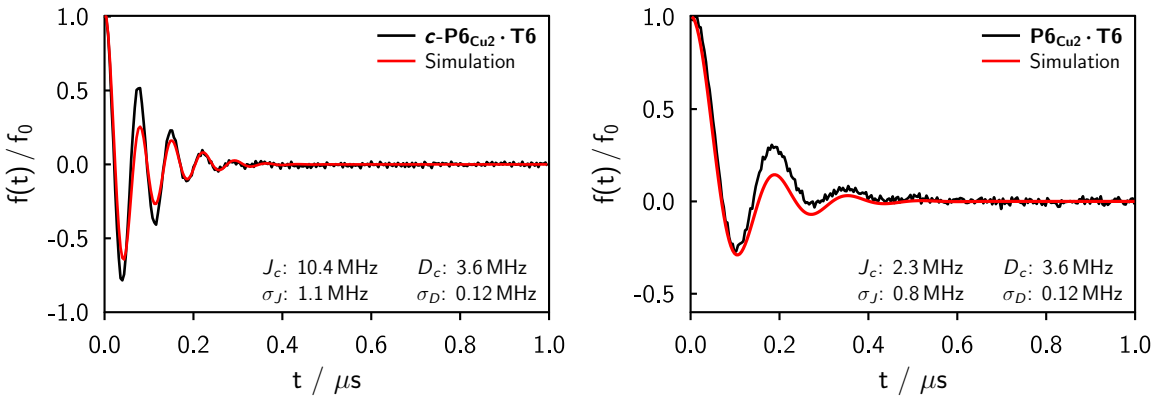


Figure 4.14: Simulation of the experimental DEER data for ***c*-P6$_{Cu2}$ · T6** (*left*) and **P6$_{Cu2}$ · T6** (*right*) using the analytic expression given in the text and including Gaussian distributions in *D* and *J* with parameters as indicated.

For ***c*-P6$_{Cu2}$ · T6**, a *J* value of +10.4 MHz ($\sigma_J = 1.1$ MHz) was determined from the simulation. Due to the definition of the exchange coupling Hamiltonian used in the derivation of **Equation (4.1)**, a positive *J* value indicates antiferromagnetic coupling ($E_S < E_T$). For the structure with one

broken conjugation, **P6$_{Cu2}$ · T6**, a J value of only $+2.3$ MHz is obtained. The enhancement of the average magnitude of the J-coupling by a factor of 4.5 in ***c*-P6$_{Cu2}$ · T6** compared to **P6$_{Cu2}$ · T6** clearly indicates constructive quantum interference in the cyclic structure with two identical, parallel coupling paths.

4.3.4 Verification of the Sign of J

According to the definition of the dipolar coupling Hamiltonian in dipolar spectroscopy, the D value (i.e. ω_{dd}) has to be positive in all cases. Since we are able to determine the relative signs of D and J from the simulations, the fact that D needs to be positive should enable us to determine the absolute sign of J. With reference to **Equation (4.1)**, the dominating modulation frequency detected in the experimental DEER trace, given by the cosine term, should correspond to the absolute value of a combination frequency of D and J. Thus, even if D is positive, two solutions for J (one positive, one negative) leading to the same absolute value could in principle be imagined. The dipolar coupling frequency in the studied systems has been determined to be $D = 3.6$ MHz. The best fit to the experimental data for ***c*-P6$_{Cu2}$ · T6** was obtained for a value of $J = +10.4$ MHz as shown above, leading to a value of roughly $+14$ MHz for $D + J$. The same absolute value could be obtained for a J value of -17.6 MHz. An analogous reasoning for **P6$_{Cu2}$ · T6** leads to an absolute value of $+5.9$ MHz which can be obtained for $J = +2.3$ MHz or $J = -9.5$ MHz. However, we find for both samples, that the simulations for the two cases are significantly different, so that the sign of J can indeed be determined from a simulation of the experimental data. The simulations carried out for the case of a negative J (ferromagnetic coupling) are shown for both samples in **Figure 4.15**. Variations of these values by up to several MHz do not noticeably improve the goodness of fit. It can clearly be stated that the agreement is much worse as compared to the data presented above (for positive J in **Figure 4.14**) demonstrating that the sign of J can be determined with confidence in the present case.

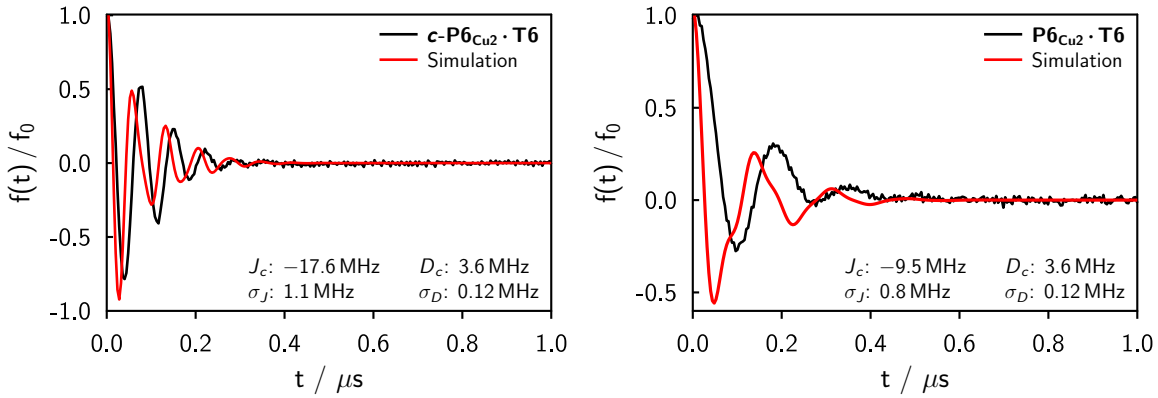


Figure 4.15: Simulation of the form factor of the background-corrected DEER data for ***c*-P6$_{Cu2}$ · T6** (*left*) and **P6$_{Cu2}$ · T6** (*right*) assuming an opposite sign of J as used for the simulations shown above. The fit is clearly worse (as compared to the preceding figure) and cannot be significantly improved when varying J without changing its sign, confirming the choice of a positive sign for J.

4.4 Conclusions

In the dipolar evolution time trace of a six-membered porphyrin nanoring containing two copper centres separated by two zinc centres on either side (***c*-P6$_{Cu2}$ · T6**), a high frequency modulation corresponding to a frequency of ∼13 MHz was observed experimentally, which could be attributed to through-bond exchange coupling (J) between the copper centres.

To determine the magnitude of the exchange coupling, we derived an analytical expression enabling us to separate the contributions of dipolar and exchange coupling to the time evolution in DEER. Gaussian distributions in D and J were assumed in the simulation of the experimental data. The simulations showed that the relatively strong exchange coupling in ***c*-P6$_{Cu2}$ · T6** partially suppresses the lower frequency modulation expected from dipolar coupling between the copper centres and allow us to quantify the magnitude of J with high precision. In addition, we were able to determine the absolute sign of the exchange interaction. Antiferromagnetic exchange is observed for both the ring structure and the sample with one broken conjugation.

The dipolar modulation corresponding to a through-space distance of 2.47 nm can be recovered if both connections between the copper centres are broken in **(P3$_{Cu}$)$_2$ · T6**. The validity of the simulations is supported by the excellent agreement of the determined Cu···Cu distance with expectations from available experimental data on a template-bound six-membered zinc porphyrin nanoring, where a distance of 2.44 nm was obtained. The fact that no J-coupling is observed in the system with two broken conjugations also demonstrates that the coupling in ***c*-P6$_{Cu2}$ · T6** occurs along the porphyrin chain and not through the **T6** template as could also be assumed. This result agrees with the results presented in Chapter 3 where it was shown that the hyperfine coupling of copper to an axial nitrogen ligand is very small.

The observed exchange coupling of about 10 MHz in ***c*-P6$_{Cu2}$ · T6** is remarkable, considering the large through-bond distance between the copper centres. No other system has so far been shown to still exhibit significant (i.e. measurable) exchange coupling at an inter-spin separation distance as large as 3.9 nm. The results suggest efficient long-range electronic communication to be favoured by the high degree of conjugation, the particular geometric arrangement of the individual units and the overall high rigidity of the structure. When the molecular template, stabilising the structure and imposing a bent geometry, is removed, no significant exchange coupling is discernible for the linear hexamer with two copper centres, **P6$_{Cu2}$**, as was shown in **Figure 4.13**.

If one of the two connections between the copper centres is broken, the average magnitude of the exchange coupling drops to only one fourth of the original value in ***c*-P6$_{Cu2}$ · T6**. This study therefore constitutes an experimental evidence for constructive quantum interference of electronic communication in a cyclic molecular system with two identical, parallel coupling paths.

Chapter 5

Introduction to Triplet State EPR

Since triplet states have (at least) two unpaired electrons, they are paramagnetic and can therefore be studied by EPR. In the literature, many examples can be found where transient EPR was successfully applied for the identification and characterisation of triplet state intermediates in photoinduced reactions of biological or technological relevance. These examples include the study of photosynthetic reaction centres [98–102], as well as structures designed for artificial photosynthesis [103–106] or wire-like charge transport [107–109]. This chapter will explain the basics of triplet state detection and characterisation by different transient EPR techniques with special focus on the measurement of triplet state delocalisation in porphyrin oligomers, serving as an introduction for Chapters 6 to 8.

The investigation of triplet state delocalisation becomes increasingly relevant for a number of applications, since knowledge of the factors governing triplet delocalisation could help to improve the performance of organic photovoltaics, OLEDs, or molecular spintronics devices [46, 50, 110, 111]. For an in-depth study of triplet delocalisation, porphyrin oligomers seem to be suitable model compounds since a large variety of such linear and cyclic π-conjugated systems are available and can rather easily be modified to accommodate different side- or end groups allowing for a systematic modification of the electronic properties [112–116]. In addition, conjugated porphyrin arrays have been found to exhibit favourable nonlinear optical and charge transport properties [51, 117–119], implying an efficient electronic communication between the individual porphyrin units, which makes these molecules promising candidates for applications as molecular wires [113, 115].

In the following chapters, the triplet states of linear zinc porphyrin oligomers with different side and end groups synthesised either in the group of Prof. H. L. Anderson (University of Oxford, UK) or Prof. M. J. Therien (Duke University, USA), will be investigated.

5.1 EPR of Porphyrin Triplets

The triplet states of the porphyrin oligomers are generated by pulsed laser excitation of the sample inside the EPR resonator to the first excited singlet state followed by intersystem crossing. The intensity of the observed triplet EPR signal is therefore mainly dependent on (i) the sample concentration (ii) the laser power used in the experiment (iii) the quantum yield of triplet formation and (iv) the lifetime of the triplet state and the spin relaxation rates. Experimentally, the triplet lifetime can be prolonged and spin relaxation considerably slowed down by performing the

measurements at low temperatures. The sample concentration as well as the laser power can be adapted to optimise signal intensities. The only parameter controlling the signal intensity which cannot (easily) be influenced is hence the quantum yield of triplet formation. Consequently, the triplet yield is often the limiting factor which determines the feasibility of a particular triplet state EPR experiment.*

5.1.1 Origin of the Triplet Spectrum

Compared to standard EPR of spin $S = \frac{1}{2}$ systems with Boltzmann distributed populations, there are some important differences in triplet state EPR which shall briefly be outlined here. The different energetic sublevels of the triplet are split in energy even if no magnetic field is applied. This so-called zero-field splitting (ZFS) is due to the dipolar interaction between the two unpaired electrons forming the triplet and is illustrated in **Figure 5.1**.

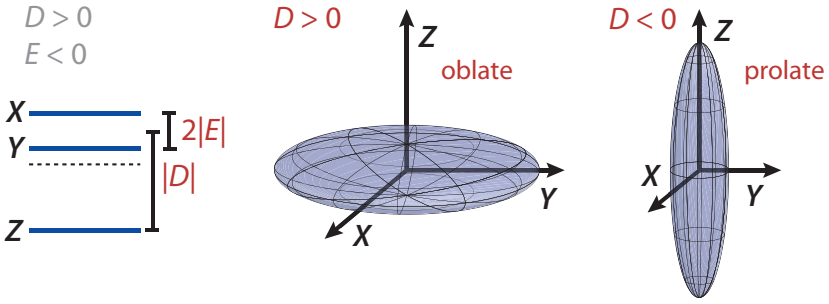


Figure 5.1: Illustration of the splitting of the triplet sublevels for $D > 0$, $E < 0$ at $B_0 = 0$ (*left*) and of the ZFS tensor orientations for an oblate ($D > 0$, *centre*) and a prolate ($D < 0$, *right*) spin distribution.

The zero-field energy levels are denoted as $|X\rangle$, $|Y\rangle$, and $|Z\rangle$, referring to the axes of the zero-field splitting interaction tensor $\boldsymbol{D}$. Since the tensor is traceless, the corresponding zero-field interaction can be parameterised by the two parameters D and E according to **Equation (1.18)**.

Significance of *D* and *E*

In general, D and E can yield valuable information about the electronic structure of the spin system. Assuming that the spin orbit and crystal field contributions to the zero-field interaction are negligible and the point-dipole approximation is valid, they can be expressed (in frequency units) as follows:

$$D = \frac{3}{4}\frac{\mu_0}{4\pi h}(g_e\beta_e)^2\left\langle\frac{r^2 - 3z^2}{r^5}\right\rangle = \frac{3}{4}\frac{\mu_0}{4\pi h}(g_e\beta_e)^2\left\langle\frac{1 - 3\cos^2\theta}{r^3}\right\rangle \tag{5.1}$$

$$E = \frac{3}{4}\frac{\mu_0}{4\pi h}(g_e\beta_e)^2\left\langle\frac{y^2 - x^2}{r^5}\right\rangle \tag{5.2}$$

where r is the distance between the unpaired electron spins, θ the angle between the spin-spin vector and the dipolar Z axis and all other parameters have their usual meanings. The angled

*In rare cases, very short triplet lifetimes or very fast spin relaxation times can also be a limiting factor for triplet state characterisation by EPR.

brackets indicate the expectation value. We can see that D can be related to the inter-spin distance, whereas the parameter E tells us about the axiality of the system. If the X and Y axes are equal, E is equal to zero, whereas a large value for E indicates a strong non-axiality of the electron spin distribution.

The signs of D and E determine the energetic ordering of the triplet sublevels. In addition, the sign of D reveals whether the spin distribution is oblate ($D > 0$) or prolate ($D < 0$): If θ is equal to $\frac{\pi}{2}$, Z is perpendicular to the molecular plane, and D is thus positive. This corresponds to an oblate ('disk-like') spin distribution, which is normally observed for planar aromatic molecules. In the other extreme case, when θ is equal to zero, and Z parallel to the molecular axis, D is negative. This indicates a prolate spin distribution ('rod-like', cf. **Figure 5.1**).

From triplet EPR experiments, only the relative signs of D and E can normally be obtained. The sign of D might be anticipated from the molecular structure, for instance using DFT, or can be determined experimentally in some cases by magneto-photoselection experiments [120, 121]. The sign of E then depends on the (arbitrary) assignment of X and Y to the molecular axes. In this and previous work, E is chosen to be negative for the porphyrin monomer, while D was shown to be positive [122].

Application of a Magnetic Field

When applying a magnetic field, the zero-field splitting parameters D and E, which contain valuable information about the electronic properties of the system, can be measured by EPR. The zero-field energies of the individual triplet sublevels, E_X, E_Y, and E_Z, are given by [1]:

$$E_X = \frac{1}{3}D - E \qquad E_Y = \frac{1}{3}D + E \qquad E_Z = -\frac{2}{3}D \tag{5.3}$$

It can thus be seen that the separation of the energy levels at zero field is solely determined by the dipolar splitting parameters D and E. In the presence of a magnetic field, the individual triplet sublevels are further split in energy due to the electronic Zeeman interaction. The high field energy levels corresponding to $m_S = +1$, 0, and -1 are typically denoted $|\mathrm{T}_+\rangle$, $|\mathrm{T}_0\rangle$, and $|\mathrm{T}_-\rangle$.

At high fields, the energies of the three triplet states are referred to as E_+, E_0, and E_- and depend on the orientation of the external magnetic field with respect to to the dipolar axes X, Y, and Z. If $B_0 \,||\, Z$, for example, the energies as a function of the magnetic field (in frequency units) can be expressed as follows:

$$\begin{aligned} E_+ &= \frac{1}{3}D + \sqrt{E^2 + \left(\frac{g\beta_e}{h}B_0\right)^2} \\ E_0 &= -\frac{2}{3}D \\ E_- &= \frac{1}{3}D - \sqrt{E^2 + \left(\frac{g\beta_e}{h}B_0\right)^2} \end{aligned} \tag{5.4}$$

Whenever the external field is parallel to one of the $\boldsymbol{D}$-tensor axes, we refer to this orientation as a so-called canonical orientation. The corresponding (zero-field) sublevel does not change its

energy as a function of field and becomes the $m_S = 0$ state at high fields, whereas the other two sublevels are split in energy and turn into the $m_S = -1$ or $m_S = +1$ states at high fields.

According to the selection rules in EPR, $\Delta m_S = \pm 1$, only transitions between the $|\mathrm{T}_0\rangle$ level and the $|\mathrm{T}_-\rangle$ or $|\mathrm{T}_+\rangle$ levels are allowed. Two EPR transitions should thus be observable for every canonical orientation as illustrated in **Figure 5.2** for the case of a porphyrin monomer, leading to a total of up to[†] six lines. Depending on whether the respective transition corresponds to a $|T_0\rangle \leftrightarrow |T_+\rangle$ or $|T_0\rangle \leftrightarrow |T_-\rangle$ transition, the EPR transition will be denoted, for instance, as $Z+$ or $Z-$ in the case of $B_0 \,||\, Z$.

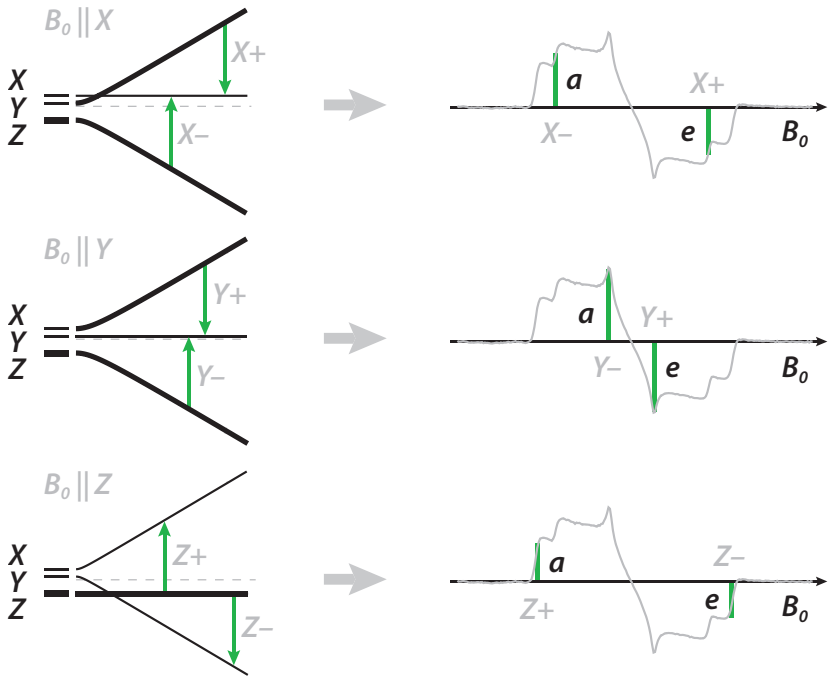


Figure 5.2: Energies of the triplet sublevels of a zinc porphyrin monomer as a function of the magnetic field at different orientations of the field relative to the dipolar axes X, Y, and Z. Whenever the energy of the microwave radiation matches the energy gap between $|\mathrm{T}_0\rangle$ and either $|\mathrm{T}_-\rangle$ or $|\mathrm{T}_+\rangle$, a transition can be observed which is either emissive or absorptive depending on the relative populations of the sublevels involved, indicated by the thickness of the level bars. In frozen solution, a total of six different transitions, at the canonical orientations $X\pm$, $Y\pm$, and $Z\pm$, can be observed for every molecule of the isotropically oriented ensemble, resulting in the depicted powder-like spectrum if the Z sublevel is primarily populated.

From **Figure 5.2** it can be seen that apart from the absorptive transitions typically observed, also emissive transitions contribute to triplet state EPR spectra. In fact, for every canonical orientation, one absorptive and one emissive transition with equal intensity are observed due to the non-Boltzmann populations of the triplet sublevels. This unusual population distribution arises since the triplet state is formed by intersystem crossing from the singlet state and the intersystem crossing rates to the different triplet sublevels are typically not identical and depend on the intersystem

[†]The number of distinct transitions observed in the experiment depends on the symmetry of the investigated system. If the system has axial symmetry, the number of transitions is reduced to four because the X and Y levels coincide ($E = 0$).

crossing mechanism. The presence of non-Boltzmann populations is referred to as spin polarisation and is a necessary condition for the observation of emissive transitions.

The populations of the high field states which determine whether a particular transition is emissive or absorptive can be calculated from the initial populations of the zero-field levels. In the framework of the high field approximation, for example, the sublevel populations for $B_0 \,||\, Z$ are given by

$$P_0 = P_Z \qquad\qquad P_{\pm 1} = \frac{1}{2}\left(P_X + P_Y\right) \tag{5.5}$$

and the intensity of the two transitions is then proportional to the population difference $P_0 - P_{\pm 1}$.

In many cases it can be very instructive to analyse the particular electronic spin polarisation (ESP) pattern observed for a certain species, since the sequence of absorptive (a) and emissive (e) transitions (*aaaeee* for a zinc porphyrin monomer) can in principle be related to the mechanism of triplet formation. In the literature, examples can be found where the observed triplet spin polarisation allowed the authors to confirm a proposed excited state reaction mechanism in complex systems where the contributing photophysical pathways were not known a priori. A radical pair intermediate could for example be identified in bacterial photosynthesis based on the spin polarisation of the triplet state of bacteriochlorophyll [100, 123]. Since the observed triplet spin polarisation *aeeaae* suggested an equal population of the high field states and could therefore not arise from intersystem crossing, it was concluded that the triplet is formed by radical pair recombination.

When looking back at the porphyrin monomer triplet spectrum shown in **Figure 5.2**, one notices furthermore that we observe a continuum of transitions rather than the six isolated ones which would be expected in the case of a single crystal sample. This is due to the fact that the spectrum has been acquired on an isotropic frozen solution sample. In frozen solution, a powder-averaged spectrum is obtained, i.e the measured spectrum is the sum of the individual spectra of an ensemble of molecules with isotropically distributed orientations. Consequently, instead of just detecting six lines, we observe a broad and continuous spectrum as shown in the figure. However, the locations of the canonical orientations can still be determined with high precision, since they manifest themselves as turning points in the experimental spectrum.

Since all other interactions, such as hyperfine interactions, which might contribute to the appearance of the experimental spectrum are typically small, relative to the value of D, they can often be neglected in any interpretation of the spectral shape. For porphyrin triplets, the dipolar interaction parameter D is typically of the order of 1000 MHz, resulting in comparatively broad spectra spanning about 70 mT. Triplet states can therefore in most cases easily be distinguished from other transient species like radical pairs since the latter exhibit much narrower spectral features.

5.1.2 Interpretation of the Triplet Spectrum

The triplet EPR spectra are recorded under continuous microwave irradiation by a technique referred to as transient cw EPR. In the experiment, the static magnetic field is varied stepwise and the transient signal is then recorded for every field point which allows one to build up the triplet spectrum as a function of field and time. The spectra are recorded in direct detection, so that

any positive signal corresponds to an absorptive transition, whereas a negative signal indicates an emissive transition.

From the shape of the triplet spectrum the zero-field splitting parameters D and E can be determined by numerical simulation. If the exact positions of the six canonical orientations corresponding to the six transitions are well resolved in the experimental spectrum, it may even be possible to directly read off the dipolar splitting parameters from the experimental spectrum by measuring the distance between the turning points in the spectrum, and considering the following equalities

$$\Delta B_Z = 2\,|D| \qquad \Delta B_X = |D| + 3\,|E| \qquad \Delta B_Y = |D| - 3\,|E| \tag{5.6}$$

where, by convention, the principal axes of the $\boldsymbol{D}$-tensor were chosen such that $|D| > |3E|$ and $|D_Z| > |D_X| \geq |D_Y|$ [124]. The relationship between the absolute magnitude of D and E and the distances of the turning points in the experimental spectrum is also illustrated in **Figure 5.3** for a zinc porphyrin monomer (**P1**) with **tBu** side groups recorded in frozen toluene.

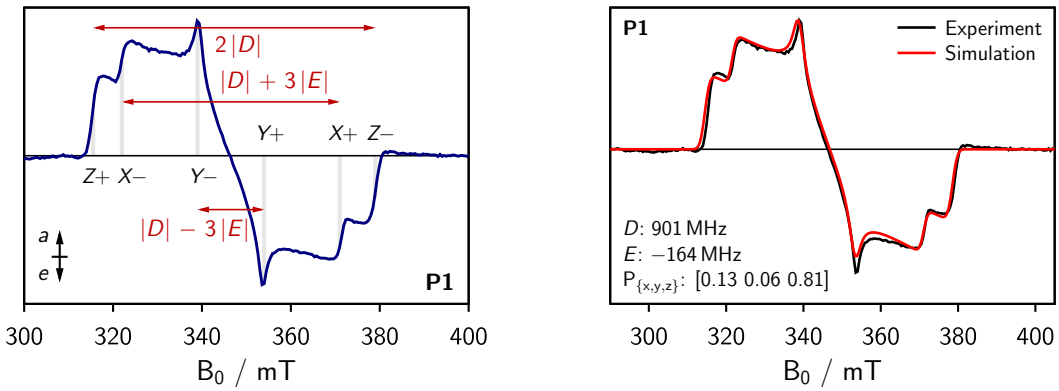


Figure 5.3: Illustration of the determination of the dipolar splitting parameters D and E from the experimental triplet EPR spectrum of **P1** (*left*) and numerical simulation of the spectrum using EasySpin (*right*).

Apart from D and E, also the information about the initial relative triplet state sublevel populations can be obtained by numerical simulation of the spectrum (cf. **Figure 5.3**, *right*). The shape of the triplet spectrum is very sensitive even to small changes in these triplet state populations. An illustration of the variation in shape upon changes in the initial populations is shown in **Figure 5.4**. The spectra were simulated for the same D and E values, but different populations with either the X, Y, or Z sublevels, or combinations thereof, primarily populated. It can be observed that the six spectra shown in the figure are very characteristic and clearly different from each other. However, only information on the *relative* sublevel populations can be obtained.

Changes in triplet state populations are not always straightforward to interpret. Yet, potentially, a lot of information on the mechanism of triplet formation can be obtained. For instance, in the case of **P1**, the out-of-plane sublevel is mainly populated which can be interpreted as arising from intersystem crossing mediated by spin orbit coupling due to mixing of the Zn d-orbitals with the porphyrin π-system. **Table 5.1** gives an overview of all possible ESP patterns that can arise from

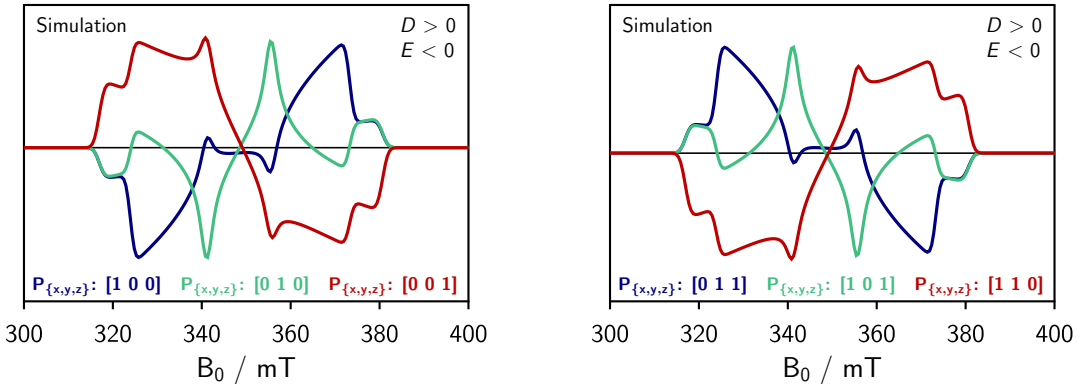


Figure 5.4: Simulation of the triplet state EPR spectra assuming $D > 0$ and $E < 0$ for different initial populations of the triplet sublevels.

different combinations of the intersystem crossing rates and therefore different initial triplet state sublevel populations. It shall be noted here that only the polarisation patterns *aeeaae* and *eaaeea* cannot result from intersystem crossing.

Table 5.1: Examples of the possible polarisation patterns that can arise from intersystem crossing together with the corresponding relative populations (for $D > 0$, $E < 0$) of the triplet sublevels.

$\mathbf{P_X}$	$\mathbf{P_Y}$	$\mathbf{P_Z}$	ESP(**Z**+)	ESP(**X**−)	ESP(**Y**−)	ESP(**Y**+)	ESP(**X**+)	ESP(**Z**−)
1	0	0	*e*	*e*	*a*	*e*	*a*	*a*
0	1	0	*e*	*a*	*e*	*a*	*e*	*a*
0	0	1	*a*	*a*	*a*	*e*	*e*	*e*
1	1	0	*e*	*e*	*e*	*a*	*a*	*a*
1	0	1	*a*	*e*	*a*	*e*	*a*	*e*
0	1	1	*a*	*a*	*e*	*a*	*e*	*e*
2	1	0	*e*	*e*	–	–	*a*	*a*
2	0	1	–	*e*	*a*	*e*	*a*	–
1	2	0	*e*	–	*e*	*a*	–	*a*
0	2	1	–	*a*	*e*	*a*	*e*	–
1	0	2	*a*	–	*a*	*e*	–	*e*
0	1	2	*a*	*a*	–	–	*e*	*e*

5.2 Probing Triplet State Delocalisation

Two different approaches to access delocalisation of the triplet state shall briefly be discussed here. The first approach makes use of transient cw EPR spectroscopy and relies on the dipolar splitting parameter D as a measure of delocalisation due to its distance dependence $\propto r^{-3}$. The second one builds on the McConnell equation [125] and uses the relative magnitudes of the hyperfine coupling constants to conclude about spin delocalisation.

Both of these approaches have widely been applied in the literature before. Many studies have focussed on the photosynthetic reaction centre and model systems thereof and it was for instance found, using pulse ENDOR spectroscopy, that the triplet state is (unevenly) delocalised over two chlorophyll units in the special pair of the bacterial reaction centre [99], whereas, under identical conditions, localisation of the triplet state on just a single unit was observed in the special pair of photosystem II [102]. Transient cw EPR was for example applied in the study of artificial linear porphyrin systems designed as molecular wires [107, 108, 112] where it was concluded from the D values that the triplet state is localised on just a single porphyrin unit.

5.2.1 Transient cw EPR

Since D is proportional to r^{-3}, where r is the distance between the two unpaired electrons, one should expect to observe a decrease in the absolute value of D if the distance between the two unpaired electrons increases upon delocalisation. The total width of the triplet spectrum being equal to $2|D|$ (cf. **Figure 5.3**), increased delocalisation should in principle manifest itself in the observation of a narrower spectrum.

However, it has been shown in the literature [122] that care needs to be taken in the interpretation of the apparent $D \propto r^{-3}$ proportionality since the orientation of the zero-field splitting tensor within the molecular framework and therefore the $1 - 3\cos^2\theta$ term in **Equation (5.1)** might change with increasing oligomer length. Unless there are good reasons to assume that the spin distribution remains invariant, the use of D as an indication of the delocalisation length might lead to wrong conclusions and should therefore be avoided or complemented by ENDOR results. As an example, a change in spin distribution from an oblate ($\theta = 90°$) to an entirely prolate ($\theta = 0°$) system would result in an increase in the absolute value of D by a factor of two, even if the delocalisation length r remains unchanged.

5.2.2 Triplet State ENDOR

A much less ambiguous way to access triplet state delocalisation is to determine the hyperfine coupling constants using pulse ENDOR (or ESEEM) spectroscopy. The McConnell equation [125] describes a linear relationship between the hyperfine coupling constants, A_i, of a system and its spin density ρ,

$$A_i = Q \cdot \rho \tag{5.7}$$

where Q is an empiric factor which is assumed to be constant for a given system. From this relation it can directly be inferred that if complete delocalisation occurs over more than one unit in an oligomeric system, the hyperfine coupling constants of the oligomer, A_i, will be reduced compared to the corresponding ones in the monomer, $A_{M,i}$, by a factor of one over the number of units N over which delocalisation occurs.

$$A_i = \frac{1}{N} A_{M,i} \tag{5.8}$$

This formula enables us to quantify delocalisation in a straightforward way (but is based on the assumption of identical spin distributions on each unit). As we will see from the experimental data obtained for the systems studied in Chapters 6 and 7, this approach will prove valuable for the study of delocalisation although it is experimentally more challenging than the determination of the dipolar splitting parameters by transient cw EPR.

Figure 5.5 shows a schematic representation of the energetic splittings and possible transitions in triplet state (^{1}H) ENDOR, where the external magnetic field, B_0, was chosen to be parallel to the Z axis.

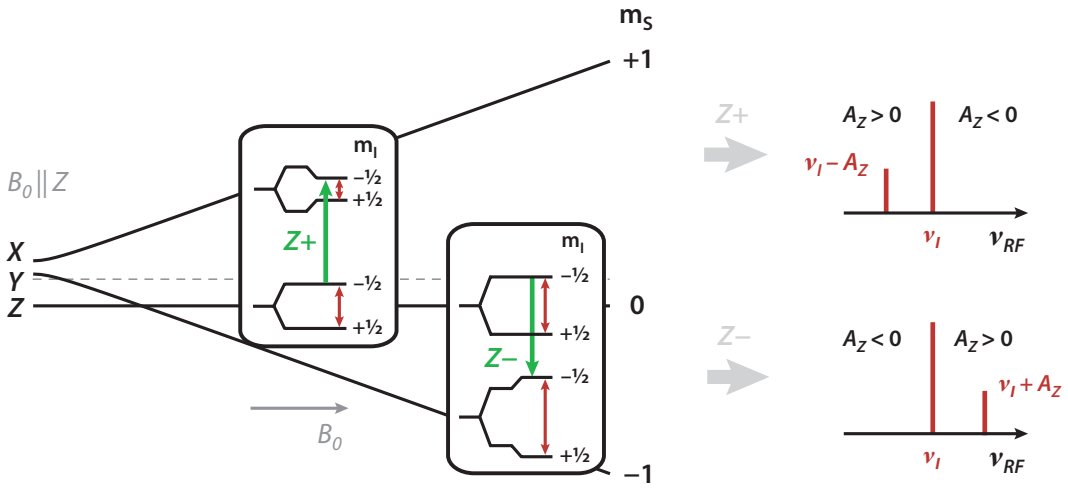


Figure 5.5: Schematic representation of the energy splittings and (^{1}H) ENDOR transitions in the triplet state for $A_Z > 0$, $D > 0$, $E < 0$ and $B_0 \,||\, Z$. The relative position of the observed ENDOR peak with respect to the Larmor peak is graphically illustrated. The position depends on the sign of the hyperfine coupling constant, A_Z, and the probed spin manifold. EPR transitions are indicated in green, whereas nuclear transitions are shown in red.

Starting from their respective zero-field energies, the three different energy levels of the triplet state are split in the presence of an external magnetic field due to the influence of the electronic and nuclear Zeeman interactions, as well as the hyperfine interaction. Here we consider the case of proton ENDOR ($I = \frac{1}{2}$) measured at a magnetic field corresponding to the $Z+$ transition ($D > 0$) and furthermore, for simplicity, we will assume that we only have one non-zero hyperfine coupling constant in our system which we will refer to as A_Z. According to **Figure 5.5** we would thus expect two peaks in the ENDOR spectrum due to the two possible transitions: One at the Larmor frequency of the protons ($m_s = 0$) corresponding to the chosen field position and another one shifted from the Larmor frequency peak by the value of A_Z ($m_s = +1$). The absolute value of A_Z can then directly be read off from the spectrum as it is given by the absolute magnitude of the shift. For representation of the ENDOR spectra of weakly coupled nuclei such as ^{1}H, which are centred around the Larmor frequency, the Larmor frequency peak is set to zero, so that the x-axis directly reflects the magnitude of the hyperfine coupling constants in MHz.

Triplet state ENDOR has the advantage that the sign of the hyperfine coupling constants can be determined provided the sign of the dipolar splitting parameter D is known. In this case, the Larmor peak serves as a reference. When referring to the $Z+$ transition, hyperfine coupling

constants associated with peaks located at frequencies lower than the Larmor peak are positive in sign, whereas those corresponding to peaks appearing at the higher frequency side of the Larmor peak are negative. The opposite is the case for the $Z-$ transition (and for the $-$ spin manifold in general). A graphic summary of this is shown in **Figure 5.5**.

Since triplet EPR spectra are typically broad, the EPR pulses of a couple of nanoseconds length applied in an ENDOR experiment cannot uniformly excite the entire spectrum. Orientation selection is therefore observed in triplet ENDOR, meaning that different subsets of orientations are probed depending on the chosen field position. If individual components of anisotropic interaction tensors are to be resolved, the orientation dependence of the spectra can be a great advantage. It can for example be used to determine relative tensor orientations.

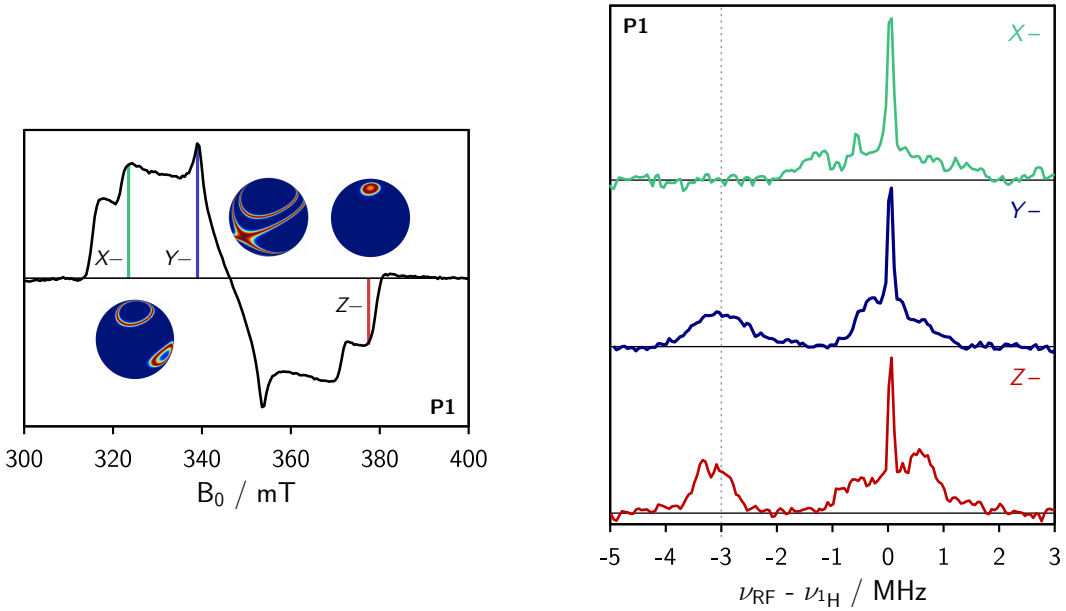


Figure 5.6: Illustration of the orientations probed at different field positions within the triplet EPR spectrum of **P1** (*left*) and corresponding triplet state ENDOR spectra (*right*).

In **Figure 5.6**, the effect of orientation selection on the ENDOR spectra, detected at different field positions within the triplet cw EPR spectrum of **P1**, is illustrated. The orientations are graphically depicted on unit spheres and excited orientations are shown in red. The figure suggests that measurements at field positions corresponding to the six different canonical orientations indicated in the spectra can be used to obtain independent information about the magnitude of the hyperfine tensor components along the three axes of the ZFS interaction tensor. Indeed such information can be obtained by orientation dependent measurements, however the spectral overlap of different contributions needs to be considered in the analysis of the spectra. As can be seen by closer inspection of **Figure 5.6**, while the information about the Z component of the tensor can easily be isolated by performing the measurements in the outer wings of the spectrum, spectra measured at field positions corresponding to the X and Y orientations will in most cases also contain minor contributions of signals belonging to other canonical orientations.

Chapter 6

Triplet State Delocalisation in Zinc Porphyrin Ladders

The linear zinc porphyrin oligomers shown in **Figure 6.1** (*left*) have been synthesised in the Anderson group (University of Oxford, UK) [126] and will be referred to as **P*n***, depending on their number *n* of porphyrin units. It has been shown by NMR and UV-vis spectroscopies [127] that especially the longer oligomers **P3** and **P4** can form ladder-type assemblies when diazabicyclo[2.2.2]octane (**DABCO**) or other bidentate ligands like 4,4'-bipyridine (**bipy**) are added in stoichiometric equivalents to a solution of the linear zinc porphyrin oligomers. The self-assembly is highly cooperative and the association constants of the corresponding processes are strongly solvent dependent and have been investigated in detail at ambient temperatures [127]. From these investigations it could be concluded that toluene is a suitable solvent for the study of the ladder structures since (i) the association constants are comparatively high in toluene and (ii) toluene is non-coordinating and therefore does not interfere with the binding of the nitrogen ligands to zinc. Although the glass forming properties of toluene are not ideal, since toluene glasses are prone to cracking, it is also suitable for low-temperature EPR.

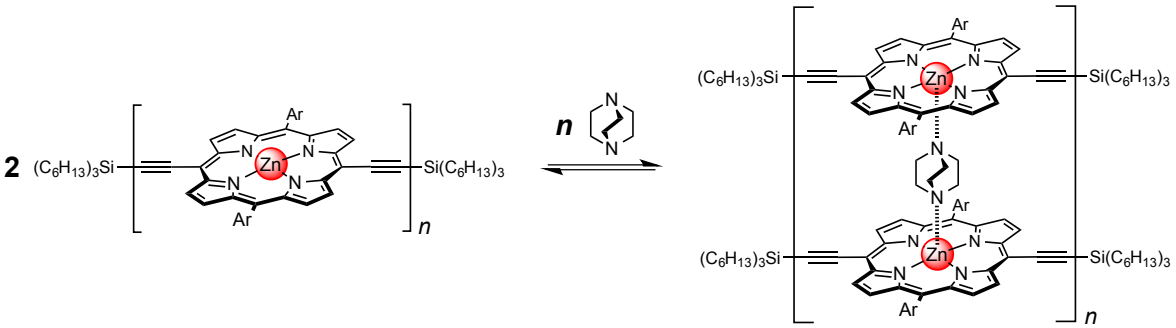


Figure 6.1: Schematic representation of porphyrin ladder formation when **DABCO** is added in stoichiometric equivalents to a solution of linear zinc porphyrin oligomers. Structures of the linear porphyrin oligomers with **tBu** side groups (*left*) and of the self-assembled porphyrin ladders containing **DABCO** (*right*). The separation distance between the porphyrin strands in the ladder complexes with **DABCO** amounts to 0.7 nm [128].

The investigated structures have been synthesised as model compounds for photosynthetic light harvesting, charge transport ('molecular wires'), and nonlinear optical applications. Conjugation in these systems can for example be observed by UV-vis spectroscopy as shown in **Figure 6.2**. Comparing the spectra of the longer oligomers with the spectrum of **P1**, it can be seen that the

porphyrin Q-bands are considerably red-shifted, which is a clear indication of a more extended conjugated π-system.

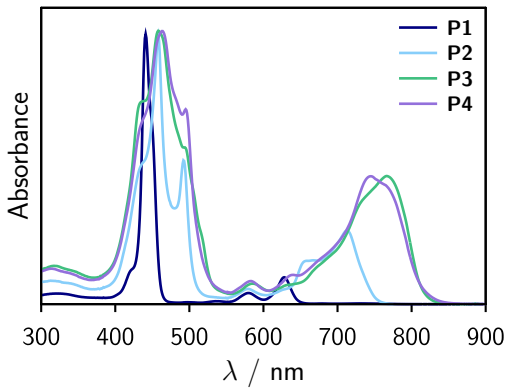


Figure 6.2: Normalised UV-vis spectra of the linear porphyrin oligomers **P1** to **P4** with **tBu** side groups recorded in toluene at room temperature.

In previous work [109, 122, 129], triplet state delocalisation has been investigated extensively in linear porphyrin oligomers with **THS** side groups in a 2-methyltetrahydrofuran:pyridine 10:1 (**MTHF:py**) solvent mixture by transient cw EPR and pulse ENDOR techniques. It has been found that complete delocalisation is restricted to just two porphyrin units. In the corresponding longer oligomers, **P3** and **P4**, uneven triplet state delocalisation was observed and confirmed by DFT calculations.

Since the barrier to rotation about the triple bonds connecting the individual porphyrin units is below 1 kcal mol^{-1} [69], free rotation of the porphyrin units is feasible in the linear oligomers, potentially leading to a large heterogeneity of torsional angles which might disrupt delocalisation.

The ladder complexes investigated in this study were designed to limit the rotation about the butadiyne linkers, thereby keeping the π-systems within a single porphyrin strand co-planar and maximising intra-oligomer π-overlap. Compared to linear porphyrin oligomers, the real and imaginary parts of the third-order nonlinear susceptibility $\chi^{(3)}$ have been shown to be enhanced by an order of magnitude in ladder complexes [118, 130, 131], making porphyrin ladders suitable candidates for nonlinear optical applications. In addition, a ten-fold increase in the charge carrier mobility was observed in ladder structures and was ascribed to enhanced conjugation in these systems as a consequence of the increased planarity of the individual porphyrin strands [132].

The predominantly co-planar arrangement of the porphyrin units in ladder complexes could potentially facilitate delocalisation. In this study, the small bidentate nitrogen ligand **DABCO** is chosen as the bridging ligand resulting in a separation distance of only 0.7 nm between the two porphyrin strands. This distance is similar in magnitude compared to that between the two chlorophyll molecules forming the special pair in bacterial reaction centres, where asymmetric delocalisation over both molecules was observed [99]. To minimise steric hindrance in ladder formation, the less bulky **tBu** side groups are chosen for the present investigation rather than **THS** side groups.

The focus of this study is to explore whether ladder formation enhances triplet state delocalisation either (i) within a single porphyrin strand by keeping the porphyrin π-system in a co-planar arrangement or (ii) between the two porphyrin stands, in analogy to the observations made in the bacterial reaction centre. Triplet state delocalisation is investigated by both transient cw EPR and pulse ENDOR spectroscopies in frozen toluene solution at 20 K.

In the following paragraphs we will continue with a basic characterisation of the porphyrin structures and ladder assemblies by room and low-temperature UV-vis spectroscopy, before we proceed to discussing the results of the EPR and ENDOR investigations, which are complemented by DFT calculations.

6.1 Ladder Formation and Stability

It has been suggested in the literature that the room temperature UV-vis spectrum of the porphyrin dimer is the sum of the spectra of different conformations [133] brought about by the low rotation barrier (< 1 kcal) about the butadiyne bridge [69]. By titration of a solution of porphyrin dimer (**P2**) with a bidentate ligand forcing the dimer into a co-planar conformation, the pure spectrum of the co-planar conformer was obtained [133], confirming the presence of different conformers at room temperature. Upon planarisation, the porphyrin Q-bands are slightly red-shifted and the spectral intensity at the red-edge of the spectrum around 735 nm (in **MTHF**) is considerably enhanced, whereas the relative intensity of the band around 670 nm is smaller compared to the spectrum of mixed conformers. In the Soret band, the increased peak intensity at higher wavelengths ($\sim$495 nm) can be attributed to the parallel conformation, whereas the intense band in the centre of the Soret band ($\sim$460 nm), present before addition of the planarising ligand, strongly decreases upon addition of the latter and is thus considered a spectral feature of the perpendicular conformation.

Similar changes in the spectra, indicative for planarisation, are also expected upon ladder formation with **DABCO**. The rotation of the individual porphyrin units in the oligomers should be considerably restricted in the presence of **DABCO** and a predominantly co-planar arrangement obtained. Moreover, the behaviour and stability of the ladder structures also needs to be tested at low temperatures to assure a good comparability of the observations from UV-vis spectroscopy with the results obtained by EPR. There are several reasons why triplet state EPR needs to be carried out in the solid state at low temperatures, a few of which shall be mentioned here: The spin lattice relaxation controls the communication between the triplet sublevels and is highly temperature dependent. We need this relaxation to be slow (i.e. no faster than the triplet lifetime) to obtain good results by pulse EPR. This is normally only possible at low temperatures and in solid matrices. Tumbling/rotation and a short triplet lifetime or a low triplet concentration (low sample concentration, excitation efficiency, or low triplet yield) can all cause problems. Moreover, the triplet state population can decay by other deactivation processes, the influence of which is much reduced at low temperatures. For further details see reference [105].

Porphyrin ladder formation can for instance be confirmed by NMR and UV-vis titrations. If the bridging ligand is added in large excess, the ladder structure can again break up to form structures

where one **DABCO** molecule is bound per zinc porphyrin unit. **Figure 6.3** shows spectra at different points of a room temperature UV-vis titration of the linear oligomers **P1** to **P4** with **DABCO** in toluene. The respective spectra at the stoichiometric point for ladder formation are shown in green, whereas the red lines represent spectra of solutions containing a large excess of **DABCO**. All UV-vis spectra presented in this chapter have been recorded by Martin Peeks (Anderson group, University of Oxford, UK). Upon addition of **DABCO**, gradual changes can be observed in the UV-vis spectra. For **P1**, no indications for the formation of an intermediate ladder-type complex are present at the employed concentrations due to a comparatively weak association constant of only $\sim 3 \cdot 10^3\,\mathrm{M}^{-1}$ [127]. However, in the case of the longer oligomers, **P2** to **P4**, a red-shift of the porphyrin Q-band is observed, along with shifts of intensity away from the blue-edge of the Q-band and the central peak of the porphyrin Soret band ($\sim$450 nm) towards the red edge of the Q- and Soret bands. Based on the literature results cited above, these changes are attributed to (i) a Q-band red-shift resulting from axial Zn$\cdots$N coordination and (ii) changes in band shape arising from planarisation as a consequence of ladder formation.

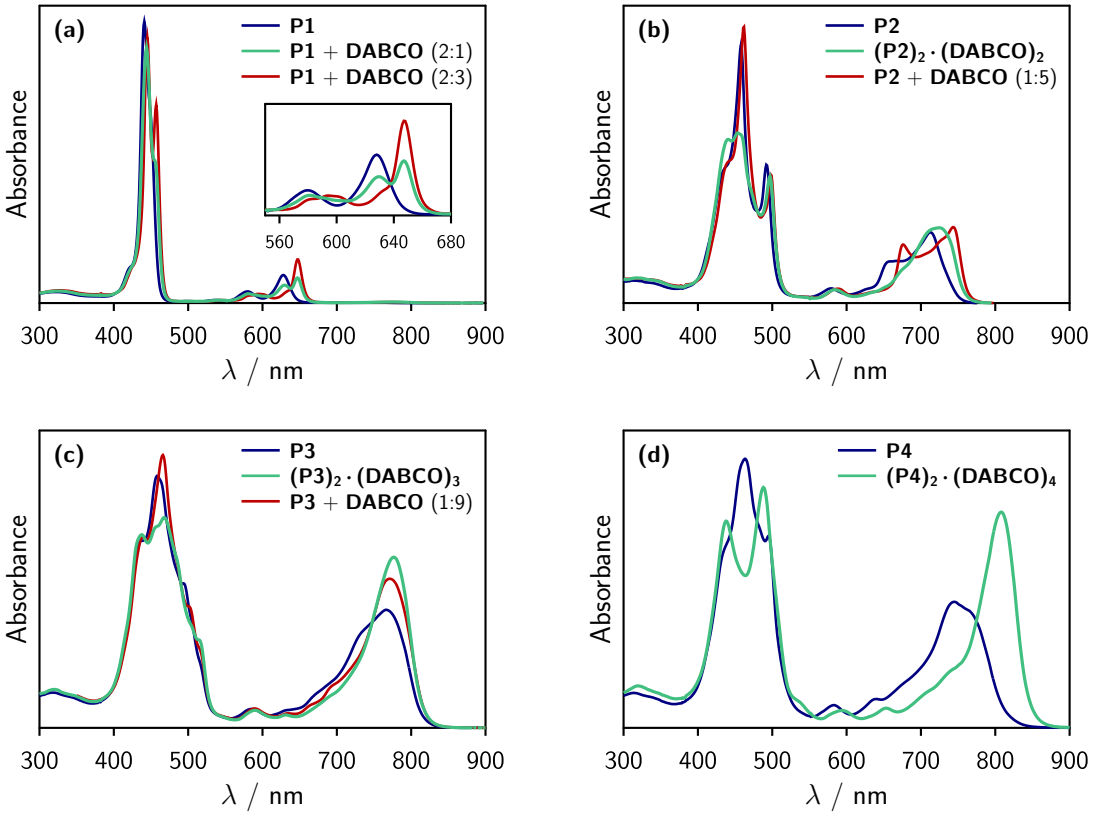


Figure 6.3: Spectra recorded at different points of UV-vis titrations of **P1** to **P4** (1 μM) with **DABCO** in toluene solution at ambient temperatures. The respective spectra at the stoichiometric point for ladder formation are shown in green. Red lines indicate a large excess of **DABCO**.

When **DABCO** is added in excess, the ladder complexes are found to break up again in the case of **P2** and **P3**, most clearly indicated by the gain in intensity of the central peak of the Soret band ($\sim$465 nm). In the case of **P4**, the stability of the ladder complex is already high enough that it cannot be broken up easily by addition of a large excess of the ligand and hence no further

changes in the UV-vis spectrum were observed once the stoichiometric point for ladder formation was reached.

To assure comparability with the EPR measurements carried out in frozen toluene, the stability of the **DABCO** ladder structures was also verified at low temperatures. For the low temperature UV-vis measurements the sample was contained in an EPR tube and the temperature was controlled using an Oxford Instruments cryostat. Due to cracks in the frozen toluene glass and the geometry of the EPR tube, a relatively large scattering background was present in all low temperature spectra and a fourth order polynomial background correction was consequently applied. Owing to these background corrections, the relative peak intensities in the low temperature UV-vis spectra might not be absolutely reliable. Nevertheless the prominent spectral features can clearly be distinguished and compared and were found to be well reproducible. The corrected low-temperature spectra recorded at 80 K in the absence and presence of **DABCO** are compared to the corresponding room temperature spectra in **Figures 6.4** and **6.5** for **P2** to **P4**. Additionally, for **P2** with **DABCO**, spectra at different temperatures were recorded with the aim to understand the peculiar results obtained with this sample at low temperatures. These spectra are also shown in **Figure 6.4**.

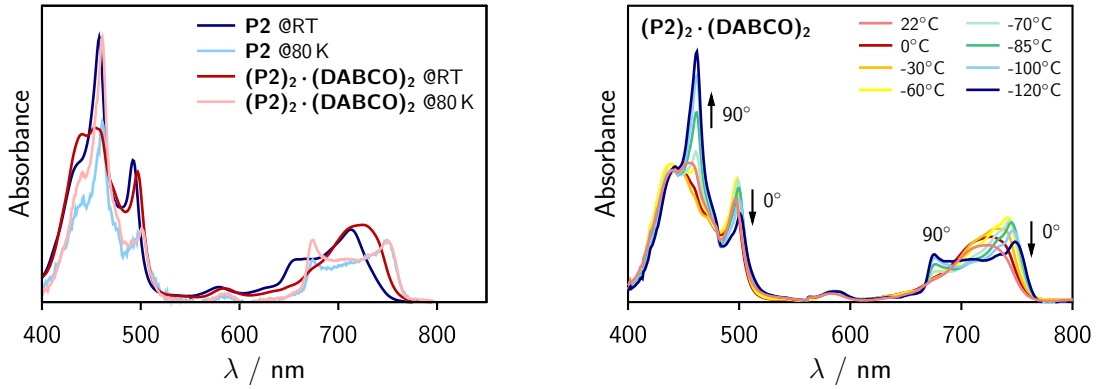


Figure 6.4: Room and low temperature (80 K) UV-vis spectra of **P2** and **(P2)$_2$ · (DABCO)$_2$** (*left*) and spectra of **(P2)$_2$ · (DABCO)$_2$** at different temperatures as indicated (*right*) in toluene.

When examining the spectra in **Figure 6.4**, it can be observed that **P2** does not behave as expected. From the spectra it appears that the **DABCO** ladder complex, present at room temperature, is not stable at low temperatures judged by the increase in intensity of the central peak of the porphyrin Soret band. In fact, the low temperature spectrum of **P2** with **DABCO** resembles the spectrum of **P2** with excess **DABCO** measured at room temperature (cf. **Figure 6.3**). It thus seems that an arrangement where the porphyrin units within a single oligomer are predominantly held at right angles with respect to each other is preferred at low temperatures.*

In the case of the longer oligomers **P3** and **P4**, however, the stability of the ladder complexes could be confirmed at low temperatures. Compared to the corresponding spectra at room temperature, the ladder spectra at 80 K are red-shifted and are more structured, especially in the spectral region of the porphyrin Q-bands, but the spectral characteristics indicative for ladder formation are conserved. Low temperature spectra were also acquired in the absence of **DABCO** and

*This might be due to low temperature aggregation of **P2** competing with ladder formation.

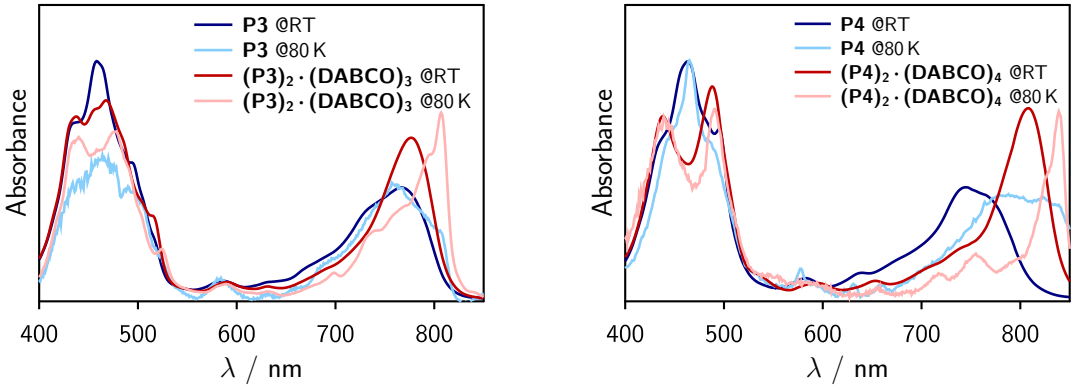


Figure 6.5: Room and low temperature (80 K) UV-vis spectra of **P3** and **$(P3)_2 \cdot (DABCO)_3$** (*left*) and **P4** and **$(P4)_2 \cdot (DABCO)_4$** (*right*) in toluene.

show convincingly that the longer oligomers do not spontaneously adopt a co-planar conformation upon cooling, but that the presence of **DABCO** indeed influences the distribution of oligomer conformations, also at low temperatures.

6.2 Transient cw EPR and Simulations

The influence of **DABCO** on triplet state delocalisation in ladder complexes can only be quantified reliably if the properties of the porphyrin oligomers in the absence of the bridging ligand are well known. Since previously published results were obtained in different solvents and with different porphyrin side groups, they should not be used for reference in this study. Consequently, the linear oligomers with **tBu** side groups were first characterised by transient EPR in the absence of **DABCO** in toluene. All samples were prepared at a concentration of 50 μM, were excited at 532 nm with a pulsed Nd:YAG laser (10 Hz, 5 mJ) and the spectra were recorded at 20 K. Further details on the sample preparation, experimental setup and data treatment can be found in Appendix A (cf. **Section A.1** and **Subsection A.3.2**).

6.2.1 Linear Oligomers

The transient cw EPR spectra obtained for the linear oligomers, **P1** to **P4**, are shown in **Figure 6.6**. The shape of the triplet spectra was found not to change significantly over the course of the triplet state lifetime as illustrated in **Figure 6.7** for **P1** and **P2**. For representation, either individual spectra are plotted at different time delays after laser excitation, or, if only the spectral shape is needed for analysis, several spectra at early delay times are averaged (typically over a time window from 0.2−1.0 μs) to obtain a better signal-to-noise ratio.

The measured spectra are in good agreement with results published earlier [109], although small differences in the triplet state polarisations are observed. In agreement with earlier work, an increase of the spectral width is observed from **P1** to **P2**. An interpretation of this finding in terms of **Equation (5.1)** would suggest that the triplet state is localised on just a single porphyrin unit, however it has been shown before that a reorientation of the zero-field splitting tensor occurs

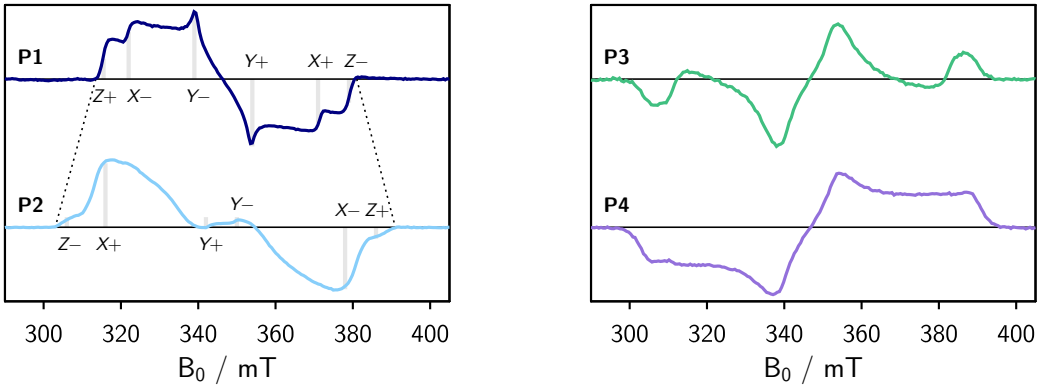


Figure 6.6: Comparison of the X-band triplet cw EPR spectra recorded at 20 K in frozen toluene for **P1** and **P2** (*left*) and **P3** and **P4** (*right*). The spectra have been averaged from 0.2–1 μs after laser excitation.

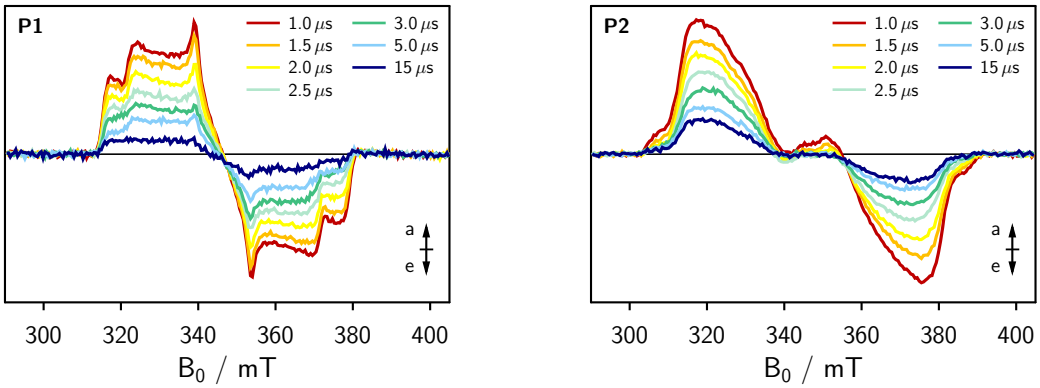


Figure 6.7: Transient cw EPR spectra at different time delays after laser excitation for the triplet state of **P1** (*left*) and **P2** (*right*) recorded at 20 K in frozen toluene.

from **P1** to **P2** and is consistent with the observed increase of the spectral width and complete delocalisation over two porphyrin units [122].

Numerical simulations of the experimental data were performed in MATLAB using the software package EasySpin, in combination with a home-written MATLAB fitting routine, to determine the zero-field splitting parameters D and E as well as the relative populations of the triplet sublevels. For **P1**, the D value was assumed to be positive, as confirmed by magnetophotoselection experiments [122], corresponding to the Z axis being the out-of-plane axis. The E value was chosen to be negative, so that the Y axis of the zero-field splitting tensor is aligned with the axis along the aryl side groups. For the longer oligomers **P2** to **P4**, D was assumed to be negative and E positive. Consequently, for these molecules, the ZFS Z axis coincides with the long axis of the molecule, while Y still corresponds to the axis along the aryl side groups. The best fit to the data is shown in **Figure 6.8** for **P1** to **P4** and the individual simulation parameters are indicated in the graphs. The smallest sublevel population, observed for the Y sublevel in all cases, was set to zero for a better visualisation of the trends.

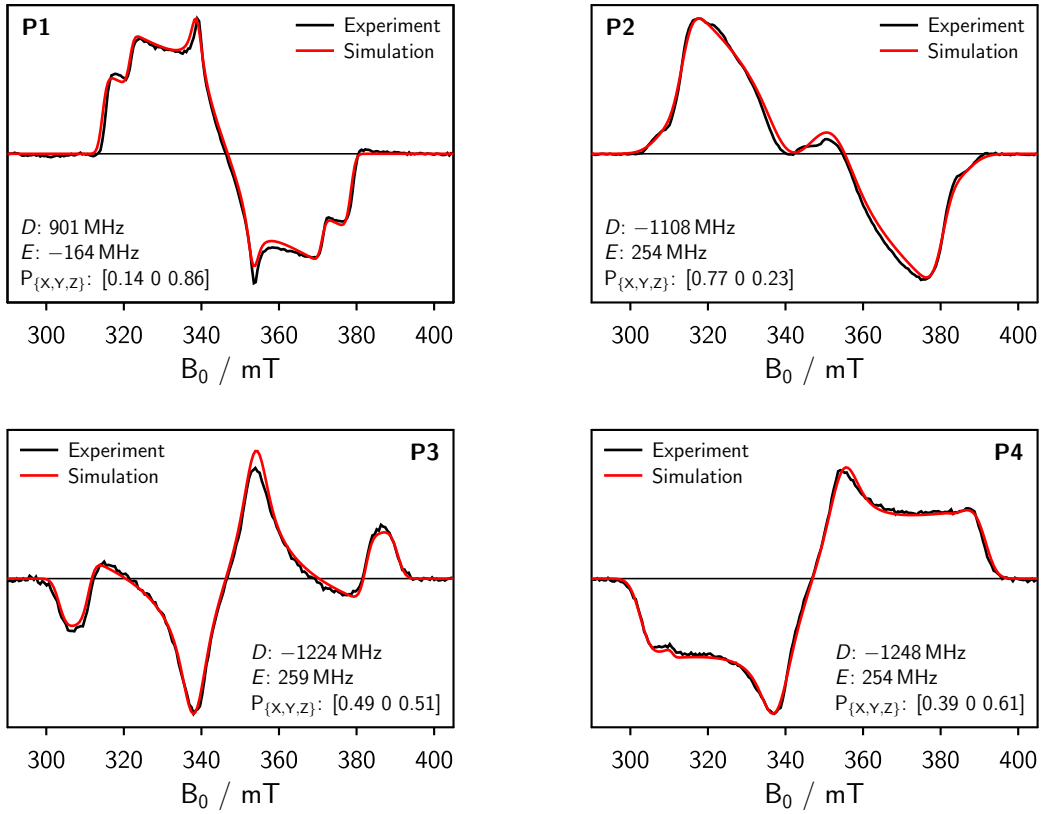


Figure 6.8: Numerical simulations of the experimental triplet spectra for **P1** (*top left*), **P2** (*top right*), **P3** (*bottom left*) and **P4** (*bottom right*) with **tBu** side groups in toluene. The simulation parameters are indicated in the figure.

In linear porphyrin oligomers with 3,5-bis(octyloxy)phenyl side groups, aggregation was observed in non-coordinating solvents [134, 135]. The relatively low concentration employed in this EPR study and the similarity of the obtained triplet state parameters to those obtained for porphyrins with **THS** side groups in a **MTHF:py** solvent mixture suggests, however, that aggregation is not a confounding variable in the present case. To further support this statement, a spectrum of **P3** with the bigger and bulkier **THS** side groups, which are less prone to aggregation, was also recorded in toluene. The result is shown in **Figure 6.9** and numerical simulation of the data resulted in triplet state parameters almost identical to those obtained for **P3** with **tBu** side groups, suggesting that the different side chains do not significantly influence the triplet state spectra and that the small differences in the triplet state polarisations with respect to earlier work are caused by the use of a different solvent. The general trend in the triplet state polarisations with increasing oligomer length is, however, identical, and the gradual decrease in the out-of-plane triplet sublevel population (P_Z in **P1** and P_X in the longer oligomers) can be ascribed to an increasing contribution of a second, competing intersystem crossing mechanism [109].

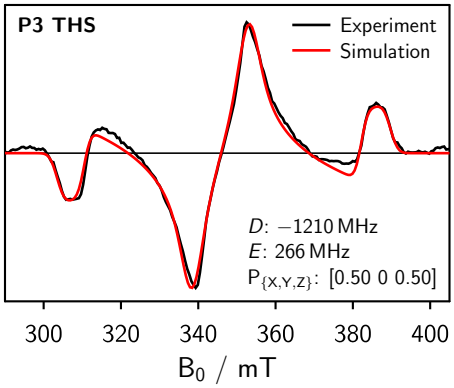


Figure 6.9: Numerical simulation of the transient cw EPR spectrum of **P3** with **THS** side groups in toluene. The simulation parameters are indicated in the figure.

6.2.2 DABCO Ladders

Transient cw EPR spectra have also been recorded for samples of the linear porphyrin strands containing **DABCO** in stoichiometric equivalents for ladder formation. Since the ladder complex of **P2** was found not to be stable at low temperatures, and complete delocalisation has already been shown beforehand to occur over two porphyrin units even in the absence of a planarising ligand, the following discussion on the effect of ladder formation on triplet state delocalisation will only focus on the longer oligomers **P3** and **P4**.

The triplet spectra of the **DABCO** ladder complexes are shown in **Figure 6.10** and are compared to the respective spectra without bridging ligand. At first glance, the spectra acquired in the presence of **DABCO** are very similar to those acquired in its absence. However, on closer inspection and simulation of the data, as shown in **Figure 6.11**, it is observed that the relative populations of the triplet sublevels, and therefore the electron spin polarisation of the spectrum of **P3**, are slightly altered in the presence of **DABCO**. The out-of-plane triplet sublevel population (P_X) is slightly decreased upon ladder formation in **P3**. This is consistent with an increased planarisation of the porphyrin π-system as suggested by comparison of the spectrum with the results from excitation wavelength dependent studies where the co-planar conformation was selectively excited [129]. The spectral differences observed for **P4** when comparing the spectra in the absence and presence of **DABCO** are almost negligible. However, the spectral shape observed is again consistent with a co-planar conformation by comparison with the spectra shown in reference [129].

Most importantly, the D value, determining the overall width of the spectra, does not seem to be affected by ladder formation, suggesting that the bridging ligand **DABCO** does not promote further delocalisation. However, since the hyperfine coupling constants provide a more accurate estimate of the extent of triplet state delocalisation, ^{1}H ENDOR experiments were carried out on the available samples, again starting with the linear oligomers in the absence of **DABCO** for reference.

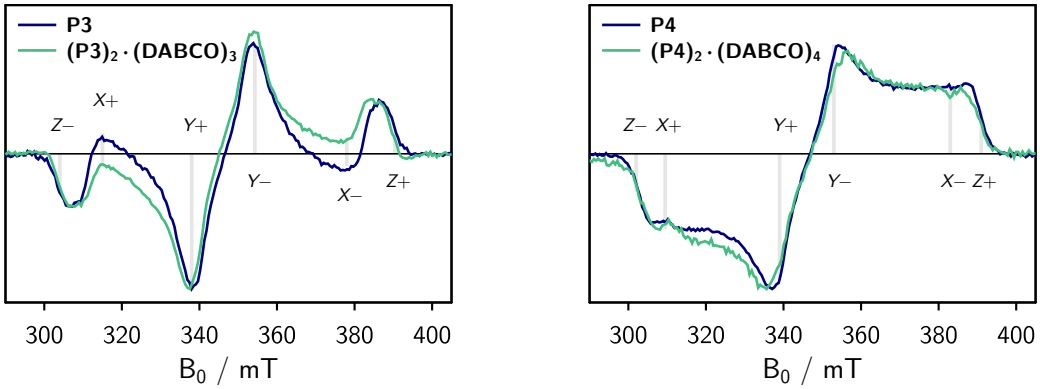


Figure 6.10: Experimental transient cw EPR triplet spectra for **P3** and **P4** and comparison of the spectra to those measured in the presence of **DABCO** added in stoichiometric amounts for ladder formation. The positions of the six canonical orientations are labelled for reference.

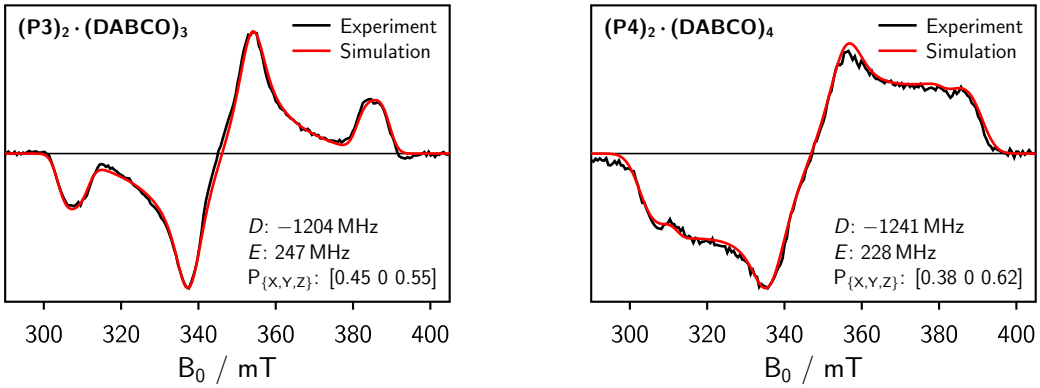


Figure 6.11: Numerical simulation of the transient cw EPR spectrum of the ladder complexes of **P3** (*left*) and **P4** (*right*) recorded at 20 K in frozen toluene. The simulation parameters are indicated in the figure.

6.3 Mims ENDOR & DFT

Both theoretically and experimentally the largest proton hyperfine coupling constants in the investigated porphyrin systems are observed along the Y axis of the $\boldsymbol{D}$-tensor, corresponding to the axis along the aryl side groups. To obtain the most reliable results when investigating delocalisation, the magnitude of this well resolved hyperfine coupling constant in the Y direction will thus be compared in all cases. ENDOR spectra for other field positions corresponding to the X and Z orientations were also recorded and are shown for **P1** and **P2** in Appendix F (**Section F.1**).

DFT calculations of the hyperfine coupling tensors, as described in Appendix A (**Section A.5**), allow assignment of this coupling to the nuclei within the porphyrin core. A visualisation of the calculated hyperfine coupling tensors is shown in **Figure 6.12** for **P1** and **P2** together with the orientation of the ZFS tensor as obtained by DFT. The magnitude of the hyperfine coupling constant compared between the different oligomers in the experiment corresponds to the projection

of the hyperfine coupling tensors shown in dark green onto the Y axis of the zero-field splitting tensor (D_Y). The corresponding calculated values are shown in **Figure 6.13**.

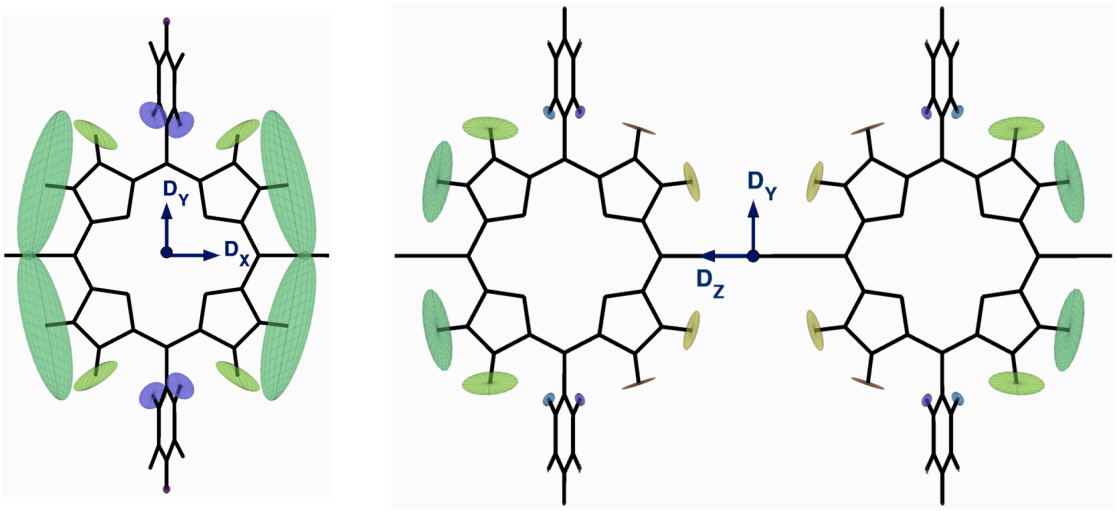


Figure 6.12: Visual representation of the calculated hyperfine coupling tensors for **P1** (*left*) and **P2** (*right*). The magnetic property calculations have been performed using ORCA V3.0 (EPRII basis set; 6-31G(p,d) on Zn) on a structure optimised with Turbomole (TZVP basis). Tensors of chemically equivalent protons are shown in the same colour and the relative tensor size reflects the relative magnitude of the hyperfine interactions. The largest hyperfine coupling tensors, used to determine the average delocalisation length from the experimental ENDOR data, are shown in dark green.

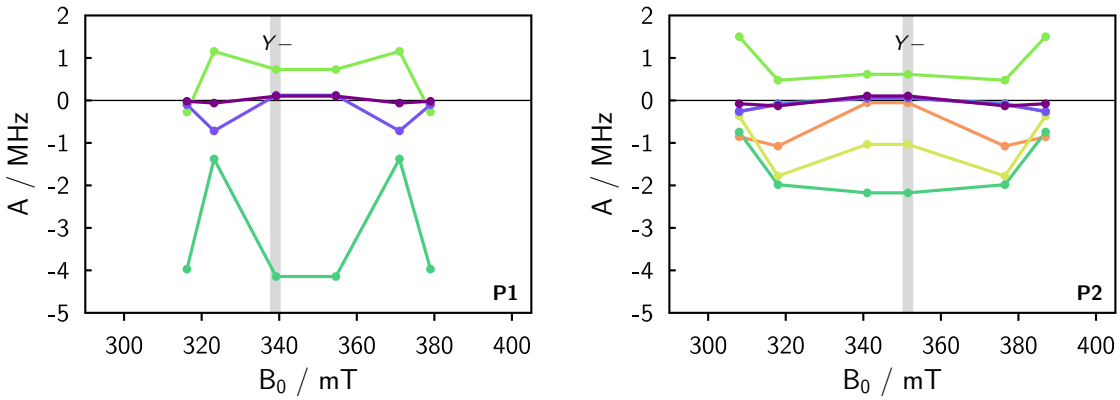


Figure 6.13: Projection of the calculated hyperfine coupling tensors onto the X, Y, and Z axes of the zero-field splitting tensor, plotted as a function of field (at the canonical orientations) for **P1** (*left*) and **P2** (*right*). The colour-coding is the same as in the previous figure. The values obtained for the $Y-$ orientation are highlighted in grey.

Mims ^{1}H ENDOR spectroscopy was applied to determine the hyperfine coupling constants of the different oligomers with and without **DABCO**. Details on the experimental setup are given in Appendix A (**Subsection A.3.2**).

The magnetic field positions for the ENDOR experiments were chosen based on the corresponding echo-detected field-swept triplet spectra. When comparing the echo-detected fieldsweep with the triplet spectrum obtained from transient cw EPR, one notices major differences in the relative

intensities of the transitions. While transient cw EPR spectra are typically symmetric about the centre of the spectrum, echo-detected field-swept EPR spectra of porphyrin triplets are normally highly asymmetric. The asymmetry is due to differences in relaxation rates between the + and the − spin manifolds. Furthermore, the appearance of the spectrum depends on the chosen τ value, since nuclear ESEEM effects result in a considerable modulation of the echo intensity as a function of time, and, generally, the intensity at the canonical field positions is larger in echo-detected spectra compared to other orientations. A comparison between a spectrum recorded by transient cw EPR and echo-detection ($\tau = 100$ ns) is shown in **Figure 6.14** for **P1**.

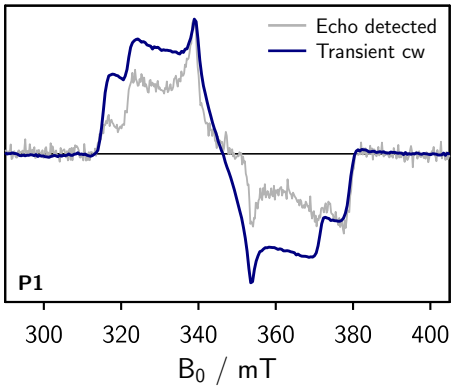


Figure 6.14: Comparison of the field-swept echo-detected EPR spectrum of **P1** to that acquired by transient cw EPR.

In order to compare the ENDOR spectra of the different porphyrin oligomers, we have to make sure that we always probe the same spin manifold. In this work, the − manifold was chosen for this purpose since the echo intensities at the corresponding field positions were higher. In order to determine which of the transitions in the experimental spectra of the longer oligomers correspond to the − manifold, the sign of D needs to be known. For example, if D is positive as in **P1**, the low field Y transition corresponds to $Y-$, whereas if D was negative, $Y-$ would correspond to the high field Y transition. An experimental approach to prove the mentioned sign change of D occurring from **P1** to **P2** shall be illustrated here. It makes use of the relative position of the measured hyperfine couplings with respect to the triplet Larmor peak: Since we know from the literature that D is positive for **P1**, we can determine the signs of the hyperfine coupling constants in our system using ENDOR and find that the dominant coupling (in $Y-$ direction) is negative. Since this sign is not expected to change for the same type of proton in the longer oligomers, this signifies that we should be able to identify the transitions corresponding to the − and + manifolds in the spectra of **P2** to **P4** and consequently deduce the sign of D in these oligomers just by looking at the position of the main ENDOR peak with respect to the triplet Larmor peak. This reasoning was applied in the interpretation of the ENDOR spectra of **P2** and the longer oligomers and it was found that D is negative in those cases [109, 122].†

†Of course, the analysis described here is not truly general. It requires that the two compared canonical orientations correspond to the same molecular axis and that there is only one large hyperfine coupling along any of the ZFS tensor axes. Otherwise, ENDOR spectra would need to be measured at all canonical field positions for all oligomers to be able to follow the individual peaks.

Mims ENDOR measurements at field positions corresponding to $Y-$ were carried out for the linear oligomers and the results are shown in **Figure 6.15**. At every field position, three spectra with different τ values of 120 ns, 180 ns, and 240 ns were recorded and added after baseline correction to compensate for blind spots.

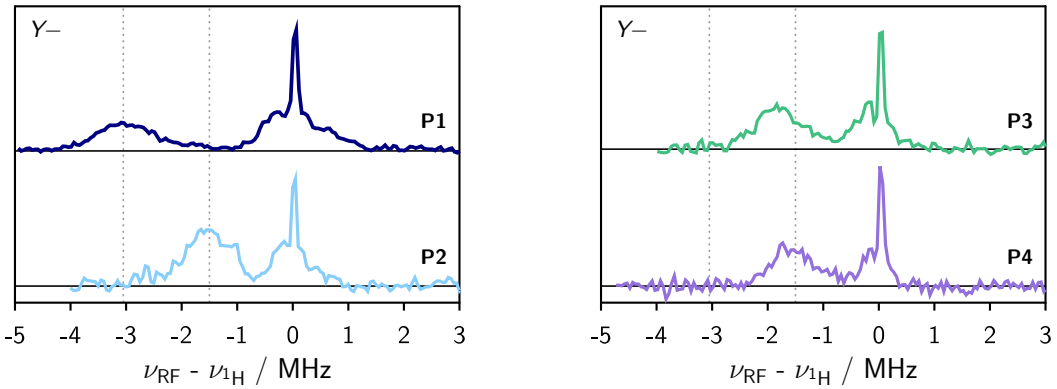


Figure 6.15: Comparison of the Mims ENDOR spectra of **P1** to **P4** recorded at 20 K at magnetic field positions corresponding to the $Y-$ orientation (339 mT, 350 mT, 352 mT and 353 mT). The depicted spectra are the sum of three spectra recorded at different τ values of 120 ns, 180 ns, and 240 ns. The dashed lines indicate the position of the hyperfine coupling peak for **P1** and half of this value.

From **Figure 6.15** it can be seen that the largest coupling in **P1** amounts to −3 MHz, whereas this value is halved in the case of **P2**, indicating complete delocalisation over two porphyrin units. In the longer oligomers, **P3** and **P4**, no further reduction in the magnitude of the hyperfine coupling constant is observed. Instead, a slight shift to lower frequencies (greater absolute magnitude) occurs and the peak shape becomes somewhat more asymmetric. The observations for **P3** and **P4** are in agreement with uneven delocalisation as shown in [109] and indicate that complete delocalisation is limited to mainly two porphyrin units in these systems.

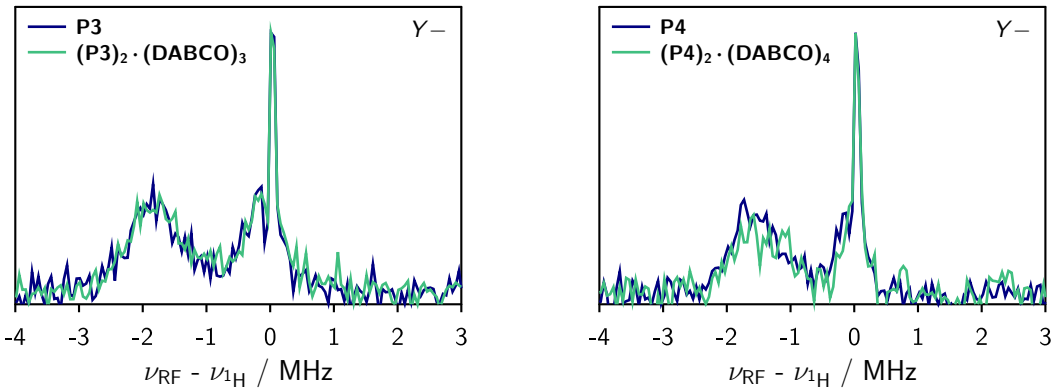


Figure 6.16: Mims ENDOR spectra of **P3** (*left*) and **P4** (*right*) recorded at magnetic field positions corresponding to the $Y-$ orientation. The spectra of samples with and without **DABCO** are compared.

The influence of the bridging ligand **DABCO** on the extent of triplet state delocalisation was explored by comparing the ENDOR spectra of **P3** and **P4** recorded at $Y-$ with those of the corresponding ladder complexes. The spectra are shown in **Figure 6.16** and it can be observed that the hyperfine coupling constants of **P3** and **P4** are not affected by ladder formation. This result implies that the extent of triplet state delocalisation is not enhanced by an increased planarisation of the π-system achieved by ladder formation.

6.4 Conclusions

The present study aimed at investigating triplet state delocalisation in ladder complexes formed by self-assembly of linear zinc porphyrin oligomers in the presence of **DABCO** as a bridging ligand. Experimentally, these systems were studied by room and low temperature UV-vis spectroscopy, transient cw EPR, as well as pulse ENDOR techniques. Since the properties of linear porphyrin strands were already well characterised [109, 122] - albeit in different solvents and using porphyrin oligomers with different side groups - the main goal in this study was to discern how structural changes in the linear porphyrin stands, which occur as a consequence of ladder type complex formation, influence triplet state delocalisation and if **DABCO** as a bridging ligand could induce communication between the two porphyrin strands forming the ladder.

In linear porphyrin oligomers with different, bulkier, **THS** side groups it was observed beforehand [122] that complete delocalisation of the electronic triplet state is limited to about two porphyrin units in frozen solution in a solvent mixture of **MTHF:py**. This finding could be confirmed in this work on similar porphyrin structures in toluene.

Delocalisation was accessed by determination of the zero-field splitting parameters, as well as of the proton hyperfine coupling constants. The latter approach allows unambiguous conclusions to be drawn, whereas when applying the former method the interpretation of the zero-field splitting parameters is not straightforward if the shape of the overall spin distribution changes between molecules. The consideration of the results from both methods applied here yielded a consistent picture and the findings are in agreement with predictions from DFT calculations. Finally, the influence of the formation of ladder-type assemblies on triplet state delocalisation was investigated by comparing the results obtained in the absence and presence of **DABCO**.

In summary, the experimental results lead to the following conclusions: The ladder complexes of **P3** and **P4** are stable in frozen solution as confirmed by low temperature UV-vis measurements. However, restricting the relative orientation of the adjacent porphyrin units in the porphyrin oligomers to a predominantly co-planar arrangement in the presence of **DABCO** does not have any influence on triplet state delocalisation, either along the porphyrin chain or between the two porphyrin strands.

In **DABCO** ladder complexes, the separation distance between the two porphyrin strands amounts to only 0.7 nm [128]. For a similar separation distance, uneven triplet state delocalisation was observed between two chlorophyll units forming the special pair in bacterial reaction centres [99], suggesting that electronic communication between the porphyrin strands should in principle be feasible in the excited triplet state. The reasons why delocalisation between the strands

is prevented in the present case are difficult to determine since delocalisation can be affected by factors as diverse as geometry, symmetry, local environment and temperature.

Interestingly, the increased planarity of the porphyrin π-systems within a single porphyrin strand in the **DABCO** ladder structures does also not seem to enhance triplet delocalisation although it has been shown in excitation wavelength dependent studies on a porphyrin dimer that selective excitation of a conformation where the porphyrin planes are held at right angles with respect to each other does lead to the observation of a monomer-like contribution to the ENDOR spectra and consequently to localisation of the triplet state on a single unit [129]. One could thus expect that reducing the heterogeneity of torsional angles upon ladder formation should favour delocalisation.

The results from low temperature UV-vis spectroscopy suggest that the porphyrin chains of **P3** and **P4** are significantly more planar in the presence of **DABCO**, however the UV-vis spectra were taken at lower concentrations and a temperature of 80 K instead of 20 K. Moreover, UV-vis spectroscopy might be more sensitive to the presence of conformers with different dihedral angles than EPR and the distributions of conformers might be different in the excited state, since the corresponding barrier to rotation has been shown to be higher [133], favouring the planar conformation.

The results from DFT calculations presented in reference [129] suggest that the transition between a dimeric and monomer-like behaviour in a porphyrin dimer occurs for dihedral angles between 50 and 60°, which could explain the apparent discrepancy between the UV-vis and EPR results: Delocalisation might be equally likely for a large range of dihedral angles up to 50°. If the majority of the porphyrin oligomers is already in a predominantly co-planar arrangement in the absence of **DABCO**, a further planarisation of the porphyrin strands upon ladder formation, as observed by low-temperature UV-vis spectroscopy, might not markedly influence the measured hyperfine coupling constants and therefore the delocalisation of the excited triplet state. The conclusions of this study are supported by the investigations presented in Chapter 7, where the influence of electronic symmetry on triplet state delocalisation is explored.

Chapter 7

On the Importance of Electronic Symmetry for Triplet State Delocalisation

In studies on triplet states of linear porphyrin oligomers [109, 122, 129] it has been found that triplet state delocalisation is mainly restricted to about two porphyrin units. Complete delocalisation was observed by ENDOR for a porphyrin dimer, while the corresponding results for the longer oligomers could be interpreted as arising from an uneven spin density distribution with the majority of the spin density being located on the central porphyrin unit(s) of the structures. For the trimer, a ratio of spin densities (on the individual porphyrin units) of approximately 0.20:0.60:0.20 was determined, whereas this ratio was found to be about 0.05:0.45:0.45:0.05 for the tetramer [109].

Several reasons for the apparent limitation of triplet state delocalisation to about two units in linear porphyrin oligomers could be imagined. These reasons include the possibilities that (i) the spatial extent of the triplet state is (for yet unknown reasons) limited to a certain number of units, (ii) conformational flexibility of the porphyrin chain disrupts delocalisation, or (iii) the restriction of delocalisation is related to the electronic symmetry of the system.

A fundamental limitation of the spatial extent of triplet state delocalisation seems unlikely, since complete delocalisation over six porphyrin units has been observed recently in a six-membered zinc porphyrin nanoring [109]. Further, it has been shown that a monomer-like contribution to the spectra is observed when selectively exciting conformations of a porphyrin dimer with dihedral angles of $\sim 90^\circ$ between the planes defined by the two porphyrin macrocycles [129], demonstrating that twisting of the porphyrin chain can indeed disrupt delocalisation. The results presented in the previous chapter suggest, however, that the disruptive effect is only observed for conformations with relatively large dihedral angles and that planarisation of the porphyrin π-system cannot enhance delocalisation beyond two units. This finding is in agreement with DFT calculations which indicate that the transition from a dimeric to a monomer-like behaviour occurs for conformations in which porphyrin-porphyrin torsional angles approach $50-60^\circ$ [129]. Based on these results, smaller magnitude dihedral angle distributions are not expected to negatively impact triplet state delocalisation.

The observation of complete triplet state delocalisation in a cyclic zinc porphyrin hexamer [109] is intriguing, since the only differences in this system with respect to the investigated linear porphyrin structures are (i) the bent, circular geometry of the porphyrin π-system and (ii) the chemical equivalence of all porphyrin units. The influence of bending of the porphyrin π-system

on triplet state delocalisation has been studied before by ligating the porphyrin chains to radial molecular templates [109]. In the presence of the molecular template, forcing the porphyrin chains to adopt a bent geometry, a significantly smaller zero-field splitting D value was found, but the triplet state delocalisation was unperturbed, relative to the linear analogs, as demonstrated by ENDOR.

Collectively, these findings suggest that the equivalence of all porphyrin units might be the decisive factor. To confirm this statement, the importance of electronic symmetry for triplet state delocalisation is investigated in the present chapter on a series of ethyne-linked zinc porphyrins with varying terminal ethyne moities.

In DFT calculations carried out for a porphyrin dimer with a butadiyne linker and terminal ethynyl groups on both sides, it is observed that a considerable amount of spin density is located on the triple bond linkers between the porphyrin units and the terminal triple bonds (cf. **Figure 7.1**).

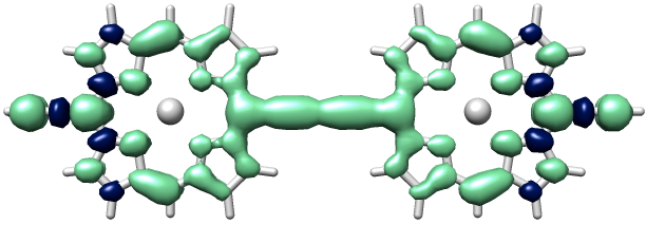


Figure 7.1: Calculated triplet state spin density of a porphyrin dimer with butadiyne linkers and terminal ethynyl groups (DFT/B3LYP, EPRII).

Considering this result, a series of three *meso*-to-*meso* ethyne-bridged zinc porphyrin dimers was examined to explore the influence of electronic symmetry on triplet state delocalisation. The molecules, synthesised in the laboratories of Prof. M. J. Therien (Duke University, USA), only differ by the presence or absence of terminal triple bonds and are referred to as **P2**, $\mathbf{P2_e}$, and $\mathbf{P2_{ee}}$, in the case of zero, one or two terminal triple bonds, respectively. Given that the spin density on those end groups is substantial, their presence or absence should significantly influence the symmetry of the electron spin distribution of the system. For reference and interpretation of the results, the monomers with one or two triple bonds, $\mathbf{P1_e}$ and $\mathbf{P1_{ee}}$, and the trimer without end groups, **P3**, are also studied.

7.1 Investigated Oligomers

The chemical structures of all investigated porphyrin oligomers are shown in **Figure 7.2**. As evident from the figure, the aryl side groups of the molecules differ in some cases, however, it was specifically verified and confirmed that the presence of different aryl side groups does not influence triplet state delocalisation.* Compared to the structures investigated in Chapter 6, the main structural difference in the oligomers studied here is the shorter linker (only one triple bond instead of two) between the porphyrin units.

*ENDOR experiments were carried out with porphyrins only differing by their aryl side groups and no marked differences were observed. In addition, this result is expected, since (almost) no spin density is observed on the aryl groups in DFT calculations.

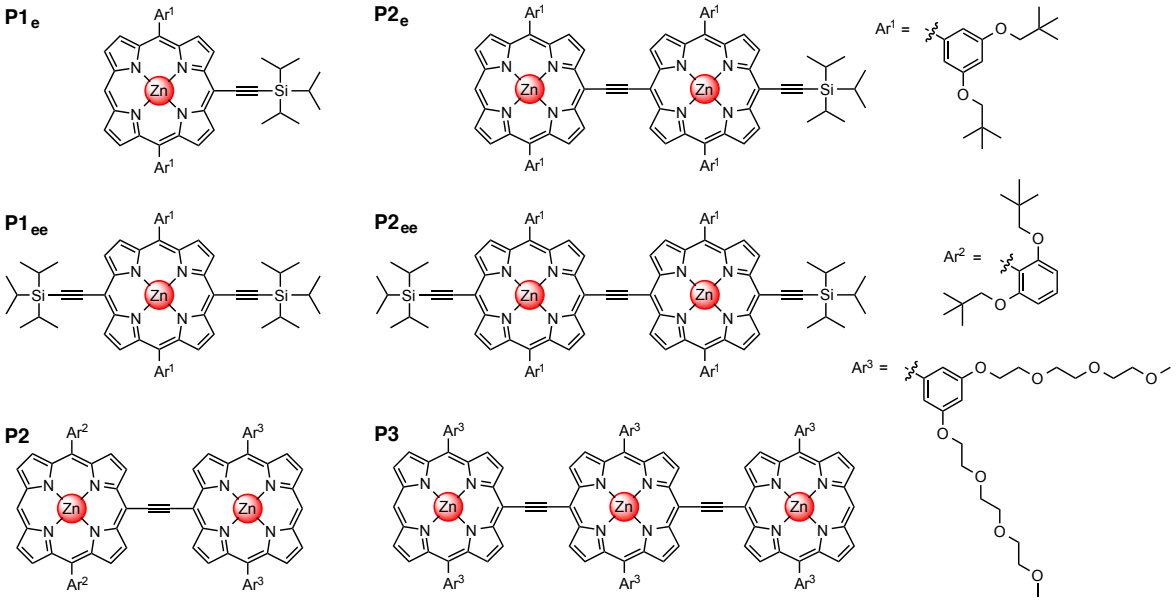


Figure 7.2: Chemical structures of the investigated zinc porphyrin oligomers.

For an initial characterisation of the compounds, UV-vis spectra were recorded in **MTHF** solution at room temperature. The data are shown in **Figure 7.3**. Upon increase of the π-conjugation length, a continuous red-shift of both the porphyrin Soret- and Q-bands is observed.

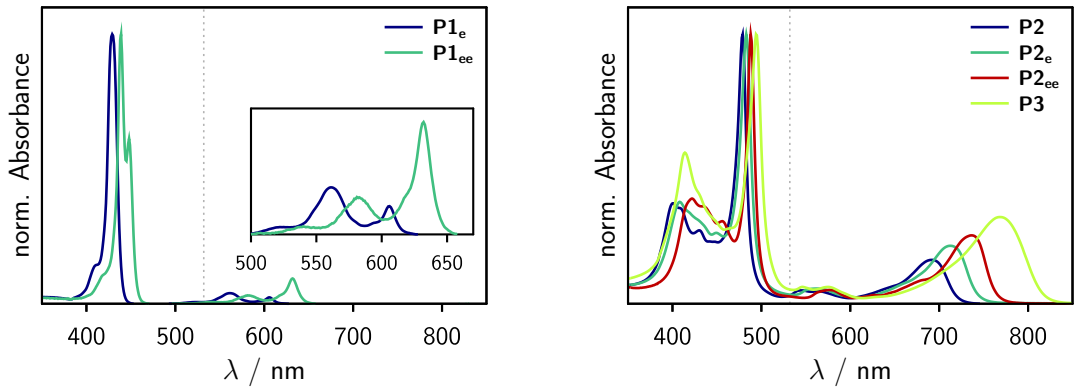


Figure 7.3: Room temperature UV-vis spectra of the available monomers (*left*) and longer oligomers (*right*) in **MTHF**. The grey dotted line indicates the excitation wavelength used in the EPR experiments.

EPR samples of the investigated compounds were prepared at a concentration of 0.2 mM in **MTHF** and the measurements were performed at 20 K. Details on the sample preparation and experimental setup are given in Appendix A (cf. **Section A.1** and **Subsection A.3.2**). As in previous work, the hyperfine coupling constants are used to judge the extent of triplet state delocalisation, since they are directly proportional to the spin density of the system.

7.2 Transient cw EPR and Simulations

To obtain the triplet state EPR parameters, in particular D and E, transient cw EPR spectroscopy was applied. For the monomer, $D > 0$ as determined by magneto-photoselection experiments [122]. In this study we chose the convention $|Z| \geq |X| \geq |Y|$, implying $E < 0$ in case of the monomers. The Y axis of the ZFS tensor corresponds to the axis along the aryl groups. For the longer oligomers $D < 0$ as confirmed by DFT, and consequently $E > 0$. The experimental spectra for all compounds are shown and compared in **Figure 7.4**. The canonical transitions for the monomers are indicated in the figure.

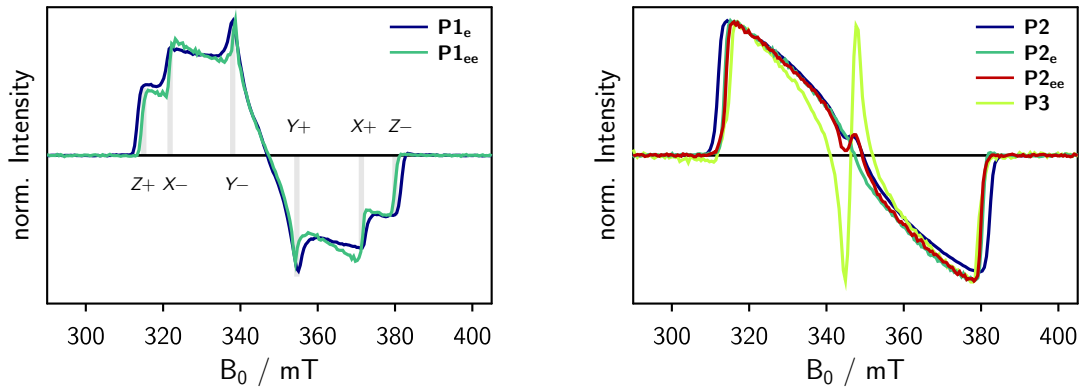


Figure 7.4: Transient cw EPR spectra of the available monomers (*left*) and longer oligomers (*right*) recorded in **MTHF** at 20 K.

No major spectral changes are observed between the triplet spectra of $\mathbf{P1_e}$ and $\mathbf{P1_{ee}}$. The spin polarisations of both spectra are very similar and the only apparent difference seems to be the slightly decreased spectral width for $\mathbf{P1_{ee}}$, suggesting slightly increased delocalisation.

When comparing the spectra of the three dimers amongst them, a similar situation is encountered. A slight decrease in the width of the triplet spectrum is observed when the conjugation length is increased from **P2** to $\mathbf{P2_e}$. However, no further significant reduction seems to occur from $\mathbf{P2_e}$ to $\mathbf{P2_{ee}}$. The spectrum of **P3** also has a comparable width, but the polarisation differs as compared to the dimer spectra.

Numerical Simulations

To quantify the spectral changes, numerical simulations of the transient cw EPR spectra were carried out using the MATLAB package EasySpin in combination with a home-written MATLAB fitting routine. In **Figure 7.5** the simulations for all investigated compounds are shown together with the experimental data. The triplet state parameters, D and E, as well as the relative populations of the triplet sublevels, are indicated in the figure.

The fact that no major change in the width of the spectrum is observed between monomers and dimers can be interpreted in terms of a change in the orientation of the ZFS tensor in combination with complete delocalisation over two porphyrin units as previously observed [122].

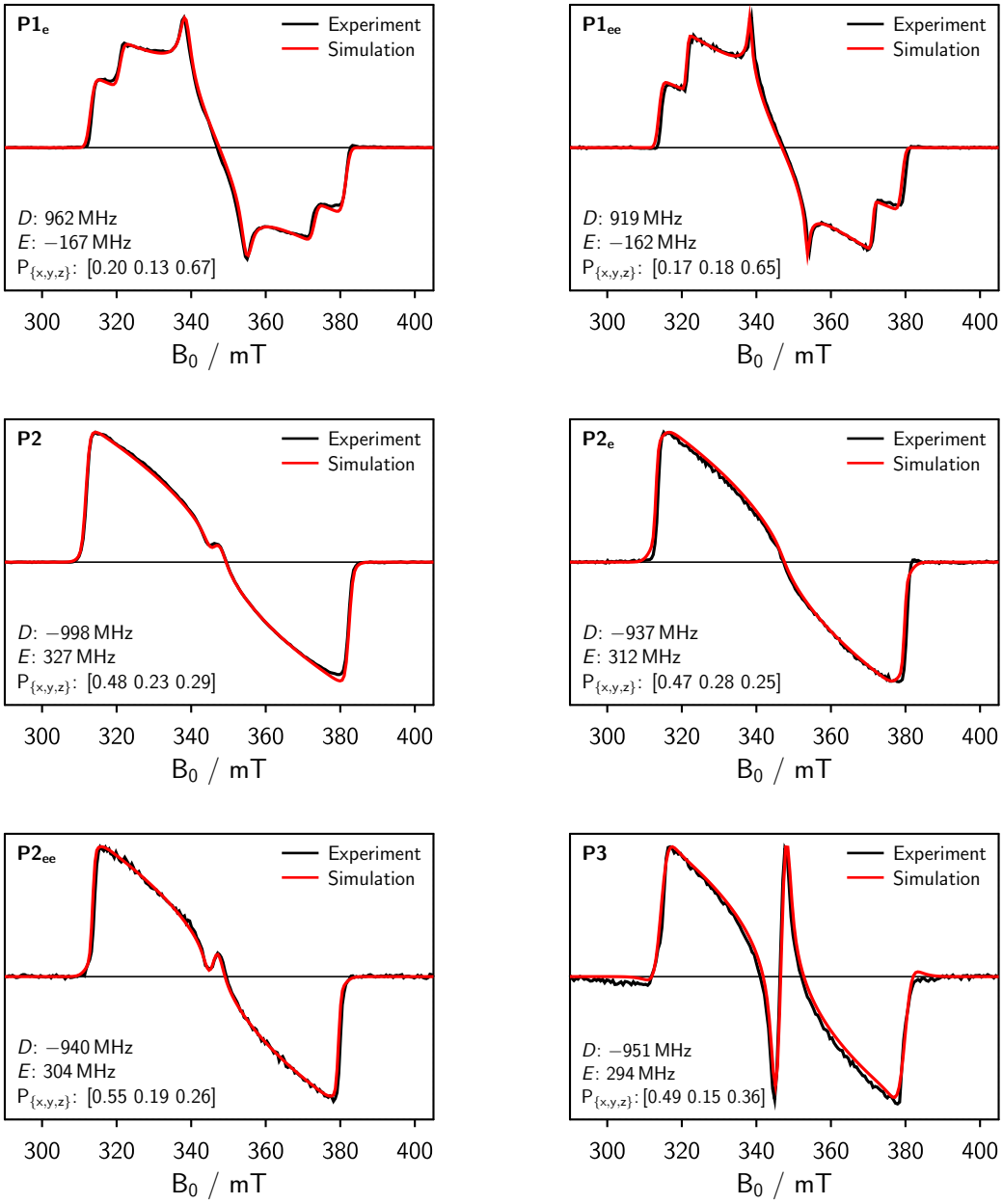


Figure 7.5: Numerical simulations of the transient cw EPR spectra of the six investigated compounds in comparison with the respective experimental data. The triplet state parameters obtained from the fit are indicated in the figure.

In the case of the two monomers **P1$_e$** and **P1$_{ee}$**, complete delocalisation of the triplet state over the porphyrin core is expected and the spin density distribution should be oblate in both cases. As a consequence, the D value, related to the width of the spectrum, is expected to decrease when increasing the conjugation length on going from **P1$_e$** to **P1$_{ee}$**. Indeed, it is observed that the D value is decreased from roughly 960 MHz to 920 MHz.

Also when comparing the two symmetric dimers, **P2** and **P2$_{ee}$**, a decrease in D is observed from roughly -1000 to -940 MHz. For the purpose of simulating the spectra, D was assumed to be negative, implying a prolate spin distribution. Further, the convention $|D| > 3|E|$ was adopted.

As a result of the simulations it is however found that $|D| \simeq 3|E|$ for all three dimers, suggesting that no preferred axis can clearly be identified and that the spin distribution in these systems cannot be classified as being truly prolate. It is likely that the reorientation of the ZFS tensor is not complete in these molecules (i.e. that the spin distribution is neither oblate nor entirely prolate) and consequently an interpretation of the delocalisation length based only on D might lead to invalid conclusions. If the ZFS tensor orientation is different in the different dimers, this incomplete reorientation of the ZFS tensor would need to be considered in the analysis. Knowledge on the actual ZFS tensor orientations for every dimer molecule is however difficult to obtain. Based on these considerations, the use of ENDOR should be preferred to reliably probe and compare the spin density distribution in the investigated structures.

7.3 Mims ENDOR & DFT

The ^{1}H ENDOR spectra for all compounds, recorded at magnetic field positions corresponding to the $Y-$ orientations, where the largest couplings are generally observed, are superimposed in **Figure 7.6**. To verify and confirm the following conclusions on triplet state delocalisation based on the magnitude of the largest hyperfine coupling in the $Y-$ direction, ENDOR measurements have also been performed at different field positions corresponding to the X and Z orientations for the monomers and dimers and are shown in Appendix F (**Section F.2**).

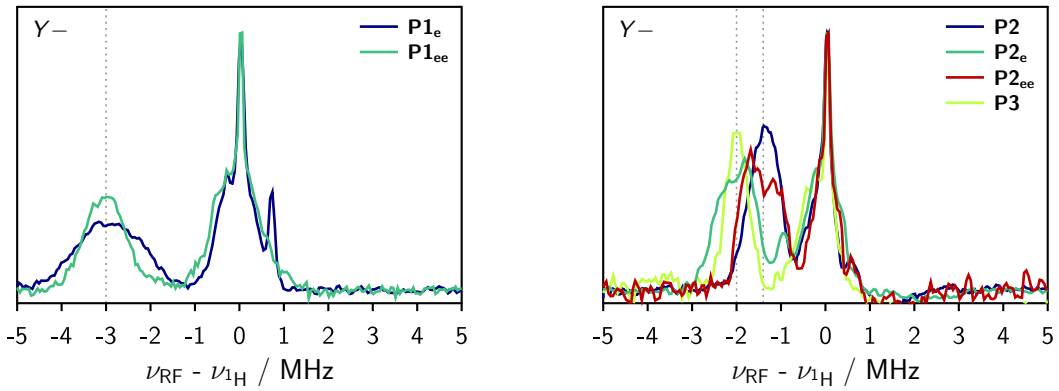


Figure 7.6: Proton Mims ENDOR spectra of the available monomers (*left*) and longer oligomers (*right*) recorded at magnetic field positions corresponding to the $Y-$ orientation in **MTHF** at 20 K.

No major changes in the hyperfine coupling constants are noted between the two monomers, $\mathbf{P1_e}$ and $\mathbf{P1_{ee}}$. The magnitudes seem to be roughly the same, although the main peak at -3 MHz appears to be wider in $\mathbf{P1_e}$, possibly indicating a larger heterogeneity of the individual couplings due to the symmetry distortion. Due to the presence of a terminal *meso*-proton on the porphyrin core, an additional proton peak should be observable in the ENDOR spectra of $\mathbf{P1_e}$ (cf. **Figure 7.2**). However, DFT predicts this coupling at the position of the missing end group to be much larger than 10 MHz. The peak is therefore expected to be outside the detection window of ± 5 MHz for $\mathbf{P1_e}$ (as well as for the asymmetric dimers).

Compared to that of the monomers, the prominent coupling in Y direction is approximately halved in **P2**, indicating complete triplet state delocalisation. A similar value of about −1.4 MHz is measured in the symmetric dimer with two terminal triple bonds, $\mathbf{P2_{ee}}$,[†] whereas larger couplings (but still smaller compared to $\mathbf{P1_{ee}}$) are present in the spectra of the asymmetric dimer, $\mathbf{P2_e}$, and the trimer **P3**.

This experiment clearly demonstrates that delocalisation is not governed only by the length of the porphyrin π-system. When increasing the length of the π-system from **P2** to $\mathbf{P2_e}$, the effective delocalisation length decreases, as judged by an increase in the magnitude of the largest hyperfine coupling. However, upon further increase of the conjugation length from $\mathbf{P2_e}$ to $\mathbf{P2_{ee}}$, complete delocalisation seems to be feasible again.

The increase in the magnitude of the largest hyperfine coupling constant from **P2** to $\mathbf{P2_e}$ can thus be interpreted as arising from an uneven spin density distribution in $\mathbf{P2_e}$ due to the broken electronic symmetry, i.e. the inequivalence of the porphyrin units. When the electronic symmetry is restored in $\mathbf{P2_{ee}}$, complete delocalisation is again observed.

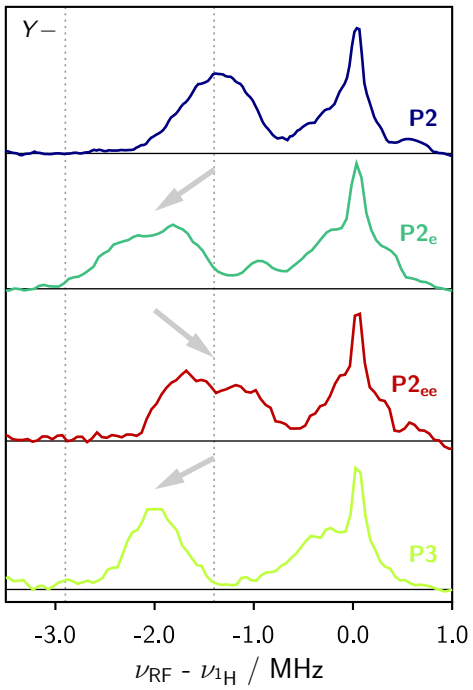


Figure 7.7: Comparison of the ^{1}H Mims ENDOR spectra of **P2**, $\mathbf{P2_e}$, $\mathbf{P2_{ee}}$ and **P3** recorded at the $Y-$ orientation in **MTHF** at 20 K. The dotted lines indicate the magnitude of the coupling for $\mathbf{P1_e}$ and half of this value.

When a third porphyrin unit is added to the system, the 'inner' and 'outer' porphyrin units are automatically inequivalent. Therefore uneven delocalisation is expected, implying an increase in the largest hyperfine coupling constant with respect to the symmetric dimers. This should in general apply to any linear system with more than two units, since the inequivalence of the 'inner'

[†]Although only one major coupling is expected in the $Y-$ ENDOR spectrum of $\mathbf{P2_{ee}}$, the corresponding peak at −1.4 MHz is found to have two local maxima. The two observed couplings likely reflect a greater degree of nuclear magnetic heterogeneity of its four sets of chemically inequivalent β-protons in $\mathbf{P2_{ee}}$ relative to **P2**.

and 'outer' units persists. The observed trends in the magnitude of the largest hyperfine coupling along the *Y* direction in the series **P2**, **P2$_e$**, **P2$_{ee}$**, **P3** are more clearly illustrated in **Figure 7.7**.

DFT Calculations

To support this tentative explanation, density functional theory calculations of the molecular geometry, hyperfine coupling constants and triplet spin density distributions were carried out. Additionally, the orientations of the hyperfine coupling and zero-field splitting tensors in the molecular frame are obtained. The aryl side groups were replaced by phenyl groups and any triisopropylsilyl (**TIPS**) protecting groups, if present in the structures, were replaced by a proton to simplify the calculations. Further details on the calculations are given in Appendix A (**Section A.5**).

A geometry optimisation of the porphyrin structures linked by a single triple bond reveals, that the porphyrin planes are tilted with respect to each other in the energetic minimum structure. The dihedral angle between the porphyrin planes amounts to roughly 30° as can be seen in **Figure 7.8**, taking **P2$_{ee}$** as an example. This twist of the chain is not predicted to disrupt delocalisation as can be concluded when looking at a visualisation of the calculated hyperfine coupling tensors for **P2$_{ee}$** also shown in the figure. For **P3**, similar torsional angles are found.

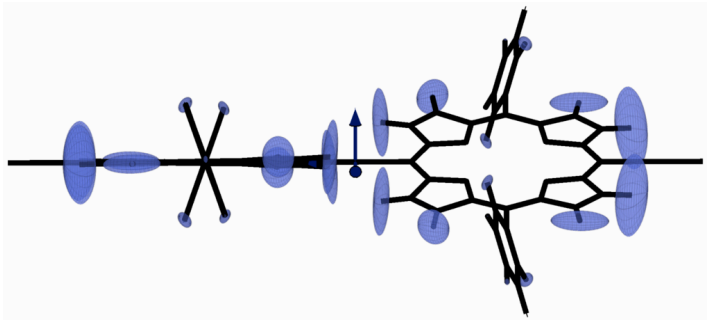


Figure 7.8: Visualisation of the calculated ^{1}H hyperfine coupling tensors of **P2$_{ee}$**. The side view illustrates the relative orientation of the porphyrin planes at the minimum geometry. The dihedral angle between the two macrocycles amounts to ∼30°.

Figure 7.9 illustrates the calculated proton hyperfine coupling tensors, triplet spin densities, and ZFS tensor orientations in the molecular frames of all six investigated compounds. The ZFS tensor orientations obtained from DFT are indicated by blue arrows in the centre of the structures. The axis orientations shown in black represent limiting cases for an entirely oblate and prolate system, respectively. Since complete delocalisation is observed experimentally for the symmetric dimers, a reorientation of the ZFS tensor (i.e. a transition from an oblate to a prolate spin density distribution) can be assumed. However, differences in the shape of the spin density distribution between the three dimers are nevertheless possible, as discussed above, so that the orientation of the ZFS tensor might not be well-defined. Since the reorientation only affects the *X* and *Z* axes, a comparison of the changes in the magnitude of the hyperfine coupling constants corresponding to the *Y* orientation is expected to be valid in all cases. In **Figure 7.9** the large couplings of the terminal *meso*-protons, present in **P1$_e$**, **P2** and **P2$_e$**, were omitted for clarity. Plots of the hyperfine coupling tensors including all protons are shown in Appendix F (**Section F.2**) for reference.

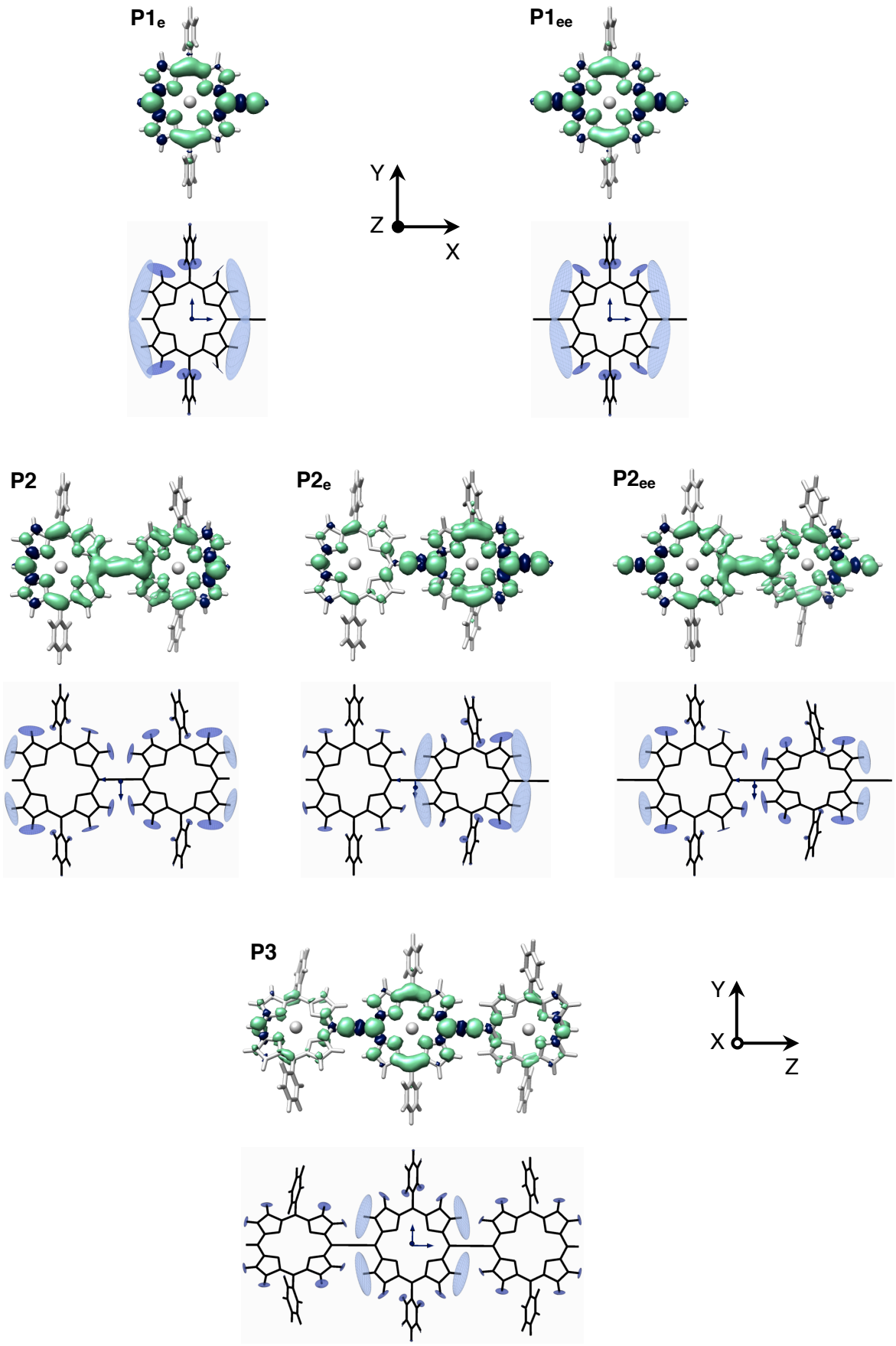


Figure 7.9: Visualisation of the calculated triplet spin densities and proton hyperfine coupling tensors for the investigated structures. The hyperfine coupling tensors corresponding to the terminal *meso*-protons are omitted in the figure for clarity. In the experiment, the magnitude of the projection of the hyperfine coupling tensors highlighted in light blue onto the *Y* axis is probed.

The hyperfine coupling constants measured in the experiment should compare to the values obtained from a projection of the calculated hyperfine tensors onto the *Y* axis of the zero-field splitting tensor. The tensors corresponding to the largest coupling in *Y* direction, compared between the different oligomers to determine the extent of delocalisation, are highlighted in the figure in light blue and the corresponding values for the *Y* orientation can be found in the appendix (**Table F.1**).

The results from DFT calculations predict an uneven spin density distribution for **P2$_e$** and **P3**, in perfect agreement with the interpretation of the experimental results presented above. The magnitudes of the calculated hyperfine coupling constants are overestimated (cf. Appendix F, **Table F.1**), but the relative changes coincide well with the experimentally observed trends. As previously observed for porphyrins with butadiyne linkers [109], the spin density is found to localise mainly on the central porphyrin unit in **P3**. In **P2$_e$**, the largest spin density is found on the porphyrin unit with the additional ethynyl end group.

7.4 Conclusions

In this study, the influence of electronic symmetry on triplet state delocalisation was explored. Both experimentally and theoretically the triplet state is found to be unevenly delocalised in **P2$_e$** but evenly delocalised in **P2$_{ee}$**, where the π-conjugation length is further increased as compared to **P2$_e$**. This result seems to indicate that the observed limitation of the extent of triplet state delocalisation to about two porphyrin units in linear porphyrin oligomers is not fundamental in nature, i.e. the triplet state is not automatically localised over only a small part of the molecule as often assumed. The extent of triplet state delocalisation rather seems to be related to the chemical equivalence of the individual monomeric units.

In the symmetric molecules, **P2** and **P2$_{ee}$**, both porphyrin units have the same neighbours, whereas in **P2$_e$** the electronic symmetry is broken and the two units are no longer equivalent, leading to an uneven spin density distribution. The results of this study suggest that complete delocalisation can only be observed over up to two porphyrin units in linear oligomers since, starting from the trimer, the 'inner' and 'outer' porphyrin units of the chain will always be in-equivalent, resulting in an uneven spin density distribution as observed before and confirmed in this study for the case of a zinc porphyrin trimer, **P3**. The findings are also in agreement with the observation of complete delocalisation in a cyclic porphyrin hexamer [109], where all units are chemically equivalent.

For the first time, we were able to experimentally demonstrate the importance of the chemical equivalence of the individual monomeric units for triplet state delocalisation in oligomeric porphyrin assemblies, which confirms the tentative conclusions of an earlier study. Based on the results presented here, it is speculated that electronic symmetry is of greater importance for triplet state delocalisation than other frequently invoked factors such as conformational rigidity or fundamental length-scale limitations.

Chapter 8

Probing the Alignment of Porphyrins in Liquid Crystals

In this study, liquid crystals (LCs) were employed as solvents for EPR investigations on porphyrin triplet states. Since the shape of the triplet EPR spectrum is very sensitive to changes in the orientational distribution of the molecules, the alignment of the porphyrin oligomers can be characterised. The influence of the oligomer chain length and of structural differences in the porphyrin side groups on the alignment of the molecules will be explored in this chapter.

Liquid crystals are viscous, fluid substances exhibiting anisotropic optical, electric and magnetic properties, similar to crystals. Many liquid crystals are thermotropic, meaning that the liquid crystal phase changes as a function of temperature, although also lyotropic and barotropic liquid crystals are known, where the liquid crystal phase is a function of concentration or pressure, respectively. Based on their molecular structures, thermotropic liquid crystals can be divided into two groups: calamitic ('rod-like') and discotic ('disk-like') liquid crystals. In the case of calamitic liquid crystals, used in this investigation, three different liquid crystal phases are generally distinguished [136].

- Compounds forming a **nematic phase** are often elongated, planar molecules like 4-cyano-4'-pentylbiphenyl (**5CB**). Nematic mesophases are characterised by long-range orientational order, meaning that the 'long' axis of the molecule aligns along a preferred direction. Even if the two 'ends' of the liquid crystal molecules are not chemically equivalent, it has been found that nematic liquid crystals behave optically as a uniaxial material with a centre of symmetry [136].

- The ensemble of molecules forming a **cholesteric phase** is always optically active. The cholesteric phase is similar to the nematic phase only that the direction of the director varies continuously with a periodicity of hundreds of nanometers along one axis of the medium, resulting in a twisted arrangement. In any plane perpendicular to the twist axis, the long axes of the molecules tend to align along a single preferred direction within that plane, but comparing successive planes, the preferred direction rotates by a fixed angle. The distance measured along the twist axis corresponding to a 360° rotation of the liquid crystal director direction is called the pitch of a cholesteric.

- In the **smectic phase**, the molecules are arranged with a high degree of positional order along the axes perpendicular to the director. For more details, the interested reader is referred to the pertinent literature in the field [136, 137].

Apart from the above-mentioned ones, crystalline and isotropic phases can normally be reached upon cooling or heating of a liquid crystal sample, respectively. In the present study we shall only be concerned with thermotropic nematic liquid crystals. Although also some other representatives of this class of liquid crystals have been employed, the majority of measurements was carried out in the liquid crystal solvent **5CB**.

5CB molecules, as shown in **Figure 8.1**, have a rigid rod-like polarisable core and a flexible aliphatic end group. **5CB** has phase transitions from the crystalline phase to the nematic phase at roughly 22°C and from the nematic to the isotropic phase at about 35°C.

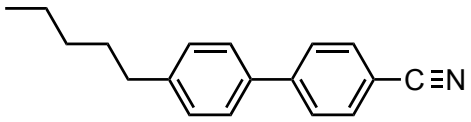


Figure 8.1: Chemical structure of the liquid crystal **5CB**.

The axis characterising the (locally) preferred average alignment is called the liquid crystal director, $\vec{n}$. It is, in principle, a vector quantity, although the direction of the vector has no physical meaning. In agreement with its optical properties, **5CB** (and other nematic liquid crystals) can be treated as having a centre of symmetry and consequently the average of the vector $\vec{n}$ vanishes. To describe liquid crystal order, higher order quantities thus have to be used. For this purpose, a symmetric and traceless second-rank tensor Q is defined from which the so-called order parameters are obtained. For a uniaxial, rod-like system only one order parameter, normally denoted by the letter S, exists. In the isotropic liquid crystal phase, $S = 0$, whereas in the nematic phase S can adopt any value between the two limits of -0.5, for a perfectly aligned oblate system, and 1, for a perfectly aligned prolate system. The order parameter S is strongly temperature dependent. For **5CB**, it is known to be around 0.6 at room temperature [138]. Liquid crystal order will be discussed in detail in the next section.

In the nematic phase, liquid crystal solvents like **5CB** are characterised by an anisotropic electric and magnetic susceptibility, implying also an orientation dependent refractive index and dielectric constant. Depending on the difference between the dielectric properties with respect to the ordinary and extraordinary axes of the liquid crystal, $\Delta\varepsilon = \varepsilon_{||} - \varepsilon_{\perp}$, liquid crystals with negative and positive dielectric anisotropy are distinguished. If $\Delta\varepsilon > 0$, the liquid crystal aligns parallel to an externally applied electric field, whereas if $\Delta\varepsilon < 0$, a perpendicular alignment is obtained. Analogous considerations can be applied with respect to the magnetic properties. Also the electric and magnetic susceptibilities change markedly as a function of temperature, where a lower temperature typically implies more pronounced anisotropic properties.

8.1 Liquid Crystal Order

As mentioned before, nematic liquid crystals can be considered as rods with cylindrical symmetry. Each of the liquid crystal molecules has a unit vector pointing along its long axis, the so-called molecular director. The direction of the liquid crystal director, $\vec{n}$, corresponding to the (local) average alignment of all molecules, shall for now be taken to be the z axis of the laboratory frame. The orientation of the individual molecular directors can then be described by the polar angles θ and φ and a distribution function $f(\theta, \varphi)\,\mathrm{d}\Omega$ can be defined which yields the probability of finding liquid crystal molecules aligned within a small solid angle $\mathrm{d}\Omega = \sin\theta\,\mathrm{d}\theta\,\mathrm{d}\varphi$ around the position (θ,φ) [137].

If the system is truly uniaxial (i.e. there is cylindrical symmetry about $\vec{n}$), the distribution function $f(\theta, \varphi)$ should be independent of φ, furthermore: $f(\theta) = f(\pi - \theta)$. The definition of θ and φ is graphically illustrated in **Figure 8.2**.

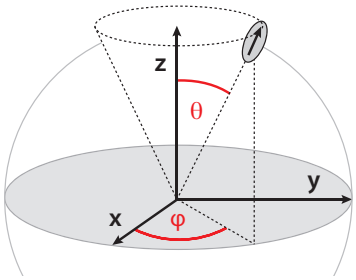


Figure 8.2: Definition of the angles θ and φ.

Since nematic liquid crystals have no average dipole, it is appropriate to define a second-rank tensor quantity, Q, to characterise molecular order. In a uniaxial system, this ordering tensor can be written as follows [136]

$$Q = \begin{pmatrix} -\frac{1}{3}S & 0 & 0 \\ 0 & -\frac{1}{3}S & 0 \\ 0 & 0 & \frac{2}{3}S \end{pmatrix} \tag{8.1}$$

where S is the only surviving order parameter. The ordering matrix Q is symmetric, real and traceless. In theory, S can adopt any values from -0.5 to 1, although experimentally no examples for negative order parameters, corresponding to a perpendicular alignment of the molecules (i.e. distribution of the molecules centred about $\theta = \pi/2$), have been found so far for rod-like uniaxial liquid crystals. If only the liquid crystal molecules are considered, the system can thus be assumed to be uniaxial.

A different situation arises when molecules are dissolved in liquid crystals. Four general cases can then be distinguished, characterised by up to four order parameters:

1. The molecules and the liquid crystal phase are both uniaxial $\rightarrow S$
2. The molecules are uniaxial whereas the phase is biaxial $\rightarrow S$, P
3. The molecules are biaxial whereas the phase is uniaxial $\rightarrow S$, U
4. Both, the molecules and the phase are biaxial $\rightarrow S$, P, U, F

In the first case, as mentioned above, one order parameter S is sufficient to describe the order of the system. If either the phase or the molecules are biaxial, a second order parameter needs to be introduced, which is normally referred to as P or U, in the cases of phase or molecular biaxiality, respectively. Since no example for phase biaxiality is known in the context of nematic rod-like liquid crystals, we shall not be concerned here with cases 2 and 4. The interested reader is referred to reference [139] for more details.

In a biaxial system, the ordering tensor Q becomes [139]

$$Q = \begin{pmatrix} -\frac{1}{2}(S-U) & 0 & 0 \\ 0 & -\frac{1}{2}(S+U) & 0 \\ 0 & 0 & S \end{pmatrix} \tag{8.2}$$

where the second order parameter, the biaxiality parameter U, ranges from $-(1-S)$ to $(1-S)$. The ordering parameter S can be obtained by averaging over all molecules

$$S = \frac{1}{2}\left\langle 3\cos^2\theta - 1 \right\rangle \tag{8.3}$$

where θ is defined as the angle between the molecular director and the z axis and the angled brackets indicate the ensemble average. From the above equation, the limits of S and the implications on the alignment can easily be deduced: If all molecules are aligned along the z axis, $\theta = 0$ therefore $\cos^2\theta = 1$ and consequently $S = 1$. On the other hand, if all molecules are aligned in the plane perpendicular to the director (but randomly oriented within that plane), $\theta = \frac{\pi}{2}$, thus $\cos^2\theta = 0$ and averaging yields $S = -0.5$.

According to [140], the ordering tensor for a biaxial system can be rewritten as

$$Q = \begin{pmatrix} \frac{1}{2}\left\langle 3\sin^2\theta\cos^2\varphi - 1 \right\rangle & 0 & 0 \\ 0 & \frac{1}{2}\left\langle 3\sin^2\theta\sin^2\varphi - 1 \right\rangle & 0 \\ 0 & 0 & \frac{1}{2}\left\langle 3\cos^2\theta - 1 \right\rangle \end{pmatrix} \tag{8.4}$$

which makes it possible to calculate not only S but also the biaxiality parameter U from an orientational distribution of the molecular directors.

Experimentally, the order parameter S for a uniaxial system is obtained from an angular distribution, $f(\theta)$, of the molecular directors by multiplication with $(3\cos^2\theta - 1)$ and integration over all angles, followed by normalisation [141, 142]

$$S = \frac{1}{2}\left\langle 3\cos^2\theta - 1 \right\rangle = \frac{\frac{1}{2}\int_0^{\pi/2} f(\theta)\,(3\cos^2\theta - 1)\,\mathrm{d}\theta}{\int_0^{\pi/2} f(\theta)\,\mathrm{d}\theta} \tag{8.5}$$

The angular distribution function is assumed to be normally distributed. The Gaussian function used in this study is parametrised as follows:

$$f(\theta) = \exp\left(-\frac{(\theta-\theta_c)^2}{2\,\sigma_\theta^2}\right)\cdot\sin\theta \tag{8.6}$$

where θ_c and σ_θ stand for the centre and the width* of the distribution, respectively, and the multiplication by $\sin\theta$ accounts for spherical averaging. The dependence of S on the width of the distribution σ_θ is illustrated in **Figure 8.3** for a Gaussian distribution centred at $\theta_c = 0°$ and $\theta_c = 90°$, respectively.

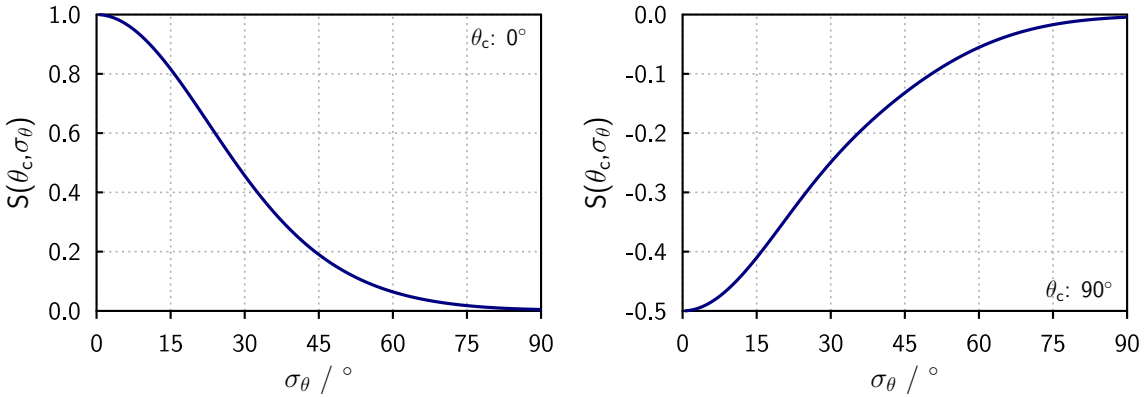


Figure 8.3: Dependence of the order parameter S on the width of the distribution σ_θ for a distribution centred at $\theta_c = 0°$ (*left*) and $\theta_c = 90°$ (*right*).

If a biaxial system is considered, the angular distribution function becomes dependent on θ and φ and a two-dimensional Gaussian function is employed to characterise the distribution of angles as follows

$$f(\theta,\varphi) = \exp\left(-\left(\frac{(\theta-\theta_c)^2}{2\,\sigma_\theta^2}+\frac{(\varphi-\varphi_c)^2}{2\,\sigma_\varphi^2}\right)\right)\cdot\sin(\theta) \tag{8.7}$$

where θ still refers to the polar angle and φ is the azimuthal angle corresponding to the angle between the projection of the director onto the xy plane and the positive x axis. φ_c and σ_φ denote the centre and the width of the distribution with respect to φ.

If the order parameter S is known, the biaxiality parameter U can be calculated from the distribution in both angles using **Equation (8.4)** and is given by

$$U - S = \left\langle 3\sin^2\theta\cos^2\varphi - 1\right\rangle = \frac{\int_0^{\pi/2}\int_0^{\pi} f(\theta,\varphi)\,(3\sin^2\theta\cos^2\varphi - 1)\,\mathrm{d}\varphi\mathrm{d}\theta}{\int_0^{\pi/2}\int_0^{\pi} f(\theta,\varphi)\,\mathrm{d}\varphi\mathrm{d}\theta}. \tag{8.8}$$

*In some cases the width of the distribution is also characterised by the full width at half maximum (FWHM). The following relation holds: $\mathrm{FWHM} = 2\,\sigma\sqrt{2\,\ln 2}$.

8.2 Alignment of Liquid Crystal Samples

Different porphyrin molecules were dissolved in liquid crystals. It is assumed that the liquid crystal imposes its alignment onto the porphyrin molecules, so that the alignment of the molecules is entirely determined by the liquid crystal director alignment.

The molecules investigated in this study are shown in **Figure 8.4** and have been synthesised in the laboratories of Prof. H. L. Anderson (University of Oxford, UK). The results obtained with **P1** and **P2** molecules with either **tBu** or **THS** side groups are compared to verify the influence of different side groups on the alignment of the porphyrin molecules in **5CB**. For a characterisation of the alignment, it is assumed that the distribution of molecules about the phase director is normal with a variance of σ^2.

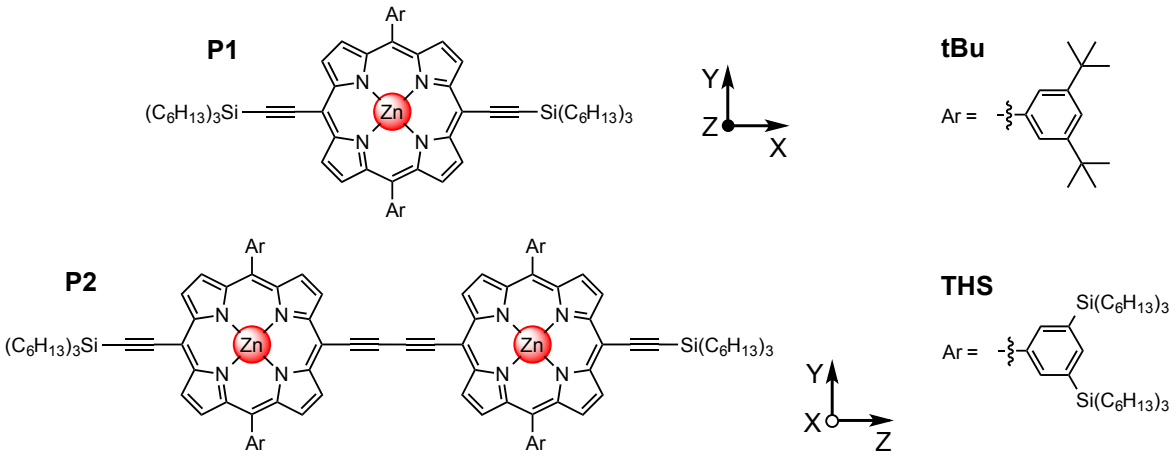


Figure 8.4: Chemical structures of **P1** and **P2** together with the structures of the two different side groups (**tBu**, **THS**) employed in this study. The orientation of the zero-field splitting tensor axes with respect to the molecular frame is indicated.

There are a number of different ways to align liquid crystal samples experimentally. The preferred procedure depends on the type of experiment that the liquid crystals are employed for. Different procedures and different sample geometries have to be chosen, for instance, if the sample needs to be optically transparent. In principle, the liquid crystal director can be aligned by electric and magnetic fields as well as by properly prepared surfaces which impose a certain pre-alignment onto the liquid crystal molecules. The latter approach only works for flat cells with very short path lengths of roughly 300 μm or smaller [143].

For EPR measurements, complete optical transparency, although advantageous for photoexcitation, is not required. For alignment, the liquid crystal samples inside the EPR tubes were warmed up to the isotropic liquid crystal phase while a field of 14 kG was applied using the X-band EPR magnet, and subsequently left to cool down to room temperature in the magnetic field.[†] The orientation of the liquid crystal director with respect to the external magnetic field, B_0, can be predicted from the sign of the diamagnetic susceptibility $\Delta\chi = \chi_{||} - \chi_{\perp}$. In **5CB**, $\Delta\chi > 0$ and thus the long axis of the molecule aligns parallel to the external magnetic field, $\vec{n} \,||\, B_0$. After alignment of the liquid crystal in the EPR tube, the sample was immediately immersed in liquid nitrogen

[†]This procedure was typically repeated at least three times.

(while still in the magnetic field) to preserve the orientational order and then directly inserted into the EPR resonator. All measurements were carried out at 90 K and porphyrin concentrations between 0.1 and 0.2 mM were used.

EPR spectra were taken at three different orientations of the liquid crystal director with respect to the external magnetic field, B_0. These orientations are schematically depicted in **Figure 8.5**. If the sample tube is inserted into the resonator in the same orientation as was adopted during the alignment, spectra at parallel alignment are obtained. For the spectra at perpendicular alignment, the sample tube is rotated by 90° about its long axis, whereas the spectra at axial alignment were recorded with a separate sample. The LC sample for axial alignment was prepared in a thinner tube, which fits into a 3.8 mm OD EPR tube, and sealed to a maximum length of 5 cm. The LC being sufficiently viscous (also in its isotropic phase), the sample could be aligned while fixed horizontally between the pole shoes of the X-band magnet and was then immediately inserted into the longer 3.8 mm OD tube and frozen to liquid nitrogen temperatures.

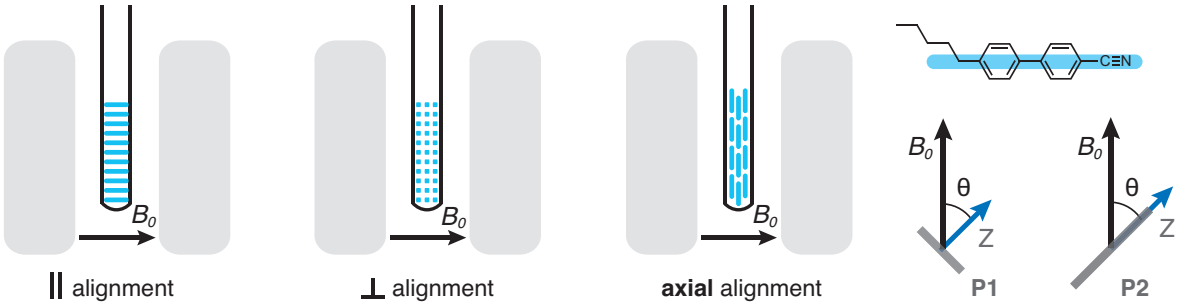


Figure 8.5: Overview of the different orientations of the liquid crystal director with respect to the external magnetic field as used in the EPR experiments.

The orientations of the ZFS tensor axes with respect to the molecular structures of **P1** and **P2** are depicted for reference in **Figure 8.4**. The Y axis of the ZFS tensor is pointing along the axis of the aryl groups in both cases, whereas the Z axis corresponds to the out-of-plane axis or the long axis of the molecule, respectively, in **P1** and **P2**.

8.3 Experimental Results

Room temperature UV-vis spectra of **P1** and **P2** with **tBu** side groups in toluene are shown in **Figure 8.6** (*left*). It can be seen that the increased conjugation length in **P2** leads to a pronounced shift of the absorption spectrum towards higher wavelengths. Additionally, the relative intensity of the porphyrin Q-bands ($S_0 \rightarrow S_1$) compared to the Soret band ($S_0 \rightarrow S_2$) is significantly increased in **P2**, indicating that the electronic $S_0 \rightarrow S_1$ transition is less forbidden in **P2**.

To explore the behaviour in liquid crystal solvents, UV-vis spectra of **P1** and **P2** with different side groups were also recorded in the isotropic phase of **5CB**. In this case, the UV-vis measurements were performed on a spectrometer equipped with a thermostatted sample holder where the temperature was held constant at 50 °C. A comparison between the room temperature spectra recorded in toluene and the elevated temperature spectra in **5CB** is also shown in **Figure 8.6** for the investigated samples.

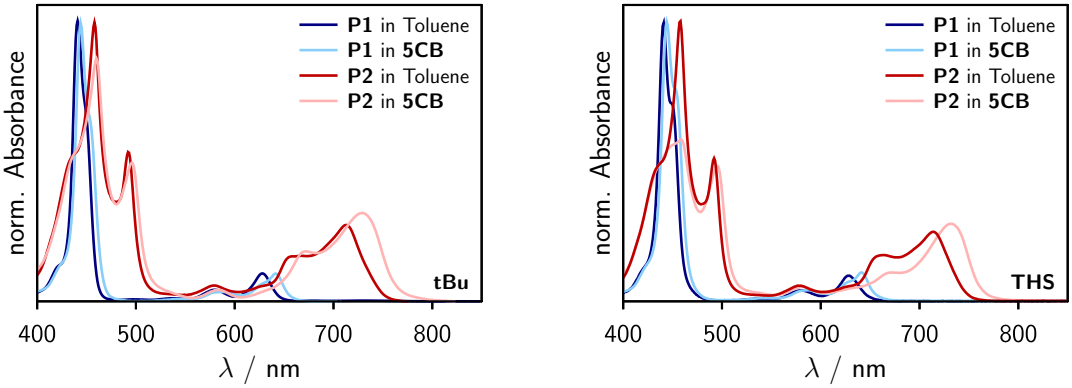


Figure 8.6: Comparison of the UV-vis spectra of **P1** and **P2** ($\sim$1 μM) recorded in toluene at room temperature with those taken in the isotropic phase of **5CB** at 50 °C for **tBu** (*left*) and **THS** (*right*) side groups.

It can be seen that all spectra are red-shifted in **5CB** as compared to toluene. While the red-shift of the porphyrin Soret-band is small, the prominent peaks in the *Q*-band region are shifted by more than 10 nm. A spectrum of **P2 THS** was also recorded in toluene at 50 °C and compared with the corresponding room temperature spectrum (comparison not shown). It was found that even in toluene an increase in temperature induces a slight red-shift by a couple of nanometers, but that this shift is negligible compared to that seen in the spectra recorded in **5CB**. Due to its apolar nature, the solvent properties of toluene are not expected to change much as a function of temperature. According to literature [144, 145] the refractive index of toluene changes from 1.497 at room temperature to 1.485 at 50 °C, whereas the static dielectric constant decreases from 2.4 to 2.3. The relevant solvent properties of **5CB** at 50 °C are considerably different ($n_D = 1.557$, $\varepsilon_r = 11.5$ [138]), which could account for the pronounced red-shift of the *Q*-band in this solvent.

When comparing the individual spectra recorded in toluene and **5CB**, one notices that, apart from the red-shift, no significant difference is observed in the spectra of **P1** and **P2** with **tBu** side groups (**Figure 8.6**, *left*). While also the spectra of **P1 THS** in toluene and **5CB** are well comparable, the spectrum of **P2 THS** in **5CB** looks considerably different from the one in toluene (**Figure 8.6**, *right*). The prominent peak of the porphyrin Soret band of **P2 THS** around 450 nm is much reduced in **5CB**. This peak was found to correspond to a 90° arrangement of the two adjacent porphyrin units in the dimer [133], thus the absence of this peak is indicative for a predominantly co-planar arrangement of the two porphyrin units of **P2 THS** in **5CB**.

Transient cw EPR

Transient cw EPR measurements at X-band were first carried out on unaligned and aligned samples of **P1** with **tBu** and **THS** side groups at 90 K. The spectra of the unaligned porphyrin triplet states were needed for data analysis and simulations as will be explained below. Furthermore, spectra of aligned samples were taken at three different sample orientations, referred to as parallel ($\parallel$), perpendicular ($\perp$) and axial alignment, as introduced in **Figure 8.5**.

In all cases, the shape of the spectra recorded at axial alignment was found to coincide very well with that of the spectra taken at perpendicular alignment, with small differences being very likely due to imperfect LC alignment. The spectra at axial alignment are therefore neither shown nor discussed in the subsequent sections.

Figure 8.7 shows the transient cw EPR spectra of **P1** with **tBu** and **THS** side groups in unaligned and aligned **5CB**. All transient EPR spectra shown below were averaged between 0.7 and 1.5 μs after the laser pulse. Pulsed laser excitation was performed at 640 nm using an OPO seeded by the third harmonic of a Nd:YAG laser with a repetition rate of 20 Hz. Unless otherwise stated, 1 mJ of depolarised laser light was used to excite the samples.

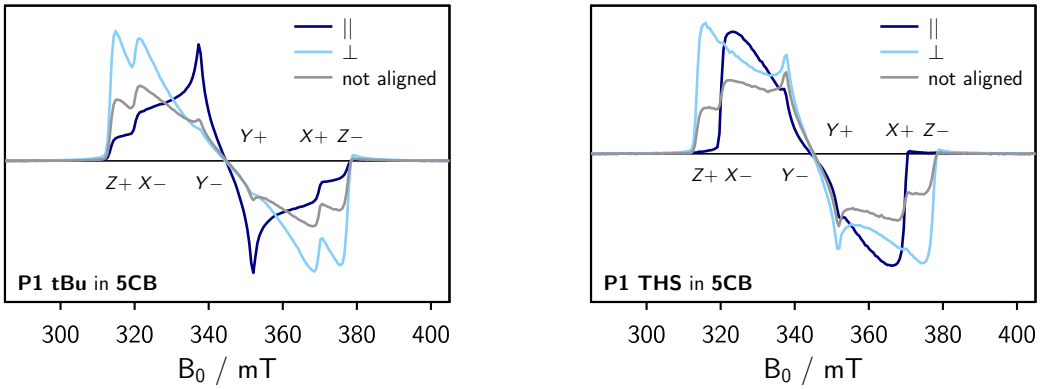


Figure 8.7: Comparison of the transient cw EPR spectra of **P1** with **tBu** (*left*) and **THS** (*right*) side groups in unaligned and aligned **5CB** at 90 K recorded after laser excitation at 640 nm (1 mJ, 20 Hz).

From the figure it can clearly be seen that the nature of the side groups seems to have a strong influence on the porphyrin alignment. While in the case of **P1 tBu** at || alignment the *Y* transition is dominant, the *X* transition prevails for **P1 THS**. Perpendicular alignment leads to a strong enhancement of the *Z* and *X* transitions in **P1 tBu**, whereas the *Z* and *Y* transitions are enhanced in **P1 THS**. These observations clearly point towards a different alignment of the porphyrin planes within the liquid crystal environment. The observations for **P1 THS** are consistent with an alignment of **P1** along the axis of the butadiyne bonds (*X* axis), whereas in the case of **P1 tBu** an alignment along the axis of the aryl groups (*Y* axis) seems to be preferred.

By visual comparison of the spectrum of **P1 tBu** in unaligned **5CB** with those taken in frozen solutions of organic solvents (cf. Chapter 6) it appears that this spectrum is not isotropic, suggesting an unexpected preferential orientation of **P1 tBu**. For **P1 THS**, no such preferential orientation is observable.

Also for **P2** with **tBu** and **THS** side groups, transient cw EPR measurements were carried out in **5CB** at 90 K. The triplet states were generated by excitation at 730 nm using an energy of around 0.8 mJ at a shot-to-shot repetition rate of 20 Hz. The spectra obtained for **P2** with different side groups are shown in **Figure 8.8**. Again, it is observed that the porphyrins with different side groups behave in a strikingly different way. If the long axis of the molecule was aligned along the liquid crystal director axis, one would expect the *Z* transition to be strongly enhanced at || alignment

and the *X* and *Y* transitions to dominate at ⊥ alignment. This scenario is observed for **P2 THS**, whereas **P2 tBu** does not seem to align in a similar way.

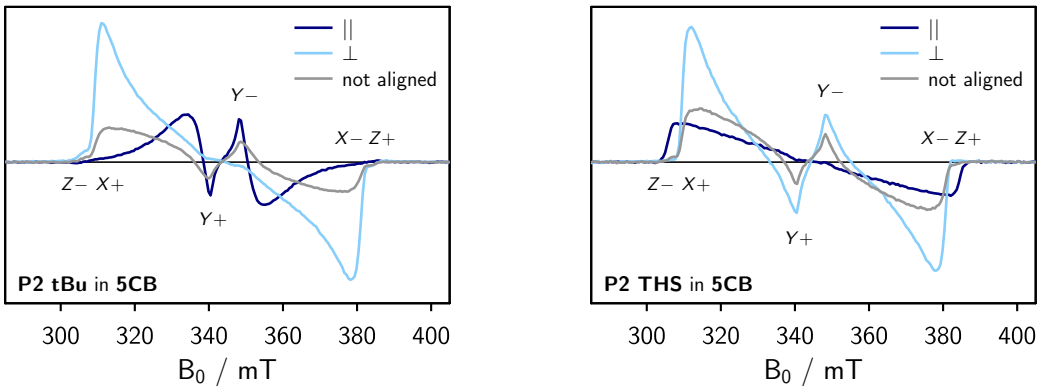


Figure 8.8: Comparison of the transient cw EPR spectra of **P2** with **tBu** (*left*) and **THS** (*right*) side groups in unaligned and aligned **5CB** at 90 K obtained after laser excitation at 730 nm (0.8 mJ, 20 Hz).

In **P2 tBu**, the *X* transition is enhanced at ⊥ alignment, whereas the *Y* transition is completely absent. In the spectra at || alignment, the *Y* transition dominates and a strong contribution of intermediate orientations, corresponding to neither one of the canonical orientations, is present. These observations for **P2 tBu** are not in agreement with an alignment along only one of the molecular axes. It thus seems that several different orientations of the porphyrin molecules with respect to the liquid crystal director (and different conformations) contribute to the spectra of **P2 tBu**.

Influence of the Excitation Wavelength

The influence of the excitation wavelength on the appearance of the aligned triplet spectra in **5CB** was tested for **P2** with different side groups to explore the contribution of porphyrins with different conformations. **Figures 8.9** and **8.10** show a comparison of the spectra taken at || and ⊥ alignment for **P2 tBu** and **P2 THS** in **5CB** recorded after excitation at different wavelengths covering the *Q*-band region of the porphyrin UV-vis spectrum. All spectra were recorded at 90 K using an excitation energy of roughly 1 mJ.

From **Figure 8.9** it can be seen that the excitation wavelength has a strong influence on the shape of the spectrum of **P2 tBu** corresponding to || LC alignment. When intensity normalised spectra are compared, the changes are most pronounced in the part of the spectrum corresponding roughly to the *X* canonical orientation. At ⊥ alignment, any spectral changes are much less prominent and occur in a similar region. The relatively big differences in spectral shape between the spectra recorded at different excitation wavelengths for || alignment are an indication for a large contribution of porphyrins with different conformations to the triplet spectrum of **P2 tBu** and therefore indicate an imperfect alignment.

Compared to **P2 tBu**, the changes in the triplet spectra observed after excitation at different wavelengths are much less significant for **P2 THS**, which is to be expected in case of a more uniform

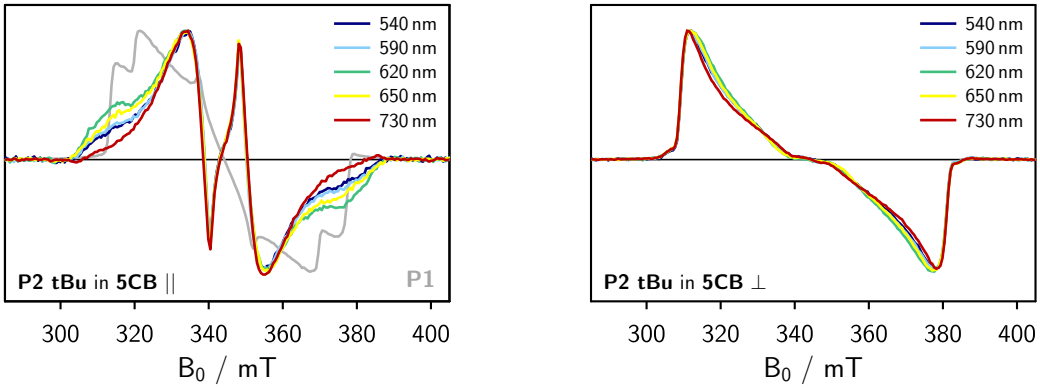


Figure 8.9: Comparison of the transient cw EPR spectra of **P2** with **tBu** side groups recorded at different excitation wavelengths (as indicated) for || (*left*) and ⊥ (*right*) alignment in **5CB** at 90 K. The excitation energy was around 1 mJ at 20 Hz.

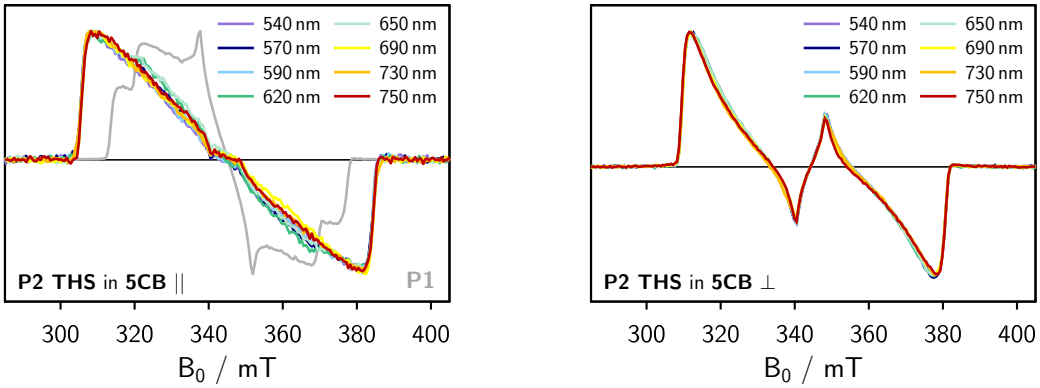


Figure 8.10: Comparison of the transient cw EPR spectra of **P2** with **THS** side groups recorded at different excitation wavelengths (as indicated) for || (*left*) and ⊥ (*right*) alignment in **5CB** at 90 K. The excitation energy was around 1 mJ at 20 Hz.

alignment. Ideally, if all molecules were perfectly aligned and only one particular conformation (i.e. dihedral angle) was contributing to the triplet spectrum, no changes in the shape of the EPR spectrum should be observed when scanning the excitation wavelength. Molecules with different conformations, however, could in principle have different EPR triplet spectra and different UV-vis spectra, so their relative contribution to the recorded triplet spectrum is expected to depend on the excitation wavelength, leading to small changes in intensity in certain parts of the EPR triplet spectrum when scanning the excitation wavelength. Since the excitation light is depolarised, any contribution of magneto-photoselection effects can be excluded.

The changes observed in the spectra corresponding to ⊥ alignment are hardly noticeable for **P2 THS**. In the case of || alignment, a shoulder in the spectrum is observed for certain excitation wavelengths, in a spectral region corresponding to neither one of the three canonical orientations of **P2**. A comparison with the triplet spectrum of **P1** reveals, however, that the onset of this shoulder is in very good agreement with the spectral position of the *X* transition of **P1**. Furthermore, the shoulder is only observed when exciting at wavelengths were **P1** absorbs and absent when exciting

at lower or higher wavelengths. It is thus speculated that these spectral changes arise from a small contribution of the twisted conformation of **P2** (i.e. a conformation where the porphyrin units are at a dihedral angle of 90°) which should have a spectrum similar to that of **P1 THS**.[‡]

8.4 Data Analysis and Simulations

The following procedure was chosen for the analysis of the recorded triplet spectra: At first, the triplet spectra in unaligned **5CB**, which were assumed to be isotropic, were simulated for every sample using the MATLAB software package EasySpin in order to determine the triplet state parameters to be used in the simulations of the spectra of the aligned samples. These parameters include the zero-field splitting parameters D and E, the g-factors, and the populations, P_X, P_Y, and P_Z, of the individual triplet sublevels. Once determined for each molecule in **5CB**, the parameters were fixed in all further simulations of the corresponding aligned spectra.

The results of the simulations in unaligned **5CB** for **P1** with **tBu** and **THS** side groups are shown in **Figure 8.11**. The simulation parameters are indicated. Already from a visual comparison of the spectra for **P1 tBu** and **P1 THS** one can conclude that the populations of the individual triplet sublevels must be considerably different in the two cases.

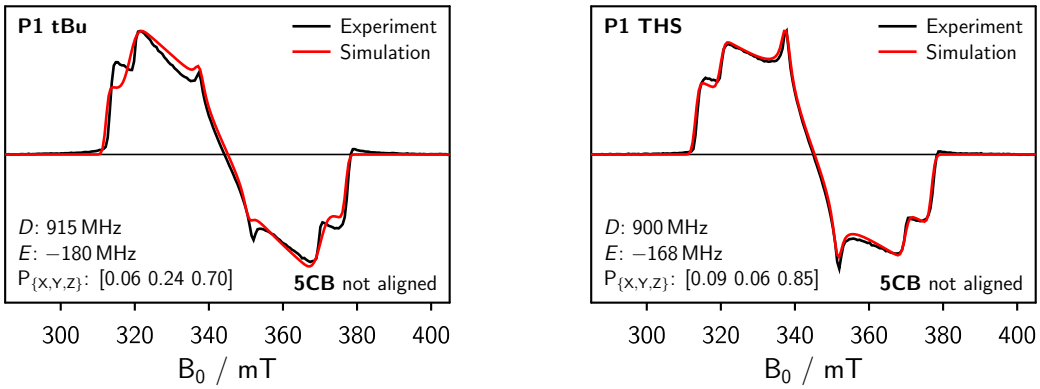


Figure 8.11: Experimental triplet cw EPR spectrum in unaligned **5CB** together with the best fit assuming isotropic alignment for **P1** with **tBu** (*left*) and **THS** (*right*) side groups. The simulation parameters are indicated in the figure and $g = 2.02$.

The spectrum of the unaligned sample of **P1 THS** looks very similar to a typical triplet spectrum of **P1** in frozen toluene, as was shown in Chapter 6, and can be simulated with almost the same parameters. In addition, the fit is acceptable, leaving little doubt that the unaligned liquid crystal sample is indeed isotropic for **P1 THS**. However, the situation is different for **P1 tBu**. As already mentioned, the spectrum looks quite different compared to spectra of **P1** in frozen solution and also the fit assuming an isotropic orientation is quite poor, which could be indicative

[‡]This hypothesis could in principle be verified by measuring triplet state Mims ENDOR at different excitation wavelengths on a sample of **P2 THS** || at a field position corresponding to the spectral position of the X transition of **P1**. A comparison between such excitation wavelength dependent ENDOR spectra recorded with an aligned sample and the corresponding spectrum of unaligned **P2 THS** in **5CB** recorded under the same conditions could be very instructive in view of confirming or rejecting the hypothesis. However, such a monomer-like contribution, if present, would probably be too small to be confirmed due to the limited signal-to-noise.

for preferential alignment. Nevertheless, the parameters obtained from the fit were used in the following simulations of the aligned spectra. We shall, however, take the poor agreement between experimental data and fit into account in the discussion of the results for **P1 tBu** at the end of this chapter.

Also for **P2** with **tBu** and **THS** side groups, the triplet spectra of the samples in unaligned **5CB** were simulated assuming an isotropic alignment. The results including the simulation parameters are shown in **Figure 8.12**. In both cases, the obtained fit is acceptable, so that the simulation parameters are considered a reasonable starting point for any further analysis.

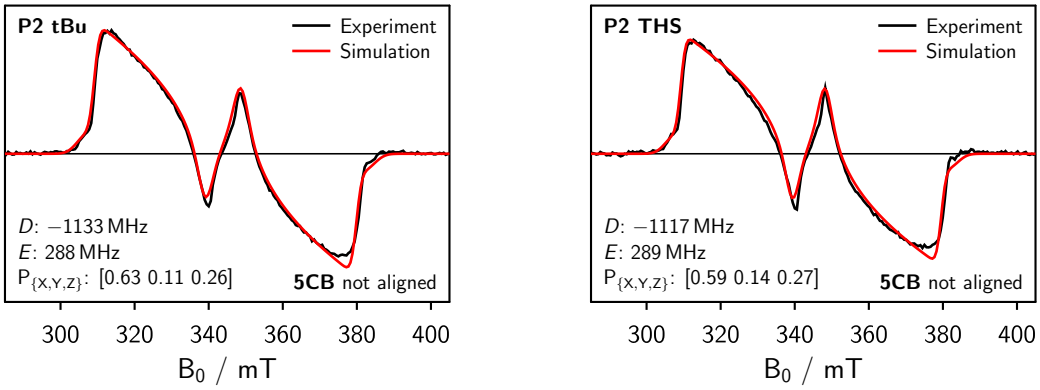


Figure 8.12: Experimental triplet cw EPR spectrum in unaligned **5CB** together with the best fit assuming isotropic alignment for **P2** with **tBu** (*left*) and **THS** (*right*) side groups. The simulation parameters are indicated in the figure and $g = 2.02$.

In the next step, the parameters obtained from the simulation of the spectra of the unaligned samples were fixed and used to simulate the spectra recorded for $\parallel$ and $\perp$ alignment and consequently to obtain the distribution of angles contributing to the individual spectra from which the order parameters can be obtained. As mentioned earlier, a Gaussian distribution of angles is assumed, so the only variable parameters in these simulations are the centres and the widths of the employed Gaussian distributions (cf. **Equations 8.6** and **8.7**).

At first, a uniaxial distribution was assumed. In this case, the only two variable parameters are θ_c and σ_θ, where θ is the angle between the magnetic field direction (i.e. liquid crystal director axis) and the Z axis of the molecule. For **P1**, $\parallel$ alignment should correspond to an angle θ of 90° since the Z axis of the zero-field splitting tensor corresponds to the out-of-plane axis of the molecule, whereas in **P2** an angle θ of 0° should be expected for $\parallel$ alignment. In general, it is reasonable to assume that the centre of the distribution will be located at either 0° or 90°, which additionally reduces the degrees of freedom of the fit.

The influence of the width of the distribution, σ_θ, on the simulated spectra was studied for $\theta_c = 0°$ and $\theta_c = 90°$ for **P1** and **P2 THS**. To this end, spectra were simulated for different values of σ_θ spanning the range between 10° and 180°, where 180° corresponds to the isotropic case and 10° represents a very well aligned sample. The distribution functions used in these simulations are shown in **Figure 8.13** and the simulated spectra together with the corresponding

experimental spectra are depicted in **Figures 8.14** and **8.15**. The colour-code used is the same in all three figures.

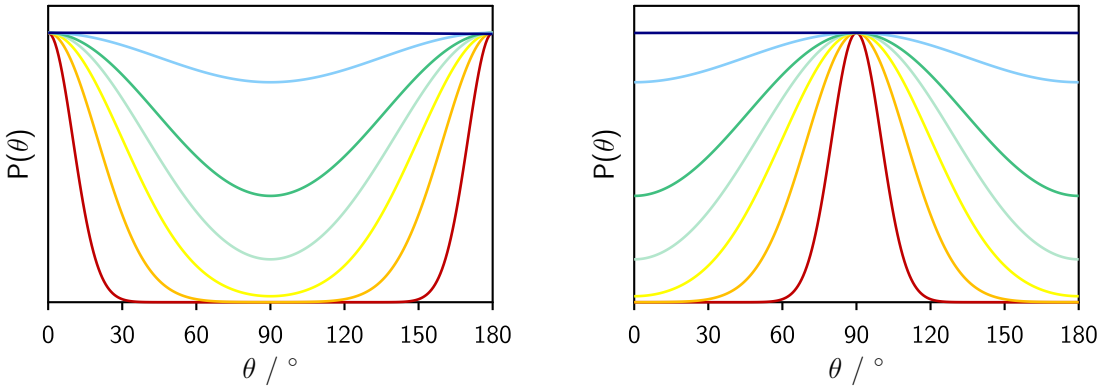


Figure 8.13: Angular distributions centred at $\theta_c = 0°$ (*left*) and $\theta_c = 90°$ (*right*) used in the simulations of the spectra of the aligned samples of **P1** and **P2 THS**. The colour-code is the same as in the figures below.

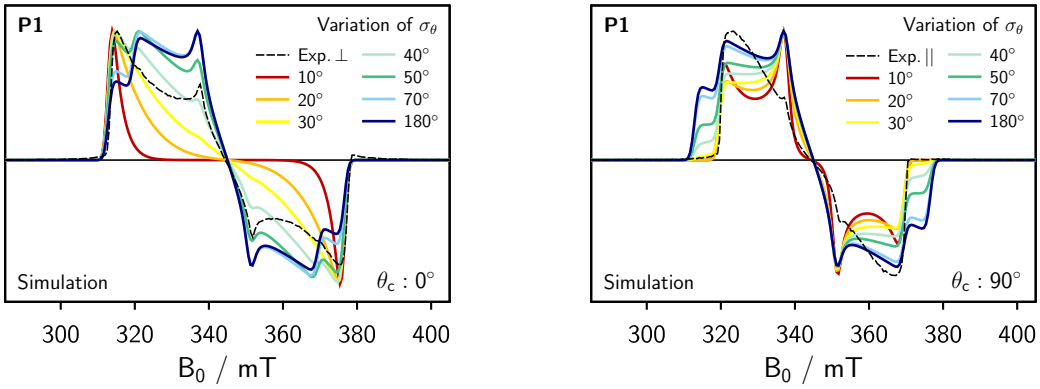


Figure 8.14: Simulated spectra using the parameters for **P1 THS** in combination with the angular distribution functions $P(\theta)$ shown above for $\theta_c = 0°$ (*left*) and $\theta_c = 90°$ (*right*). The corresponding experimental spectrum is superimposed in black (dashed line).

When having a closer look at the spectra for different σ_θ in comparison with the experimental spectra, one realises, especially in the case of **P1 THS**, that the experimental spectra cannot satisfactorily be reproduced if only a distribution in θ is considered. The discrepancy between experiment and simulation is particularly large for **P1 THS** and $||$ alignment where $\theta_c = 90°$: In the experimental spectrum, the X transition strongly dominates, whereas the two other transitions are almost absent. In the simulated spectra, however, the Y transition is always strongly present no matter the width of the distribution, σ_θ, and consequently no distribution can be found which allows the shape of the simulated spectrum to closely approach the experimental one. This is maybe not surprising given that for $\theta_c = 90°$ the porphyrin molecule might have a strong preference to align either along the X or along the Y axis which should lead to marked differences in the respective triplet spectra. In such cases, the influence of the azimuthal angle φ can become significant.

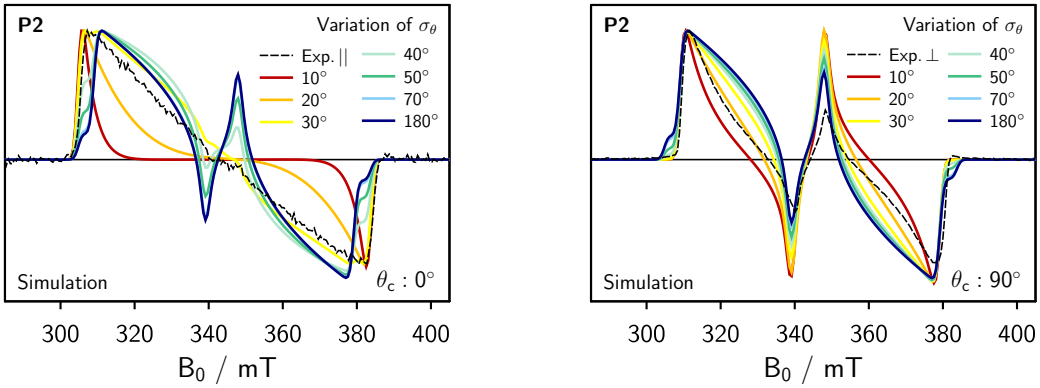


Figure 8.15: Simulated spectra using the parameters for **P2 THS** in combination with the angular distribution functions $P(\theta)$ shown above for $\theta_c = 0°$ (*left*) and $\theta_c = 90°$ (*right*). The corresponding experimental spectrum is superimposed in black (dashed line).

8.4.1 Simulations Assuming Biaxiality

In addition to the distribution in θ, a distribution in φ was thus included in the simulations and a home-written MATLAB fitting routine was implemented which allowed to fit the experimental data for || and ⊥ alignment simultaneously. The centres of the distributions were fixed but shifted by 90° between || and ⊥ alignment. The width of the distributions, σ_θ and σ_φ, were allowed to vary independently from each other but were required to be identical for || and ⊥ alignment. The best fits to the experimental data together with the parameters used in the simulations are shown for **P1** and **P2 THS** in **Figure 8.16**.

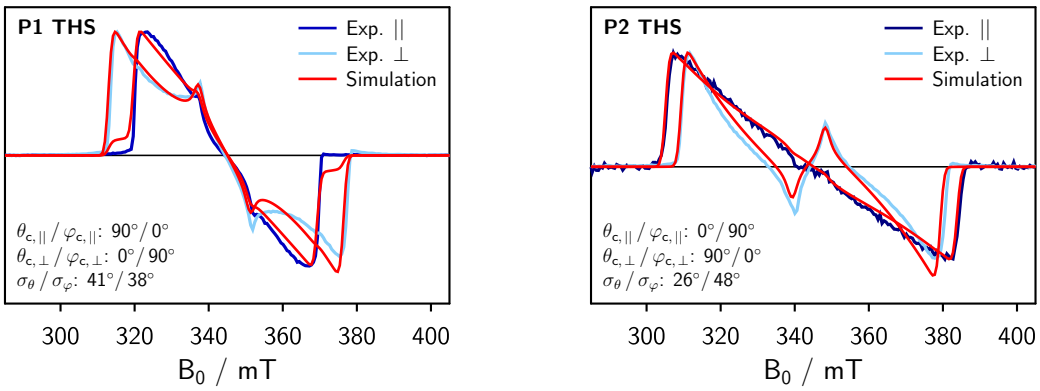


Figure 8.16: Simulated spectra assuming a biaxial distribution $P(\theta, \varphi)$ in comparison with the corresponding experimental spectra for **P1 THS** (*left*) and **P2 THS** (*right*). The parameters yielding the best fit to the experimental data are indicated in the figure.

From the figure it can clearly be seen that the agreement between the simulation and the experimental data was much improved by including a distribution in φ. The fits are certainly not perfect, but given the experimental uncertainty on the spectral shape due to (variably) imperfect alignment, the match is considered satisfactory. For **P1 THS**, the distributions in θ and φ are

found to be fairly wide with $\sigma_\theta \simeq \sigma_\varphi \simeq 40°$, whereas for **P2 THS** a narrower distribution in θ of 26° is found in combination with a relatively wide distribution in φ of 48°.

Simulations assuming a biaxial angular distribution were also attempted for **P1** and **P2** with **tBu** side groups and the results are shown in **Figure 8.17**. While the fit for **P1 tBu** is satisfactory, no acceptable fit could be obtained for **P2 tBu**.

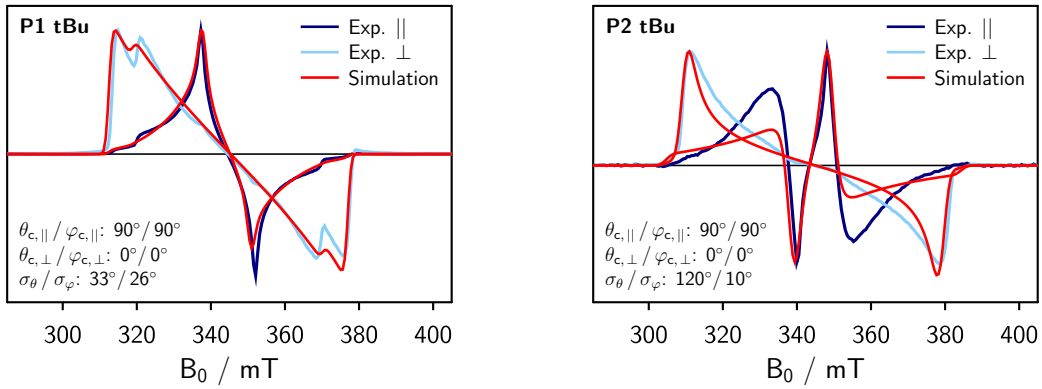


Figure 8.17: Simulated spectra assuming a biaxial distribution $P(\theta, \varphi)$ in comparison with the corresponding experimental spectra for **P1 tBu** (*left*) and **P2 tBu** (*right*). The parameters yielding the best fit to the experimental data are indicated in the figure.

Interestingly, it is found that, in the case of || alignment of **P1 tBu** ($\theta_c = 90°$), the porphyrin molecules tend to align along the Y axis (i.e. the axis pointing along the aryl groups, $\varphi_c = 90°$), in contrast to **P1 THS**, where the X transition is strongly enhanced in agreement with $\varphi_c = 0°$, corresponding to an alignment along the axis of the alkyne bonds. Again it is noted that the different side chains have a strong influence on the alignment of the porphyrins.

No good agreement between experiment and simulation could be reached for **P2 tBu**. In **Figure 8.17** the best simulation attempt is shown, but the agreement is clearly not satisfactory. However, simulations for all other combinations of parameters regarding the centres of the distributions ($\theta_{c,||}$, $\varphi_{c,||}$, $\theta_{c,\perp}$, $\varphi_{c,\perp}$) do not come even close to reproducing the experimental data so that the direction of preferential orientation of the molecule can nevertheless be predicted with certainty. It seems that the molecule does not align along its long axis (Z) as would have been expected for a prolate system and is observed for **P2 THS**, but rather along the Y axis, corresponding to the axis along the aryl groups. The distribution in θ resulting from the simulation is fairly large, indicating a rather poor alignment.

8.4.2 Validation of the Simulations

It was shown in **Figures 8.14** and **8.15** that simulations which rely on angular distributions depending only on θ are not able to satisfactorily reproduce all experimental spectra. The large discrepancies between such simulations and the experimental spectra, particularly for **P1**, where $\theta_c = 90°$, justify the use of a biaxial angular distribution $P(\theta, \varphi)$.

To validate the simulations, the effect of the width of the distribution in φ on the spectral shape was verified. If σ_φ is chosen to be sufficiently large, the obtained spectrum should be identical to

that for a uniaxial distribution $P(\theta)$. Generally, the influence of σ_φ should be large for $\theta_c = 90°$ and relatively small for $\theta_c = 0°$, except if σ_θ is also large. For a fixed distribution in θ and a fixed φ_c, the width of the distribution in φ was varied and the simulated spectra were compared to the corresponding experimental ones. The results are shown in **Figure 8.18** for **P1 THS** and in **Figure 8.19** for **P2 THS**. From these figures, in comparison with **Figures 8.14** and **8.15**, the following observations can be made:

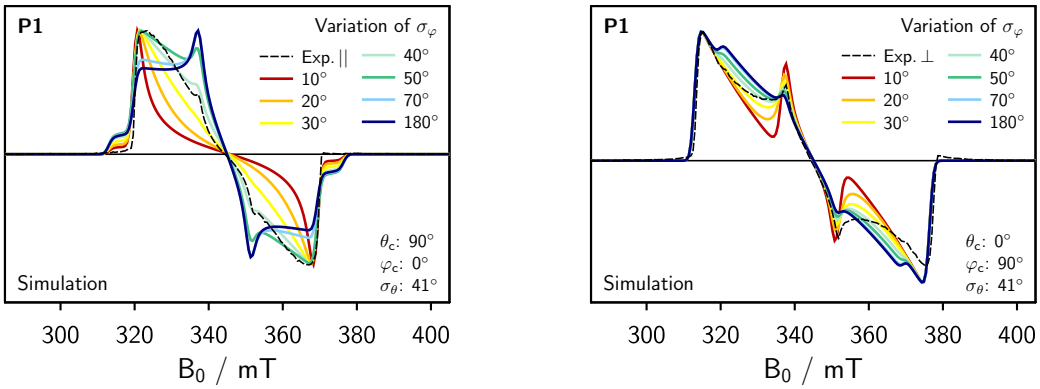


Figure 8.18: Simulated spectra for different values of σ_φ using the parameters for **P1 THS** in combination with a biaxial angular distribution $P(\theta, \varphi)$ with $\theta_c = 90°$ (*left*) and $\theta_c = 0°$ (*right*). The corresponding experimental spectra are superimposed in black (dashed line) and σ_θ and φ_c were fixed to the indicated values.

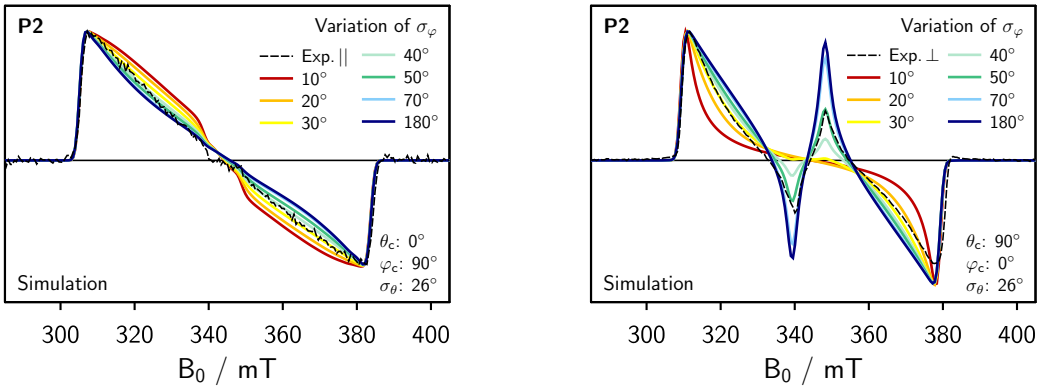


Figure 8.19: Simulated spectra for different values of σ_φ using the parameters for **P2 THS** in combination with a biaxial angular distribution $P(\theta, \varphi)$ with $\theta_c = 0°$ (*left*) and $\theta_c = 90°$ (*right*). The corresponding experimental spectra are superimposed in black (dashed line) and σ_θ and φ_c were fixed to the indicated values.

- The spectra for $\sigma_\varphi = 180°$ are identical to the corresponding uniaxial ones where only a distribution in θ is considered.
- The influence of σ_φ is large for $\theta_c = 90°$ and smaller for $\theta_c = 0°$. The reason why the influence of σ_φ is still not negligible for $\theta_c = 0°$ is most likely the relatively wide distribution in θ observed in all cases.

- The influence of σ_φ on the experimental spectrum of **P1 THS** for $\theta_c = 90°$ is striking (cf. **Figure 8.18**, *left*). For a proper description of the experimental observations, a biaxial distribution is clearly required.

- In the case of **P2 THS** (**Figure 8.19**), since the value of σ_φ which was found to best reproduce the experimental data is relatively large, the experimental spectra can nearly be simulated taking only a distribution in θ into account. However, the improvement of the simulations obtained when using a biaxial distribution is significant.

Order Parameters

From the width of the distributions, σ_θ and σ_φ, obtained from the simulations of the experimental data, order parameters were calculated for **P1** and **P2 THS**. An overview of the parameters characterising the distributions which resulted from the simulations and of the obtained order parameters for || alignment is given in **Table 8.1**. For **P1** the order parameter S is found to be negative, while U is positive since $\theta_c = 90°$ and $\varphi_c = 0°$, whereas for **P2** S is positive and U is negative ($\theta_c = 0°$, $\varphi_c = 90°$). The degree of order in **P2 THS** is generally higher, although a detailed comparison proves difficult. Any more detailed discussion, potentially leading to over-interpretation of the data, shall be avoided here.

Table 8.1: Overview of the parameters used in the simulations of the spectra of the aligned samples of **P1** and **P2 THS** in **5CB**. The order parameters S and U calculated from the distributions in θ and φ are listed only for || alignment.

Sample	θ_c / °	σ_θ / °	φ_c / °	σ_φ / °	S	U
P1 ||	90	41	0	38	−0.17	0.51
P1 ⊥	0	41	90	38		
P2 ||	0	26	90	48	0.55	−0.10
P2 ⊥	90	26	0	48		

8.5 Conclusions

Based on the experimental observations and results from the simulations, a couple of conclusions can be drawn. The investigated porphyrin molecules with different side chains do align in the nematic phase of the liquid crystal **5CB**. The experimental cw EPR spectra for || and ⊥ alignment are clearly different and reasonably reproducible. When the liquid crystal is not aligned, triplet spectra are obtained which closely resemble the spectra obtained for the same compounds in isotropic frozen solution, indicating an isotropic distribution of orientations. The triplet state parameters obtained from a simulation of such an isotropic liquid crystal spectrum were fixed and used in the simulations of the spectra of the respective aligned samples. The agreement between the experimental data and the simulations is reasonably good, justifying the chosen approach.

Different side groups were found to have a strong influence on the alignment of the porphyrin molecules. Based on UV-vis measurements, results from laser excitation wavelength dependent studies and simulations, it is concluded that many different orientations and conformations contribute to the spectra of **P1** and **P2 tBu**, indicating a rather poor alignment. Consequently, most of the analysis focused on **P1** and **P2 THS**.

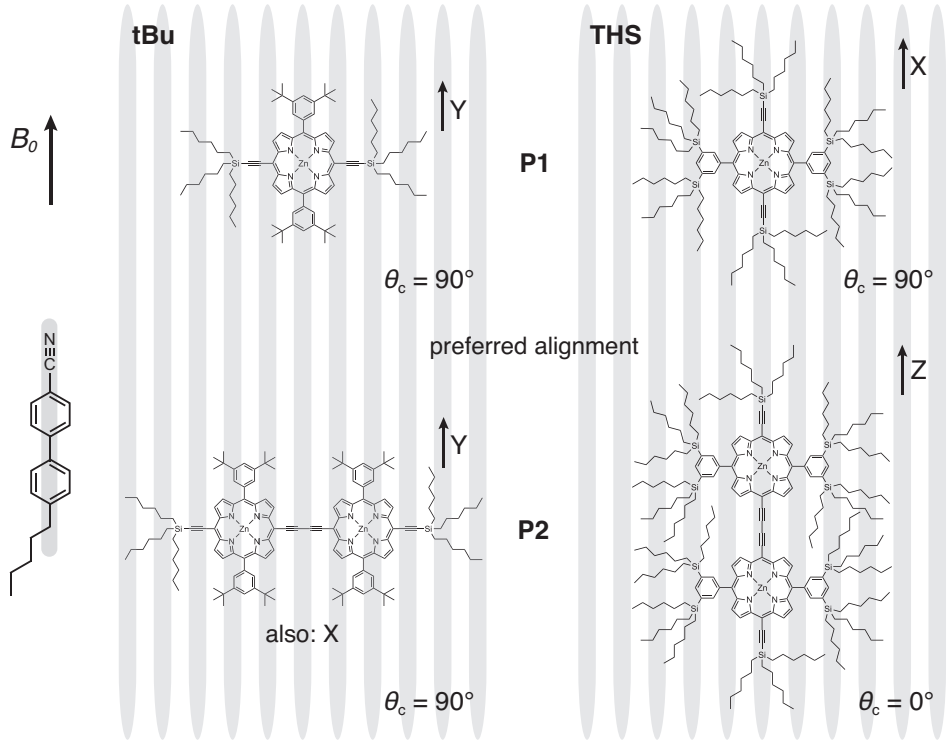


Figure 8.20: Overview of the preferred alignment of **P1** and **P2** with **tBu** and **THS** side groups in **5CB** as obtained from the analysis of the triplet state EPR data.

It was found that most experimental spectra cannot be reproduced in a satisfactory way if only a distribution in the polar angle θ is considered in the simulations. However, assuming a biaxial distribution $P(\theta, \varphi)$, resulted in a good agreement between experimental data and simulations. The use of a biaxial distribution was justified and a validation of the simulations was carried out. From a simultaneous fit of the spectra for $||$ and $\perp$ alignment, the centres and widths of the distributions in θ and φ were obtained. Once the values of σ_θ and σ_φ were determined, also the biaxial order parameters S and U could be calculated and compared. **Figure 8.20** gives a graphic summary of the preferred alignment of the four investigated molecules in **5CB**.

Chapter 9

Radical Pair Photophysics under the Influence of Magnetic Fields

In this chapter, the influence of weak magnetic fields on the recombination kinetics of photogenerated radical pairs is discussed. If the product yield or the kinetics of product formation of a chemical reaction can be influenced by the presence of a magnetic field, we speak of this reaction as showing a magnetic field effect (MFE). The latter is defined as the relative change of the monitored yield or molecular property as compared to zero field. The theory underlying the origin of such MFEs is well understood [146–150] and extensive experimental studies have been carried out in liquid solution for organic, freely-diffusing, donor-acceptor pairs [151], however the magnetic field strengths employed in these experiments were typically high (i.e. $>100\,\mathrm{G}$).*

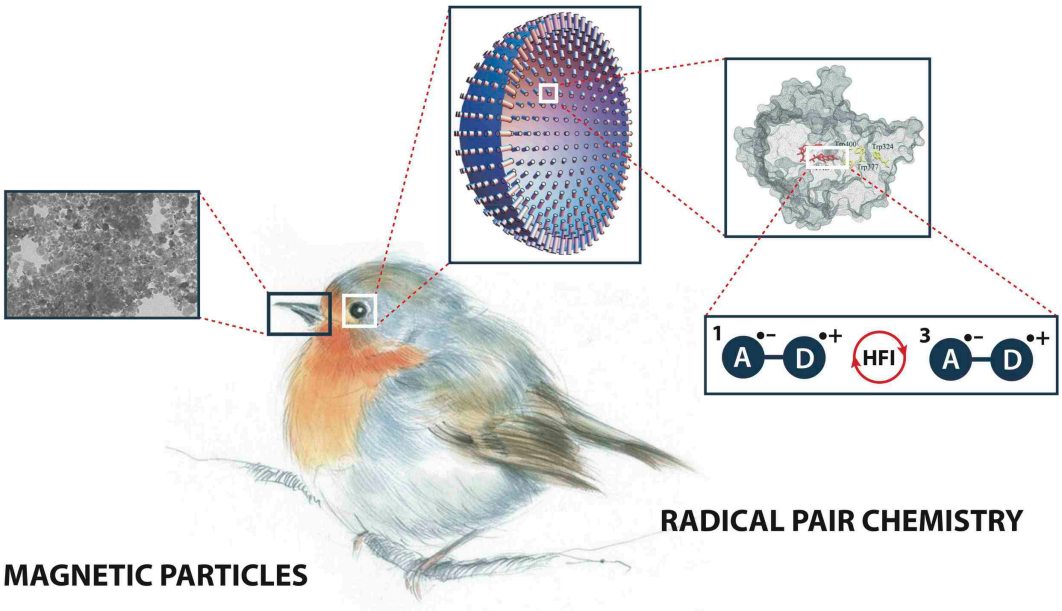


Figure 9.1: Overview of the two main hypotheses proposed to be at the origin of the avian magnetocompass.

Magnetic field effects have also been proposed to be involved in avian magnetoreception. Since roughly the 1960s it is scientifically proven that birds use the Earth's magnetic field for orientation

*In the following two chapters the magnetic field strength will be expressed in Gauss instead of milli-Tesla. This unit is more common in the spin chemistry community, since it is better suited for the description of small fields. The following conversion applies: $1\,\mathrm{mT} = 10\,\mathrm{G}$.

and compass-navigation. Yet the mechanism by which this information is perceived is still under debate [152–155]. Two viable hypotheses have been proposed, an overview of which is provided in **Figure 9.1**.

According to the first hypothesis, bird navigation relies on the presence of magnetite crystals in their beaks [156–162]. The second hypothesis is based on the radical pair model, according to which magnetoreception relies on the magnetic-field sensitivity of the product yield of a chemical reaction involving photo-generated radical pairs [163–165]. It has been proposed that these radical pairs are generated in photoreceptor molecules which are aligned in the bird's retina, so that the birds are in fact thought to be able to 'see' the magnetic field.

In principle, two different magnetic-field-based sensory mechanisms could be imagined to play a role in magnetoreception. Every point on the globe is characterised by a certain magnetic intensity, an inclination, and a declination, where the magnetic intensity ranges from about 0.25 G at the equator to 0.65 G at the poles. The inclination is defined as the angle between the magnetic field lines and the Earth's surface, and the magnetic declination, also referred to as polarity, is the angle between magnetic and geographic North. It is believed that the intensity and/or inclination could be important for a 'map-like' sense, to locate a certain position, whereas the polarity and/or inclination could be involved in a 'compass-like' sense to obtain directional information.

Experiments suggest that both of the proposed hypotheses are in fact relevant for magnetoreception [166], but it seems probable that the magnetite and photoreceptors fulfill different tasks [153]. Magnetite receptors could be used to obtain positional information [167–169], whereas there is strong evidence from behavioural studies on birds that the radical pair model can explain the bird's magnetic compass behaviour [170]. Some of this evidence in support of the radical pair mechanism (RPM) shall be outlined in the following section on magnetoreception.

Figure 9.2 shows a very general reaction scheme illustrating the origin of the magnetic-field sensitivity of the product yield of a chemical reaction in the framework of the radical pair model. In the most general case, we start from an organic donor-acceptor pair, where donor and acceptor may be part of the same molecule or individual molecules. Photoexcitation then yields the singlet excited state of either donor or acceptor and is followed by electron transfer to generate the singlet radical pair under the laws of spin conservation.

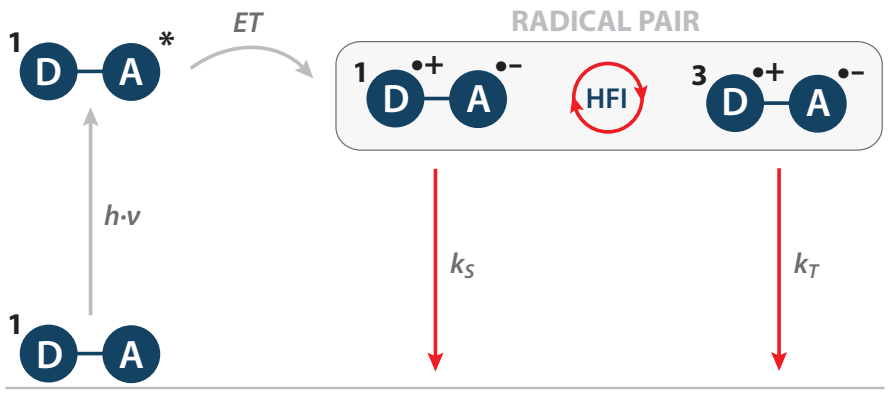


Figure 9.2: Example of a simplified photoscheme illustrating the radical pair mechanism.

Since, in the absence of strong dipolar and/or exchange interactions, the singlet radical pair is created in a non-eigenstate of its Hamiltonian, the singlet radical pair state is a non-stationary state. Consequently, time-dependent coherent mixing between the singlet and corresponding triplet radical pair states is observed as is illustrated in **Figure 9.3**, which shows the singlet probability of a singlet-born radical pair as a function of time after its creation for a hypothetic one-proton radical pair with a single hyperfine coupling of 10 G (blue line).

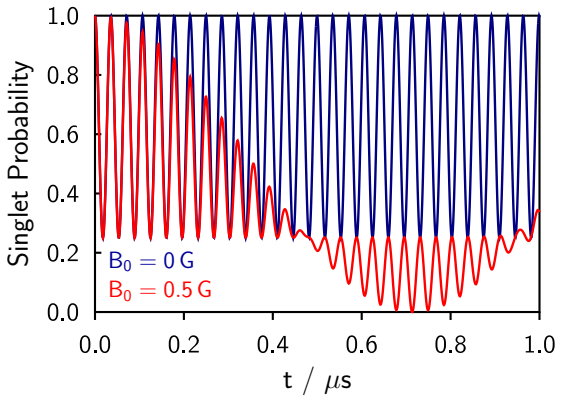


Figure 9.3: Singlet probability as a function of time calculated for a one proton radical pair with a single hyperfine coupling of 10 G (28 MHz). The influence of a magnetic field of 0.5 G is illustrated, corresponding to a Larmor frequency of 1.4 MHz.

The mixing between singlet and triplet states is driven by the hyperfine interaction[†] and therefore only takes place if at least one of the radical pair partners has nuclei with non-zero hyperfine couplings. The mixing frequency depends on the magnitude of the effective hyperfine coupling. The interconversion between singlet and triplet states is magnetic field dependent, as also illustrated in **Figure 9.3** (red line) for an external magnetic field of 0.5 G. Due to the magnetic field dependence of the mixing between singlet and triplet states, also the product yield and/or the kinetics of product formation of a chemical reaction involving such spin-correlated radical pairs will be field-dependent if (i) the singlet and triplet states have different fates or (ii) the recombination rates from the singlet (k_S) and triplet (k_T) states are different. Since the radical pair mechanism involves an activationless process far from thermal equilibrium, any thermodynamic considerations do not apply.

9.1 Magnetoreception and the Radical Pair Mechanism

The singlet yield of a singlet-born radical pair typically has a dependence on the magnetic field similar to that shown in **Figure 9.4**. Such a curve, showing the MFE as a function of the magnetic field, is typically referred to as a so-called MARY curve, for Magnetically Altered Reaction Yield. Its functional shape can be understood by considering the selection rules for spin angular momentum in combination with the influence of a magnetic field on the energies of the singlet and triplet

[†]Various other mechanisms inducing singlet-triplex mixing exist, but are not relevant for the organic donor-acceptor systems discussed here. These mechanisms include the Δg-mechanism, relaxation, and spin-orbit coupling. For a more complete picture, the interested reader is referred to [148, 150].

states. Depending on the relative magnitude of the external and hyperfine fields, three different field regimes can be distinguished as shown in **Figure 9.5**. In the following discussion of the different regimes, we shall assume the radical pair to be singlet-born.

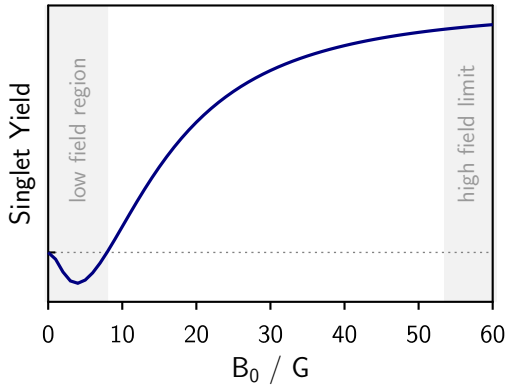


Figure 9.4: Magnetic field dependence of the singlet yield for a singlet-born radical pair. The low- and high field regions are indicated.

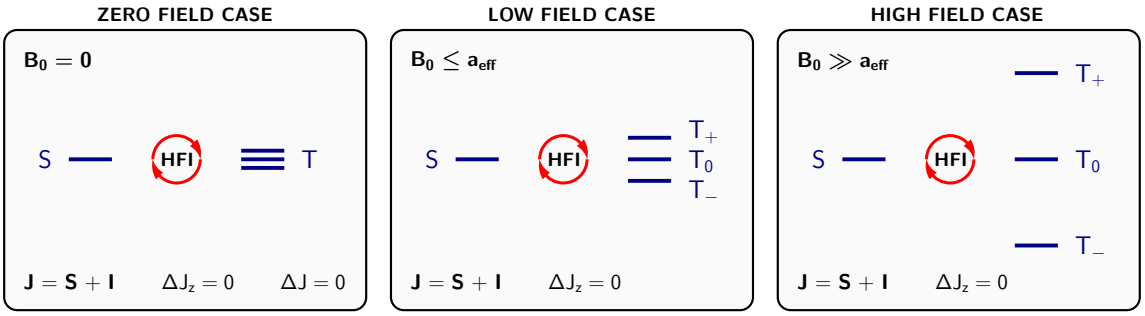


Figure 9.5: Overview of the relative energies of the singlet and triplet sublevels and corresponding selection rules in the three magnetic field regimes to be considered in the description of the field dependence of the singlet-triplet interconversion efficiency. The three field regions, referred to as the 'zero-field', the 'low-field' and the 'high-field' regimes, are defined according to the relative magnitudes of the Zeeman and hyperfine fields.

At zero field (**Figure 9.5**, *left*), the singlet and the three triplet states are degenerate. The singlet-triplet mixing is subject to strict spin selection rules, which require the total spin angular momentum, J, as well as its projection onto the z axis, J_z, to stay invariant. At high fields (**Figure 9.5**, *right*), where the Zeeman field is much higher than the hyperfine field, the triplet states are split in energy due to the electronic Zeeman interaction and so the $|T_+\rangle$ and $|T_-\rangle$ states can no longer participate in singlet-triplet interconversion. Consequently, the singlet state population will be increased as compared to zero field as depicted in **Figure 9.4**.

When investigating the mechanism underlying the magnetic compass behaviour of birds, we will need to consider an intermediate regime between the zero and high field limits, since the Earth's magnetic field is only of the order of 1 G. The corresponding intermediate field region is referred to as the low-field region. In the low-field region, the hyperfine field generated by the radical pairs is of the same order of magnitude as the externally applied field. Consequently, the external magnetic

field is no longer the quantisation axis and we need to consider an effective field, which is the vector sum of the external and hyperfine fields. Since the external magnetic field is relatively weak, all three triplet states still need to be considered for singlet-triplet interconversion. Compared to zero field, the spin selection rules are relaxed (cf. **Figure 9.5**), so that additional spin mixing pathways become allowed. This 'enhanced mixing' leads to a decrease in the singlet population as compared to zero field. The phenomenon leading to this inverted field dependence with reference to the high field region, as shown in **Figure 9.4**, is referred to as the low-field effect [171–174].

The outlined radical pair model was first proposed to be at the origin of avian magnetoreception in the late 1970s by K. Schulten et. al. [163] who suggested that radical pairs are created by a light-driven electron transfer reaction and undergo coherent spin motion, driven by anisotropic hyperfine interactions and the external magnetic field. About 30 years later, T. Ritz et al. [164] demonstrated in a theoretical study that photoreception could be imagined to occur in the bird's eyes and the information transmitted *via* the visual pathway.

Nowadays it is believed that cryptochrome could be the photoreceptor molecule [164, 175–177]. It is a flavoprotein found in many plants and animals and is, for example, known to be involved in the entrainment of the circadian rhythm or the regulation of plant growth [178]. Its cofactor, flavin, can be excited by blue light and cryptochrome itself has many electro-active residues that could be involved in the photoinduced electron transfer to generate the radical pair. Most importantly, cryptochrome has been found in the eyes of migratory birds and is concentrated in cells which show a high activity when birds perform magnetic orientation [179, 180], making it a suitable candidate molecule. Since cryptochrome binds a redox-active FAD molecule, the radical pair in question has been proposed to be formed between FAD and tryptophan residues of the cryptochrome protein [181, 182], although other radical pairs for cryptochrome-based magnetoreception have also been proposed [183].

Directional information is believed to result from anisotropic hyperfine couplings [184]. If the hyperfine field of (at least) one of the radical pair partners is anisotropic, the total effective field, which is the vector sum of the external and hyperfine fields, will depend on the orientation of the molecule with respect to the external field. In turn, if the orientation of the molecules is fixed, this signifies that their field response, and therefore the product yield, will vary depending on the orientation of the external magnetic field. An orientation-dependent magnetic field response based on anisotropic hyperfine interactions can thus be imagined if the orientation of the molecules is preserved in a fixed arrangement. Therefore the bird's retina has been proposed to be the location of the photoreceptor molecules. Anchoring of the molecules across the retina would lead to a perfectly spherical arrangement of the photoreceptors. The different orientation of the molecules in different locations of the retina would imply a different product yield and therefore a different concentration of a certain signalling state. Depending on the inclination of the external magnetic field, different, distinguishable visual modulation patterns could be generated. The theoretical feasibility of the generation of such patterns has been demonstrated for weak magnetic fields of the order of the Earth's [164].

The visual signal is then thought to be transmitted as optical information to the brain *via* the visual nervous system. In the brain, a specific area, named cluster N, has been identified and shown to be involved in the processing of the directional information [185–187].

As briefly mentioned earlier, most of the evidence for the involvement of the RPM in avian navigation has been provided by behavioural studies. During the migratory season, the birds' urge to migrate is so strong, that even captive birds still show a directional behaviour, which can be studied under different artificially generated conditions [188, 189]. By inverting the vertical and horizontal components of the magnetic field individually, it could be shown convincingly that the birds respond to the inclination of the magnetic field rather than its polarity [190]. The birds seem only to distinguish 'polewards' and 'equatorwards' rather than North and South, which is perfectly in line with a chemical compass based on the RPM. Magnetic orientation was also tested under different light conditions [191–195]. In experiments, the birds were able to orient under UV, blue and green light, whereas they became disoriented under darkness and yellow or red light. This finding can be understood in the framework of the RPM considering that the photoreceptor might only absorb in a certain part of the visible spectrum. A number of other experiments in support of the radical pair mechanism also revealed that the magnetoreceptor is located in the bird's eye [196] and that radio frequency fields interfere with compass orientation [197–199].

Additional recommended review and summary articles on the topic of avian magnetoreception not mentioned in the above paragraphs include [200–208].

9.1.1 Experimental Requirements and Considerations

The aforementioned behavioural studies on birds suggest that the RPM is likely to be at the origin of the avian magnetic compass, although information about the nature of the radical pair and the signalling pathway remains scarce. In particular, only one chemical system has been reported so far, which responds to fields as weak as the Earth's [209]. A better understanding of the external factors and molecular properties influencing the observation of pronounced magnetic field effects would be desirable since it might help us to identify the missing steps involved in the generation and processing of the magnetic information. For such investigations, model systems are required which need to fulfill certain requirements as detailed in the following.

In order to observe a MFE and a pronounced low field effect [172] experimentally, a suitable model system needs to exhibit long-lived spin coherence and relatively slow radical pair recombination rates to allow for spin evolution. Case studies and theoretical calculations [172] have shown that radical pair lifetimes of the order of 100 ns to 1 μs are favourable. The spin relaxation rates should not be shorter than the radical pair lifetime, suggesting values of $>1\,\mu$s. Further, for the observation of MFEs, the recombination rates from the singlet and triplet state must not be equal or lead to different products, and finally, to observe an orientation-dependent signal, anisotropic hyperfine tensors are required and motional averaging of the anisotropic response must be avoided (or at least limited).

In the discussion of MFEs based on the separation of the energy levels between singlet and triplet states in **Figure 9.5** we indirectly assumed that the exchange interaction between the radicals equals

zero. The exchange interaction, J, determines the splitting between the singlet and triplet states, ΔE_{ST}, at zero field and can prevent singlet-triplet mixing and therefore the observation of MFEs. J typically has an approximately exponential dependence on distance as is illustrated in **Figure 9.6** for $J > 0$ (i.e. $E_T > E_S$). If J is large, the singlet and triplet states are eigenstates of the Hamiltonian and spin evolution is inhibited. However, also weak exchange interactions can be problematic since they lift the zero-field degeneracies. Consequently one might expect the low field effect to be absent or much attenuated since no (or much fewer) additional spin mixing pathways become allowed upon application of a small magnetic field.

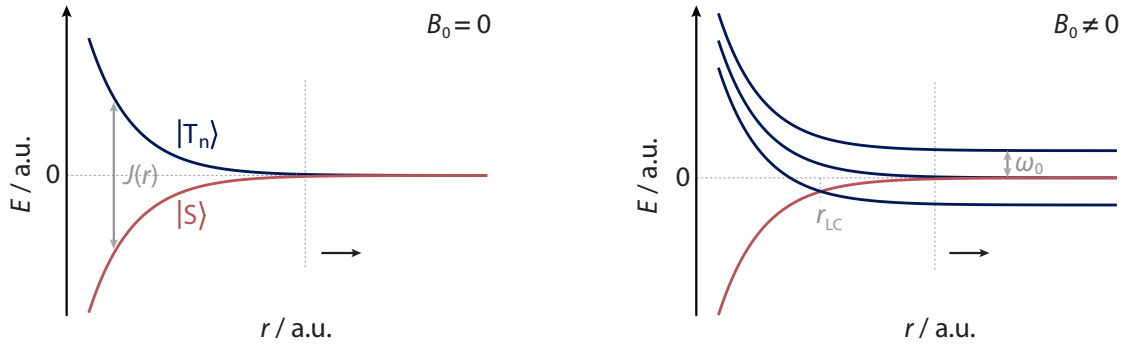


Figure 9.6: Illustration of the distance dependence of the exchange coupling interaction J and its implications for singlet-triplet mixing in the absence (*left*) and presence (*right*) of an external magnetic field for $J > 0$ ($D = 0$). The vertical dotted line indicates the minimum inter-radical separation distance for spin mixing to become feasible.

In the case of freely diffusing pairs, the radicals are formed at the contact distance and thus first need to diffuse apart for singlet-triplet mixing to set in. It typically takes a couple of nanoseconds until a separation distance is reached where singlet and triplet states are approximately isoenergetic, and consequently, a radical pair lifetime of at least several tens of nanoseconds is normally required for the observation of MFEs. In linked systems with fixed inter-radical distances, a separation between the radicals of at least 1 nm, but ideally about 1.5−2 nm or longer, is desirable to avoid perturbations caused by the exchange interaction.[‡]

The influence of the exchange interaction can thus be contained by designing a system with a suitable inter-radical distance. Many of the other requirements for the observation of MFEs can, to a certain extent, be controlled by a careful choice of the properties of the solvent or solid matrix: The radical pair recombination rates typically depend on the polarity of the solvent. The spin coherence time is determined by the relaxation rates which are strongly temperature dependent, and the motional averaging of the anisotropic response can be reduced by increasing the viscosity.

Literature studies on bimolecular systems suggest that the magnetic field effect (for charged radical pairs) is maximised for dielectric constants, ε_r, between 18 and 20 [213, 214]. In the experiments presented in the following chapter, 2-methyltetrahydrofuran (**MTHF**) is used as the solvent and the dielectric constant and viscosity of the medium are controlled *via* the sample

[‡]Apart from the exchange interaction, also the presence of a (large) dipolar interaction can be unfavourable for spin evolution, but its magnitude can be controlled more easily *via* the radical pair separation distance. The effect of D on spin evolution has been investigated theoretically in references [210, 211].

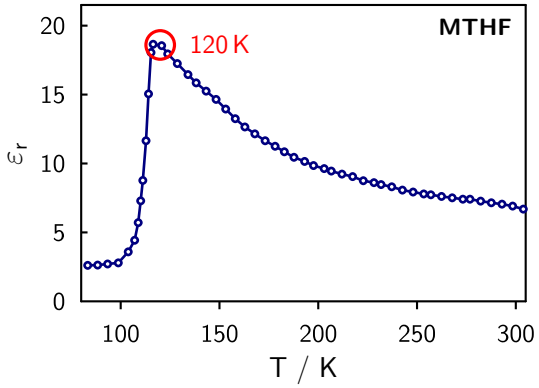


Figure 9.7: Temperature dependence of the dielectric constant of **MTHF**. The graph has been reproduced from reference [212].

temperature. An optimum is found at 120 K, where the viscosity is high[§] and the relative dielectric constant is around 19 as shown in **Figure 9.7**. The data points in the graph were reproduced from reference [212].

The influence of the solvent properties on the photoinduced electron transfer reaction generating the radical pair and on radical pair recombination can be understood in the framework of Marcus theory [215–219]. It is assumed that the electron transfer is faster than the nuclear motions (i.e. the nuclear positions are fixed during the reaction) and that the energies of the states before and immediately after the electron transfer are equal. The rate of a non-adiabatic electron transfer reaction,[¶] k_{ET}, is given as

$$k_{ET} = \frac{2\pi}{\hbar} V_{el}^2 \frac{1}{\sqrt{4\pi\lambda k_B T}} \exp\left(-\frac{\Delta G^*}{k_B T}\right) \tag{9.1}$$

where V_{el} denotes the electronic matrix element, roughly equivalent to the wavefunction overlap (i.e. coupling) between reactants and product states. If this overlap is small, $V_{el} \ll k_B T$, the reaction is non-adiabatic (i.e. diabatic), whereas if it is large, $V_{el} \gg k_B T$, it is referred to as an adiabatic reaction. The activation energy, ΔG^*, assuming a linear dielectric response between solvent and reactant, can be described according to [220, 221]

$$\Delta G^* = \frac{(\lambda + \Delta G_0)^2}{4\lambda} \tag{9.2}$$

where λ is the so-called reorganisation energy.

Depending on the free energy gap, ΔG_0, between the reactant (**R**) and product (**P**) states, three different regimes can be distinguished as illustrated in **Figure 9.8**. In the Marcus normal region, where $-\Delta G_0 < \lambda$, the electron transfer rate constant, k_{ET}, increases as the driving force, $-\Delta G_0$, increases. The region where $-\Delta G_0 > \lambda$ is referred to as the Marcus inverted region since

[§] **MTHF** has a freezing point of roughly 110 K.

[¶] The classical Marcus theory is only valid for non-adiabatic reactions. Further developments of the model to account for adiabatic reactions exist, but are beyond the scope of this work.

the reaction rate is found to decrease with increasing driving force, and finally, if $-\Delta G_0 = \lambda$, the reaction proceeds barrier-less.

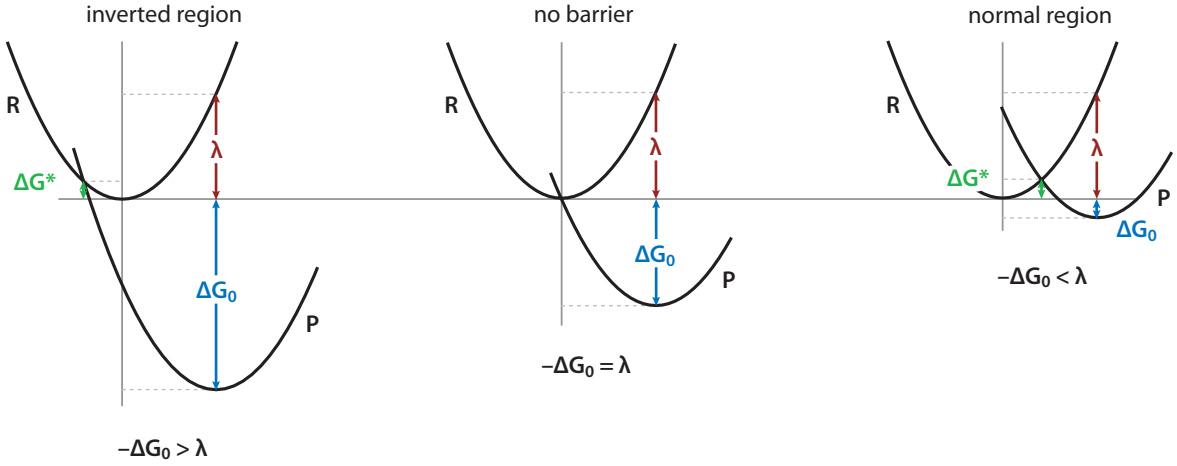


Figure 9.8: Illustration of the relative position of the free energy surfaces of reactant (**R**) and product (**P**) in the three distinguishable driving force regimes accounted for in Marcus theory.

The logarithm of the electron transfer rate constant, $\ln(k_{ET})$, is thus predicted to have a bell-shaped dependence on driving force, with the maximum rate reached at $-\Delta G_0 = \lambda$. The reorganisation energy λ is composed of two contributions, referred to as the outer (λ_{out}) and inner (λ_{in}) reorganisation energies

$$\lambda = \lambda_{\text{in}} + \lambda_{\text{out}} \tag{9.3}$$

The inner reorganisation energy accounts for structural differences between the equilibrium configurations of the reactant and product states, such as differences in equilibrium bond lengths, and can be described by [221]

$$\lambda_{\text{in}} = \frac{1}{2} \sum_i f_i \left(r_R^{eq} - r_P^{eq} \right)^2 \tag{9.4}$$

where r_R^{eq} and r_P^{eq} are the equilibrium bond lengths in the reactant and product states, f_i is the reduced force constant of the i^{th} vibration, and the sum runs over all significant intramolecular vibrations of the molecule.

The outer reorganisation energy is the energy necessary for the solvent to adapt to the new equilibrium configuration and thus accounts for differences between the orientation and polarisation of the solvent molecules around the reactant and product states. Assuming a spherical model, λ_{out} can be defined as

$$\lambda_{\text{out}} = \frac{e^2}{4\pi\varepsilon_0} \left(\frac{1}{2r_D} + \frac{1}{2r_A} - \frac{1}{r_{DA}} \right) \left(\frac{1}{n^2} - \frac{1}{\varepsilon_r} \right) \tag{9.5}$$

where e is the electronic charge, ε_0 the vacuum permittivity, r_D, r_A and r_{DA} the ionic radii of donor and acceptor and the distance between them, respectively, and the term $\left(\frac{1}{n^2} - \frac{1}{\varepsilon_r}\right)$ is often referred to as the so-called Pekar factor, γ, and depends on the refractive index, n, and the dielectric constant, ε_r, of the solvent.

For organic donor-acceptor pairs, λ_{in} is typically small ($\sim$0.1$-$0.3 eV) so that the contribution of λ_{out} frequently dominates. If λ_{in} can be neglected, the kinetics of the electron transfer are largely

determined by the solvent properties, i.e. the refractive index and relative permittivity. In apolar solvents, $\varepsilon_r \sim n^2$, the Pekar factor tends to zero and λ vanishes, whereas in highly polar solvents the Pekar factor can reach a maximum value of roughly $0.550 \approx \frac{1}{n^2}$.

The driving force of an electron transfer reaction can be estimated from the redox potentials of donor and acceptor [222]. For a charge separation (CS) reaction, the driving force is given by

$$-\Delta G_0(CS) \approx E^{\text{red}}_{1/2,\,A} - E^{\text{ox}}_{1/2,\,D} + E_{00} - C \tag{9.6}$$

whereas it can be approximated to

$$-\Delta G_0(CR) \approx E^{\text{ox}}_{1/2,\,D} - E^{\text{red}}_{1/2,\,A} - C \tag{9.7}$$

in case of a charge recombination (CR) reaction. In these equations, $E^{\text{ox}}_{1/2,\,D}$ is the oxidation potential of the donor, $E^{\text{red}}_{1/2,\,A}$ the reduction potential of the acceptor and E_{00} the excited state energy. The correction term, C, accounts for the Coulomb interaction between the radicals and is often neglected in polar media.

Considering charge recombination to a neutral product (**P**), we should expect the radical pair (**R**) to be stabilised in polar media as compared to **P** and therefore the driving force $-\Delta G_0$ to decrease. Hence, the polarity of the solvent can considerably influence the recombination rates by shifting the energy levels of reactant and product states. Depending on whether a particular charge recombination reaction occurs in the Marcus normal or inverted region, an increased polarity (ε_r) implying a decrease in ΔG_0 either leads to a decrease (Marcus normal) or increase (Marcus inverted) in the electron transfer reaction rate, k_{ET}.

Charge recombination reactions from the singlet and triplet radical pair states are expected to have a different dependence on driving force. Typically, it has been observed that charge recombination from the singlet state occurs in the Marcus inverted region [223–226], while CR from the triplet falls into the Marcus normal region. A high solvent dielectric constant should therefore favour k_S over k_T.

9.1.2 Magnetic Field Effect Anisotropy

Once the properties of the sample and reaction medium have been optimised for the detection of magnetic field effects at low field strengths, we can turn to the measurement of magnetic field effect anisotropy. In the following paragraphs the experimental apparatus as well as the basic steps of data treatment shall be outlined. In the framework of this thesis, the optics and detection parts of the experimental setup have been completely redesigned, whereas the data acquisition software and magnetic field calibration routines have been developed beforehand and are described in detail in reference [227].

A schematic drawing of the setup used for all measurements of magnetic field effects in this work is shown in **Figure 9.9**. It is based on a standard nanosecond transient absorption experiment. The sample is excited with linearly polarised pulsed laser light (pulse duration $\sim 5\,\text{ns}$) at 532 nm with a repetition rate of 10 Hz (Nd:YAG, Continuum Minilite) using pulse energies of $<1\,\text{mJ}$. A cw

laser diode with a central wavelength of 980 nm (Thorlabs, L975P1WJ) is used as the probe light source and the signal is detected using an infrared sensitive Si photodiode (Thorlabs, FDS100). To prevent excessive sample heating, the probe light is only switched on during a narrow time window needed for data acquisition, corresponding to a duty cycle of 4 %. Measured in cw mode, the probe laser power amounts to 1.2 mW, implying a peak power of roughly 30 mW.

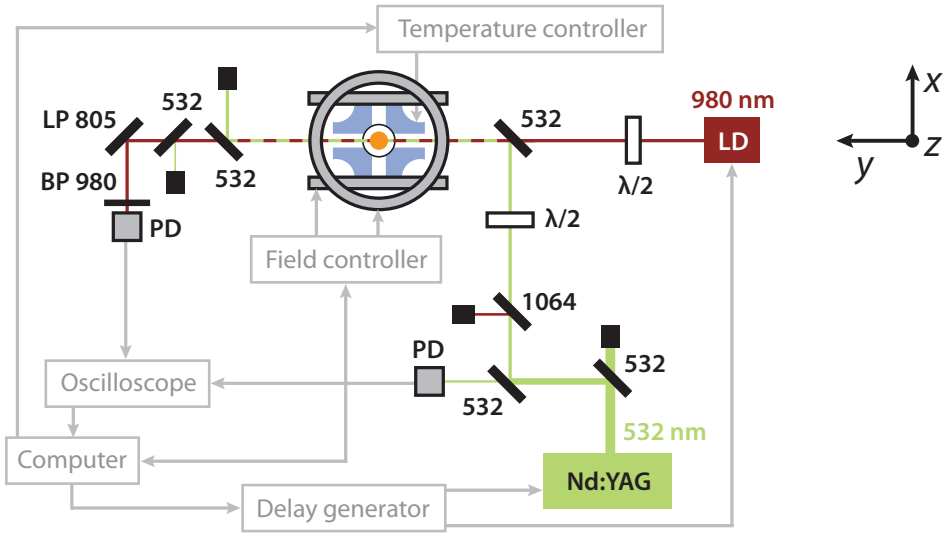


Figure 9.9: Schematic drawing of the experimental setup used for magnetic field effect experiments. Dielectric mirrors are labelled according to the wavelength (in nm) of their reflective coating and the sample position is indicated in orange; PD: photo diode; LD: laser diode; LP: long pass filter; BP: band pass filter.

The polarisations of the pump and probe beams are controlled by means of two half-wave plates and are chosen to be identical in any particular experiment to facilitate the analysis of the anisotropy data. Pump and probe beams are collinear at the sample to ensure maximum overlap. Before and after the sample, dielectric mirrors serve to couple the pump beam in and out of the probe light path. In addition, two dielectric long pass filters are used after the sample to eliminate any residual pump light scatter prior to signal detection. The sample is sitting in a liquid nitrogen flow cryostat (Oxford Instruments) which maintains a constant sample temperature. The cryostat itself is surrounded by three pairs of orthogonal Helmholtz coils which are carefully calibrated, according to a procedure described in [227].

Figure 9.10 (*left*) schematically illustrates the sample geometry and axis definitions used in the experiment. The two sets of Helmholtz coils in x and z direction allow precise control of the magnetic field strength and field angle, measured with respect to the $-z$ axis, while the third pair of coils is adjusted to a constant offset and serves to cancel out the component of the Earth's magnetic field in the propagation direction (y).

The effect of photoselection is exploited to excite and probe only a small subset of molecular orientations within the isotropic frozen solution sample. Molecules can only be excited efficiently if their electronic transition dipole moment, $|\vec{\mu}_{ba}|$, for the transition between two states, $|a\rangle \rightarrow |b\rangle$, is aligned with the electric field vector, $\vec{E}$, and the transition probability varies with the angle α between $|\vec{\mu}_{ba}|$ and $\vec{E}$ according to $\cos^2\alpha$. The transition dipole moment only depends on

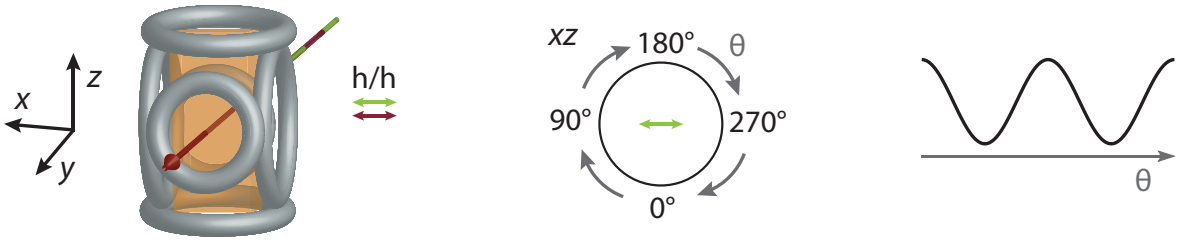


Figure 9.10: Illustration of the sample geometry and axes definitions used in magnetic field effect measurements (*left*), variation of the magnetic field angle θ in the *xy* plane (*centre*) and expected angle dependence of the magnetic field effect (*right*).

the oscillator strength (f) of absorption, $f \propto \varepsilon(\lambda)$, and is not related to the (difference of) permanent dipole moment(s). During an electronic transition, the molecule is in a superposition state between $|a\rangle$ and $|b\rangle$ and its properties oscillate with time. The transition dipole moment describes the amplitude and direction of the electric field induced oscillating electric dipole. Upon a second interaction with the oscillating electric field, the final population state is reached. Using photoselection, the anisotropic response, caused by the effect of a (directional) static magnetic field in the presence of anisotropic hyperfine interactions, can be preserved.

For the measurement of anisotropy curves, a certain magnetic field strength is kept constant and only the angle θ between the magnetic field direction and the $-z$ axis is varied in the *xz* plane as illustrated in **Figure 9.10** (*centre*). As a function of θ, a sinusoidal variation of the magnetic field effect is expected [209], cf. **Figure 9.10** (*right*).

9.2 Radical Pair EPR

Valuable information about the characteristics of radical pairs can also be obtained from EPR experiments. By out-of-phase (OOP) ESEEM measurements [34, 35, 228, 229], the dipolar, D, and exchange interactions, J, in radical pairs can often be determined [230–232] and inter-radical pair separation distances deduced. Detailed information on the origin and theoretical treatment of OOP-ESEEM is provided in references [233–237].

Furthermore, the spin polarisation of the radical pair EPR spectrum contains information on D and J as well as on the nature of the radical pair precursor. In the product basis of α and β states, the four radical pair states can be expressed as follows

$$\begin{aligned} |S\rangle &= \frac{1}{\sqrt{2}}\Big(|\alpha\beta\rangle - |\beta\alpha\rangle\Big) \\ |T_+\rangle &= |\alpha\alpha\rangle \\ |T_0\rangle &= \frac{1}{\sqrt{2}}\Big(|\alpha\beta\rangle + |\beta\alpha\rangle\Big) \\ |T_-\rangle &= |\beta\beta\rangle \end{aligned} \tag{9.8}$$

and consequently, if the radical pair is initially created in its singlet state, both $|\alpha\beta\rangle$ and $|\beta\alpha\rangle$ states are equally populated as shown in **Figure 9.11**. The transition frequencies of the four possible EPR transitions between the states, indicated in the figure, depend on the magnitude and sign of

D and J. Absorptive as well as emissive transitions are observed, due to either (i) the exclusive population of $|\alpha\beta\rangle$ and $|\beta\alpha\rangle$, if the radical pair is singlet-born, or (ii) the increased population[‖] of the $|\alpha\alpha\rangle$ and $|\beta\beta\rangle$ states in case of a triplet-born radical pair.

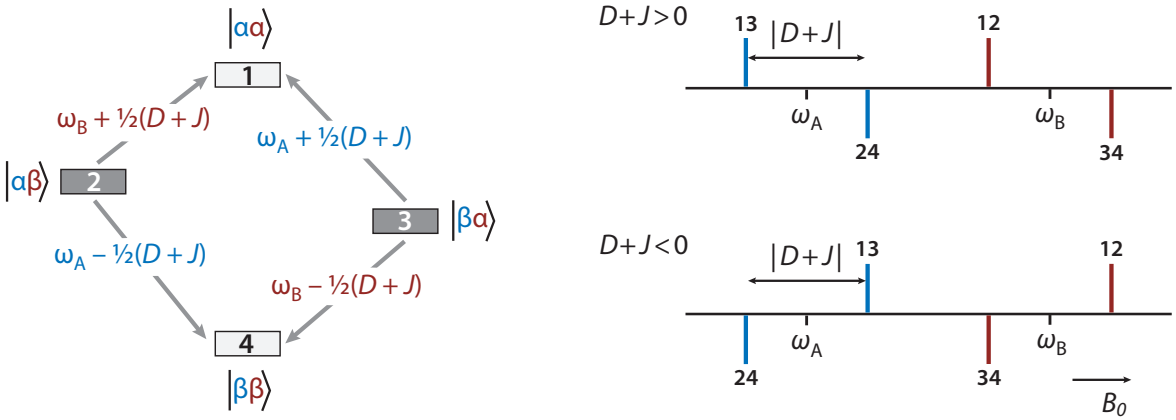


Figure 9.11: Illustration of the spin states of a singlet-born radical pair and the transitions between the states leading to the observation of a spin-polarised EPR signal.

For a given spin multiplicity the sign of $D+J$ determines the order of absorptive (a) and emissive (e) transitions (cf. **Figure 9.11**, *right*). Specified in order from low to high field, one distinguishes a/e and e/a polarisation patterns. The polarisation pattern is usually only indicated for the first radical, A, since that of the second radical, B, is identical. In typical organic systems, the g-factors of the two radicals forming the pair are usually not much different ($\omega_A \sim \omega_B$), so that the four transitions are rarely completely resolved at commonly used spectrometer frequencies (X-band). If more resolution is required, the experiments can for example be performed at Q- (34 GHz) or W-band (95 GHz). For a singlet-born radical pair, if $D + J > 0$, an a/e pattern is observed, whereas the order of transitions would be reversed in case of a triplet-born radical pair.

The situation becomes somewhat more complicated in isotropic frozen solution, where D is a function of the angle θ between the orientation of the molecule and the external field, $D = \omega_{dd}\,(3\cos^2\theta - 1)$, and a powder average over all possible orientations needs to be considered as illustrated in **Figure 9.12** for $J = 0$. The positions and polarisations of the individual transitions are indicated for the two extreme cases of $\theta = 0°$ and $\theta = 90°$ (*left*). Orientational averaging over all angles θ results in a Pake pattern for every transition (cf. **Figure 9.12**, *top right*) and the EPR signal observed in isotropic frozen solution is the sum of all signals and exhibits a characteristic anti-phase Pake lineshape as shown in **Figure 9.12** (*bottom right*).

In many cases, a good estimate of D is obtained from the inter-radical pair separation distance as determined for example by DFT calculations. If the nature (i.e. multiplicity) of the radical pair precursor is known, the sign of J can be determined from an analysis of the EPR polarisation pattern, sometimes also referred to as Chemically Induced Dynamic Electron Polarisation (CIDEP).

[‖] In case of a triplet-born radical pair the population of $|\alpha\alpha\rangle$ and $|\beta\beta\rangle$ is larger compared to the population of the $|\alpha\beta\rangle$ and $|\beta\alpha\rangle$ states. The latter are also populated if the radical pair is triplet-born owing to population of $|T_0\rangle$.

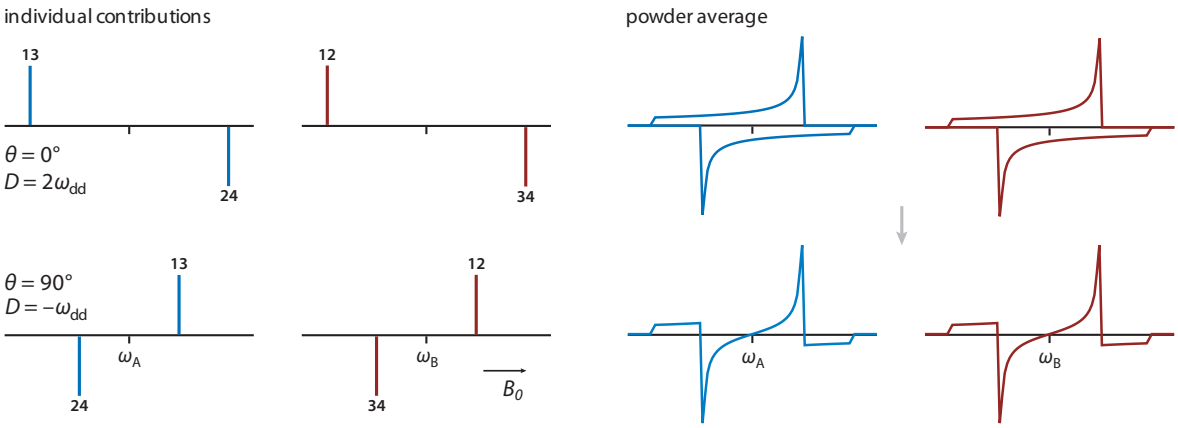


Figure 9.12: Illustration of the EPR transitions for a singlet-born radical pair at $\theta = 0°$ and $\theta = 90°$ for $J = 0$ (*left*) and the anti-phase Pake patterns resulting from powder averaging over all angles in isotropic frozen solution (*right*).

The exchange interaction, J, indicates the energy difference between singlet and triplet states ΔE_{ST}. Defining

$$\Delta E_{ST} = J(r) = E_T - E_S \tag{9.9}$$

so that the singlet state lies below the triplet states if $J > 0$, the following sign rule

$$\Gamma = \mu \cdot \text{sign}(J) \tag{9.10}$$

can be used to determine the sign of J. The factor μ is equal to $+1$ for a singlet precursor and -1 for a triplet precursor, and Γ equals $+1$ for a/e polarisation and -1 for e/a polarisation [238]. It shall be noted here that the definition of the factors μ and Γ depends on the definition of ΔE_{ST} and therefore the exchange coupling Hamiltonian. Different variations are encountered in the literature and so only the relative order of the singlet and triplet states should be compared which must be equal for any particular case. An example of an application of **Equation (9.10)** shall be given here: Assuming a low field e, high field a polarisation pattern was observed for a radical pair formed from a singlet precursor molecule, we have $\mu = +1$ and $\Gamma = -1$, indicating $J < 0$ and therefore that the triplet state is lower in energy as compared to the singlet state, $E_S > E_T$.

For charged radical pairs, the singlet-triplet energy gap, ΔE_{ST}, and therefore also the sign of J has been proposed to depend on the reaction free energy, ΔG_0, and the reorganisation energy, λ [239, 240] and both cases, $E_S \gtrless E_T$, have been encountered depending on the studied radical pair system and the properties of the reaction medium.

Chapter 10

Chemical Compass Behaviour of a Carotenoid–Porphyrin–Fullerene Triad

In Chapter 9 it was argued that the results from behavioural studies on birds are in good agreement with the radical pair hypothesis. However, to date, it has not yet been shown convincingly that fields as small as the Earth's magnetic field can have a sufficiently significant effect on a chemical reaction so as to account for the avian compass behaviour. In order to provide experimental support for the involvement of the RPM in birds' navigation, it therefore needs to be demonstrated that a model system can act as a chemical compass. Such a chemical compass system is required to (i) be sensitive to fields as weak as the Earth's magnetic field and (ii) additionally exhibit an orientation-dependent magnetic field response.

The system we chose for the experimental investigations is a molecular triad system, composed of a carotenoid (**C**), a porphyrin (**P**) and a fullerene (**F**) moiety, which has been synthesised in the laboratories of Prof. Devens Gust (Arizona State University, USA). The chemical structure of the molecule, henceforth referred to as **CPF**, is shown in **Figure 10.1**.

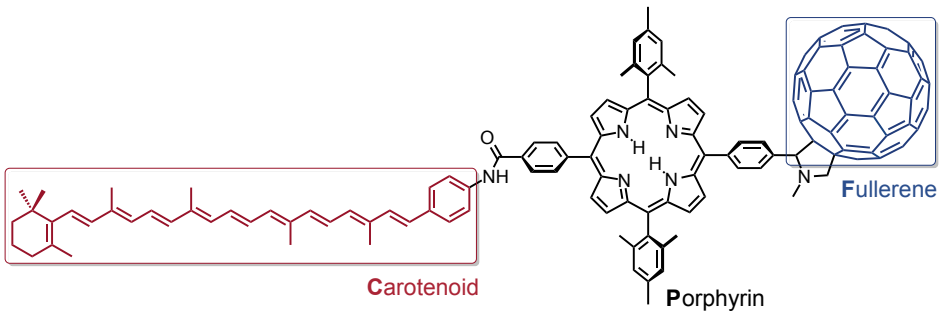


Figure 10.1: Chemical structure of the investigated **CPF** triad.

Previous studies revealed that this system fulfills all the necessary requirements of a suitable model system for the detection of hyperfine-driven magnetic field effects [209, 241] and MFEs at very small fields have indeed been detected. However, so far, no orientation-dependence of these effects could be shown in the low field region, relevant to avian magnetoreception. In the only published study reporting anisotropic magnetic field effects, magnetic fields about 100 times larger than the Earth's magnetic field were employed.

The mechanism underlying the magnetic field dependence is known to be considerably different in the low field region [171, 172] as compared to higher fields. Consequently, in order to demonstrate

convincingly that the radical pair model can be at the origin of the avian magnetic compass, it needs to be shown that anisotropic MFEs can be observed in the low field region.

Similar triad systems to that investigated in this study, possessing different side groups and linkers, have been synthesised in the last decades for the study of artificial photosynthesis and their photophysics were thoroughly characterised both by optical studies [242–244] and transient EPR [104, 245]. In general, it is found that the overall excited state reaction scheme is similar for these molecules, although the time constants for charge separation and charge recombination can be considerably influenced by small structural changes. The properties of a variety of cartenoid–porphyrin–fullerene triad molecules are compared in reference [246], also including a photophysical characterisation of the investigated **CPF** triad in **MTHF** at room temperature.

Based on the available data, a (simplified) photoscheme can be proposed for triad **CPF** as shown in **Figure 10.2**. Photoexcitation of the triad molecule mainly yields the first excited state of the porphyrin and is followed by energy and electron transfer to generate the primary radical pair ^{1}**[C-^{2}P$^{\bullet+}$-^{2}F$^{\bullet-}$]**. The long-lived singlet state radical pair ^{1}**[^{2}C$^{\bullet+}$-P-^{2}F$^{\bullet-}$]** is then formed upon further charge separation and can undergo hyperfine-driven singlet-triplet interconversion. A small fraction of the radical pairs (∼7 %) have also been shown to be initially formed in the triplet state [241]. Charge recombination from the singlet state mainly regenerates the ground state, whereas the triplet radical pairs recombine to yield the low-lying triplet state of the carotenoid. Some of the kinetic time constants of the involved processes and spectral features of the reaction intermediates are known from the studies at room temperature.

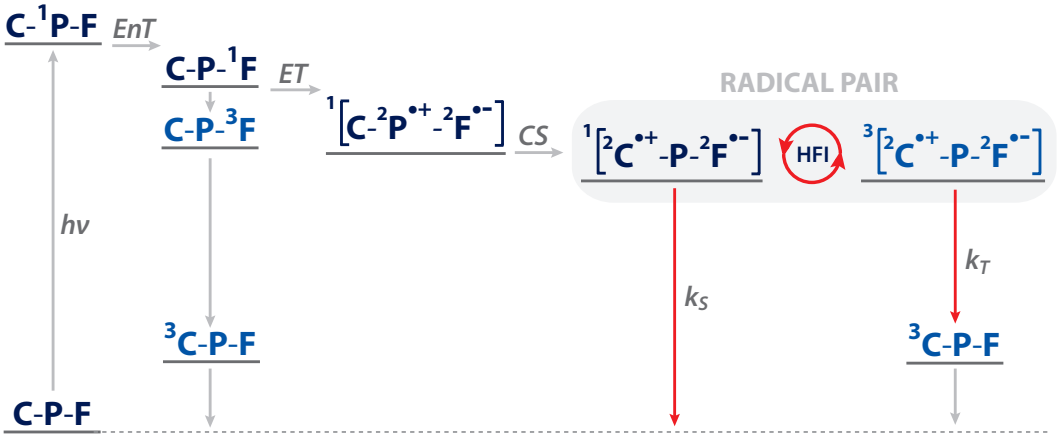


Figure 10.2: Simplified photoscheme postulated for the **CPF** triad. *EnT*: energy transfer; *ET*: electron transfer; *CS*: charge separation.

However, as mentioned in the preceding chapter, to optimise the properties of the medium (η, ε_r) for the observation of anisotropic magnetic field effects, the MFE experiments in this study are performed in frozen **MTHF** at 120 K and it is therefore also desirable to carry out the photophysical characterisation of the triad system under the same conditions. The corresponding experiments will be presented in the following section.

At 120 K, the charge recombination from the singlet state was found to be faster for **CPF** as compared to recombination from the triplet state, $k_S > k_T$ [241]. Furthermore, it has been established that the charge recombination reactions from the singlet and triplet states in this

system proceed in the Marcus inverted and Marcus normal regions, respectively [246]. Therefore, k_S should dominate in high polarity solvents, whereas k_T should be favoured at lower polarities, in agreement with the experimental observations at 120 K ($\varepsilon_r \sim 19$).

10.1 Characterisation by Optical Spectroscopy and Transient EPR

To validate the proposed excited state reaction scheme for **CPF** at 120 K, a basic photophysical characterisation of the triad was carried out. All optical experiments in this section were performed in the laboratories of Prof. M. R. Wasielewski (Northwestern University, USA) under the supervision of Prof. Ryan Young and with help from Claire Miller, Brian Phelan and Dr. Ma Lin. The data analysis was performed at Oxford using home-written MATLAB routines. Further details on the sample preparation, experimental setup and data treatment are given in Appendix A (cf. **Sections A.1** and **A.6**).

10.1.1 Absorption and Fluorescence

Figure 10.3 (*left*) shows a comparison of the UV-vis spectra recorded for **CPF** at room temperature and 120 K. It can be observed that the absorption bands are considerably sharpened at lower temperature. The porphyrin Soret and Q-bands (peaks at ~420 nm, 550 nm, 590 nm, 650 nm) are observed roughly at the same wavelengths in both spectra, whereas the three prominent absorption bands of the carotenoid between 450 and 540 nm are red-shifted at 120 K as compared to room temperature. In the MFE experiments carried out at 120 K, the molecule can thus be excited at 532 nm. In **Figure 10.3** (*right*) the room temperature fluorescence spectrum of the triad is displayed, which coincides with the fluorescence spectrum of a typical free-base porphyrin with intensity maxima at 650 and 720 nm.

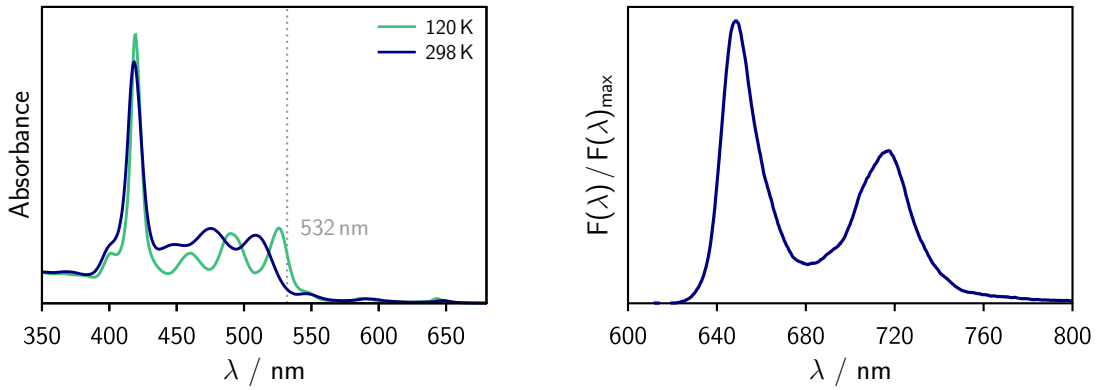


Figure 10.3: Comparison of the UV-vis absorption spectra at 120 K and room temperature (*left*) and steady state fluorescence spectrum recorded at room temperature (*right*) of the **CPF** triad in **MTHF**. The dotted line indicates the excitation wavelength chosen for the MFE experiments.

The time-resolved fluorescence traces recorded for **CPF** in **MTHF** at room temperature using a streak camera are shown in **Figure 10.4**. Different time windows were used for different time resolution. The time-resolution using a time window of 1 ns amounts to roughly 40 ps. The kinetics

of the fluorescence decay does not markedly depend on the chosen emission wavelength and is at least bi-exponential. About 80 % of the intensity has decayed after 200 ps, suggesting a lifetime of the shortest component of less than 100 ps, in good agreement with the results presented in [246], where a value of 34 ps was determined.

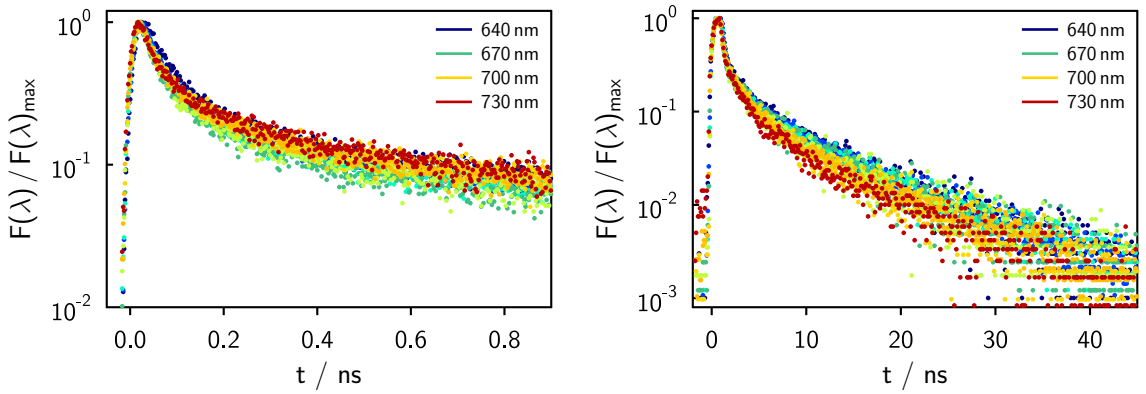


Figure 10.4: Fluorescence decay traces recorded at different emission wavelengths (as indicated) for **CPF** after excitation at 415 nm. The time window of the streak camera was set to either 1 ns (*left*) or 50 ns (*right*).

10.1.2 Transient Absorption Spectroscopy

In reference [246], the results from transient absorption studies are presented for **CPF** in **MTHF** at room temperature. It is suggested that the primary radical pair ^{1}[**C**-^{2}**P**$^{\bullet+}$-^{2}**F**$^{\bullet-}$] is formed from **C**-^{1}**P**-**F** in 34 ps, following generation of ^{1}[^{2}**C**$^{\bullet+}$-**P**-^{2}**F**$^{\bullet-}$] in 120 ps. The radical pair lifetime of 57 ns is found to correlate with the rise of the absorption of ^{3}**C**-**P**-**F**, which decays with a lifetime of 4.9 μs.

In the present work, transient absorption spectra from the femtosecond to the millisecond time regime were acquired for **CPF** in **MTHF** at different temperatures to elucidate the spectral characteristics of the reaction intermediates and the approximate kinetics at the temperature chosen for the MFE experiments. The corresponding data recorded in the visible and near infrared regions are shown in **Figure 10.5** for temperatures of 95 K, 120 K, 160 K, and room temperature, corresponding to dielectric constants of 2.7, 19, 13, and 7.0, respectively. As discussed in the previous chapter, the polarity of the medium should considerably influence the radical pair formation yield and recombination kinetics. In the figure, the TA spectra are shown at selected time delays (as indicated).

In agreement with previous literature results and **Figure 10.2**, it is observed at all temperatures that the excited state absorption of the porphyrin (∼550–800 nm), present at early times (<10 ps), decays at the same time as the absorption of the carotenoid radical cation rises in the near infrared (bands at ∼1000 nm and 1450 nm). The decay of the **C**$^{\bullet+}$ ion band is correlated with the formation of the carotenoid triplet state (∼550 nm). By visual inspection, the involved reaction steps appear to be the same at different temperatures, while the time constants of the different processes and the relative reaction yields vary significantly. The spectral position of some absorption bands -

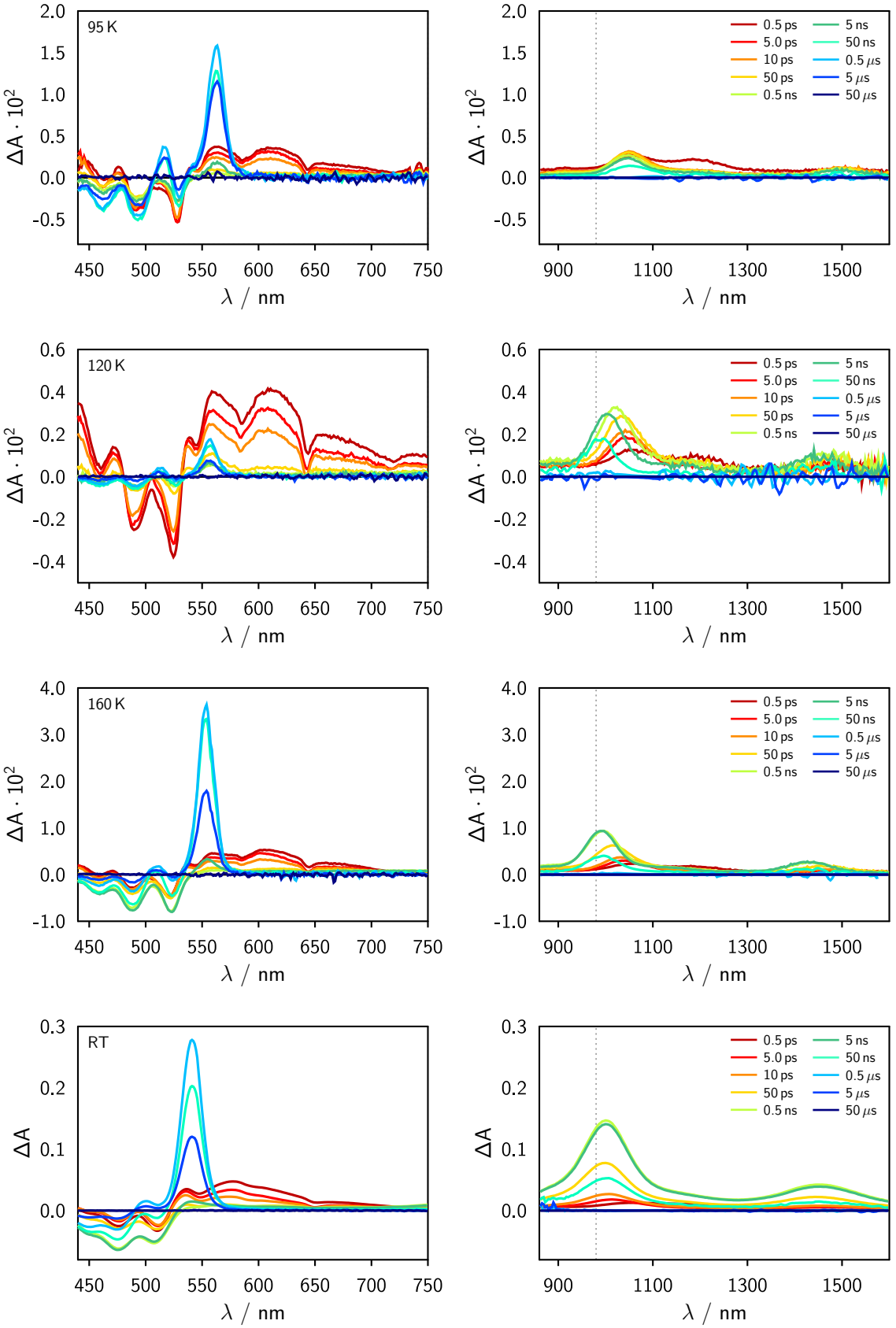


Figure 10.5: Transient absorption spectra at selected time delays (as indicated) recorded in **MTHF** solution after photoexcitation of **CPF** at 415 nm. The spectra were taken at four different temperatures of 95 K, 120 K, 160 K, and room temperature (*top* to *bottom*). The dotted line indicates the probe wavelength chosen in the MFE experiments.

especially of those corresponding to carotenoid features - appears to be strongly dependent on the properties of the medium.

Looking in particular at the TA spectra recorded at 120 K, the ground state bleach ($\Delta A < 0$) can be observed (mainly) below 550 nm at early times. During the same time window, the excited state absorption ($\Delta A > 0$) of the porphyrin is observed between 550 and 800 nm, with superimposed stimulated emission bands ($\Delta A < 0$) at 650 and 720 nm. In the near infrared, we can see the rise of the carotenoid radical cation bands with peaks around 1050 and 1450 nm, which considerably blue-shift with time, and finally, after decay of the ion band, a peak at 560 nm, characteristic for the carotenoid triplet state, appears and later decays.

In **Figure 10.6**, the absorption and fluorescence spectra of the triad are displayed on the same wavelength scale as the TA spectra for better illustration of the contributions of ground state bleach and stimulated emission to the shape of the TA spectra.

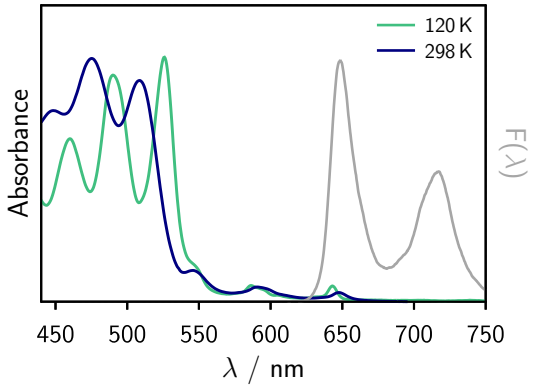


Figure 10.6: Absorption and fluorescence spectra of **CPF** depicted on the same wavelength axis as the TA data for better comparison as well as illustration of the contributions of ground state bleach and stimulated emission to the shape of the TA spectra.

The TA spectra at 120 K and room temperature were also subjected to a kinetic analysis. The species associated spectra obtained from global target analysis following the sequential model $A \rightarrow B \rightarrow C \rightarrow D \rightarrow E$ are shown in **Figure 10.7** together with the corresponding time constants. Since the time constants for the different steps are sufficiently different, the spectral separation works well. For 120 K it is found that the excited state of the porphyrin (species A) decays in about 15 ps to form the radical pair (species B) which has a lifetime of roughly 100 ns and finally the carotenoid triplet state (species D) is found to decay with a lifetime of about 6 μs to the ground state (species E).* At room temperature, all of these processes seem to be slightly faster (as also indicated in the figure) and the relative amplitudes of the individual species associated spectra are clearly different. Judged by the relative spectral intensities, the relative formation yield of the carotenoid triplet state appears to be increased at room temperature as compared to 120 K, suggesting that recombination from the triplet state is preferred at room temperature, while the opposite seems to be the case at 120 K.

*The fifth species, species C in the sequential model, is needed to account for the pronounced blue-shift of the ion absorption band at 120 K. The data at room temperature might be fit with only three time constants (four species), but was nevertheless fit with four time constants here for better comparability.

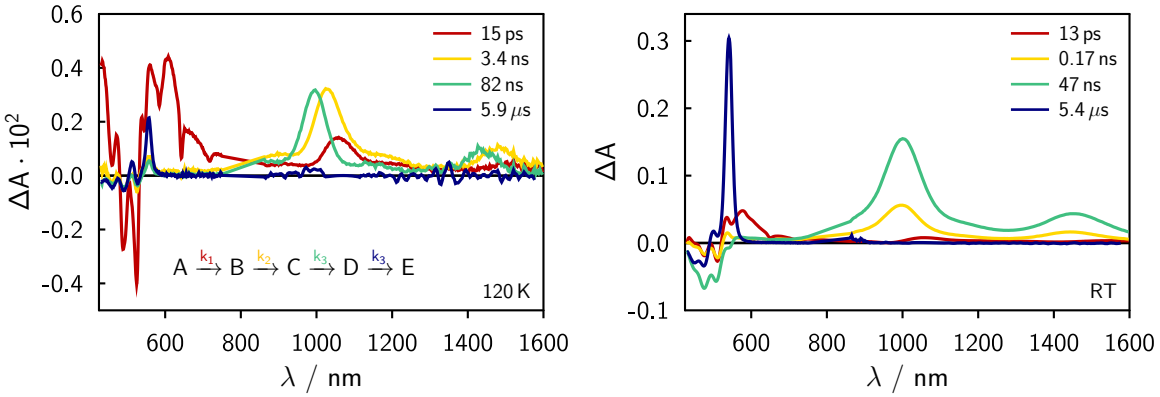


Figure 10.7: Species associated difference spectra calculated for the TA data of **CPF** recorded at 120 K (*left*) and room temperature (*right*). A sequential reaction scheme, as shown in the figure, was assumed and the time constants are indicated.

The spectral features of the reaction intermediates and their time behaviour at 120 K are also shown in form of a TA contour plot in **Figure 10.8**. The solvent-induced pronounced blue shift of the carotenoid radical cation absorption band can clearly be seen in this representation of the data.

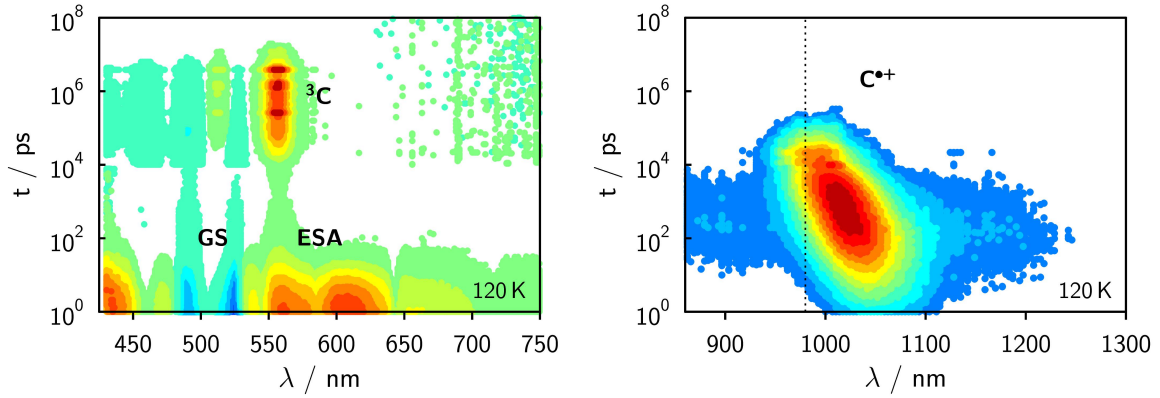


Figure 10.8: Contour plot of the TA data recorded for **CPF** in **MTHF** solution at 120 K in the visible (*left*) and near infrared (*right*) regions. The dotted line indicates the probe wavelength chosen in the MFE experiments. GS: ground state; ESA: excited state absorption.

In **Figure 10.9** the solvent shift of the $\mathbf{C^{\bullet+}}$ ion band is illustrated at different temperatures. It is interesting to note how strongly the position of the ion band is influenced by the polarity of the medium. In apolar environment, encountered for instance at 95 K and room temperature (cf. **Figure 10.5**), the position of the band does not change markedly with time, while both at 120 K and 160 K the ion band shifts towards the blue by about 50 nm (albeit at different rates), from 1050 to 1000 nm.

Based on the results from TA experiments and the wavelength characteristics of the available NIR laser diodes, a probe wavelength of 980 nm was chosen to detect the absorbance of the carotenoid radical cation in the MFE experiments.

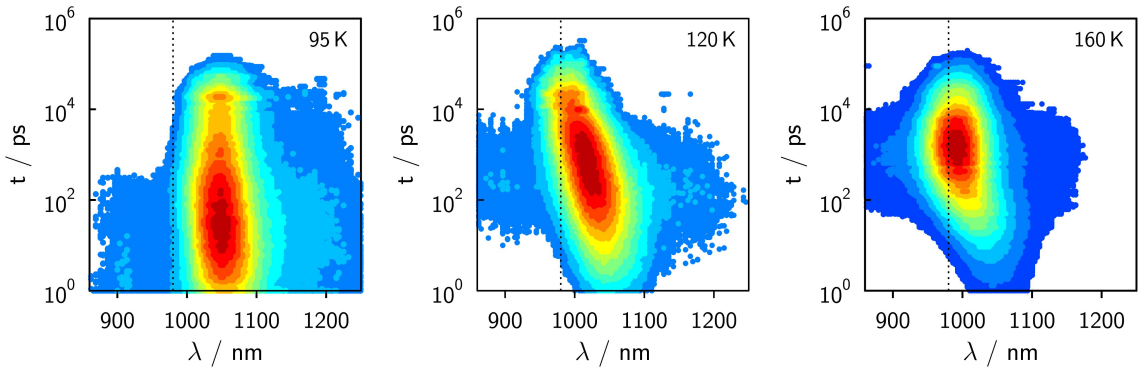


Figure 10.9: Illustration of the temperature dependence of the characteristic $\mathbf{C}^{\bullet+}$ absorption band in the near infrared. Contour plots are shown for three temperatures of 95 K, 120 K, and 160 K, corresponding to relative permittivities ε_r of about 2.7, 18.5, and 13.0, respectively.

10.1.3 Transient cw EPR

Some of the excited state intermediates postulated to be present in the studied system, like $^3\mathbf{F}$ or $\mathbf{F}^{\bullet-}$, cannot easily be detected optically, mainly due to their small excited state extinction coefficients. Transient EPR spectroscopy was thus employed to get some complementary information. By EPR we expect to be able to see all intermediates with unpaired electron spins, i.e. the radical pair and any formed triplet states. The EPR spectra shown in **Figure 10.10** were performed at 90 K.[†] In the central part of the spectrum, the radical pair, with its narrow antiphase spectral feature and a comparatively short lifetime, can clearly be identified. Additionally, two different triplet states with different time behaviour are detected, which can be attributed to the fullerene and the carotenoid [104, 247]. EPR thus allows the detection of the fullerene triplet state, which could not be observed optically.

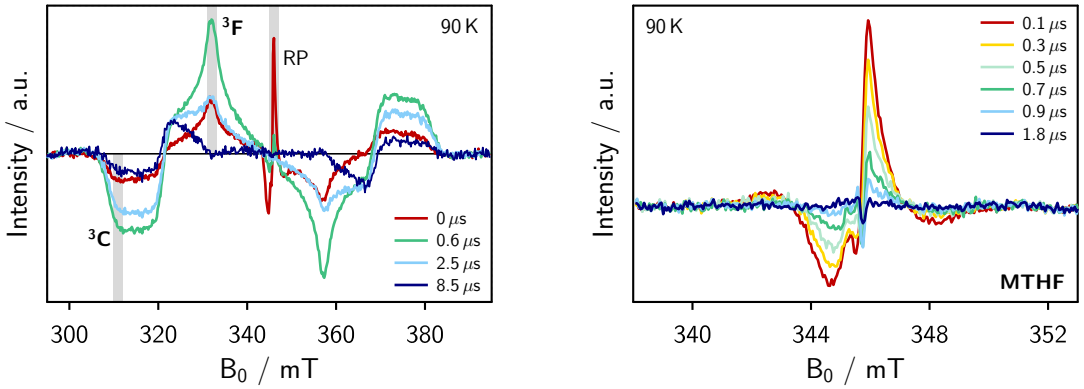


Figure 10.10: Transient cw EPR spectra of **CPF** recorded in frozen **MTHF** at 90 K averaged for different delay times after laser excitation (as indicated). Scans over a wider (*left*) and narrower (*right*) field range are shown.

[†]At 120 K, the high dielectric constant of the solvent leads to increased losses in the cavity and critical coupling of the EPR resonator becomes challenging. Experiments were also performed at 120 K, but are not shown here. The reaction kinetics differ between 90 K and 120 K, but the relative spectral intensities and spectral shapes were found to be virtually identical.

In **Figure 10.10** (*right*) the EPR spectrum is shown in a narrower field range, only covering the features of the radical ion pair. The radical pair EPR spectra recorded at different times after laser excitation reveal the time evolution of the signal. A two dimensional background correction was applied to remove the sloping background stemming from the superimposed triplet signals. The spin polarisation of the radical pair, *e*/*a*, is consistent with a singlet precursor (cf. **Figure 9.12**). By comparison of the spin polarisation of the observed fullerene triplet spectrum with that of a model fullerene triplet, it could be shown [247] that the fullerene triplet is formed by normal intersystem crossing. On the contrary, the carotenoid triplet state seems to be formed by radical pair recombination, based on its spin polarisation, *eaaeea*, which cannot arise from intersystem crossing and is characteristic for a triplet with $D < 0$ populated exclusively in the $|T_0\rangle$ high field sublevel.

Combining the results from UV-vis, fluorescence, transient absorption and transient EPR spectroscopies, the validity of the proposed reaction scheme for **CPF** (cf. **Figure 10.2**) could be confirmed.

10.2 Magnetic Field Effects in the Low Field Region

In the magnetic field effect experiments, using the setup presented in detail in the preceding chapter, the porphyrin moiety is excited at 532 nm and the absorbance of the carotenoid radical cation is probed in the near infrared at 980 nm. The sample preparation is outlined in Appendix A (cf. **Section A.1**) and the results presented in the following sections have been obtained in collaboration with Dr. Christian Kerpal.

Figure 10.11 shows exemplary kinetics of the **CPF** triad recorded at 15 G in comparison with the reference data taken at zero field. The presence of a magnetic field changes the relative concentrations of the singlet and triplet radical pairs and therefore the relative amplitudes of k_S and k_T contributing to the overall kinetics detected by transient absorption. The two transient absorption signals in the presence and absence of a magnetic field are then subtracted from each other to obtain the signal labelled $\Delta\Delta A$, referred to as the so-called subtraction signal and defined according to

$$\Delta\Delta A(t) = \Delta A(t, B_0) - \Delta A(t, B_0 = 0) \tag{10.1}$$

When dividing the subtraction signal by the transient absorption signal in the absence of any field, the time dependent magnetic field effect is obtained, indicating the relative variation of the change in product yield.

When looking at the time-dependence of the subtraction signal in **Figure 10.11**, a biphasic behaviour is observed, suggesting a complex interplay of radical pair recombination and spin relaxation rates. The recombination rates k_S and k_T for any particular system should only depend on the solvent properties and should therefore be constant at a chosen temperature, whereas spin relaxation may be field dependent. At a magnetic field of 15 G, we are outside the low field region of this system. Compared to $B_0 = 0$, the singlet population should therefore be increased at a field of 15 G. If $k_S \gg k_T$, recombination is expected to be enhanced in the presence of a magnetic field as compared to its absence, leading to a decrease in the overall radical population and

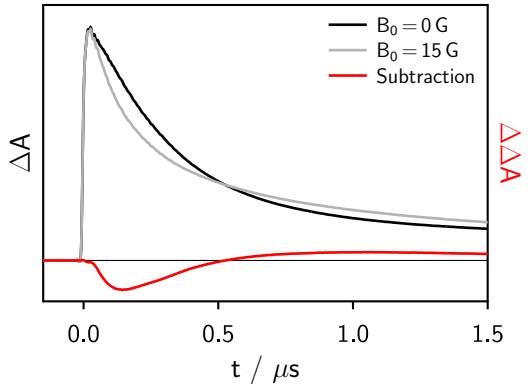


Figure 10.11: Illustration of the magnetic field sensitivity of the radical pair recombination kinetics of **CPF** probed at 980 nm in **MTHF** solution at 120 K.

consequently a negative $\Delta\Delta A$ signal. A negative subtraction signal is indeed observed at 15 G for early times. The unusual phase inversion at times beyond 500 ns could be simulated and explained considering additionally that about 7 % of all radical pairs are initially born in their triplet state [241]. A corresponding inversion of the cw EPR polarisation pattern from e/a for a singlet-born radical pair to a/e for a triplet-born radical pair could also be observed in the cited work. In the spectra shown in **Figure 10.10** (*right*) for 90 K, only the onset of this inversion can be seen from the spectrum shown in dark blue (1.8 μs).

According to the considerations outlined in Chapter 9, the time-dependence of the subtraction signal of this system is expected to be inverted in the low field region. The width of the low field region depends on the magnitude of the effective hyperfine coupling constant and extends to roughly 7 G for **CPF** as illustrated in **Figure 10.12**. In this figure, three MARY curves are shown, averaged for time windows of 20 ns centred around the indicated times. As expected from the subtraction curve for 15 G discussed above, it can be seen that the MARY curve flips between early and later times. In **Figure 10.12** (*right*) the subtraction curves obtained at magnetic field strengths of 2 G and 15 G are compared. The time-dependence of the subtraction curve corresponding to the low field region (2 G) is inverted as compared to that for higher fields. The times after laser excitation corresponding to the MARY curves are indicated.

Considering the field-dependence of the MFE for **CPF**, it is noted that the detection of a field effect becomes increasingly difficult as we go to fields lower than 2 G, but measurements at fields comparable to the Earth's magnetic field were motivated by the aim of validating the radical pair hypothesis for avian magnetoreception.

10.2.1 Earth's Field Effect

Compared to the subtraction signal obtained at 15 G, the field effect at Earth's field (0.5 G) is almost invisible as shown in **Figure 10.13** (*left*), but optimisation of the signal-to-noise eventually allowed the detection of a reasonable signal at 0.5 G. The subtraction curve has the expected time dependence, confirming that the **CPF** triad indeed shows a magnetic field effect at Earth's field. The displayed subtraction signal corresponds to a MFE of +0.4 % at 80 ns and −0.6 % at 0.6 μs.

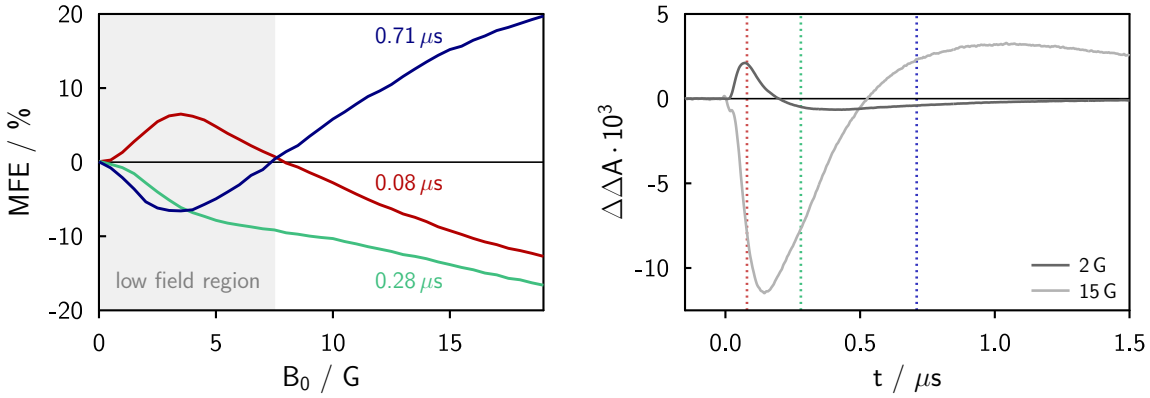


Figure 10.12: Magnetic field effect as a function of field at three different characteristic times of 0.08 μs, 0.28 μs, and 0.71 μs after laser excitation (*left*) and subtraction signal ΔΔA as a function of time for two different field strengths of 2 G and 15 G (*right*) for the **CPF** triad measured in frozen **MTHF** at 120 K.

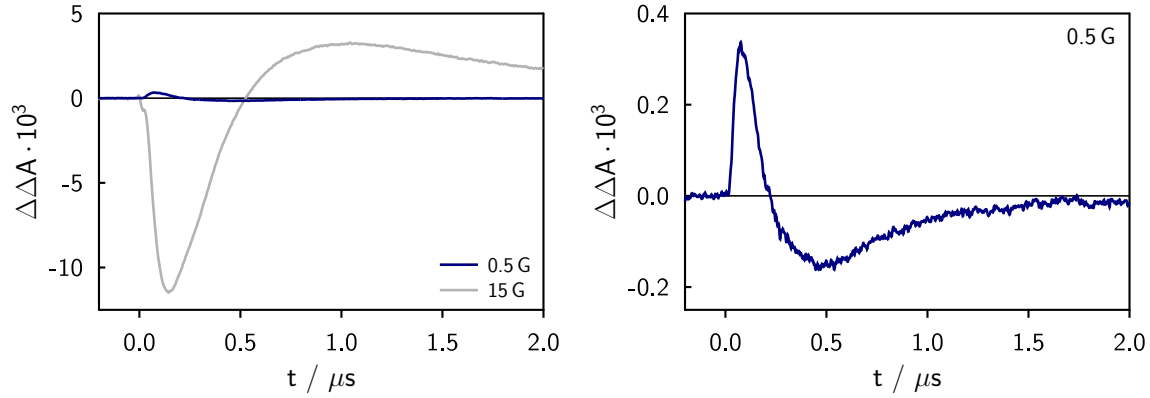


Figure 10.13: Subtraction signal ΔΔA as a function of time measured at 0.5 G for **CPF** in frozen **MTHF** at 120 K.

10.2.2 Isotope Effect

To prove that the MFEs in this system are hyperfine-driven, complementary experiments were performed on a partially deuterated analogue of the **CPF** triad. In the partially deuterated molecule shown in **Figure 10.14**, some of the hydrogens on the carotenoid backbone have been replaced by deuterium.

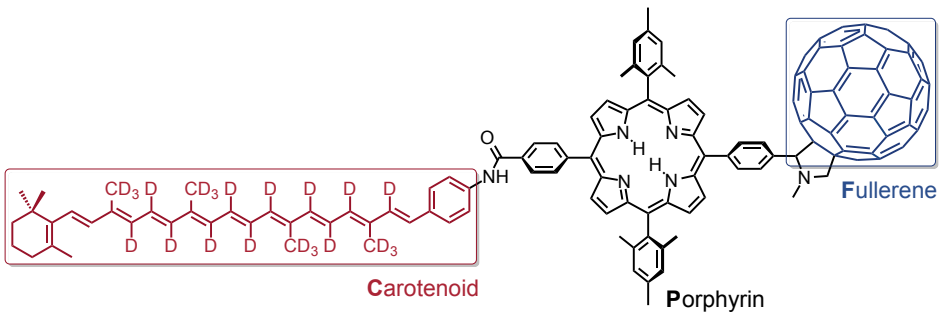


Figure 10.14: Chemical structure of the partially deuterated analogue of the **CPF** triad.

Deuteration decreases the proton hyperfine couplings by a factor of roughly 6.5 according to the ratio of the respective nuclear g-factors ($\frac{g_{n,H}}{g_{n,D}} = \frac{5.586}{0.857}$). Consequently, the effective hyperfine field created by the radicals is expected to be smaller in the case of (partial) deuteration, which should influence the magnetic field dependence of the MFE. In **Figure 10.15** (*left*) MARY curves recorded for a field range from −5 G to +5 G are shown for the protonated and partially deuterated **CPF** triad at different time delays after laser excitation. When comparing the results, it is observed that the field-dependence of the MARY curve is altered for the deuterated analogue, showing that the effect indeed depends on the hyperfine coupling constants of the system. In particular, the low field region is narrower for the deuterated triad, seen most clearly from the curves recorded at 0.71 μs after laser excitation, as it would be expected in case of a smaller effective hyperfine coupling.[‡] Within experimental error, the kinetics of the molecule in the absence of any field do not seem to be affected by deuteration as shown in **Figure 10.15** (*right*).

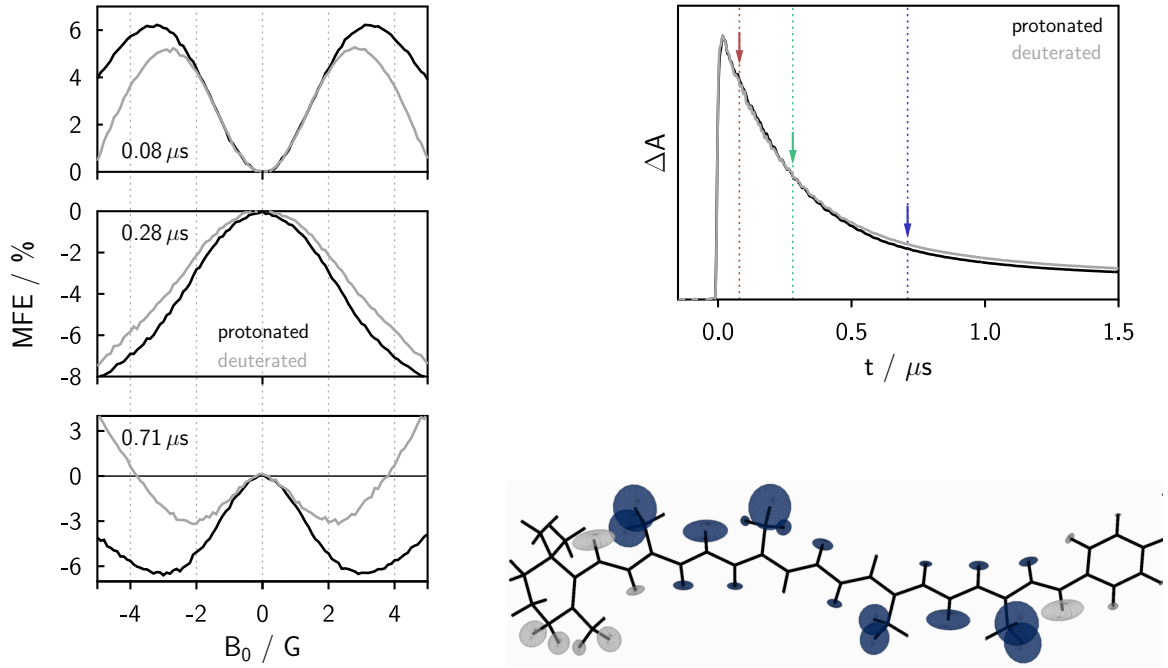


Figure 10.15: Isotope effect on the magnetic field effect of **CPF** recorded in **MTHF** solution at 120 K. Comparison of the MARY curves of the protonated and partially deuterated triad (*left*) and the corresponding kinetics in the absence of any external magnetic field (*right*). The hyperfine coupling tensors of the protons on the carotenoid backbone which were replaced by deuterium in the partially deuterated triad are marked in dark blue.

The figure also shows a visualisation of the proton hyperfine coupling tensors on the carotenoid moiety calculated for the molecular triplet state of the triad. For the charge separated state, geometry optimisation was unfortunately not successful. However, the structural changes and therefore the effect on the electronic structure as well as the hyperfine couplings are expected to be small. The DFT (B3LYP/EPRII) calculations were performed by Dr. Christian Kerpal and

[‡]Considering a molecule with n nuclei, characterised by a hyperfine coupling constant, a, and spin I, the effective hyperfine coupling a_{eff} is formally defined as $a_{\text{eff}} = \sqrt{\frac{1}{I_m(I_m+1)} \sum_{i=1}^{n} a_i^2 \, I_i(I_i+1)}$, where I_m is the spin of the chosen model nucleus.

the results are in good agreement with the data presented in reference [209]. In the figure, the hyperfine tensors of the protons replaced by deuterium in the deuterated triad are highlighted in dark blue.

10.3 Orientation Dependent Magnetic Field Effects

As already discussed, only one case can be found in the literature where hyperfine-driven anisotropic magnetic field effects have been reported [209]. However, these experiments were performed at comparatively high fields of $>30\,\mathrm{G}$, well outside the low field region. Since the design of the experimental setup used for the detection of anisotropic MFEs was considerably improved in this work, leading to better signal stabilities and a higher signal-to-noise ratio, anisotropy measurements in the low field region could be attempted.

The sample geometry was illustrated in the preceding chapter. All the anisotropy curves presented in this section have been recorded at horizontal laser polarisation with respect to the surface of the laser table for both pump and probe beams. This polarisation is referred to as h/h. The $\lambda/2$ plates used to adjust the polarisations were both precisely calibrated. The electric field of the laser beam is thus parallel to the x axis of the laboratory frame. In the anisotropy experiments, the field angle θ is varied in the xz plane, where $\theta = 0^\circ$ corresponds to a field applied in $-z$ direction of the laboratory frame. Both laser beams propagate along the y axis.

It has been proposed that the transition dipole moment of **CPF** is approximately aligned along the long axis of the molecule based on DFT calculations [227]. Consequently, using h/h polarisation, we should expect to excite molecules preferentially with their long axis aligned along $\pm x$. The orientation of the hyperfine coupling tensors visualised in the molecular frame in **Figure 10.16** suggests that the effective hyperfine field in **CPF** is also approximately aligned along the long axis of the molecule, which should facilitate the data analysis. Furthermore, it may be concluded that the large anisotropic hyperfine couplings responsible for the anisotropic effect correspond to protons directly attached to the carotenoid backbone, whereas the methyl protons on the carotenoid moiety contribute with large isotropic hyperfine couplings and are thus somewhat unfavourable for the detection of anisotropic effects.[§]

The dependence of the magnetic field effect on the angle θ between the magnetic field direction and the $-z$ axis of the laboratory frame is expected to respect the symmetry relationship [209]

$$\mathrm{MFE}(\theta) = \mathrm{MFE}(\theta + \pi) \tag{10.2}$$

For a more precise evaluation of the effect, the following function [209] is fitted to the experimental data

$$\mathrm{MFE}(\theta) = \mathrm{A} \cdot \cos\big(2(\theta - \phi)\big) \tag{10.3}$$

where A is a constant MFE offset value and ϕ characterises the phase.

[§] Also in view of the fast rotation of the methyl groups, the presence of these functional groups might hinder the detection of anisotropic effects.

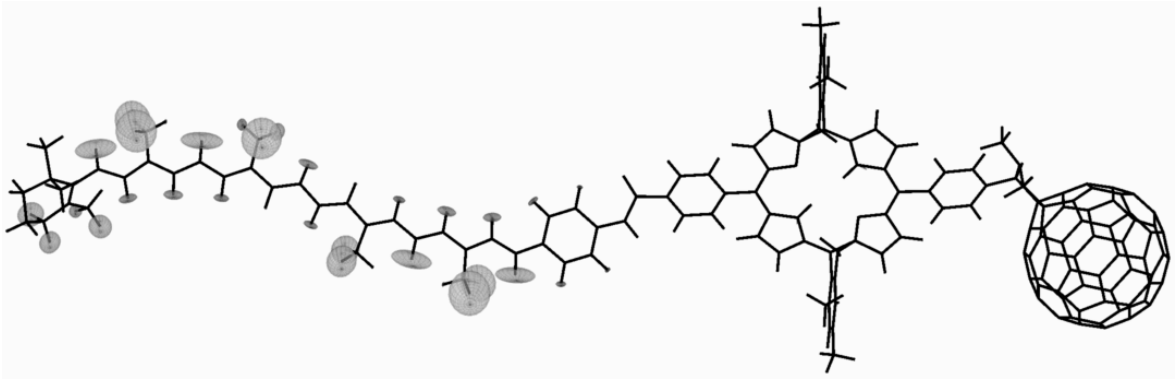


Figure 10.16: Visualisation of the hyperfine coupling tensors of the **CPF** triad calculated in ORCA using DFT (B3LYP/EPRII) for the triplet state as mentioned in the section above. The length of the whole molecule amounts to roughly 5.6 nm.

For the magnetic field effect anisotropy measurements, magnetic field strengths of 1 G and 2 G were chosen. **Figure 10.17** shows the corresponding MFE subtraction curves for **CPF**. The centre values of the two time windows with a width of 20 ns, over which the magnetic field effect anisotropy was averaged, are indicated in the figure and correspond to delay times of 0.08 and 0.28 μs after laser excitation.

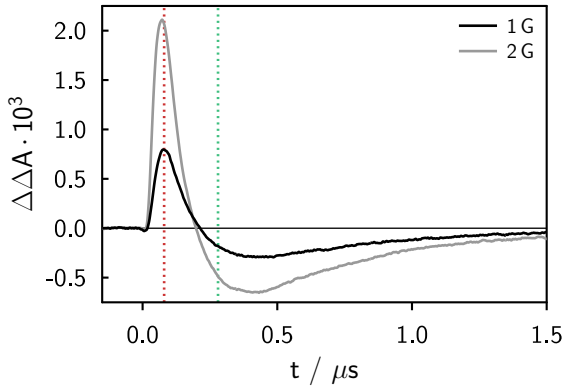


Figure 10.17: Magnetic field effect subtraction signal ΔΔA of **CPF** as a function of time for two field strengths of 1 G and 2 G. The centre values of the time windows for which the anisotropy curves were averaged are indicated by dotted lines.

In **Figure 10.18** the MARY curves for the **CPF** triad are shown for magnetic fields up to 5 G together with the corresponding anisotropy curves recorded at 1 G and 2 G. In all cases a sinusoidal variation of the magnetic field effect with θ could clearly be observed. The good fit of **Equation (10.3)** to the data (black lines) shows that the data follow the expected functional dependence. Representative error bars are shown in grey and indicate that the observed anisotropy is significant.

Looking back at the MARY curves (**Figure 10.18**, *left*), averaged over the same time windows as the anisotropy data, we can see again that the MARY curve flips between early (0.08 μs) and later (0.28 μs) times. We should thus expect to see a corresponding phase flip also in the anisotropy data, which is indeed observed in the data for both field strengths. Phenomenologically, this phase

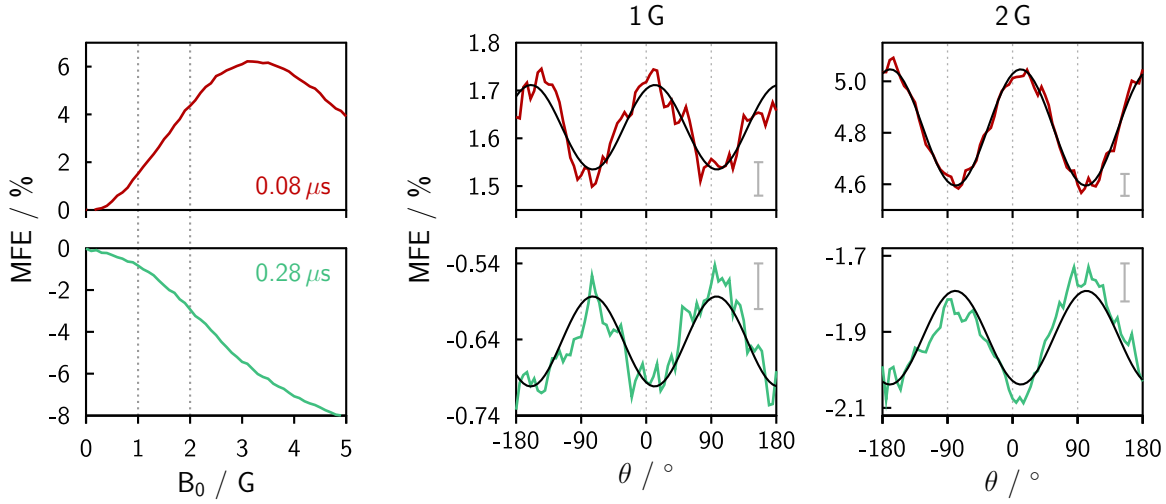


Figure 10.18: MARY curves recorded at two different times of 0.08 μs (red) and 0.28 μs (green) after laser excitation (*left*) and corresponding MFE anisotropy curves measured at two different magnetic field strengths of 1 G (*centre*) and 2 G (*right*) for triad **CPF**. Fits to the data are shown in black and representative error bars are indicated in grey. The averaging time window around the indicated centre values had a width of 20 ns.

flip can be explained as follows: To a first approximation it can be assumed that the phase of the anisotropy is related to the slope of the corresponding MARY curve. The effective field experienced by the radicals is the vector sum of the external and hyperfine fields. If the effective field, at a particular orientation of the molecule, is bigger than the external field (plotted on the x axis of the MARY curve), we would expect an increased signal intensity in case of a positive slope, while a negative slope of the MARY curve should result in a smaller signal. Consequently, whenever the relative orientation between the molecules and the external magnetic field changes, we are effectively moving up and down the respective MARY curve, leading to the sinusoidal dependence of the MFE signal detected in the anisotropy experiments.

In **Figure 10.19** the phase flip in the anisotropy data is additionally illustrated in form of a polar plot for the two field strengths of 1 G and 2 G. The colour-coding is the same as in previous figures.

Validation of the Results

The results from the anisotropy measurements presented above indicate that a hyperfine-driven orientation-dependent magnetic field effect is observed for **CPF** at fields comparable to the Earth's and thus provide strong experimental support for the radical pair hypothesis of avian magnetoreception. However, considering the way the anisotropy data are acquired in the experiment, it is crucial to confirm the authenticity of the anisotropic effect: Let us assume the field calibration was slightly off and we had a bigger external field in one axis as compared to the other one. If the magnetic field angle θ was turned in such a situation, an artificial sinusoidal dependence of the magnetic field effect as a function of the angle would result.

Two ways of verifying that the orientation-dependent response is caused by the molecule rather than a calibration artifact are presented below. Since we make use of photoselection to choose

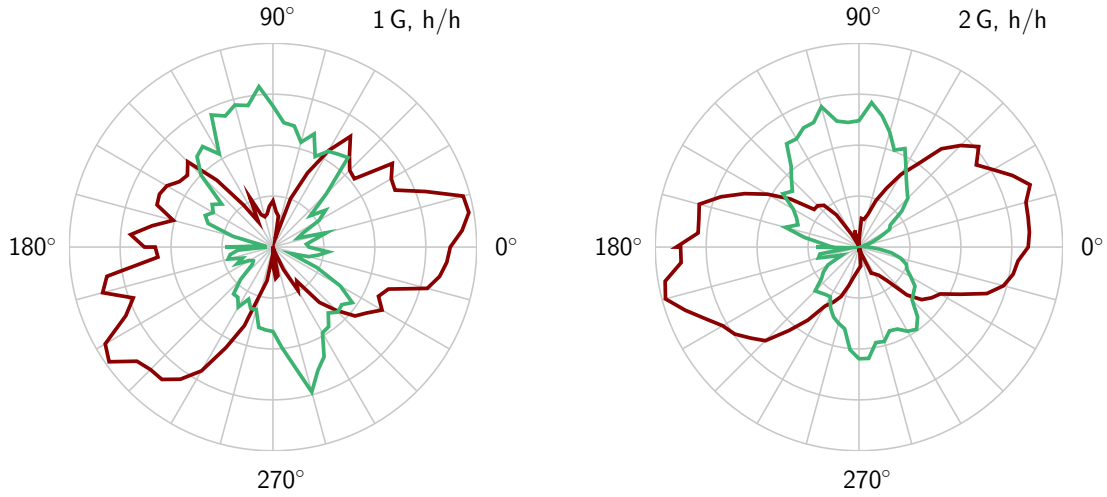


Figure 10.19: Polar plots of the MFE anisotropy curves of triad **CPF** recorded in **MTHF** (120 K) at 1 G (*left*) and 2 G (*right*). The colour-coding is the same as in previous figures.

the subset of molecular orientations probed in the experiment, one way of verifying whether the anisotropic response originates from the sample itself is to leave the magnetic field setup unchanged and repeat the experiment after only turning the laser polarisation of both laser beams by a certain angle. In this way, a different subset of molecular orientations is probed and the maximum of the anisotropy curve is expected to shift by the same angle. The results presented in **Figure 10.20** confirm that this is indeed the case. In the anisotropy data recorded at a field of 2 G for the partially deuterated triad, a 45° phase shift is observed when turning the laser polarisations of both pump and probe beams by 45°.

Another proof that the orientation-dependence of the field effect is a molecular property rather than an artifact, is provided by the dependence of the signal phase on the slope of the MARY curve at two magnetic field strengths corresponding to opposite sides of the maximum low field effect. **Figure 10.21** shows the MARY curves for the partially deuterated analogue of **CPF** for up to 5 G averaged for two time windows centred at 0.08 and 0.28 μs after laser excitation and the corresponding anisotropy curves for magnetic field strengths of 2 G and 4 G. From the slope of the MARY curves we would anticipate to observe a phase flip between early and later times in the anisotropy data for 2 G, while the phase of the anisotropy data recorded at 4 G should remain unchanged. It can be seen from the figure that the phase of the anisotropy data exactly follows these predictions, confirming the authenticity of the orientation-dependent data. The results of the two experiments presented in **Figures 10.20** and **10.21** provide unambiguous evidence that the anisotropic effect is indeed of molecular origin and therefore caused by the presence of anisotropic hyperfine coupling tensors in **CPF**.

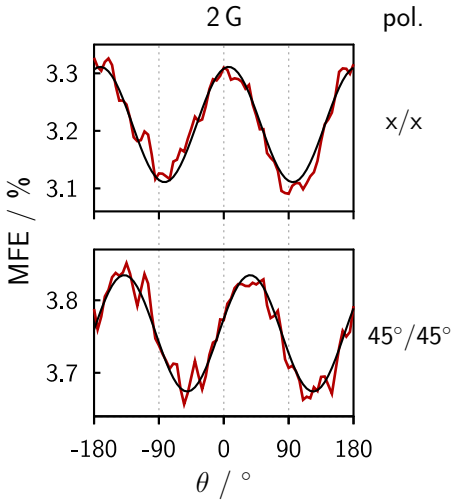


Figure 10.20: Magnetic field effect anisotropy curves of the partially deuterated analogue of triad **CPF** measured at 2 G in **MTHF** (120 K). The results obtained for two different laser polarisations shifted by 45° with respect to each other are compared. The polarisations of pump and probe beams are collinear in each individual experiment and x/x corresponds to both laser beams being horizontally polarised.

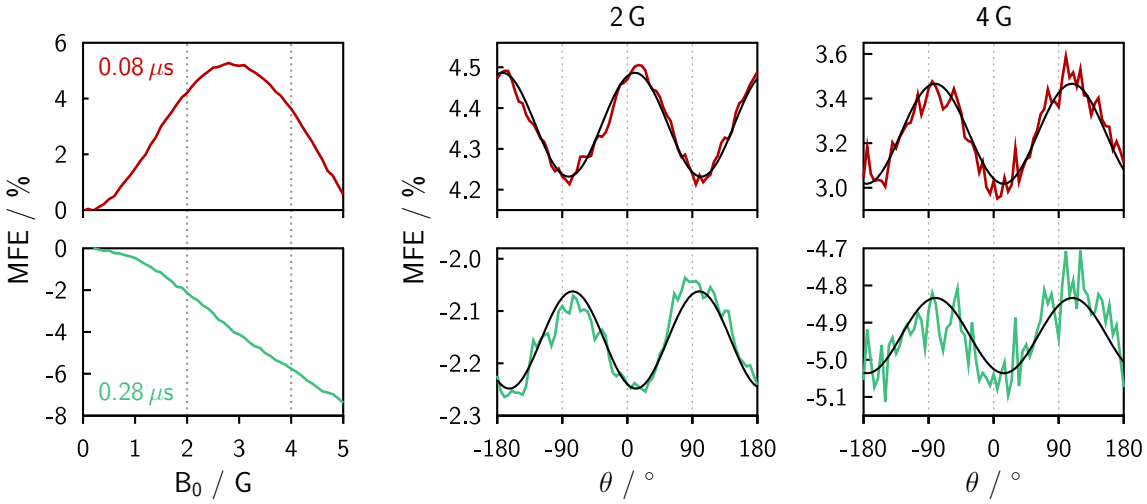


Figure 10.21: MARY curves recorded at two different times of 0.08 μs (red) and 0.28 μs (green) after laser excitation (*left*) and corresponding MFE anisotropy curves measured at two different magnetic field strengths of 2 G (*centre*) and 4 G (*right*) for the partially deuterated analogue of triad **CPF** in **MTHF** at 120 K. Fits to the data are shown in black. The time window used for data averaging was 20 ns.

10.4 Conclusions

Although it has long been known that magnetic fields can influence the yields of chemical reactions, no convincing experimental evidence was presented up to now that fields as weak as the Earth's can have a sufficiently significant effect on product yields as to account for the avian compass behaviour.

In this work, the chosen triad model system, **CPF**, was characterised by optical spectroscopic techniques to identify the reaction intermediates and determine the kinetics of the processes occurring after photoexcitation. Results obtained at room temperature could be compared to published data, whereas no information on the low temperature behaviour of this particular triad molecule was available beforehand. The photophysics of the triad were thus studied in **MTHF** at different temperatures, including 120 K, by UV-vis and transient absorption spectroscopy to assure comparability of the photophysical characterisation with the results from MFE experiments. The validity of the photocycle, suggested in the literature for similar triad molecules with different linkers and side groups, could be corroborated.

The MFE experiments confirmed that **CPF** is indeed an ideal model compound for these type of investigations. A magnetic field effect was detected at Earth's field and could be shown to be hyperfine-driven by comparison of the results for the partially deuterated and non-deuterated **CPF** triad analogues.

A dependence of the MFE response on the orientation of the molecule with respect to the external magnetic field direction could be demonstrated at magnetic field strengths comparable to the Earth's. This study presents the first observation of anisotropic magnetic field effects in the low field region and therefore underlines the feasibility of a chemical compass for bird navigation.

Although there is strong experimental support for the radical pair model, many open questions still remain. Future challenges to be overcome certainly include showing an anisotropic magnetic field response in a biological environment and elucidating the processes involved in signal transduction on a molecular level.

Appendix A: Experimental Details

A.1 Sample Preparation

Copper Porphyrin and Triplet State EPR

For the preparation of the EPR samples, the porphyrin oligomers were dissolved in the respective solvent (toluene, toluene-d_8, or 2-methyltetrahydrofuran) and the concentration ($\sim$0.2 mM for copper samples, $\sim$0.1 mM for triplet samples) and nature of the samples was verified by UV-vis spectroscopy. The solutions were degassed by the freeze-pump-thaw method (several cycles) and backfilled with argon. The deoxygenated solutions were then transferred into an EPR tube and the EPR tube closed with a subaseal. For storage in a liquid nitrogen dewar the subaseal was removed. The frozen samples were directly inserted into the EPR resonator for the measurements at 15 or 20 K.

Radical Pair EPR

The triad solutions were prepared in a glass vial using purified solvents (toluene or **MTHF**, passed over a column of activated aluminium oxide) and transferred into an EPR tube. The solutions were then degassed by the freeze-pump-thaw method (several cycles) and the tube flame sealed under vacuum. The EPR measurements were typically performed at 90 K and the samples stored in a -80°C freezer.

Magnetic Field Effect Experiments

In all magnetic field effect experiments, performed at 120 K, 2-methyltetrahydrofuran was used as the solvent. The inhibitor-free solvent (Sigma-Aldrich, anhydrous, $\geq$99 %) was passed over a column of activated aluminum oxide to remove any traces of water and possibly formed peroxides prior to sample preparation. A solution of the **CPF** triad in **MTHF** was prepared at an OD of ca. 0.4 (@3 mm) at the excitation wavelength and transferred into a custom made rectangular optical cell with an optical path length of about 3 mm. Oxygen was removed by several freeze-pump-thaw cycles and the cell was subsequently flame sealed under vacuum.

Transient Absorption (Northwestern University)

The solvent, **MTHF**, was distilled, deoxygenated and stored in a glove box. For experiments at low temperatures using a cryostat, the sample solutions were prepared from solid triad compound in the glove box. The sample cell, composed of two quartz windows separated by a teflon spacer ($\sim$2 mm), was filled with the solution and assembled under oxygen exclusion in the glove box. The sample

concentration was adjusted to yield an OD of about 0.3−0.5 at the excitation wavelength in the sample cuvette. For the room temperature experiments, the solid sample was dissolved in **MTHF** (from the glove box) and transferred into Schlenk cuvettes with an optical path length of 2 mm. The sample solution was then degassed applying several freeze-pump-thaw cycles immediately before the measurements.

The UV-vis spectra at low temperatures were recorded using the same sample and cryostat as for the transient absorption measurements.

A.2 Continuous Wave EPR

The continuous wave EPR spectra of copper porphyrin oligomers were recorded on a Bruker EMX spectrometer equipped with an ER 4122SHQE resonator and a liquid nitrogen flow cryostat. The measurements were performed in frozen toluene-d_8 or regular toluene at a temperature of 100 K as specified in the main part. The modulation frequency was set to 100 kHz and the modulation amplitude to 0.5 mT at a microwave power of 0.5 mW (26 dB). After data acquisition, the individual spectra were baseline-corrected, using the spectrum of the corresponding pure solvent as a reference, to compensate for resonator background signals, normalised and frequency-corrected to a common value of 9.39 GHz for direct comparison.

A.3 Pulse EPR

A.3.1 Copper Porphyrin EPR

The experimental details in this subsection refer to the EPR data acquired on linear and cyclic copper porphyrin oligomers presented in Chapters 2 to 4.

Field-swept EPR Spectra

Field-swept echo-detected EPR spectra were recorded at 15 K using the same pulse lengths as applied in the DEER experiments (12 or 16 ns) and a τ value corresponding to τ_1 as used for DEER (160 or 400 ns). A two-step phase cycle was applied and integration was performed over the whole echo. Typically two scans were recorded with 50 shots per point at a shot-repetition-rate of 2 μs.

Davies ENDOR

Davies ENDOR measurements at 15 K were carried out at Q-band frequencies (34.0 GHz) on a Bruker ELEXSYS E580 pulse EPR spectrometer equipped with a Bruker EN 5107D2 resonator and an Oxford Instruments liquid helium flow cryostat (CF935) in order to determine the nitrogen hyperfine and nuclear quadrupole couplings. All experimental ENDOR spectra were obtained using the pulse sequence $\pi - T - \pi/2 - \tau - \pi - \tau -$ echo with $\pi/2$ and π pulse lengths of 20 and 40 ns, respectively, and an evolution period T of 27 μs during which a 25 μs RF π pulse was applied. The inter-pulse delay τ in the detection sequence was chosen to be 220 ns. The whole echo signal

was integrated and recorded as a function of the RF frequency in stochastic mode with an RF increment of 0.1 MHz. The RF power was adjusted based on a nutation experiment.

Relaxation Measurements

Measurements of T_1 of the copper porphyrin compounds (15 K) by echo-detected saturation recovery were carried out at X- and Q-band frequencies by making use of the Picket fence method [12, 13]. The saturation pulse was composed of a train of 28 π pulses with a length of 32 ns each and an inter-pulse delay, t, of 128 ns between the individual π pulses. The magnetisation was detected after a delay T with a Hahn echo sequence with pulse lengths of 16 ns and 32 ns for $\frac{\pi}{2}$ and π pulses, respectively, and an inter-pulse delay τ of 400 ns. The delay T between the last π pulse of the Picket train and the echo detection sequence was incremented in logarithmic steps, such that $T_{n+1} = T_n + n\,\Delta t_{\text{step}}$. A relaxation curve with $n = 128$ points was then recorded with a time step Δt_{step} of 12304 ns corresponding to a maximum T value of 100 ms. Unwanted echoes were averaged out making use of a four-step phase cycle.

DEER

Four-pulse DEER experiments were performed at 15 K and Q-band frequencies on a Bruker ELEXSYS E580 spectrometer equipped with a Bruker EN 5107D2 resonator and a liquid helium flow cryostat using the sequence $\pi/2 - \tau_1 - \pi - \tau_1 - \tau_2 - \pi - \tau_2 -$ echo at the detection frequency ν_{det} while applying a single π pulse at the pump frequency ν_{pump} during the interval $\tau_1 - \tau_2$. The pump π pulse position was varied step-wise starting at a time $t_0 < \tau_1$ after the first detection π pulse up to a time $t < \tau_1 + \tau_2$, shortly before the second π pulse at ν_{det}.

A pulse length of 12 ns was chosen for the pump pulse, whereas all detection pulses had a length of 16 ns. A 16-step phase cycle needed to be employed to remove unwanted echos (AWG, coherent source). Deuterium nuclear modulations were averaged out by increasing τ_1 in eight steps of 16 ns, typically starting at $\tau_1 = 160$ or $\tau_1 = 400$ ns. To record the traces shown in the main text, the pump frequency was set to the maximum of the field-swept EPR spectrum (xy) and the detection frequency was $\nu_{\text{det}} = \nu_{\text{pump}} + 100$ MHz. The positions of the pump and detection pulses in the resonator were symmetric with respect to the resonator dip. The pump pulse position was varied in steps of either 4 ns, 8 ns, 12 ns, or 16 ns depending on the length of the trace (between 2 μs and 4.5 μs) and data were collected at a repetition rate of 2 μs or 3 μs.

The experimental DEER data were then phase-corrected and in most cases also background-corrected using an exponential background function with a dimensionality of $d = 3$.

The DEER measurements at X-band frequencies (Bruker ELEXSYS E580, ER 4118X-MS3 resonator) were performed using the same pulse sequence, temperature and shot repetition rate as employed for the measurements at Q-band. Since the pump pulse was applied using an incoherent microwave source, a two-step phase cycle on the first observer pulse was sufficient to remove any unwanted echos. Deuterium nuclear modulations were averaged out by increasing τ_1 in eight steps of 56 ns, typically starting at $\tau_1 = 400$ ns. Pulse lengths of 16 ns and 32 ns were chosen for the pump and detection pulses, respectively, and the detection frequency was $\nu_{\text{det}} = \nu_{\text{pump}} + 100$ MHz.

HYSCORE

HYSCORE experiments at 15 K were performed at X-band frequencies (Bruker ELEXSYS E680, ER 4118X-MS3 resonator) using the pulse sequence $\pi/2-\tau-\pi/2-t_1-\pi-t_2-\pi/2-\tau-$echo. The $\pi/2$ and π microwave pulses had a length of 16 ns. t_1 and t_2 were incremented in steps of $dt = 8$ ns starting at $t_1 = t_2 = 64$ ns and a data matrix of 400×400 points was collected. For every sample, three data sets with τ values of 140 ns, 216 ns, and 284 ns, respectively, were recorded (and added after data treatment) to compensate for blind-spots. A four-step phase cycle was applied to remove unwanted echos [248]. The HYSCORE spectra were recorded at a field position corresponding to the maximum of the field-swept EPR spectrum (330 mT $\hat{=}$ xy).

After data collection, the spectra were analysed in MATLAB. A third-order polynomial baseline correction was applied to all time traces, which were then subjected to apodisation with a Hamming window and zero-filled to 1024 points before a 2D Fourier transformation was carried out. The experimental spectra shown in the main part correspond to the absolute-value spectra obtained after Fourier transformation.

Since the deuterium modulations strongly dominated the ESEEM time traces when working with samples in deuterated toluene, all HYSCORE experiments were carried out on samples in regular toluene.

A.3.2 Triplet EPR Studies

The experimental details in this subsection refer to the EPR data acquired on the triplet states of linear zinc porphyrin oligomers presented in Chapters 6 to 8.

Transient cw EPR

All transient cw EPR measurements were carried out at X-band frequencies (9.75 GHz) on a Bruker ELEXSYS E680 spectrometer using a Bruker EN 4118X-MD4 resonator. The temperature was held constant at 20 K using a helium gas-flow cryostat. Typically, the samples were photo-excited with 1−5 mJ pulses of 5 ns duration at 532 nm using a Nd:YAG laser operated at a repetition rate of either 10 or 20 Hz. Before reaching the sample, the excitation light was depolarised.

The transient cw EPR spectra were acquired in direct detection mode using the transient recorder and a microwave power of 0.2 mW (30 dB). Typically, for every field value, a time trace with 4096 points was recorded using a time base of 4 ns. Considering a background of about 800 ns before the laser pulse, these settings result in a time window of about 15 μs. After data acquisition, the 2D spectra were baseline-corrected in both dimensions using a home-written MATLAB routine. The spectra shown in the main part were typically averaged over a time window from 0.2 μs to 1 μs after laser excitation and the spectral shape was generally found not to change significantly with time.

Mims ENDOR

Proton Mims ENDOR spectra at X-band frequencies were acquired using the same resonator as for the transient cw EPR experiments and applying the pulse sequence $\frac{\pi}{2} - \tau - \frac{\pi}{2} - T - \frac{\pi}{2} - \tau$ with microwave pulse lengths of 16 ns. Between the second and third pulse of the stimulated echo pulse sequence (i.e. during the delay T) a 15 μs RF pulse was applied. The RF power was adjusted based on a nutation experiment such that the flip angle corresponded to π. The integrated echo intensity was then monitored as a function of the RF frequency, in stochastic acquisition mode, in a range centred about the ^{1}H Larmor frequency at the respective field position. For every chosen field position, three spectra with different τ values of 120 ns, 180 ns, and 240 ns were recorded to compensate for blind spots and added to yield the spectra shown in the main part. For better visualisation of the hyperfine coupling constants, the proton Larmor frequency was subtracted from the frequency axis in all cases.

A.4 Transient EPR Laser Setup

The laser used as the excitation source in the experiments was either a Nd:YAG (Continuum Surelite) operated at 10 Hz or an optical parametric oscillator (OPO, Opotek Opolette 355) seeded by the third harmonic of a Nd:YAG operated at 20 Hz. For all standard experiments the samples were excited at 532 nm, whereas the OPO was employed whenever tunability of the excitation wavelength was required. Generally, it was found that no more than 1 mJ of energy is needed to excite the sample. In some cases it has been observed that higher laser energies than 1 mJ lead to sample degradation; in other cases the signal intensity, and therefore also the quality of the spectra, could be improved considerably by using higher laser powers of up to 80 mW (4 mJ @20 Hz).

The laser was operated at its optimum Q-switch value and the laser power was adjusted using a combination of a $\lambda/2$ waveplate followed by a polariser. Two or three turning mirrors were used after the polariser to slightly adapt the beam height and direct the laser beam straight through the optical window of the cryostat into the resonator. To adapt the beam size to the size of the optical window of the resonator, and therefore also the sample size, and to correct for beam divergence, a plano-convex lens (N-BK7, FL 500 mm) was placed between the last mirror and the resonator. The focal point of the lens was chosen to be located well before the resonator so that the divergent beam entering the cryostat had just the right dimensions so as to illuminate the entire optically accessible sample area. Either broad-band dielectric mirrors with a coating for the visible range (400 – 750 nm) or aluminium mirrors ($\sim$500 nm – NIR) were used as turning mirrors. If linearly polarised light was required, an additional polariser was placed after the last mirror.* An achromatic depolariser was used to generate depolarised light whenever needed.†

*The use of this additional polariser just before the sample is preferred because the polarisation of the light exiting the first polariser (used to adjust the laser power) might have been turned slightly after reflection at the mirrors since small height differences needed to be compensated in most cases.

†Although achromatic, the depolariser still needs to be realigned slightly for different wavelengths if high precision is required and *complete* depolarisation of the light is likely not achievable. An alternative would be to use a $\lambda/4$ waveplate to generate circularly polarised light.

A.5 DFT Calculations

A.5.1 Geometry Optimisations

The linear copper or zinc porphyrin oligomer structures were first optimised in Turbomole V6.1 [249, 250] under C_1 symmetry using DFT/B3LYP in combination with the TZVP basis set [251] and RI-approximation [252]. Vibrational frequency calculations confirmed that the obtained structures corresponded to minima of the potential energy surface.

A.5.2 Hyperfine Coupling Calculations

Triplet States of Linear Zinc Porphyrin Oligomers

The hyperfine interaction tensors and their orientation were calculated for the optimised structures using the program package ORCA V3.0 [253]. The ORCA DFT calculations with the B3LYP functional were performed using the EPR II basis set [254] for H, C, and N and the 6-31G(d) basis on zinc.

The triplet spin densities were plotted with Chimera [255] using a contour level of 0.001. The hyperfine coupling tensors were visualised from the ORCA *.out file using a home-written MATLAB routine. The tensor orientations were checked against the programme orca_euler implemented in ORCA.

Copper Porphyrins

The hyperfine and nuclear quadrupole interaction tensors and their orientations were calculated for the optimised structures of $\mathbf{P1_{Cu}}$ and $\mathbf{P1_{Cu}\cdot py}$ using the program package ORCA V3.0. DFT calculations with the B3LYP functional were performed using the EPR II basis set for H, C, and N and the Wachters basis [256] on copper. This combination of functional and basis sets was chosen since it was previously shown to yield computational results that are reasonably close to the corresponding experimental values in a series of detailed theoretical investigations on hyperfine coupling parameters for comparable copper compounds with and without axial ligands [257–259]. For the calculation of core properties, the choice of the basis set can be crucial. Generally, specialised basis sets are required, which allow for additional flexibility in the core region. Hybrid functionals, such as B3LYP, include a certain percentage of exact Hartree-Fock exchange, which often leads to a better agreement with the experiment as compared to generalised gradient functionals.

Although the B3LYP functional is known to overestimate the nitrogen couplings [257], the trends and relative variations in the individual values are informative since the computational error on these properties seems to be fairly systematic. For the copper hyperfine couplings, DFT/B3LYP was shown to perform well [258], however the $A_\perp$ value is generally predicted to be much smaller than experimentally observed even if relativistic and spin-orbit contributions are considered. The error on the calculated g-values is normally large, since DFT generally overestimates the covalence in Cu(II) complexes, but trends can safely be predicted. The overestimation of covalence is also the reason why the metal hyperfine couplings (especially $A_\perp$) are normally predicted to be too small, while the opposite is true for the ligand hyperfine couplings.

A.6 Transient Absorption Setup and Data Analysis

The transient absorption measurements were performed in the laboratories of Prof. M. R. Wasielewski (Northwestern University, USA). Pulses of about 90 fs duration, centred at 827 nm are provided by an amplified Ti:Sapphire system (Spitfire, Spectra Physics) at a repetition rate of 1 kHz. The fundamental beam at 827 nm is split into two parts. A small fraction is used for probe white light generation, the other part is either frequency doubled for excitation at 414 nm or guided through an optical parametric amplifier if excitation wavelength tunability is required.

The commercially available Helios and EOS spectrometers (Ultrafast Systems) were used for data acquisition in combination with a slightly modified optical layout. For femtosecond to nanosecond measurements, the probe beam is delayed on an optical stage prior to white light generation in a sapphire plate and is then split in a signal and reference beam for signal detection and compensation of intensity fluctuations, respectively. An external white light source (Nd:YAG pumped photonic crystal fibre) is used for the sub-nanosecond to millisecond TA experiments using the EOS system. The delay between pump and probe beams is generated electronically and the probe light is again divided into a reference and signal beam.

To obtain the transient absorption difference signal, ΔA, the absorption needs to be recorded in the absence and presence of the pump beam. For fs to ns experiments, this is achieved by chopping the pump beam. In the sub-ns to ms experiments the pump beam is not chopped, but instead the electronically triggered supercontinuum probe source is operated at 2 kHz. The excitation beam is in both cases provided by the amplified femtosecond laser system.

To limit the electronic jitter between the pump and probe beams in the sub-ns to ms experiments, which could adversely affect the time-resolution of the experiment, the data are acquired using single photon timing electronics. Similar as in a single-photon timing experiment, the data are built up as a histogram. The time delay is measured rather than initially set and the acquired spectra are sorted according to this delay.

The white light used for the sub-ns to ms experiments has an unexpectedly large chirp of about 600 ps originating from the photonic crystal fibre (self-phase-modulation broadening). This chirp, as well as the chirp in the fs experiments of about 2 ps, needs to be corrected for during data treatment.

During the TA measurements, the room temperature samples were constantly stirred (magnetic stirrer) to assure that a fresh sample volume was probed at all times. To acquire the low temperature data, several scans needed to be averaged until an acceptable signal-to-noise ratio was obtained. Between individual scans, the cryostat was laterally displaced, whenever necessary, to minimise the effects of sample degradation on the acquired spectra. All TA spectra were acquired using an excitation energy of 1 μJ at 414 nm.

The TA data were analysed using home-written MATLAB routines. After background subtraction, the data were chirp-corrected by interpolation in the time domain using a function of the form $f(x) = p_1 + \frac{p_2}{x^2} + \frac{p_3}{x^4}$ with parameters p_n determined from suitable background solvent spectra (i.e. fit of $f(x)$ to the background data as a function of wavelength). The wavelength region was truncated, if necessary. To merge the data sets obtained from the two different measurements with

fs to ns and sub-ns to ms time resolution for every sample, a (wavelength-dependent) intensity scaling factor was applied to the kinetics of one of the data sets to assure a satisfactory overlap of the kinetics in the region from 6 to 8 ns. The complete data set was then obtained by stitching the two amplitude-matched sets, usually by down-sampling of the femtosecond data in the kinetic overlap region.

Finally, to analyse the kinetics, global target analysis was performed using a sequential reaction scheme as detailed in Chapter 10.

Appendix B: Additional EPR Data on Copper Porphyrins

B.1 Pulse EPR Data of Linear Bis-Copper Porphyrin Oligomers

A series of linear porphyrin oligomers with three to five porphyrin units containing two copper centres at the terminal positions were synthesised by Jonathan Cremers (Anderson group, University of Oxford, UK). The corresponding structures are shown in **Figure B.1**.

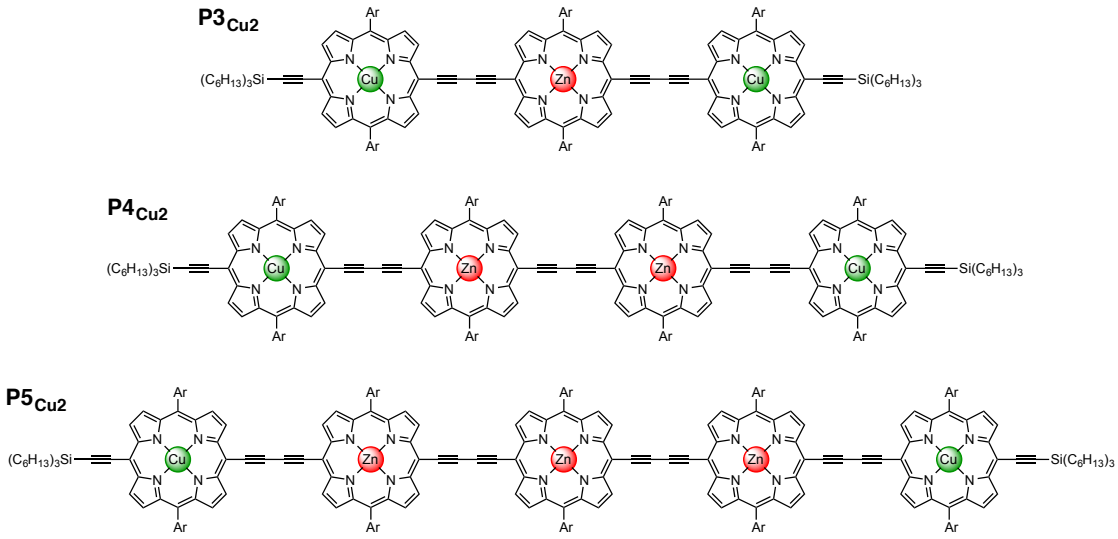


Figure B.1: Chemical structures of the linear bis-copper porphyrin oligomers **P3$_{Cu2}$**, **P4$_{Cu2}$** and **P5$_{Cu2}$**.

According to predictions from DFT, the distances between the copper centres amount to 2.7 nm, 4.1 nm, and 5.4 nm, respectively, for **P3$_{Cu2}$**, **P4$_{Cu2}$** and **P5$_{Cu2}$** and should therefore lie well within the range accessible by DEER spectroscopy. In fact, these molecules were originally thought to be suitable as 'distance rulers' for DEER between two copper centres. When investigating the compounds, it was found, however, that the large flexibility of the structures precludes the observation of clearly resolved modulations in the dipolar evolution data, in contrast to the results obtained when nitroxide spin labels are used instead of copper [260]. In addition, it is observed that also transverse relaxation is considerably accelerated in these linear compounds as compared to the cyclic and more rigid copper-containing porphyrin structures presented in Chapters 3 and 4. The fast relaxation considerably limits the detection of long distances.

Figure B.2 shows the transverse relaxation behaviour and the 4-pulse DEER traces for the three linear compounds recorded at Q-band frequencies in frozen toluene-d_8 solution (15 K). The DEER traces have been recorded at an *xy* field position, where the pump pulse was placed at the maximum

of the field-swept EPR spectrum and the detection pulses had a frequency offset of +100 MHz. It can be seen from the figure that the longest trace that can be recorded for these compounds is of the order of 3 μs. No pronounced modulations are observed for any of the three compounds, indicating the presence of many different distances, presumably due to a considerable flexibility of the structures. To a first approximation, rotation of the porphyrin planes about the triple bonds should only affect the modulation depth but not the dipolar frequencies. It is therefore likely that bending of the structures needs to be invoked to explain the experimental observations.

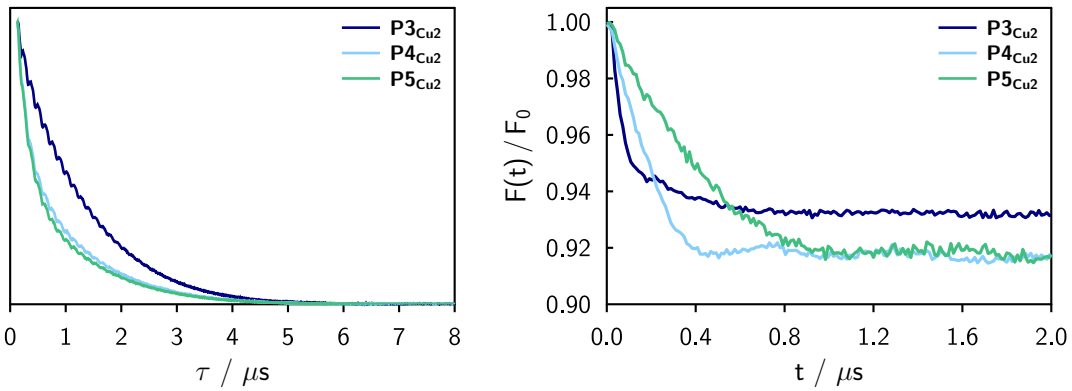


Figure B.2: Phase memory time measurement (*left*) and 4-pulse DEER traces (*right*) of the available linear bis-copper porphyrin oligomers in toluene-d_8 recorded at Q-band (15 K).

In summary, it is interesting to note that moderate flexibility seems to strongly affect the observation of dipolar modulations for copper-containing porphyrin structures, while this is not the case for nitroxides [260], which could have important implications for the design of copper spin labels for use in distance measurements. Additionally, also the relaxation times of copper porphyrin oligomers seem to be strongly affected by an increased flexibility of the structure which imposes severe constraints on the detectable distances.

B.2 Variable Temperature cw EPR of Linear Copper Porphyrin Oligomers

The temperature dependence of the cw EPR spectra of the copper porphyrin monomer (**P1$_{Cu}$**) and dimer (**P2$_{Cu2}$**) was investigated in detail in the range from 100 K to 300 K and compared to the (known) behaviour of 5,10,15,20-tetraphenyl-21H,23H-porphine copper(II) (**CuTPP**, Sigma Aldrich). The corresponding spectra are presented in **Figures B.3** to **B.5**. The frozen solution spectra of **P1$_{Cu}$** and **CuTPP** are very similar. However, it is found that the presence of bulky side groups in **P1$_{Cu}$** considerably influences the temperature dependence of the spectra. While the isotropic limit can be reached for **CuTPP** at room temperature, the room temperature spectrum of **P1$_{Cu}$** rather resembles the spectrum of **CuTPP** at 200 K. Since the isotropic tumbling limit cannot be reached with **P1$_{Cu}$** at room temperature, the influence of isotropic and anisotropic spin-spin interactions (J and D) on the EPR spectrum cannot be separated easily in **P2$_{Cu2}$** as discussed in detail in Chapter 2.

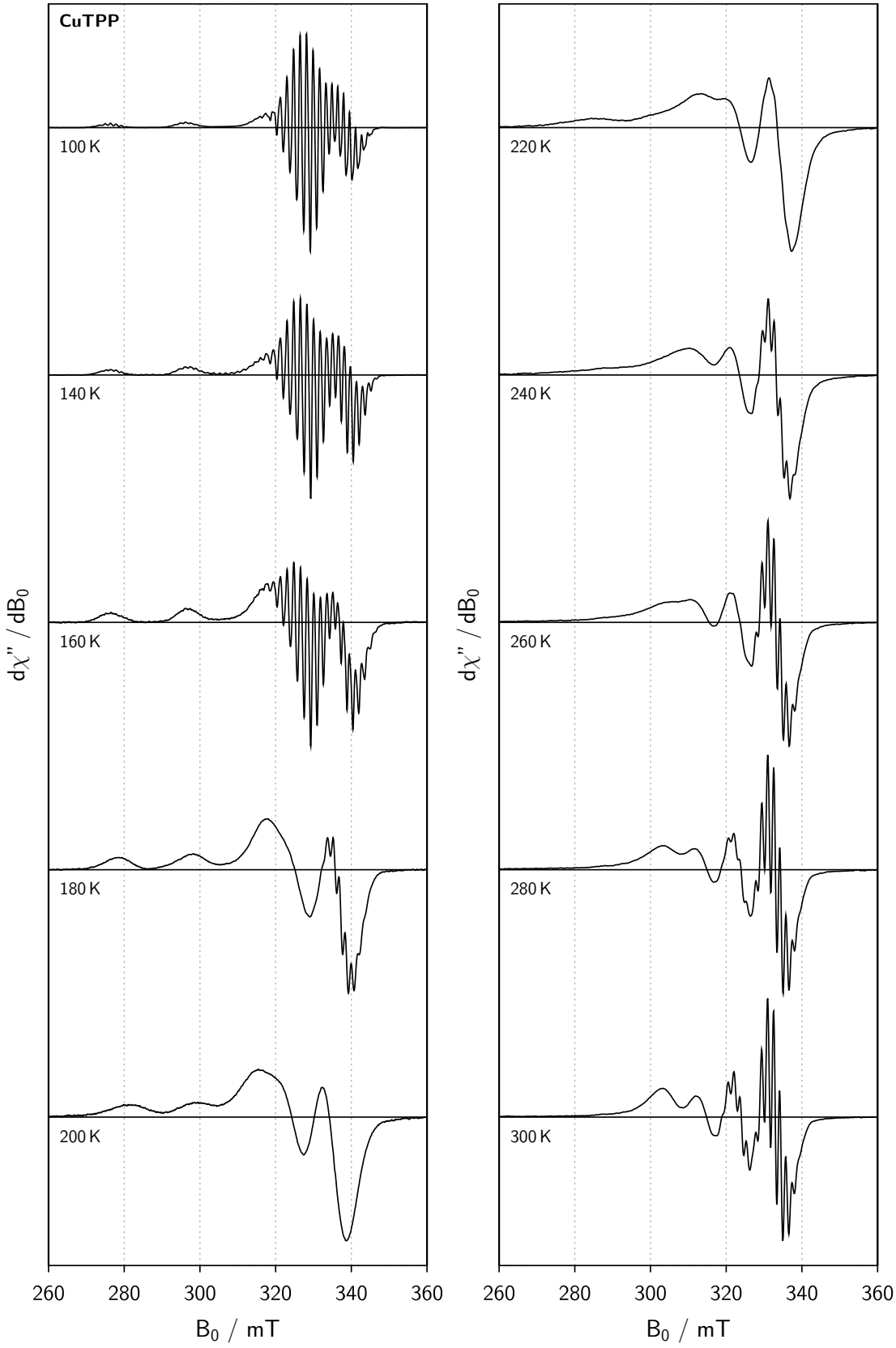


Figure B.3: Cw EPR spectra of **CuTPP** in toluene at various temperatures (as indicated) in the range from 100 K to 300 K.

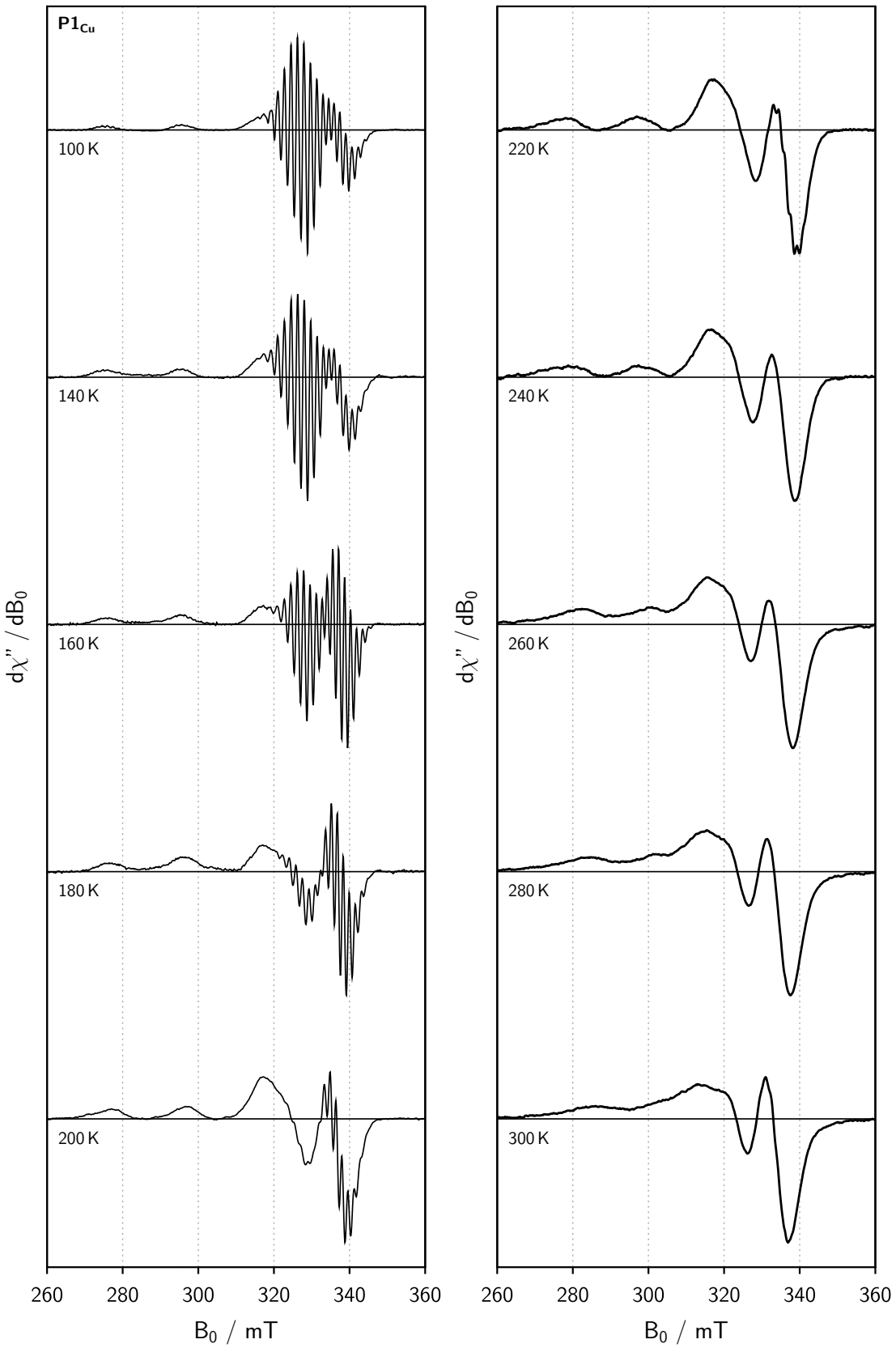


Figure B.4: Cw EPR spectra of $\mathbf{P1_{Cu}}$ with **THS** side groups in toluene at various temperatures (as indicated) in the range from 100 K to 300 K.

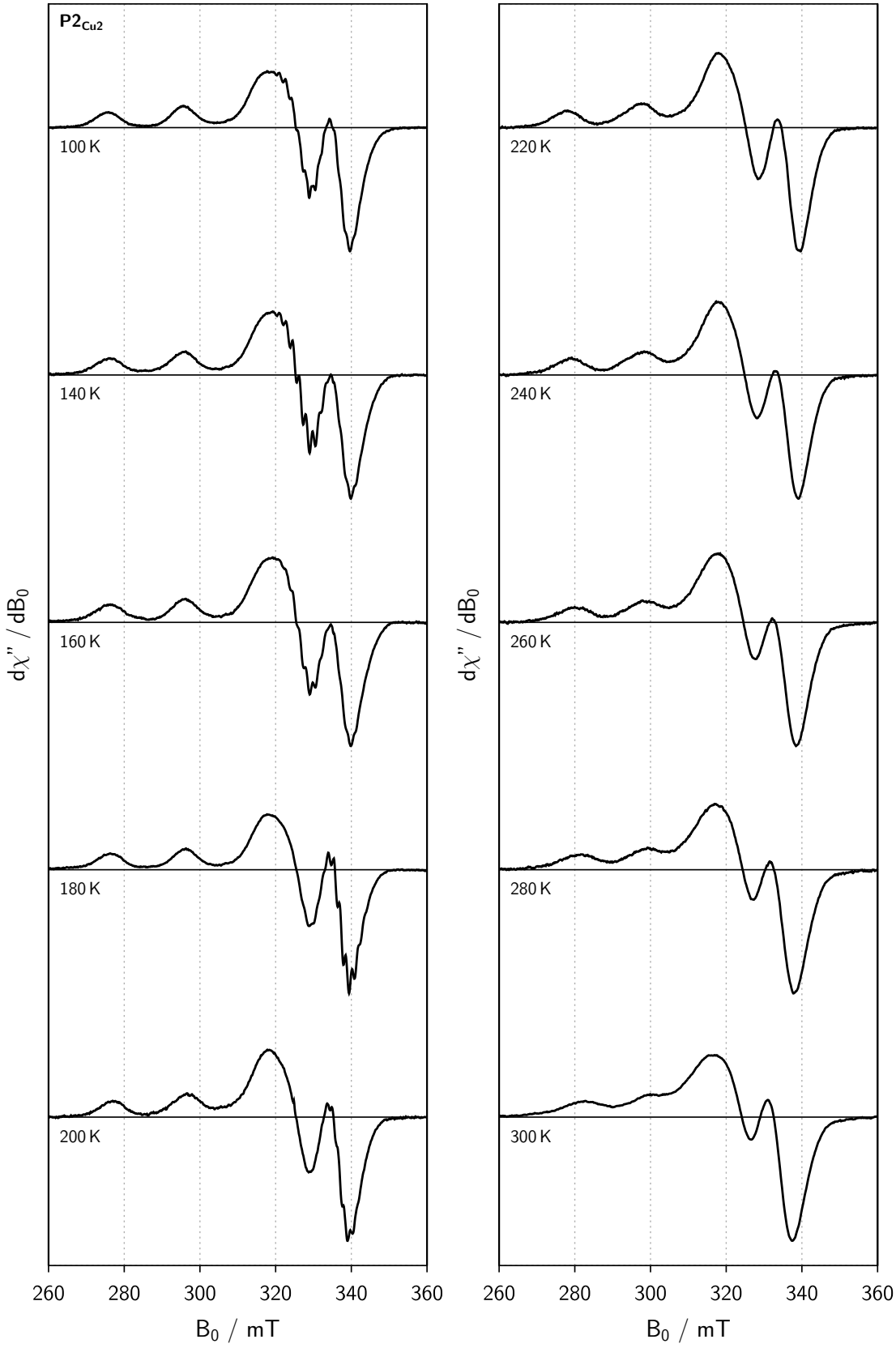


Figure B.5: Cw EPR spectra of **P2$_{Cu2}$** with **THS** side groups in toluene at various temperatures (as indicated) in the range from 100 K to 300 K.

B.3 EPR Characterisation of *c*-P6$_{Cu6}$

The six-membered hexa-copper porphyrin nanoring (***c*-P6$_{Cu6}$**), synthesised by Martin Peeks (Anderson group, University of Oxford, UK), was investigated by cw and pulse EPR spectroscopy in the presence and absence of **T6** template. The structures of the molecules are shown in **Figure B.6**.

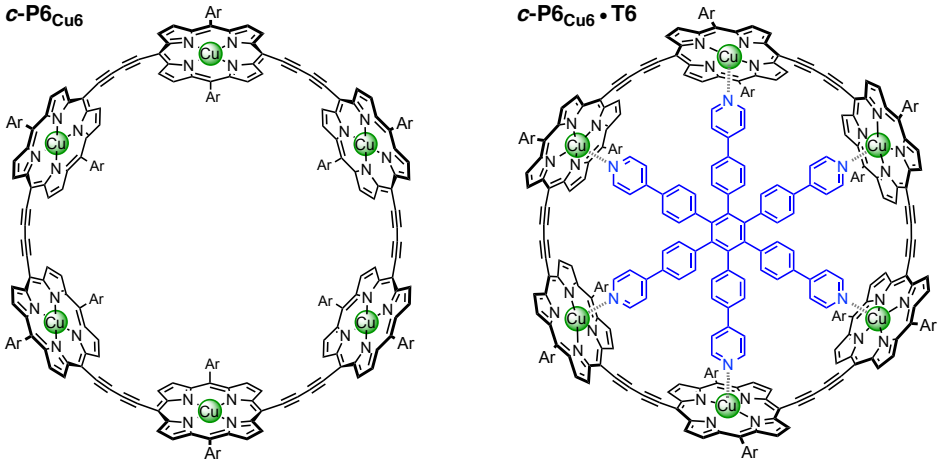


Figure B.6: Chemical structures of the six-membered hexa-copper porphyrin nanoring, ***c*-P6$_{Cu6}$**, with and without **T6** template (Ar = 3,5-bis(tri(hexyl)silyl)phenyl, **THS**).

The influence of different side groups (**tBu**, **THS**) on the low temperature cw EPR spectrum of ***c*-P6$_{Cu6}$** in toluene was tested and a comparison is shown in **Figure B.7** alongside a comparison of the spectra of **P1$_{Cu}$** with different side groups. No major differences are observed between the frozen solution EPR spectra of samples with either **tBu** or **THS** side groups.

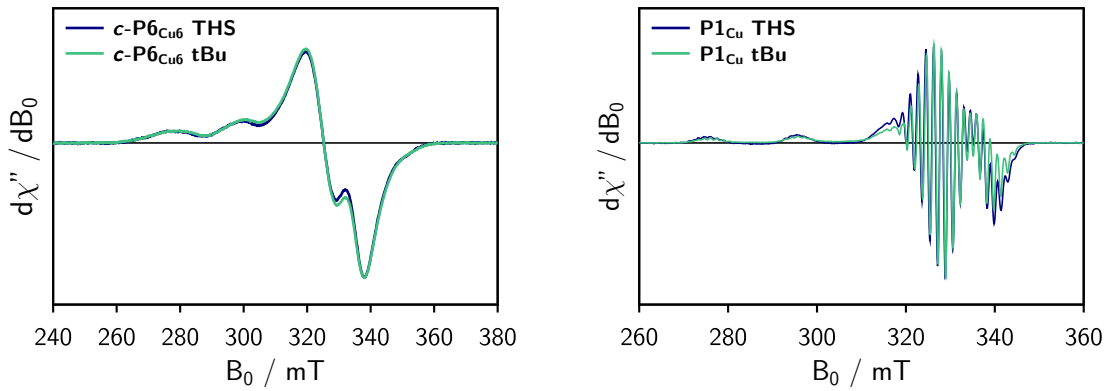


Figure B.7: Illustration of the effect of different (**THS**, **tBu**) porphyrin side groups on the cw EPR spectra of ***c*-P6$_{Cu6}$** (*left*) and **P1$_{Cu}$** (*right*). All spectra were recorded in frozen toluene at 100 K.

Compared to the monomer spectrum, the cw EPR spectrum of ***c*-P6$_{Cu6}$** is significantly broadened due to the presence of dipolar as well as exchange interactions between different copper ions in the structure. No nitrogen hyperfine structure is resolved. **Figure B.8** shows the dependence of the cw EPR spectrum of ***c*-P6$_{Cu6}$** on temperature in the range from 100 K to 300 K.

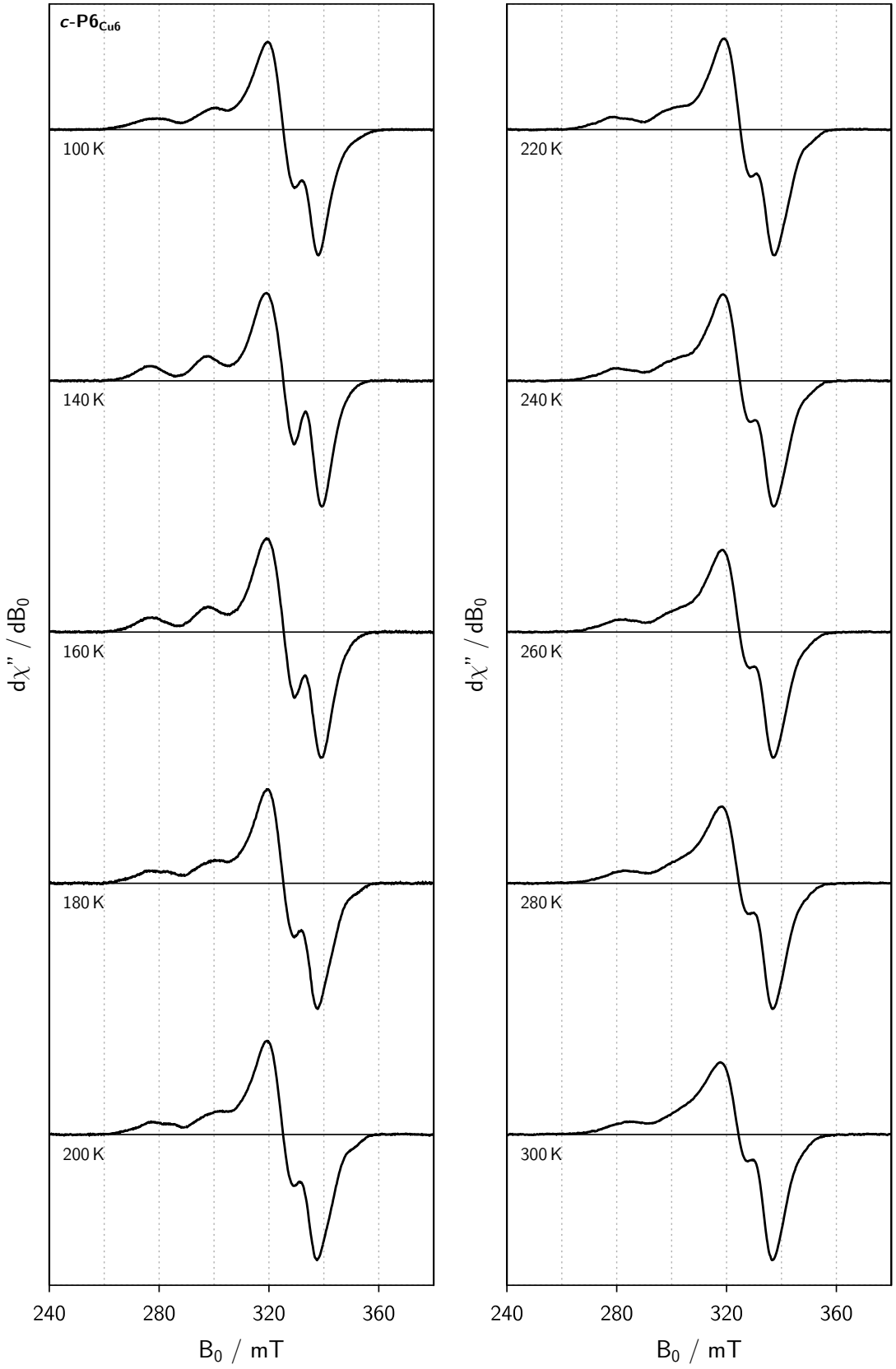


Figure B.8: Cw EPR spectra of ***c*-P6$_{Cu6}$** with **THS** side groups in toluene at various temperatures (as indicated) in the range from 100 K to 300 K.

As a function of temperature, the overall shape of the spectrum of ***c*-P6$_{Cu6}$** does not change significantly. Additional spectra were also recorded at higher temperatures, approaching the boiling point of the solvent (∼380 K). The corresponding spectra are overlaid in **Figure B.9** with those shown before, covering a temperature range from 100 K to 360 K. Although the highest temperature is just 20 K below the boiling point of the solvent, no major spectral changes are observed. The isotropic limit cannot be reached in toluene with this compound.

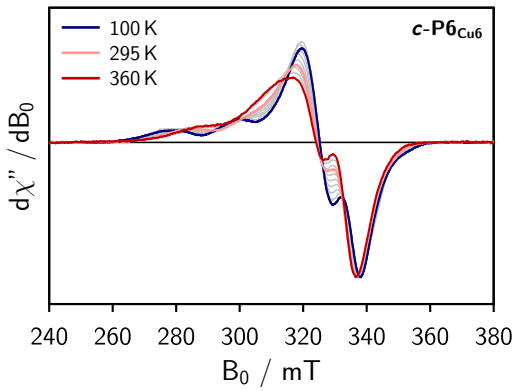


Figure B.9: Comparison of the cw EPR spectra of ***c*-P6$_{Cu6}$** with **THS** side groups in toluene at various temperatures in the range from 100 K to 360 K.

In **Figure B.10**, the frozen solution cw EPR spectrum of ***c*-P6$_{Cu6}$**, recorded at 100 K, is directly compared with those of **P1$_{Cu}$** (*left*) and a linear six-membered hexa-copper porphyrin oligomer (**P6$_{Cu6}$**, *right*). Even compared to **P6$_{Cu6}$**, the spectrum of ***c*-P6$_{Cu6}$** is significantly broadened which could indicate enhanced inter-spin coupling in the ring structure as compared to the corresponding linear oligomers, in perfect agreement with the results presented in Chapter 4.

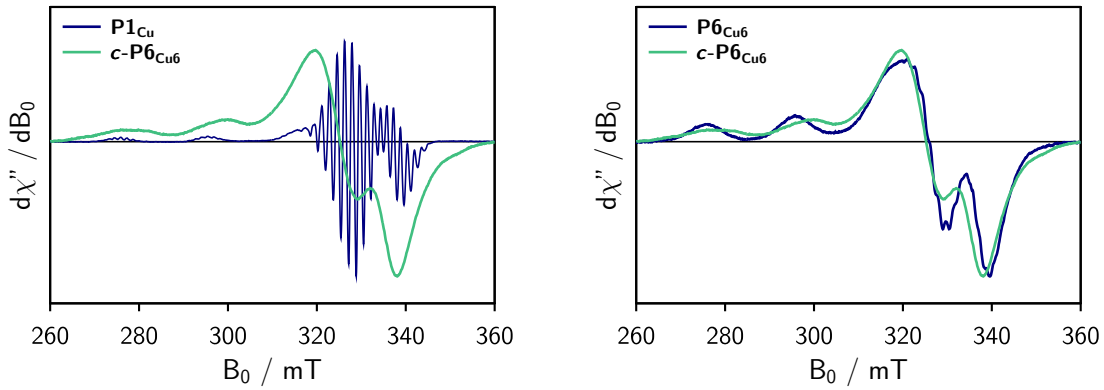


Figure B.10: Comparison of the frozen solution cw EPR spectrum of ***c*-P6$_{Cu6}$** recorded at 100 K to those of **P1$_{Cu}$** (*left*) and **P6$_{Cu6}$** (*right*).

Figure B.11 shows a comparison of the frozen solution ^{14}N Davies ENDOR spectra of ***c*-P6$_{Cu6}$** recorded at 15 K at magnetic field positions corresponding to the *xy* and *z* orientations, with those of **P1$_{Cu}$** and **P2$_{Cu2}$**. Compared to the spectra of the monomer, the spectra of ***c*-P6$_{Cu6}$** are slightly broadened, but no changes in the nitrogen hyperfine coupling constants can be discerned.

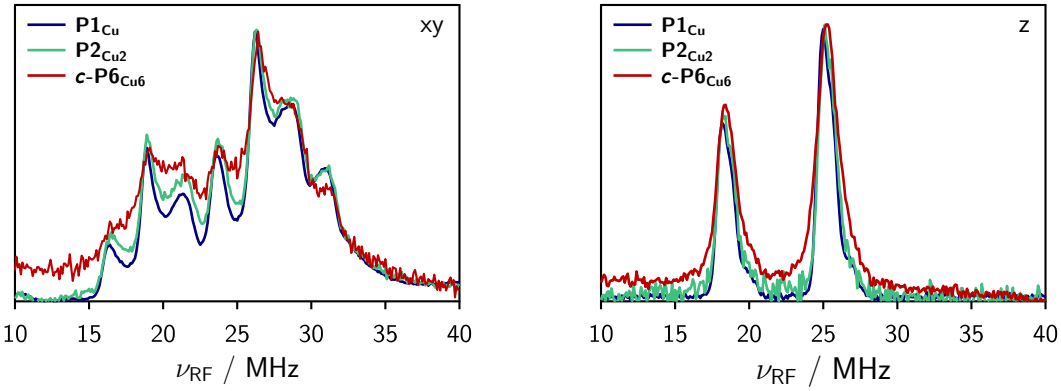


Figure B.11: Comparison of the frozen solution Davies ENDOR spectra of **P1$_{Cu}$**, **P2$_{Cu2}$**, and ***c*-P6$_{Cu6}$** recorded at 15 K at magnetic field positions corresponding either to *xy* (*left*) or *z* (*right*).

An increase in intensity is however observed in the low frequency part of the spectrum below 15 MHz, which could result from exchange coupling: Strong exchange coupling, bigger in magnitude than the hyperfine coupling, should result in the hyperfine coupling constants being halved. Due to the coupling between the two spin centres, the spin density should be spread evenly over both centres. Although the exchange coupling in **P2$_{Cu2}$** and ***c*-P6$_{Cu6}$** is most certainly larger than 58 MHz (cf. Chapter 2), corresponding to the biggest nitrogen hyperfine coupling observed in these systems, the large hyperfine coupling constant of copper ($A_{||}$) seems to largely prevent the observation of this effect (i.e. the reduction of the hyperfine couplings by a factor of two might in this case only be observable for exchange coupling interactions larger than $A_{||}$ of copper of about 600 MHz).

DEER traces were also recorded for ***c*-P6$_{Cu6}$** for different pump pulse flip angles to judge the influence of multi-spin effects [261, 262] on the DEER trace. A frequency offset between detection and pump pulses of 110 MHz was chosen in this experiment and the pump pulse was placed on the maximum of the field-swept echo-detected EPR spectrum as indicated in **Figure B.12**.

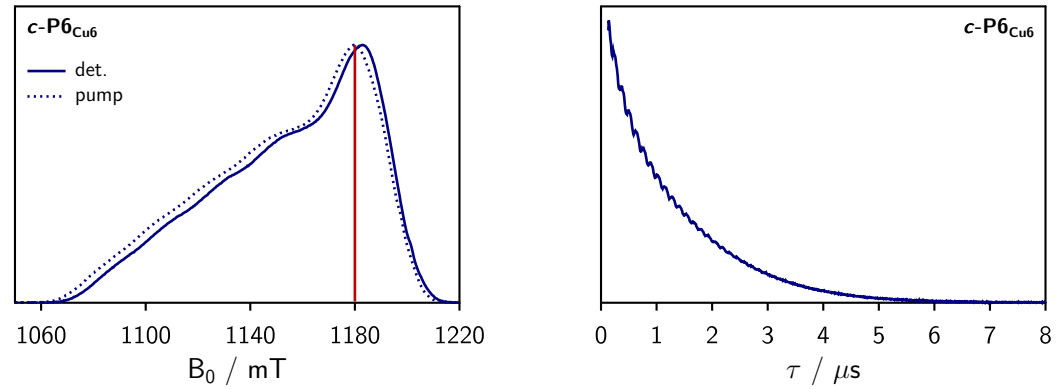


Figure B.12: Echo-detected field-swept EPR spectra (Q-band) measured at pump and detection frequencies (*left*) and transverse relaxation (T_m) measured at *xy* (*right*) of ***c*-P6$_{Cu6}$** in toluene-d_8 at 15 K.

The high rigidity of the structure results in a relatively slow transverse relaxation behaviour and allows for the measurement of DEER traces up to 3.5 μs (cf. **Figure B.12**). Pump pulse flip angles of π and $\frac{2}{5}\pi$ were chosen in the DEER experiment together with pulse lengths of 12 ns for all pulses and the results are compared in **Figure B.13**. Applying a reduced flip angle of $\frac{2}{5}\pi$, the two-spin contribution should be considerably enhanced in a system containing six spins (maximum expected at $\frac{1}{5}\pi$ [261]). When comparing the reduced form factors of the two DEER traces, no significant differences are observed, indicating that multi-spin effects do not contribute markedly to the measured time evolution of the trace. This finding is maybe not surprising considering the low modulation depth generally obtained for copper porphyrins, since three-spin correlation terms are roughly proportional to the square of λ which becomes vanishingly small for small λ [262] (*here*: $\lambda = 0.054$).

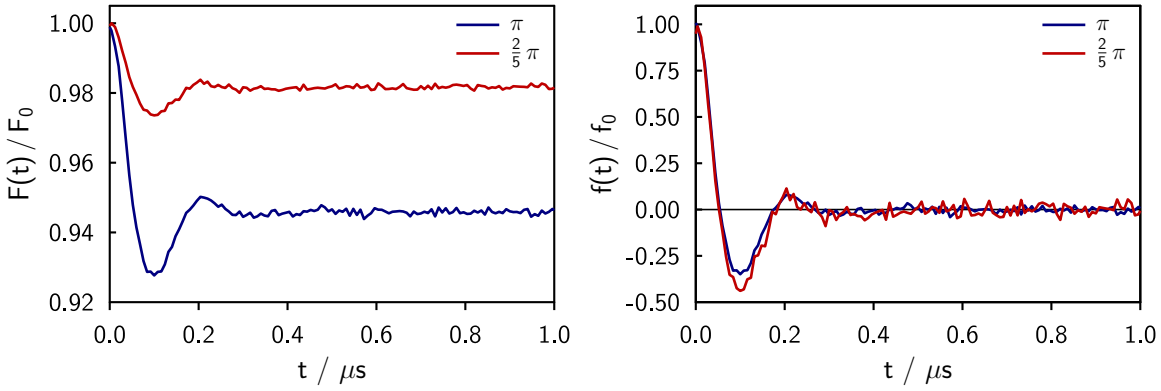


Figure B.13: DEER traces recorded for ***c*-P6$_{Cu6}$** at Q-band (15 K, *xy* orientation) using two different flip angles of π and $\frac{2}{5}\pi$ for the pump pulse. The form factors (*left*) and reduced form factors (*right*) of the two traces are compared.

In general, it is noted that the dampening of the modulation observed in the 4-pulse DEER trace of ***c*-P6$_{Cu6}$** is fairly rapid, due to the presence of many different inter-spin couplings with different frequencies (and possibly large distributions). The main modulation frequency of the trace corresponds to an apparent distance of 2.1 nm (FWHM of 0.34 nm) when analysed using a model-free approach and therefore assuming the absence of any exchange coupling contributions. Given the results from cw EPR spectroscopy, the latter assumption is likely not to hold true in the present case which considerably complicates any analysis of the time behaviour of the DEER trace. In this system, three inter-copper distances of 1.3 nm, 2.2 nm and 2.6 nm are expected to be present with a ratio of 2:2:1, leading to three different dipolar coupling frequencies, the shortest of which is beyond the distance range accessible by DEER and might not be observable. Furthermore, a range of different exchange couplings between the six copper centres might contribute to the measured dipolar evolution, making a more quantitative analysis impractical without any complementary information.

Influence of the T6 Template

Measurements on ***c*-P6$_{Cu6}$** were also carried out in the presence of a molecular **T6** template. Since the binding affinity to axial nitrogen ligands is much lower for copper than for zinc (cf. Chapter 3), a large excess needed to be used to force the ***c*-P6$_{Cu6}$** molecules to bind **T6**. UV-vis spectroscopy was employed to confirm the binding as is shown in **Figure B.14**. Upon binding of **T6**, the porphyrin Q-band of ***c*-P6$_{Cu6}$** red-shifts and becomes considerably more structured.

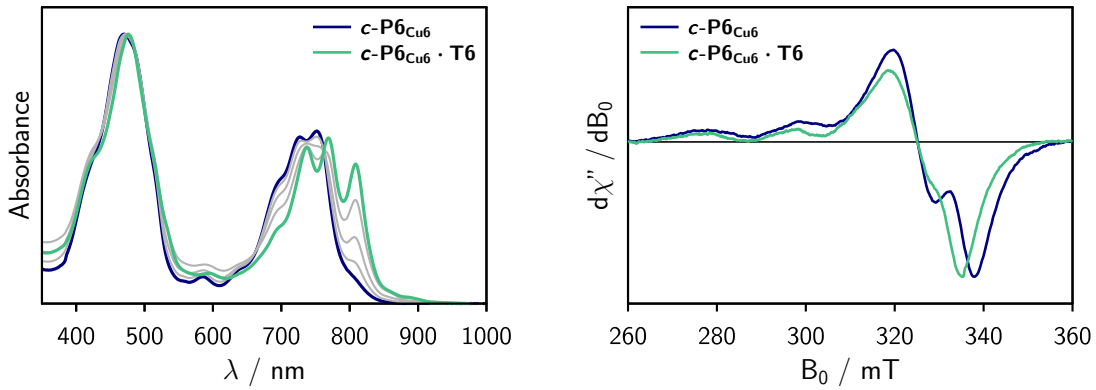


Figure B.14: Comparison of the room temperature UV-vis spectra (*left*) and cw EPR spectra recorded at 100 K (*right*) of ***c*-P6$_{Cu6}$** in toluene-d_8 with and without template.

Compared to the structure without template, the frozen solution cw EPR spectrum of ***c*-P6$_{Cu6}$ · T6** is shifted to lower fields (**Figure B.14**, *right*), indicating an increase in the principal g-values. In addition, the separation of the two low-field copper lines corresponding to $A_{||}$ seems to be decreased in the spectrum of ***c*-P6$_{Cu6}$ · T6**. Both of these observations are in excellent agreement with the changes observed upon binding of an axial ligand to copper porphyrin units as discussed in Chapter 3.

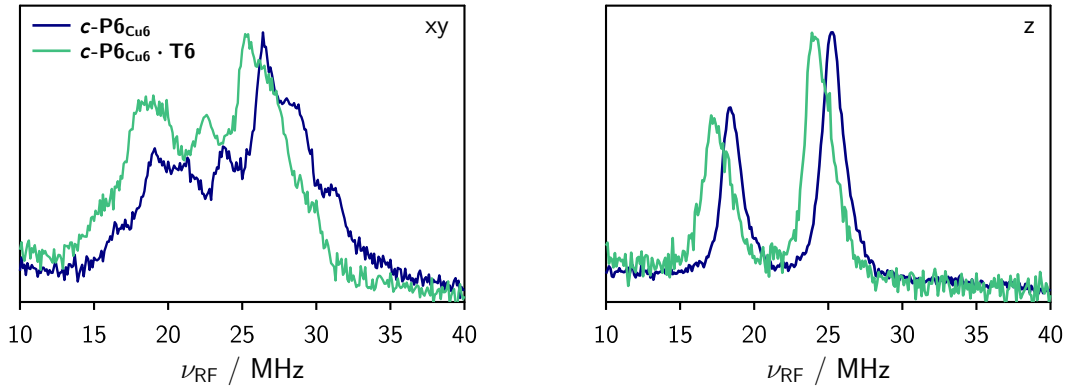


Figure B.15: Comparison of the Davies ^{14}N ENDOR spectra of ***c*-P6$_{Cu6}$** with and without template recorded at Q-band in frozen toluene-d_8 (15 K) at field positions corresponding to the *xy* (*left*) and *z* (*right*) orientations.

Figure B.15 shows a comparison of the ^{14}N Davies ENDOR spectra of ***c*-P6$_{Cu6}$** and ***c*-P6$_{Cu6}$ · T6** recorded at *xy* and *z* orientations. It can be seen that the spectra of ***c*-P6$_{Cu6}$ · T6** are shifted to

lower frequencies as compared to those of ***c*-P6$_{Cu6}$**. The spectral shifts seems to be complete, indicating quantitative binding of **T6**.

Finally, a 4-pulse DEER trace was also recorded at Q-band (15 K) for the sample with **T6** and is contrasted with that of the sample without template in **Figure B.16**. Upon coordination to the central metals of the porphyrin units, the **T6** template considerably reduces the conformational flexibility of the structure. Since the dipolar frequencies should be roughly the same in both structures,* the observed drastic reduction in the modulation frequency can be ascribed to be caused by exchange coupling. Although a significant exchange interaction is certainly also present in the sample without **T6**, its clear visibility in the DEER trace is most likely favoured by the fixed relative orientation of the porphyrin planes leading to a considerably narrower distribution.

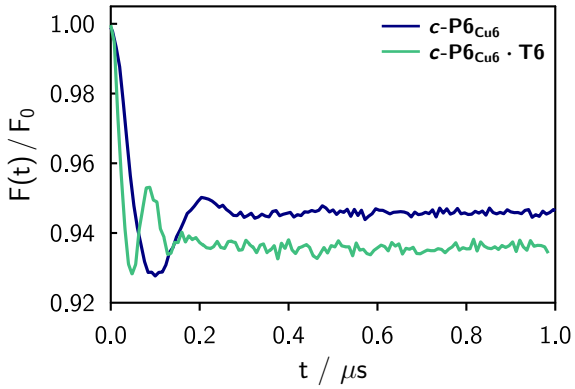


Figure B.16: Comparison of the form factor of the 4-pulse DEER traces of ***c*-P6$_{Cu6}$** with and without template.

*The template being slightly smaller than the ring, a small reduction in the inter-spin distances is expected from 2.6 nm, 2.2 nm and 1.3 nm to 2.44 nm, 2.11 nm and 1.22 nm, based on DFT calculations for a six-membered zinc porphyrin nanoring.

Appendix C: Details of the EPR Simulations using Spinach

C.1 Simulation of the Exchange Coupling in $P2_{Cu2}$

The following strategies were employed in order to make the time domain simulation of the dimer cw EPR spectrum, presented in Chapter 2, manageable. They were implemented in Spinach [68] and the simulations were performed by Prof. Ilya Kuprov (University of Southampton, UK).

1. System level state space restriction [263]. Correlations between an electron located on one of the porphyrin units and the nuclei located on the other porphyrin unit were dropped from the basis set. Nuclei located on different porphyrin units were also assumed to stay uncorrelated. This reduces the Liouville space dimension from 688747536 to 3359216 since the biggest order of spin correlation that must be included under these assumptions is seven. The validity of this assumption may be demonstrated by partitioning the system trajectory into contributions from different levels of spin coherence and correlation [264]. Even in the monomer, several coherence orders may in practice be ignored. In the dimer, the population of the seven-spin correlation sub-space stays below 5 % of the total at all times and it may reasonably be expected that higher levels of spin correlation can be ignored altogether, along with multiple coherence orders that stay unpopulated to very high accuracy.

2. Full symmetry factorisation [265]. The copper hyperfine coupling constants in this system are very large and anisotropic, but the ^{14}N hyperfine coupling tensors can be assumed to be approximately isotropic. Constraining them to be isotropic produces a very reasonable fit. For the purposes of the simulation this signifies that two groups of nuclei have S_4 permutation symmetry each and the full symmetry group of the system is $S_4 \times S_4$. Spinach auto-generates character tables for product groups [68] and a full symmetry factorisation is therefore possible over 576 elements and 25 irreducible representations. Because only the fully symmetric irreducible representation is required for Liouville space simulations [265], the state space dimension is reduced further from 3359216 to 253424.

3. Trajectory level state space restriction [266]. Because the initial condition in our time-domain simulation is very sparse ($\mathcal{L}_+$ state on the electrons), and there are multiple hidden conservation laws in high-field EPR Hamiltonians of symmetric systems with multiple isotropic couplings [265], trajectory level basis pruning algorithms in Spinach [265, 266] were able to reduce the state space dimension further: The zero track elimination module [266] reports that the actual trajectory is confined to a 1916-dimensional sub-space of the 253424-dimensional

space produced at the previous stage. Matrix-matrix and matrix-vector operations involving arrays of dimension 1916 are realistic, but rather slow.

4. Sparse GPU processing. A workstation with two *Tesla K40c* coprocessor cards was used for the simulations. Spinach supports sparse CUDA exponentiation, which, in this case, results in an about ten-fold acceleration relative to a 32-core CPU simulation. This brings the simulation time for a single spin system orientation down to several seconds.

With all of these measures in place, a simulation involving a 10-point conformational grid (spanning a quadrant of the full circle) and an 800-point spherical averaging grid (a two-angle REPULSION set [267] spanning an octant of the full sphere) takes a few hours on a 32-core workstation with 256 GB of memory and two *Tesla K40c* coprocessor cards.

C.2 Derivation of the Analytic Expression for DEER Including *D* and *J*

The following derivation of the analytic expression for DEER including D and J, used for the simulations presented and discussed in Chapter 4, was carried out by Prof. Ilya Kuprov (University of Southampton, UK):

A two electron system with dipole-dipole and exchange couplings has the the following Hamiltonian:

$$\begin{aligned}\mathcal{H}(\Omega) = \; & \omega_1\mathcal{L}_Z^{(1)} + \omega_2\mathcal{L}_Z^{(2)} - \sqrt{6}\,\frac{\mu_0}{4\pi}\,\frac{\gamma_1\gamma_2\hbar}{r^3}\sum_{m=-2}^{2}\mathcal{T}_{2,m}D_{m,0}^{(2)}(\Omega) \\ & + J\left(\mathcal{L}_X^{(1)}\mathcal{L}_X^{(2)} + \mathcal{L}_Y^{(1)}\mathcal{L}_Y^{(2)} + \mathcal{L}_Z^{(1)}\mathcal{L}_Z^{(2)}\right)\end{aligned} \tag{C.1}$$

where Ω represents a set of three Euler angles, $D_{m,0}^{(2)}(\Omega)$ are second-rank Wigner D functions, J is defined in the NMR convention in angular frequency units and the irreducible spherical tensor operators are:

$$\begin{aligned}\mathcal{T}_{2,2} &= +\frac{1}{2}\,\mathcal{L}_+^{(1)}\mathcal{L}_+^{(2)} \\ \mathcal{T}_{2,1} &= -\frac{1}{2}\left(\mathcal{L}_Z^{(1)}\mathcal{L}_+^{(2)} + \mathcal{L}_+^{(1)}\mathcal{L}_Z^{(2)}\right) \\ \mathcal{T}_{2,0} &= +\sqrt{\frac{2}{3}}\left(\mathcal{L}_Z^{(1)}\mathcal{L}_Z^{(2)} - \frac{1}{4}\left(\mathcal{L}_+^{(1)}\mathcal{L}_-^{(2)} + \mathcal{L}_-^{(1)}\mathcal{L}_+^{(2)}\right)\right) \\ \mathcal{T}_{2,-1} &= +\frac{1}{2}\left(\mathcal{L}_Z^{(1)}\mathcal{L}_-^{(2)} + \mathcal{L}_-^{(1)}\mathcal{L}_Z^{(2)}\right) \\ \mathcal{T}_{2,-2} &= +\frac{1}{2}\mathcal{L}_-^{(1)}\mathcal{L}_-^{(2)}\end{aligned} \tag{C.2}$$

Applying the rotating frame with respect to the Zeeman Hamiltonian

$$\mathcal{H}_0 = \omega_1\mathcal{L}_Z^{(1)} + \omega_2\mathcal{L}_Z^{(2)} \tag{C.3}$$

and relying on the fact that the spin echo would refocus the g-factor offset variations, we obtain the following rotating frame Hamiltonian in the limit when $|\omega_1 - \omega_2| \gg |D| + |J|$ (high field and weak coupling approximations):

$$\begin{aligned}\mathcal{H}(\Omega) &= \frac{\mu_0}{4\pi}\frac{\gamma_1\gamma_2\hbar}{r^3}\left(1-3\cos^2\theta\right)\,\mathcal{L}_Z^{(1)}\mathcal{L}_Z^{(2)} + J\mathcal{L}_Z^{(1)}\mathcal{L}_Z^{(2)}\\ &= \omega_{dd}\left(1-3\cos^2\theta\right)\,\mathcal{L}_Z^{(1)}\mathcal{L}_Z^{(2)} + J\mathcal{L}_Z^{(1)}\mathcal{L}_Z^{(2)}\end{aligned} \tag{C.4}$$

which, when acting on the transverse magnetisation, would produce the following oscillation:

$$s(\theta, t) = \cos\left(\left[\omega_{dd}\left(1-3\cos^2\theta\right) + J\right]t\right) \tag{C.5}$$

Averaging this over all molecular orientations yields:

$$\begin{aligned}f(t) &= \frac{1}{2}\int_0^{\pi}\cos\left(\left[\omega_{dd}\left(1-3\cos^2\theta\right)+J\right]\,t\right)\,\sin\theta\,\mathrm{d}\theta\\ &= \sqrt{\frac{\pi}{6\,D\,t}}\left[\cos\Big(\left(D+J\right)t\Big)\,\mathrm{FrC}\left(\sqrt{\frac{6\,D\,t}{\pi}}\right) + \sin\Big(\left(D+J\right)t\Big)\,\mathrm{FrS}\left(\sqrt{\frac{6\,D\,t}{\pi}}\right)\right]\end{aligned} \tag{C.6}$$

with the Fresnel functions defined according to:

$$\mathrm{FrC}(x) = \int_0^{x}\cos\left(t^2\right)\,\mathrm{dt} \qquad\qquad \mathrm{FrS}(x) = \int_0^{x}\sin\left(t^2\right)\,\mathrm{dt} \tag{C.7}$$

Appendix D: Characterisation of the Metal-Ligand Interaction between $\mathbf{P1_{Cu}}$ and Pyridine

In the experimental ENDOR spectra of ***c*-P10$_{Cu2}$ · (T5)$_2$** an additional nitrogen hyperfine coupling was observed (cf. Chapter 3), as compared to the spectra of ***c*-P10$_{Cu2}$** without template or ***c*-P10$_{Cu2}$ · (T4)$_2$**, which was suspected to arise from ligand coordination. To confirm the origin of this coupling, the influence of the metal-ligand interaction between a copper porphyrin monomer and an axial pyridine ligand on the EPR properties was characterised. A copper porphyrin monomer without (**P1$_{Cu}$**) and with an axial pyridine ligand bound to the central copper atom (**P1$_{Cu}$· py**) were investigated by EPR and their properties compared. The structures of the two studied compounds are illustrated in **Figure D.1**.

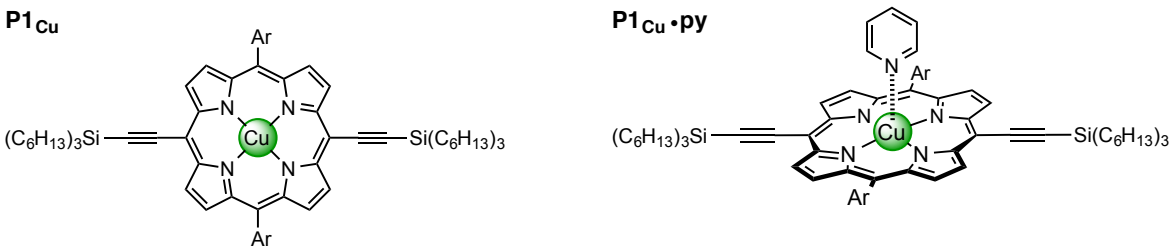


Figure D.1: Chemical structures of the two compounds investigated to characterise the influence of the metal-ligand interaction between copper and an axial nitrogen ligand on the EPR spectra.

The experiments were performed on 0.1 mM solutions of **P1$_{Cu}$** with **tBu** side groups in either toluene or toluene:pyridine 1:1.

D.1 Experimental Results

The experimental X-band cw EPR spectra of **P1$_{Cu}$** and **P1$_{Cu}$· py** recorded at 100 K are compared in **Figure D.2**. It can clearly be observed that the coordination of an axial nitrogen ligand to copper shifts the entire spectrum to lower fields, indicative for an increase in the g-values. Furthermore, the out-of-plane hyperfine coupling constant of copper, $A_{||}$, seems to be markedly reduced.

Since changes in the nitrogen hyperfine coupling constants are difficult to discern from the cw EPR spectra, pulse ^{14}N Davies ENDOR measurements were carried out at 15 K at Q-band frequencies. Only a small fraction of the EPR spectrum can be excited by the microwave pulses and the Davies ENDOR spectra are therefore governed by orientation selection. Depending on whether orientations on $g_{||}$ or $g_{\perp}$ are excited at a particular field position, different spectra are obtained as is illustrated in **Figure D.3**.

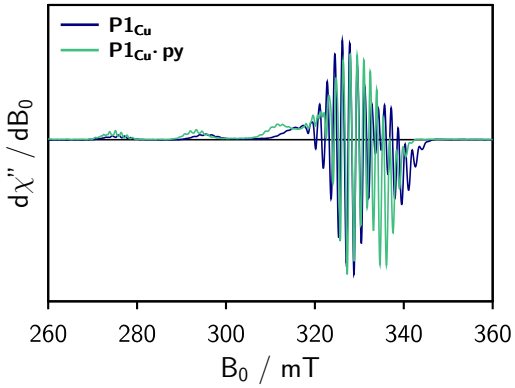


Figure D.2: Comparison of the cw EPR spectra of $\mathbf{P1_{Cu}}$ and $\mathbf{P1_{Cu}}\cdot\mathbf{py}$ recorded at 100 K.

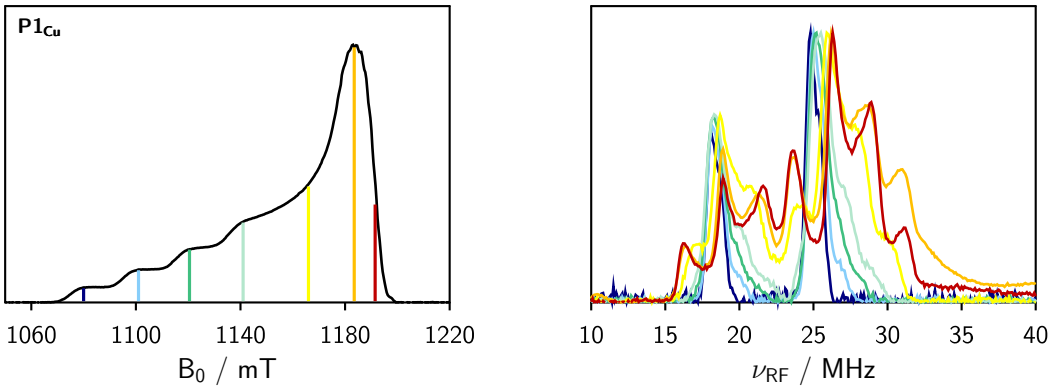


Figure D.3: Field-swept echo-detected EPR spectrum of $\mathbf{P1_{Cu}}$ (*left*) and comparison of the Davies ^{14}N ENDOR spectra (*right*) recorded at different field positions as indicated in the spectrum.

For comparison of the properties of $\mathbf{P1_{Cu}}$ and $\mathbf{P1_{Cu}}\cdot\mathbf{py}$, two representative ENDOR spectra recorded at field positions corresponding to the parallel (z) and perpendicular (xy) orientations of the **g**-tensor are contrasted. The field positions, where the spectra were taken, are indicated for both samples in **Figure D.4**, while the ENDOR data are compared in **Figure D.5**.

It can be observed that the spectra of $\mathbf{P1_{Cu}}\cdot\mathbf{py}$ are entirely shifted to lower frequencies by about 1.5 MHz as compared to those of $\mathbf{P1_{Cu}}$. In the strong coupling regime, the peak positions relative to the frequency axis indicate the hyperfine couplings ($A/2$) as shown in **Figure D.6**, suggesting that ligand coordination leads to a reduction in the nitrogen hyperfine coupling constants by about 3 MHz (in all directions).

D.2 Numerical Simulations of the Spectra

To determine the ^{14}N hyperfine coupling constants, the ENDOR spectra were simulated in MATLAB using EasySpin in combination with a home-written fitting routine. The spectra recorded for the xy and z orientations were fitted simultaneously in a least-squares sense until the best possible

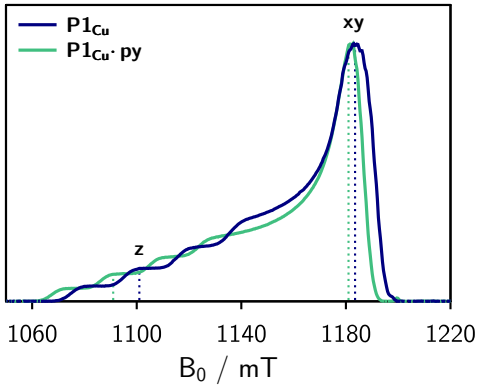


Figure D.4: Comparison of the field-swept echo-detected Q-band EPR spectra of **P1$_{Cu}$** and **P1$_{Cu}$· py** corrected to a common frequency of 34.0 GHz. The field positions where the ENDOR spectra were taken are indicated by dotted lines.

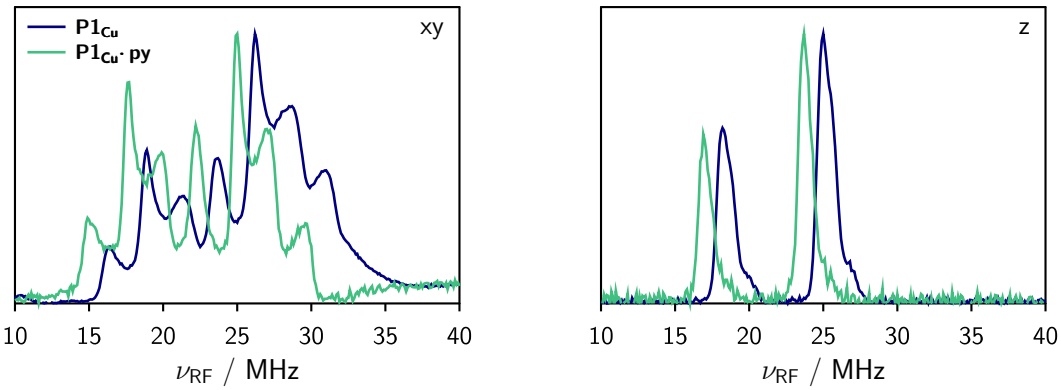


Figure D.5: Comparison of the Davies ^{14}N ENDOR spectra of **P1$_{Cu}$** and **P1$_{Cu}$· py** recorded at field positions corresponding to the *xy* (*left*) and *z* (*right*) orientations of the **g**-tensor at 15 K.

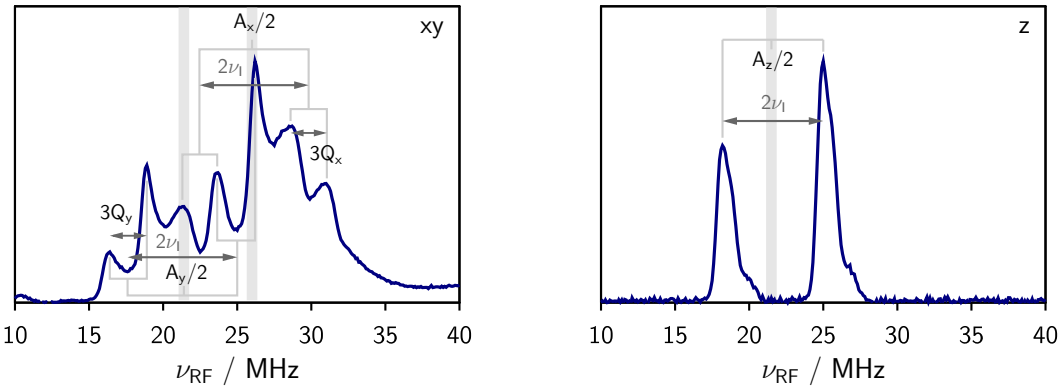


Figure D.6: Illustration of the connection between the ENDOR peak positions and the hyperfine and nuclear quadrupole couplings in the strong coupling regime for an $S = \frac{1}{2}$, $I = 1$ system. The spectra shown have been recorded for **P1$_{Cu}$** in toluene (15 K) at field positions corresponding to the *xy* (*left*) and *z* (*right*) orientations.

agreement between simulation and experimental data was obtained. The results for both samples are shown in **Figure D.7**.

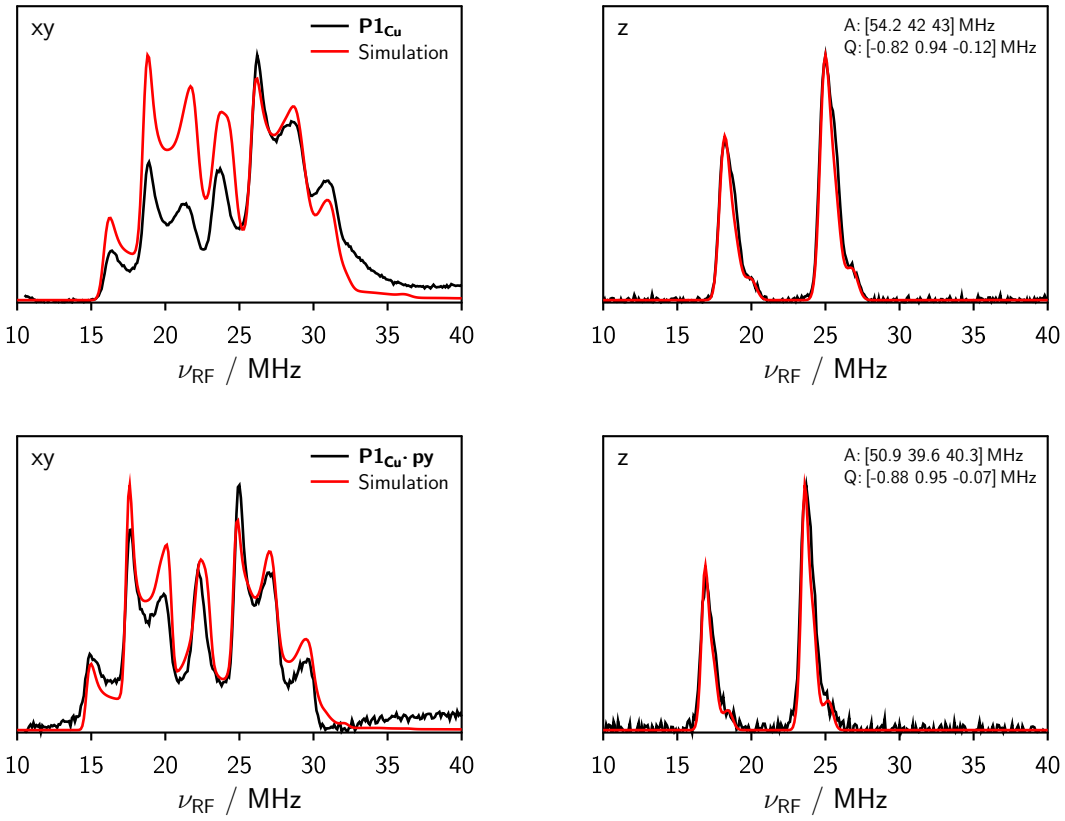


Figure D.7: Davies ENDOR spectra of $\mathbf{P1_{Cu}}$ (*top*) and $\mathbf{P1_{Cu}}$**· py** (*bottom*) recorded at field positions corresponding to the *xy* (*left*) and *z* (*right*) orientations together with the corresponding simulations. The simulation parameters are indicated in the figure.

As could already be anticipated by visual comparison of the spectra, smaller nitrogen hyperfine coupling constants are obtained for $\mathbf{P1_{Cu}}$**· py** as compared to $\mathbf{P1_{Cu}}$. The respective values are indicated in the figure. The nuclear quadrupole couplings could also be quantified for both samples but trends are less obvious.

When comparing simulation and experimental data for the *xy* orientation in **Figure D.7**, it is noted, especially in the case of $\mathbf{P1_{Cu}}$, that the relative intensities of the individual experimental ENDOR peaks cannot be reproduced satisfactorily in all cases by the simulation. However, since all the relevant information is contained in the peak positions, the mismatch in the relative peak intensities is not crucial for the interpretation of the spectra. The differences could be due to the neglect of hyperfine enhancement effects in the simulations. The absence of saturation of the ENDOR lines during the measurement was verified experimentally by recording ENDOR spectra at a 10-times slower repetition rate and comparing the relative line intensities. Saturation can be ruled out as a possible cause of the intensity differences, as is shown in **Figure D.8**, since the two spectra recorded for shot repetition times of 4 μs and 40 μs are virtually identical.

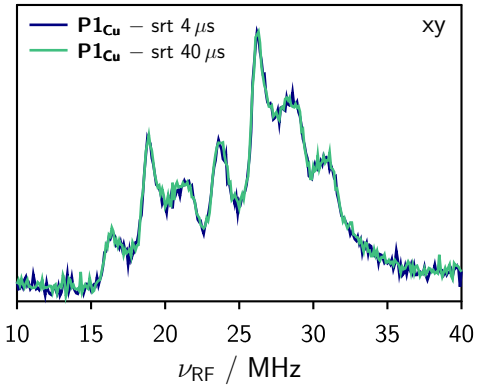


Figure D.8: Comparison of the Davies ENDOR spectra of **P1$_{Cu}$** in toluene recorded at two different shot-to-shot repetition times as indicated. The spectra were taken at 15 K at a field position corresponding to the *xy* orientation.

Simulations of the cw EPR Spectra

To determine the *g*-factors and copper hyperfine coupling constants, numerical simulations of the cw EPR spectra of **P1$_{Cu}$** and **P1$_{Cu}$· py** were carried out as follows: The nitrogen hyperfine coupling parameters were taken from the simulations of the corresponding ^{14}N ENDOR spectra and were kept fixed during the simulations. The *g*-factors, copper hyperfine couplings and linewidth parameters were then varied until an acceptable fit was obtained. The results are shown in **Figure D.9** together with the corresponding simulation parameters.

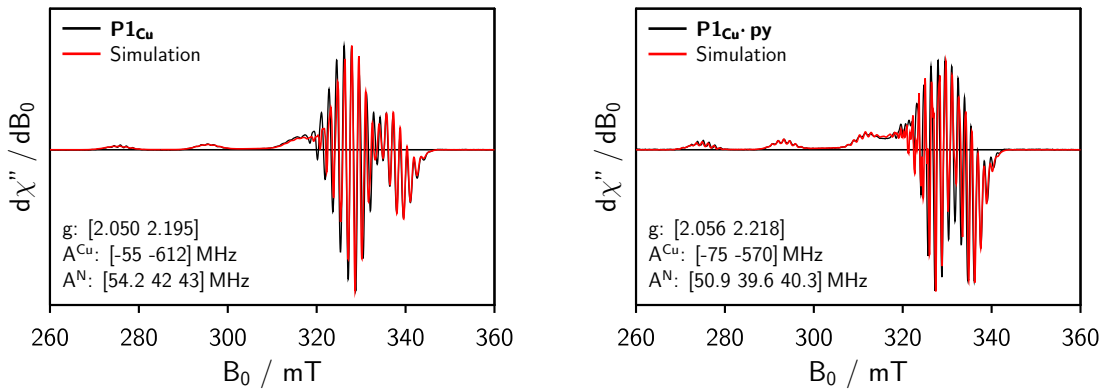


Figure D.9: Experimental cw EPR spectra of **P1$_{Cu}$** (*left*) and **P1$_{Cu}$· py** (*right*) recorded at 100 K together with the corresponding simulations. The simulation parameters are indicated in the figure.

The experimental spectra can be reproduced reasonably well if an increase in the *g*-values and a decrease in the out-of-plane copper hyperfine coupling constant are assumed in the presence of pyridine. The in-plane copper hyperfine coupling constant, $A_\perp$, cannot be determined reliably by cw EPR due to a strong overlap of the lines and the absence of any indicative features in the relevant spectral region. Trends in this parameter shall therefore not be interpreted here. More precise information about the magnitude of $A_\perp$ could be obtained making use of a recently developed approach using ultra-wideband excitation with frequency-swept chirp pulses [268].

Table D.1 gives an overview of the parameters obtained from simulations of the cw EPR and ^{14}N ENDOR spectra for $\mathbf{P1_{Cu}}$ and $\mathbf{P1_{Cu}\cdot py}$. Although the differences in the parameters are not large between the two samples, the changes in the experimental spectra occurring upon ligand coordination are remarkable, illustrating the power of EPR to detect subtile changes in the local coordination environment of the paramagnetic centre. The absolute values of the hyperfine coupling constants are thus a very sensitive measure of the strength of the metal-ligand interaction.

Table D.1: Overview of the hyperfine coupling parameters and *g*-values obtained from a numerical simulation of the experimental ENDOR and cw EPR spectra of $\mathbf{P1_{Cu}}$ and $\mathbf{P1_{Cu}\cdot py}$.

	$A^{N}_{[x,y,z]}$ / MHz	$A^{Cu}_{\|\|}$ / MHz	$[g_{\perp}, g_{\|\|}]$
$\mathbf{P1_{Cu}}$	[54.2, 42, 43]	-612	[2.050, 2.195]
$\mathbf{P1_{Cu}\cdot py}$	[50.9, 39.6, 40.3]	-570	[2.056, 2.218]

Appendix E: Orientation Selective DEER on *c*-P10$_{Cu2}$

Already at X-band, the EPR spectrum of copper porphyrins has a spectral width of almost 2 GHz owing to a large **g**- (and **A**)-tensor anisotropy. At Q-band, the field positions of $g_\perp$ and $g_{||}$ are split apart even further, resulting in a spectral width of about 3.4 GHz.

A 16 ns pump pulse, for example, only has an excitation bandwidth of about 75 MHz and can therefore only excite a very small fraction of the experimental spectrum. Depending on the field position where the pump pulse is applied in the DEER experiment, a different (small) subset of orientations is excited and we should thus be able to observe effects of orientation selection [42, 269].

In general, such effects should be more pronounced at higher spectrometer frequencies, since the different orientations are more spread out, however the resonator bandwidth strongly limits the maximum frequency separation between pump and detection pulses, so that it becomes more difficult to pump and detect truly different orientations at higher frequencies. To get a maximum amount of information and therefore constraints for the analysis, it would for example be desirable to be able to pump on $g_\perp$ and detect on $g_{||}$ and vice versa, in addition to pumping and detecting on either $g_\perp$ or $g_{||}$. While this could still be imagined to work at X-band, the bandwidth of the available Q-band resonator ($\sim$130 MHz) precludes such an experiment.

The orientations excited when pumping or detecting at selected field positions in the X-band and Q-band spectra of ***c*-P10$_{Cu2}$** are indicated on unit spheres in **Figure E.1** and **Figure E.2**, respectively. Excited orientations are shown in red. The orientations have been calculated using the MATLAB package EasySpin using the spin Hamiltonian parameters obtained from a simulation of the corresponding cw EPR spectrum. While at X-band prominent features corresponding to $g_\perp$ and $g_{||}$ still overlap, parallel and perpendicular orientations are completely separated at Q-band.

Orientation selective effects on the DEER time traces were simulated using the program described in reference [43]. To specify the relative orientations of the A and B spins, the parameter definitions illustrated in **Figure 1.22** were used. The **g**-tensor frame of the A spins is taken as the reference frame. The position of the second spin is defined by the inter-spin distance r_{AB}, the polar angle θ and the azimuthal angle φ. The orientation of the second spin with respect to the reference frame is given by the three Euler angles α, β, and γ, where the *zyz*-convention was adopted. For every unique molecular orientation of the spin system, a vector $p = [\theta, \varphi, r_{AB}, \alpha, \beta, \gamma]$ is built up, which serves as an input for the program.

The microwave frequencies and pulse lengths of detection and pump pulses being known as well as the spectrum of the sample and the magnetic field position where the DEER trace was acquired, the pulse profiles and therefore the fractions of spins excited by the detection and pump pulses

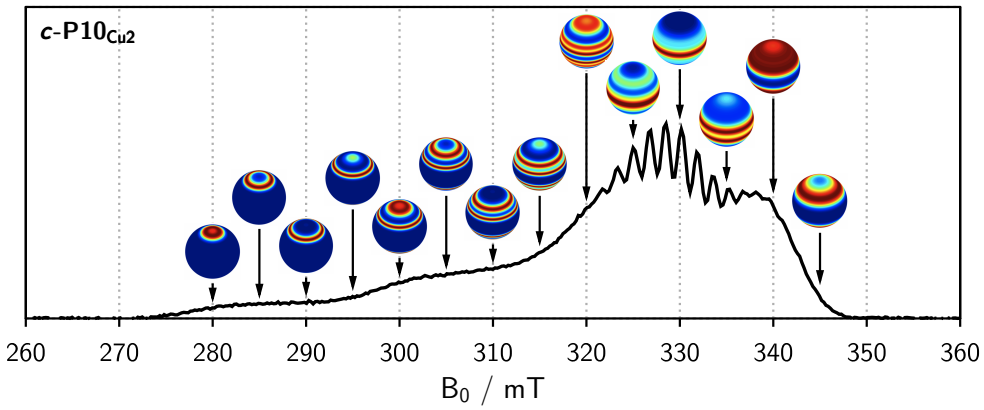


Figure E.1: Illustration of the orientations excited at different field positions within the X-band spectrum of *c*-**P10**$_{Cu2}$. Excited orientations are shown in red.

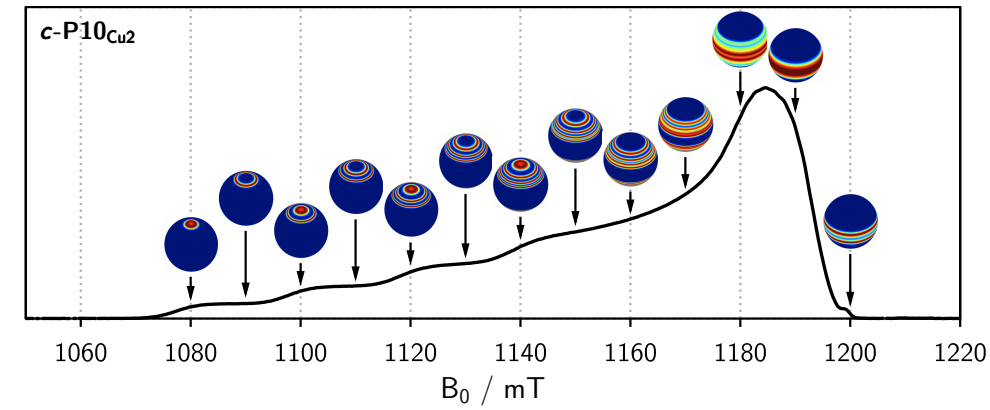


Figure E.2: Illustration of the orientations excited at different field positions within the Q-band spectrum of *c*-**P10**$_{Cu2}$. Excited orientations are shown in red.

and their weights can be calculated. To account for powder averaging, the program then loops over all possible (unique) orientations of the magnetic field with respect to the reference frame. For every field orientation corresponding to a part of the spectrum excited by the detection pulses, the pump spin spectrum and modulation depth are calculated followed by the dipolar frequencies. The dipolar frequencies are weighted by the excitation fractions and added and the final calculated DEER trace is obtained by inverse Fourier transformation of the frequency spectrum.

For comparison with the experimental data, a structural model needs to be assumed and the DEER traces are then calculated for every possible molecular orientation within this model, characterised by a vector p and a weight w_p. The simulated DEER trace, $V_S(t)$, to be compared with the experiment, which includes the zero-frequency background, is modeled as

$$V_S(t) = \left[1 - \lambda + \lambda S(t)\right] \exp\left(-kt\right) \tag{E.1}$$

where $S(t)$ is the weighted sum of the reduced form factors of the calculated DEER traces.

Figure E.3 shows DEER traces acquired at three different field positions within the spectrum of ***c*-P10$_{Cu2}$** measured at Q-band (15 K). The field positions are indicated in the spectrum. The blue trace corresponds to a frequency offset of 200 MHz, whereas an offset of 100 MHz was used in the case of the green and red traces.

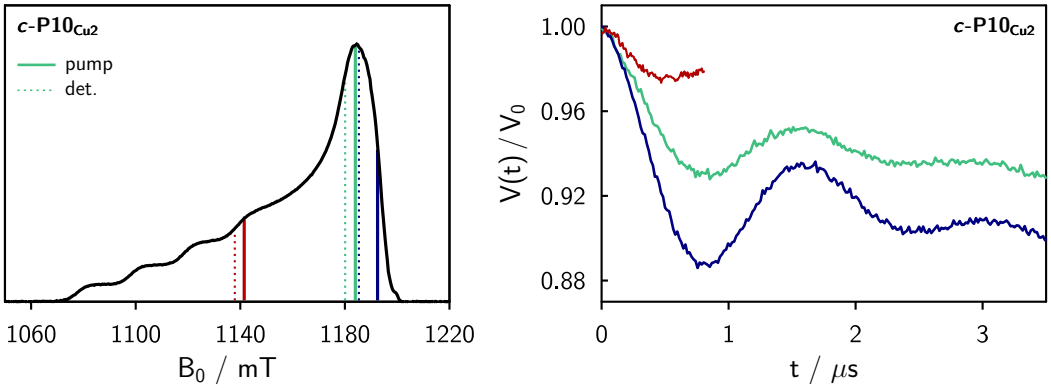


Figure E.3: Field-swept echo detected EPR spectrum of ***c*-P10$_{Cu2}$** measured at Q-band at 15 K (*left*) and DEER traces recorded at different field positions as indicated in the spectrum (*right*).

Recording data in the $g_{||}$ (z) part of the spectrum turns out to be more difficult than expected, since not only the signal intensity is much lower, but also relaxation is faster as can be seen from **Figure E.4**. While traces up to 4 μs can be recorded in the xy part of the spectrum, the maximum trace length feasible for z is rather of the order of 2 μs.

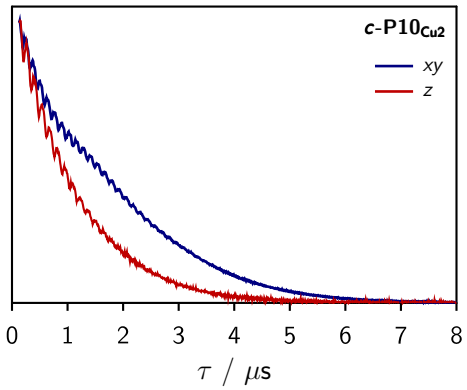


Figure E.4: Phase memory time T_m recorded for ***c*-P10$_{Cu2}$** at two different field positions corresponding to the xy and z part of the spectrum.

It is observed that the frequency dominating the DEER trace when pump and detection pulses are both placed on xy is very similar in all cases,* while it is clearly different (higher) when the z part of the spectrum is probed. A model-free analysis using Tikhonov regularisation as implemented in DeerAnalysis yields the distance distributions shown in **Figure E.5** and confirms this observation.

*More traces than shown here were acquired at various positions on xy and no significant variations in the modulation frequency were observed.

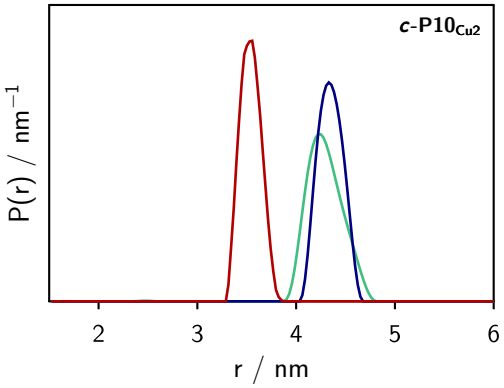


Figure E.5: Distance distributions obtained for the three DEER traces shown above applying Tikhonov regularisation as implemented in DeerAnalysis.

Apart from differences in modulation frequencies, orientation selection also manifests itself in differences in the modulation depth. However, since modulation depths are generally difficult to analyse in detail as they are strongly dependent on the experimental setup,[†] we shall only be concerned here with the effect of orientation selection on the measured dipolar frequencies.

Before defining a particular geometric model or parameter grid for the simulation of the DEER traces of ***c*-P10$_{Cu2}$**, the influence of certain input parameters on the simulated trace was tested. Since the spin system is axial, the number of variable input parameters used to construct the vector p can be reduced as shown in **Table E.1** [42, 84]. For a definition of the angles see **Figure 1.22**. It was confirmed by simulations that the azimuthal angle φ and one of the Euler angles, α, do not have any influence on the simulated time traces. These parameters were therefore set to zero in all further calculations.

Table E.1: Overview of the parameter range which needs to be considered for an axially symmetric system. The Euler angles are defined according to the *zyz*-convention.

θ	φ	α	β	γ
$0 - \frac{\pi}{2}$	–	–	$0 - \frac{\pi}{2}$	$0 - \pi$

Considering the structure of the molecule, no large variations from 0° are expected for γ due to geometric constraints. To begin with, the angle γ was therefore set to zero, so that the only fitting parameters were thus r_{AB}, θ, β and their distributions, where β describes the rotation of the porphyrin plane about the connecting triple bonds. All parameter distributions were assumed to be Gaussian, with the Gaussian function $G(x)$ parametrised as follows

$$G(x) = \exp\left(-\frac{(x - x_c)^2}{2\,\sigma_x^2}\right) \tag{E.2}$$

[†]For a valid comparison of the modulation depths of different traces, at least the pump frequency, pulse length and resonator position of the pump pulse should be the same, which is very often not the case when comparing data acquired on different measurement days.

where x_c is the centre of the distribution and σ_x characterises its width.[‡] To be able to fit distributions in the parameters listed above (r_{AB}, θ, β), a grid of traces accounting for all possible variations within a certain parameter space was calculated. The chosen parameter space includes variations in r_{AB} from 3.7 nm to 4.8 nm in steps of 0.02 nm, variations in θ from 0° to 90° in steps of 2°, and variations in β from 0° to 90° in steps of 2°, resulting in $>10^5$ traces.

For comparison of experimental and calculated DEER traces, no background correction was applied beforehand to the experimental data. Instead, an exponential background was added to the calculated traces, as evident from **Equation (E.1)**, and fitted alongside the other parameters, resulting in a total of eight variable parameters, namely, k, λ, r_c, σ_r, θ_c, σ_θ, β_c, and σ_β. Trying to fit eight freely variable parameters at once is not very sensible; therefore the fitting was performed step-wise in an iterative manner.

To reduce the parameter space, the values for r_c and σ_r were determined beforehand from a model-free analysis of the DEER traces recorded at *xy* using DeerAnalysis. Values of $r_c = 4.30$ nm and $\sigma_r = 0.21$ nm were obtained and agree well with those obtained from a fit accounting for orientation selection where (φ_c, σ_φ,) θ_c, σ_θ and the Euler angles were set to zero. These values were thus kept fixed in any further simulations. In the course of the analysis it was also found that the width of the distribution in θ has no marked influence on the appearance of the resulting weighted trace, possibly due to the high symmetry of the system. The parameter σ_θ was consequently kept fixed at 3° in all simulations. Furthermore, given the expected geometry of ***c*-P10$_{Cu2}$**, it seems reasonable to assume that the distribution in β is centred at 0°.

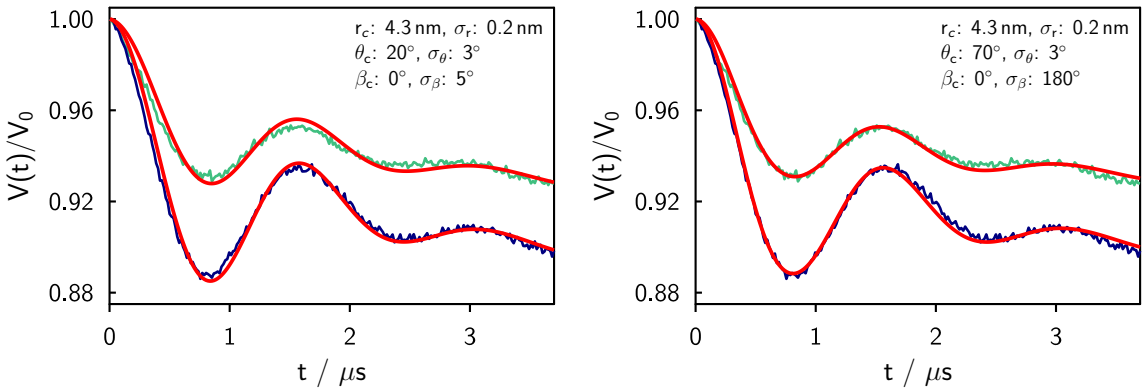


Figure E.6: Comparison of experimental and simulated DEER time traces for ***c*-P10$_{Cu2}$** when only considering the data recorded at *xy*. Two local minima are obtained for $\theta_c = 20°$ (*left*), and $\theta_c = 70°$ (*right*).

For every value of θ, σ_β and the background parameters were then optimised using a least-squares fitting routine. At first, only the two traces recorded on *xy* were considered. It is observed that for θ_c smaller than 20°, no good agreement with the experimental data can be obtained. For θ_c between 20° and 27°, a rather good fit is obtained with relatively narrow distributions σ_β of around 5° for $\theta = 20°$ and roughly 18° for $\theta_c = 27°$. The optimum value for σ_β then increases

[‡]The parameter σ describing the width of the distribution is sometimes also expressed in terms of the full width at half maximum (FWHM) given as: FWHM $= 2\sigma\sqrt{2\ln 2}$.

further with increasing θ_c, however between $\theta_c = 30°$ and 60° the agreement between experiment and simulation is significantly worse. A good fit is again obtained for θ_c between 70° and 75° when very broad distributions in β (almost equal weighting) are assumed, while the fit is worse for $\theta_c = 90°$. Two local minima at $\theta_c = 20°$ and $\theta_c = 70°$ thus result from this analysis, with either a narrow or a very broad distribution in β, respectively, when considering only the *xy* traces.

The corresponding simulations are compared with the experimental data in **Figure E.6**. A broad distribution in β could be feasible since the barrier to rotation about the triple bond is only of the order of 0.5 kcal mol^{-1} at room temperature and 0.8 kcal mol^{-1} at the freezing point of the solvent (toluene, 180 K) [69], while $k_B T$ amounts to 0.6 kcal mol^{-1} and 0.4 kcal mol^{-1} at room temperature and 180 K, respectively. However, within experimental error, both of the fits have to be considered satisfactory and a narrower distribution in β is also plausible under the applied conditions. It is therefore not possible to exclude either local minimum with certainty unless other constraints can be applied.

In summary, in the present case, the distance distributions obtained by using Tikhonov regularisation agree closely with the results of the simulations including orientation selective effects. Regarding orientational selectivity, it was noticed that, due to the high symmetry of the system, any particular change in the weighted calculated curve can often be achieved in two different ways, e.g. going to lower values of θ_c and a narrower distribution in β has a similar effect as going to high values of θ_c and choosing a wider distribution in β, which makes it difficult to draw any definite conclusions. The experimentally recorded DEER traces at different field positions on *xy* at X- and Q-band are very similar; only variations in the modulation depth are observed. Consequently, to exclude one of the two local minima found when analysing the *xy* traces, further constraints are necessary.

It was found that including the DEER trace recorded at *z* orientation is sufficient for this purpose. When including this trace in the analysis, only one clear minimum is obtained with $\theta_c = 20°$ as demonstated in **Figure E.7**. The early onset of the modulation in the *z* trace cannot be reproduced when $\theta_c = 70°$.

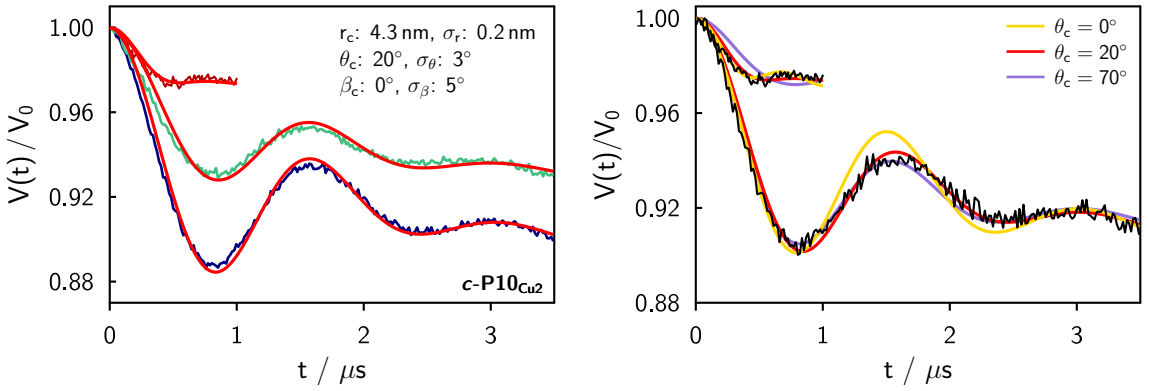


Figure E.7: Comparison of experimental and simulated DEER time traces for ***c*-P10$_{Cu2}$** including the data recorded at *z*. The best fit is obtained for $\theta_c = 20°$ (*left*), while the agreement for other values of θ_c (0°, 70°) is clearly worse (*right*).

So far, in this analysis, any variations in γ were neglected. However, the influence of σ_γ on the outcome of the analysis was tested in retrospective. As for β, it is reasonable to assume that the distribution is centred around 0°. Small variations in the width of the distribution in γ (0° up to 30°) were found not to influence the calculated trace for the two considered local minima significantly. Since large variations can be excluded due to geometric constraints, the neglect of γ in the optimisation procedure seems justified.

The results of this orientation selective analysis of the DEER traces of ***c*-P10$_{Cu2}$**, recorded at field positions corresponding to the *xy* and *z* orientations of the electronic **g**-tensor, suggest that the ring structure is fairly shape persistent in solution. The porphyrin planes of two opposite units at a distance of 4.3 nm seem to be mostly parallel, but with a slight offset of about 20° with respect to the out-of-plane axis of the first porphyrin unit.

Appendix F: Additional Triplet EPR Data on Zinc Porphyrin Oligomers

F.1 Butadiyne-Linked Oligomers

Figure F.1 shows a comparison of the echo-detected field-swept triplet EPR spectra of the linear zinc porphyrin oligomers **P1** to **P4** investigated in Chapter 6. The data were recorded with and without **DABCO** in frozen toluene solution at 20 K. No major changes in the spectra are observed upon addition of **DABCO**. As mentioned in Chapter 6, the ENDOR spectra were recorded at field positions corresponding to the − spin manifold, since the echo intensities were found to be larger.

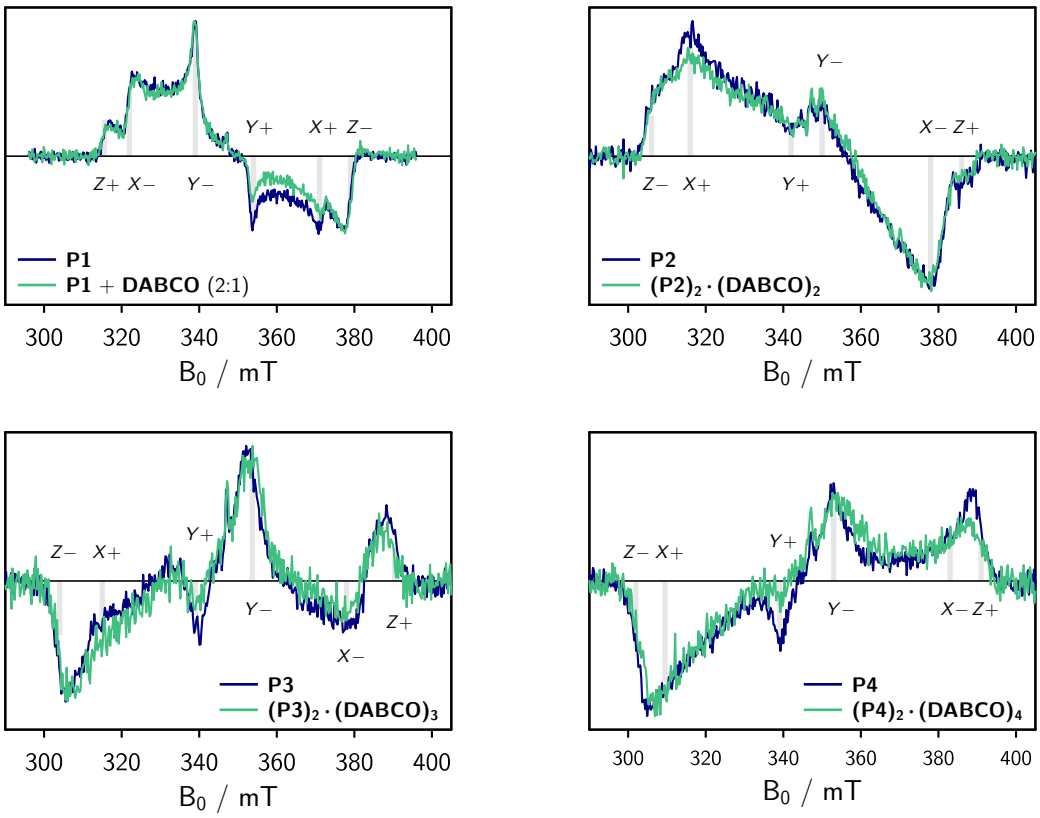


Figure F.1: Comparison of the field-swept echo-detected triplet EPR spectra recorded in frozen toluene (20 K) in the absence and presence of **DABCO** for **P1** (*top left*), **P2** (*top right*), **P3** (*bottom left*) and **P4** (*bottom right*).

In **Figure F.2** the ^{1}H Mims ENDOR spectra recorded at different field positions corresponding to the X, Y and Z orientations of the ZFS tensor are compared for **P1** and **P2**. It can be seen

that the largest and most prominent coupling is observed in the *Y* direction. This coupling was compared between the different oligomers to determine the extent of triplet spin delocalisation in Chapter 6.

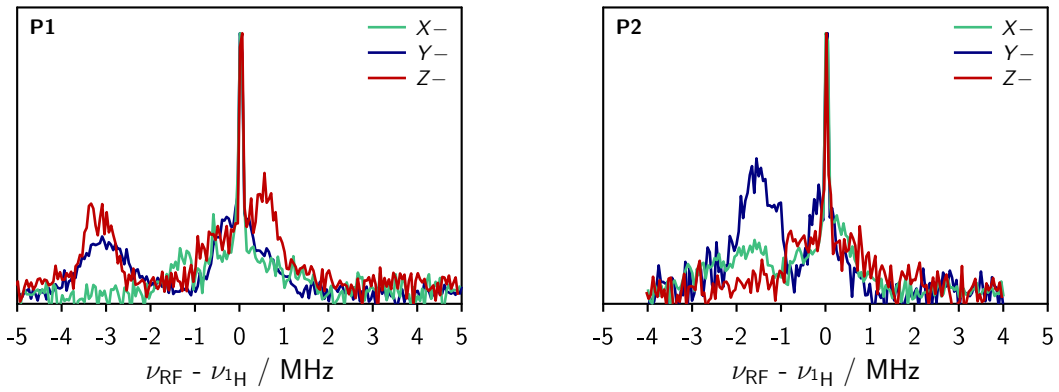


Figure F.2: Comparison of the ^{1}H Mims ENDOR spectra of **P1** (*left*) and **P2** (*right*) recorded at different canonical orientations in frozen toluene (20 K).

F.2 Ethyne-Linked Oligomers

The field-swept echo-detected triplet EPR spectra of the linear *meso*-to-*meso* ethyne-linked zinc porphyrin oligomers investigated in Chapter 7 are shown in **Figure F.3** for reference. **Figures F.4** to **F.8** show the ^{1}H Mims ENDOR spectra recorded at different canonical orientations for the monomers and dimers together with a visualisation of the calculated proton hyperfine coupling tensors. The relative size of the tensors reflects the magnitude of the coupling. The couplings of the terminal *meso*-protons present in **P1$_e$**, **P2** and **P2$_e$**, neglected for clarity in **Figure 7.9**, are also illustrated and **Table F.1** summarises the largest couplings calculated by DFT for the *Y* direction. The orientation of the ZFS tensor as obtained from DFT is indicated by arrows.

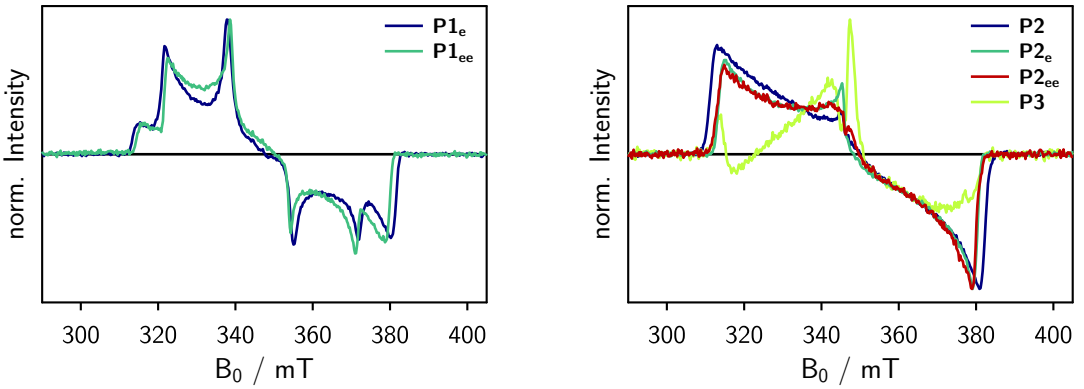


Figure F.3: Field-swept echo-detected triplet EPR spectra of the investigated monomers (*left*) and longer oligomers (*right*) recorded in frozen **MTHF** at 20 K.

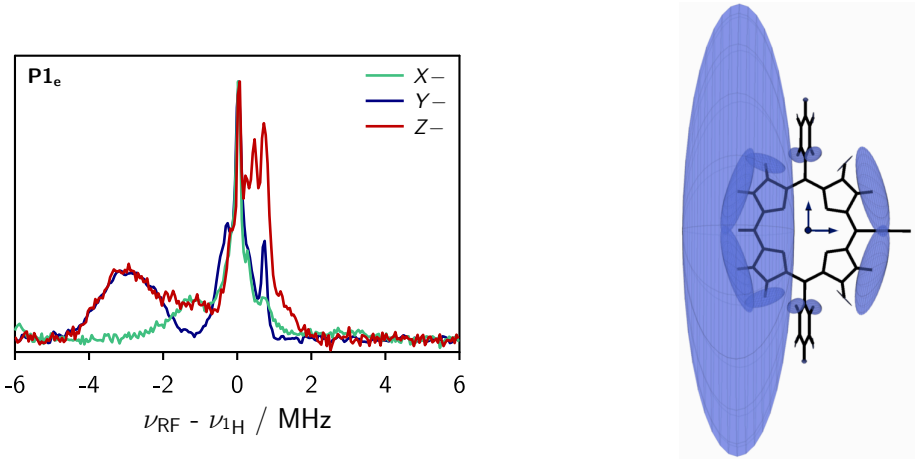


Figure F.4: Comparison of the ^{1}H Mims ENDOR spectra recorded at different canonical orientations in frozen **MTHF** (*left*) and visualisation of the proton hyperfine coupling tensors calculated by DFT (*right*) for **P1$_e$**.

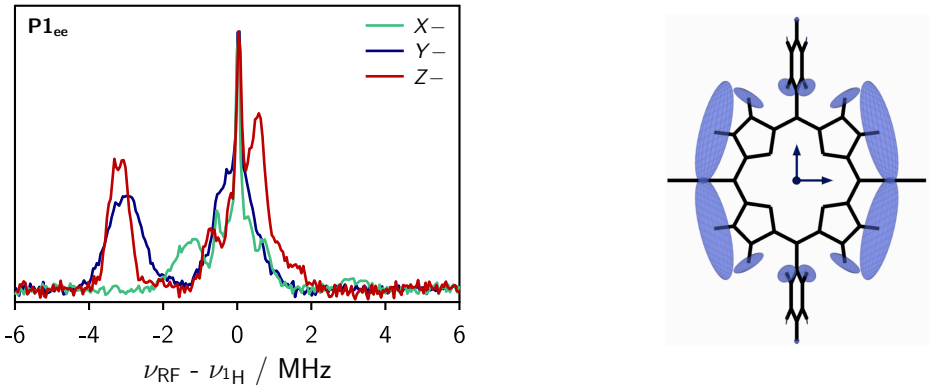


Figure F.5: Comparison of the ^{1}H Mims ENDOR spectra recorded at different canonical orientations in frozen **MTHF** (*left*) and visualisation of the proton hyperfine coupling tensors calculated by DFT (*right*) for **P1$_{ee}$**.

Table F.1: Projection of the largest hyperfine coupling tensors, calculated for the monomers and dimers, onto the *Y* ZFS tensor axis.

Position	P1$_e$	P1$_{ee}$	P2	P2$_e$	P2$_{ee}$
A$_{meso}$ / MHz	−20.5	-	−12.5 (x2)	−5.21	-
A$_{outer}$ / MHz	−4.18 (x2)	−4.18 (x4)	−2.30 (x4)	−3.71 (x2); −0.90 (x2)	−2.37 (x4)
A$_{inner}$ / MHz	−4.47 (x2)	-	−1.24 (x4)	−3.15 (x2); −0.35 (x2)	−1.20 (x4)

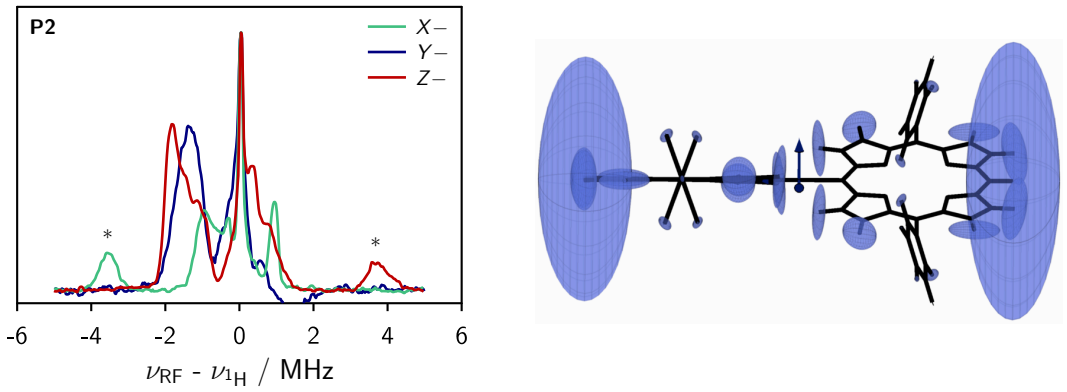


Figure F.6: Comparison of the ^{1}H Mims ENDOR spectra recorded at different canonical orientations in frozen **MTHF** (*left*) and visualisation of the proton hyperfine coupling tensors calculated by DFT (*right*) for **P2**. The couplings marked with $*$ might be due to the terminal *meso*-proton.

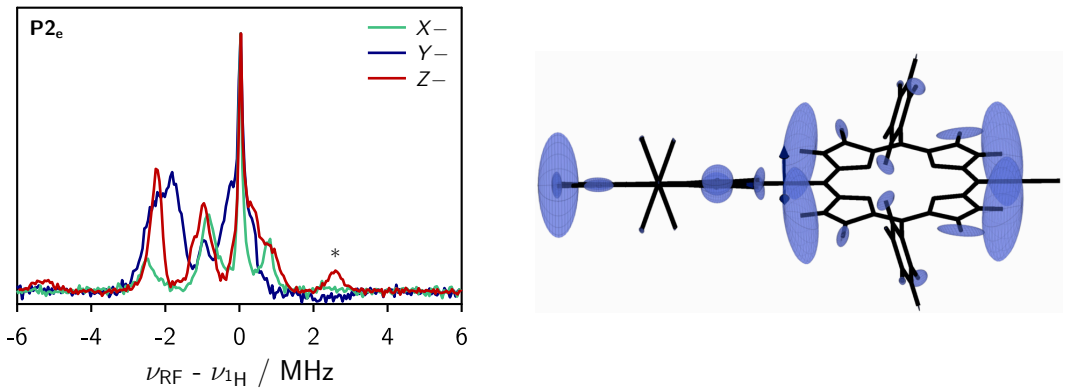


Figure F.7: Comparison of the ^{1}H Mims ENDOR spectra recorded at different canonical orientations in frozen **MTHF** (*left*) and visualisation of the proton hyperfine coupling tensors calculated by DFT (*right*) for **P2$_e$**. The coupling marked with $*$ might be due to the terminal *meso*-proton.

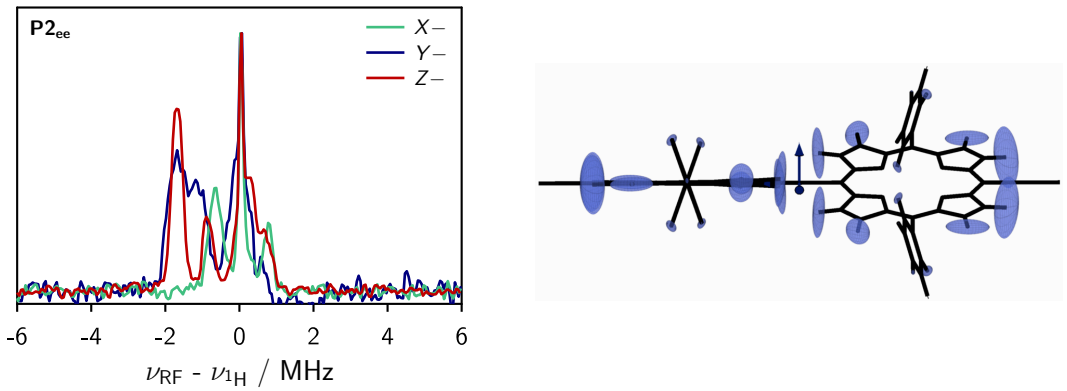


Figure F.8: Comparison of the ^{1}H Mims ENDOR spectra recorded at different canonical orientations in frozen **MTHF** (*left*) and visualisation of the proton hyperfine coupling tensors calculated by DFT (*right*) for **P2$_{ee}$**.

References

[1] Atherton, N. M. *Principles of Electron Spin Resonance*; Ellis Horwood Ltd.: New York, 1993.

[2] Jeschke, G.; Polyhach, Y. Distance Measurements on Spin-Labelled Biomacromolecules by Pulsed Electron Paramagnetic Resonance. *Phys. Chem. Chem. Phys.* **2007**, *9*, 1895–1910.

[3] Eaton, G. R.; Eaton, S. S.; Barr, D. P.; Weber, R. T. *Quantitative EPR*; Springer: Wien, 2010.

[4] Jeschke, G. Instrumentation and Experimental Setup. In *ESR Spectroscopy in Membrane Biophysics*; Hemminga, M. A., Berliner, L. J., Eds.; Biological Magnetic Resonance; Springer: New York, 2007; Vol. 27; Chapter 2, pp 17–47.

[5] Misra, S. K. *Multifrequency Electron Paramagnetic Resonance: Theory and Applications*; Wiley-VCH: Weilheim, 2011.

[6] Schweiger, A.; Jeschke, G. *Principles of Pulse Electron Paramagnetic Resonance*; Oxford University Press: Oxford, 2001.

[7] Eaton, S. S.; Eaton, G. R. Relaxation Times of Organic Radicals and Transition Metal Ions. In *Distance Measurements in Biological Systems by EPR*; Berliner, L. J., Eaton, G. R., Eaton, S. S., Eds.; Biological Magnetic Resonance; Springer: New York, 2000; Vol. 19; Chapter 2, pp 29–154.

[8] Schweiger, A. Pulsed Electron Spin Resonance Spectroscopy: Basic Principles, Techniques, and Examples of Applications. *Angew. Chem. Int. Ed.* **1991**, *30*, 265–292.

[9] Kingsley, P. B. Product Operators, Coherence Pathways, and Phase Cycling. Part I: Product Operators, Spin-Spin Coupling, and Coherence Pathways. *Concepts Magn. Reson.* **1995**, *7*, 29–47.

[10] Kingsley, P. B. Product Operators, Coherence Pathways, and Phase Cycling. Part II: Coherence Pathways in Multipulse Sequences: Spin Echoes, Stimulated Echoes, and Multiple-Quantum Coherences. *Concepts Magn. Reson.* **1995**, *7*, 115–136.

[11] Kingsley, P. B. Product Operators, Coherence Pathways, and Phase Cycling. Part III: Phase Cycling. *Concepts Magn. Reson.* **1995**, *7*, 167–192.

[12] Eaton, S. S.; Eaton, G. R. Saturation Recovery EPR. In *Biomedical EPR, Part B: Methodology, Instrumentation, and Dynamics*; Eaton, S. S., Eaton, G. R., Berliner, L. J., Eds.; Biological Magnetic Resonance; Springer: New York, 2005; Vol. 24; Chapter 1, pp 3–18.

[13] Cernescu, A.; Maly, T.; Prisner, T. F. 2D-REFINE Spectroscopy: Separation of Overlapping Hyperfine Spectra. *J. Magn. Reson.* **2008**, *192*, 78–84.

[14] Höfer, P.; Grupp, A.; Nebenführ, H.; Mehring, M. Hyperfine Sublevel Correlation (HYSCORE) Spectroscopy: A 2D ESR Investigation of the Squaric Acid Radical. *Chem. Phys. Lett.* **1986**, *132*, 279–282.

[15] Jeschke, G. Determination of the Nanostructure of Polymer Materials by Electron Paramagnetic Resonance Spectroscopy. *Macromol. Rapid Commun.* **2002**, *23*, 227–246.

[16] Eaton, S. S.; Eaton, G. R. Distance Measurements by CW and Pulsed EPR. In *Distance Measurements in Biological Systems by EPR*; Berliner, L. J., Eaton, G. R., Eaton, S. S., Eds.; Biological Magnetic Resonance; Springer: New York, 2000; Vol. 19; Chapter 1, pp 1–27.

[17] Borbat, P. P.; Freed, J. F. Pulse Dipolar Electron Spin Resonance: Distance Measurements. In *Structural Information from Spin-Labels and Intrinsic Paramagnetic Centres in the Biosciences*; Timmel, C. R., Harmer, J. R., Eds.; Structure and Bonding; Springer: Berlin Heidelberg, 2013; Vol. 152; Chapter 1, pp 1–82.

[18] Wautelet, P.; Bieber, A.; Turek, P.; Le Moigne, J.; André, J.-J. Magnetic Properties of Iminonitroxide and Nitronylnitroxide based Diradicals. *Mol. Cryst. Liq. Cryst.* **1997**, *305*, 55–67.

[19] Eaton, S. S.; Eaton, G. R. Measurement of Spin-Spin Distances from the Intensity of the EPR Half-Field Transition. *J. Am. Chem. Soc.* **1982**, *104*, 5002–5003.

[20] Eaton, S. S.; More, K. M.; Sawant, B. M.; Eaton, G. R. Use of the EPR Half-Field Transition to Determine the Interspin Distance and the Orientation of the Interspin Vector in Systems with Two Unpaired Electrons. *J. Am. Chem. Soc.* **1983**, *105*, 6560–6567.

[21] Borbat, P. P.; Freed, J. H. Multiple-Quantum ESR and Distance Measurements. *Chem. Phys. Lett.* **1999**, *313*, 145–154.

[22] Saxena, S.; Freed, J. H. Double Quantum Two-Dimensional Fourier Transform Electron Spin Resonance: Distance Measurements. *Chem. Phys. Lett.* **1996**, *251*, 102–110.

[23] Saxena, S.; Freed, J. H. Theory of Double Quantum Two-Dimensional Electron Spin Resonance with Application to Distance Measurements. *J. Chem. Phys.* **1997**, *107*, 1317–1340.

[24] Astashkin, A. V.; Hara, H.; Kawamori, A. The Pulsed Electron-Electron Double Resonance and '2+1' Electron Spin Echo Study of the Oriented Oxygen-Evolving and Mn-Depleted Preparations of Photosystem II. *J. Chem. Phys.* **1998**, *108*, 3805–3812.

[25] Kurshev, V. V.; Raitsimring, A. M.; Tsvetkov, Y. D. Selection of Dipolar Interaction by the '2+1' Pulse Train ESE. *J. Magn. Reson.* **1989**, *81*, 441–454.

[26] Raitsimring, A.; Peisach, J.; Lee, H. C.; Chen, X. Measurement of Distance Distribution between Spin Labels in Spin-Labeled Hemoglobin Using an Electron Spin Echo Method. *J. Phys. Chem.* **1992**, *96*, 3526–3531.

[27] Shigemori, K.; Hara, H.; Kawamori, A.; Akabori, K. Determination of Distances from Tyrosine to D and Q_A and Chlorophyll$_z$ in Photosystem II Studied by '2+1' Pulsed EPR. *Biochem. Biophys. Acta* **1998**, *1363*, 187–198.

[28] Milov, A. D.; Salikhov, K. M.; Shchirov, M. D. Application of the Double Resonance Method to Electron Spin Echo in a Study of the Spatial Distribution of Paramagnetic Centers in Solids. *Sov. Phys. Solid State* **1981**, *23*, 565–569.

[29] Milov, A. D.; Ponomarev, A. B.; Tsvetkov, Y. D. Electron-Electron Double Resonance in Electron Spin Echo: Model Biradical Systems and the Sensitized Photolysis of Decalin. *Chem. Phys. Lett.* **1984**, *110*, 67–72.

[30] Martin, R. E.; Pannier, M.; Diederich, F.; Gramlich, V.; Hubrich, M.; Spiess, H. W. Determination of End-to-End Distances in a Series of TEMPO Diradicals of up to 2.8 nm Length with a New Four-Pulse Double Electron Electron Resonance Experiment. *Angew. Chem. Int. Ed.* **1998**, *37*, 2834–2837.

[31] Pannier, M.; Veit, S.; Godt, A.; Jeschke, G.; Spiess, H. W. Dead-Time Free Measurement of Dipole-Dipole Interactions between Electron Spins. *J. Magn. Reson.* **2000**, *142*, 331–340.

[32] Kulik, L. V.; Dzuba, S. A.; Grigoryev, I. A.; Tsvetkov, Y. D. Electron Dipole-Dipole Interactions in ESEEM of Nitroxide Biradicals. *Chem. Phys. Lett.* **2001**, *343*, 315–324.

[33] Milikisyants, S.; Scarpelli, F.; Finiguerra, M. G.; Ubbink, M.; Huber, M. A Pulsed EPR Method to Determine Distances between Paramagnetic Centers with Strong Spectral Anisotropy and Radicals: The Dead-Time Free RIDME Sequence. *J. Magn. Reson.* **2009**, *201*, 48–56.

[34] Salikhov, K. M.; Kandrashkin, Y. E.; Salikhov, A. K. Peculiarities of Free Induction and Primary Spin Echo Signals for Spin-Correlated Radical Pairs. *Appl. Magn. Reson.* **1992**, *3*, 199–216.

[35] Tang, J.; Thurnauer, M. C.; Norris, J. R. Electron Spin Echo Envelope Modulation due to Exchange and Dipolar Interactions in a Spin-Correlated Radical Pair. *Chem. Phys. Lett.* **1994**, *219*, 283–290.

[36] Jeschke, G. DEER Distance Measurements on Proteins. *Annu. Rev. Phys. Chem.* **2012**, *63*, 419–446.

[37] Jeschke, G. Interpretation of Dipolar EPR Data in Terms of Protein Structure. In *Structural Information from Spin-Labels and Intrinsic Paramagnetic Centres in the Biosciences*; Timmel, C. R., Harmer, J. R., Eds.; Structure and Bonding; Springer: Berlin Heidelberg, 2013; Vol. 152; Chapter 2, pp 83–120.

[38] Jeschke, G. Distance Measurements in the Nanometer Range by Pulse EPR. *Chem. Phys. Chem.* **2002**, *3*, 927–932.

[39] Jeschke, G.; Koch, A.; Jonas, U.; Godt, A. Direct Conversion of EPR Dipolar Time Evolution Data to Distance Distributions. *J. Magn. Reson.* **2002**, *155*, 72–82.

[40] MATLAB, *version 7.11.0 (R2010b)*; The MathWorks Inc.: Natick, Massachusetts, 2010.

[41] Jeschke, G.; Chechik, V.; Ionita, P.; Godt, A.; Zimmermann, H.; Banham, J.; Timmel, C. R.; Hilger, D.; Jung, H. DeerAnalysis2006 — a Comprehensive Software Package for Analyzing Pulsed ELDOR Data. *Appl. Magn. Reson.* **2006**, *30*, 473–498.

[42] Bowen, A. M.; Tait, C. E.; Timmel, C. R.; Harmer, J. R. Orientation-Selective DEER Using Rigid Spin Labels, Cofactors, Metals, and Clusters. In *Structural Information from Spin-Labels and Intrinsic Paramagnetic Centres in the Biosciences*; Timmel, C. R., Harmer, J. R., Eds.; Structure and Bonding; Springer: Berlin Heidelberg, 2013; Vol. 152; Chapter 7, pp 283–327.

[43] Lovett, J. E.; Bowen, A. M.; Timmel, C. R.; Jones, M. W.; Dilworth, J. R.; Caprotti, D.; Bell, S. G.; Wong, L. L.; Harmer, J. Structural Information from Orientationally Selective DEER Spectroscopy. *Phys. Chem. Chem. Phys.* **2009**, *11*, 6840–6848.

[44] Eaton, G. R.; Eaton, S. S. EPR Studies of Long-Range Intramolecular Electron-Electron Exchange Interaction. *Acc. Chem. Res.* **1988**, *21*, 107–113.

[45] Bencini, A.; Gatteschi, D. *EPR of Exchange Coupled Systems*; Dover Publications: New York, 2012.

[46] Wolf, S. A.; Awschalom, D. D.; Buhrman, R. A.; Daughton, J. M.; von Molnár, S.; Roukes, M. L.; Chtchelkanova, A. Y.; Treger, D. M. Spintronics: A Spin-Based Electronics Vision for the Future. *Science* **2001**, *294*, 1488–1495.

[47] Rocha, A. R.; García-Suárez, V. M.; Bailey, S. W.; Lambert, C. J.; Ferrer, J.; Sanvito, S. Towards Molecular Spintronics. *Nat. Mater.* **2005**, *4*, 335–339.

[48] Sanvito, S. Molecular Spintronics. *Chem. Soc. Rev.* **2011**, *40*, 3336–3355.

[49] Aradhya, S. V.; Venkataraman, L. Single-Molecule Junctions Beyond Electronic Transport. *Nat. Nanotech.* **2013**, *8*, 399–410.

[50] Rao, A.; Chow, P. C. Y.; Gélinas, S.; Schlenker, C. W.; Li, C.-Z.; Yip, H.-L.; Jen, A. K.-Y.; Ginger, D. S.; Friend, R. H. The Role of Spin in the Kinetic Control of Recombination in Organic Photovoltaics. *Nature* **2013**, *500*, 435–440.

[51] Sedghi, G.; García-Suárez, V. M.; Esdaile, L. J.; Anderson, H. L.; Lambert, C. J.; Martín, S.; Bethell, D.; Higgins, S. J.; Elliott, M.; Bennett, N.; Macdonald, J. E.; Nichols, R. J. Long-range Electron Tunnelling in Oligo-Porphyrin Molecular Wires. *Nat. Nanotech.* **2011**, *6*, 517–523.

[52] Nitzan, A. Electron Transmission Through Molecules and Molecular Interfaces. *Annu. Rev. Phys. Chem.* **2001**, *52*, 681–750.

[53] Taylor, P. N.; Huuskonen, J.; Rumbles, G.; Aplin, R. T.; Williams, E.; Anderson, H. L. Conjugated Porphyrin Oligomers from Monomer to Hexamer. *Chem. Commun.* **1998**, 909–910.

[54] Greiner, S. P.; Rowlands, D. L.; Kreilick, R. W. EPR and ENDOR Study of Selected Porphyrin- and Phthalocyanine-Copper Complexes. *J. Phys. Chem.* **1992**, *96*, 9132–9139.

[55] Finazzo, C.; Calle, C.; Stoll, S.; Van Doorslaer, S.; Schweiger, A. Matrix Effects on Copper(II)phthalocyanine Complexes. A Combined Continuous Wave and Pulse EPR and DFT Study. *Phys. Chem. Chem. Phys.* **2006**, *8*, 1942–1953.

[56] Smith, T. D.; Pilbrow, J. R. The Determination of Structural Properties of Dimeric Transition Metal Ion Complexes From EPR Spectra. *Coord. Chem. Rev.* **1974**, *13*, 173–278.

[57] Asano-Someda, M.; Toyama, N.; Kaizu, Y. Weak Exchange Interaction of Copper(II) Pairs in Rigidly Linked Porphyrin Dimers. *Mol. Cryst. Liq. Cryst.* **2002**, *379*, 165–170.

[58] Toyama, N.; Asano-Someda, M.; Kaizu, Y. EPR Spectra of Gable-Type Copper(II) Porphyrin Dimers in Fluid Solution: Extraction of Exchange Interaction in Weakly Coupled Doublet Pairs. *Mol. Phys.* **2003**, *101*, 733–742.

[59] Calvo, R. EPR Measurements of Weak Exchange Interactions Coupling Unpaired Spins in Model Compounds. *Appl. Magn. Reson.* **2007**, *31*, 271–299.

[60] Eaton, S. S.; Eaton, G. R.; Chang, C. K. Synthesis and Geometry Determination of Cofacial Diporphyrins. EPR Spectroscopy of Dicopper Diporphyrins in Frozen Solution. *J. Am. Chem. Soc.* **1985**, *107*, 3177–3184.

[61] Eaton, S. S.; DuBois, D. L.; Eaton, G. R. Metal-Nitroxyl Interactions. VI. Analysis of EPR Spectra of Spin-Labeled Copper Complexes. *J. Magn. Reson.* **1978**, *32*, 251–263.

[62] More, K. M.; Eaton, G. R.; Eaton, S. S. Metal-Nitroxyl Interactions. 47. EPR Spectra of Two Spin-Labeled Derivatives of EDTA Coordinated to Paramagnetic Metal Ions. *Inorg. Chem.* **1986**, *25*, 2638–2646.

[63] Hanson, G. R.; Gates, K. E.; Noble, C. J.; Griffin, M.; Mitchell, A.; Benson, S. XSophe-Sophe-XeprView. A Computer Simulation Software Suite (v. 1.1.3) for the Analysis of Continuous Wave EPR Spectra. *J. Inorg. Biochem.* **2004**, *98*, 903–916.

[64] Stoll, S.; Schweiger, A. EasySpin, a Comprehensive Software Package for Spectral Simulation and Analysis in EPR. *J. Magn. Reson.* **2006**, *178*, 42–55.

[65] Liao, M.-S.; Scheiner, S. Electronic Structure and Bonding in Metal Porphyrins, Metal=Fe, Co, Ni, Cu, Zn. *J. Chem. Phys.* **2002**, *117*, 205–219.

[66] Moro, G.; Freed, J. H. Calculation of ESR Spectra and Related Fokker-Planck Forms by the Use of the Lanczos Algorithm. *J. Chem. Phys.* **1981**, *74*, 3757–3773.

[67] Edwards, L. J.; Savostyanov, D. V.; Welderufael, Z. T.; Lee, D.; Kuprov, I. Quantum Mechanical NMR Simulation Algorithm for Protein-Size Spin Systems. *J. Magn. Reson.* **2014**, *243*, 107–113.

[68] Hogben, H. J.; Krzystyniak, M.; Charnock, G. T. P.; Hore, P. J.; Kuprov, I. Spinach – A Software Library for Simulation of Spin Dynamics in Large Spin Systems. *J. Magn. Reson.* **2011**, *208*, 179–194.

[69] Peeks, M. D.; Neuhaus, P.; Anderson, H. L. Experimental and Computational Evaluation of the Barrier to Torsional Rotation in a Butadiyne-Linked Porphyrin Dimer. *Phys. Chem. Chem. Phys.* **2016**, *18*, 5264–5274.

[70] Liu, S.; Kondratuk, D. V.; Rousseaux, S. A. L.; Gil-Ramírez, G.; O'Sullivan, M. C.; Cremers, J.; Claridge, T. D. W.; Anderson, H. L. Caterpillar Track Complexes in Template-Directed Synthesis and Correlated Molecular Motion. *Angew. Chem. Int. Ed.* **2015**, *54*, 5355–5359.

[71] Kondratuk, D. V.; Perdigão, L. M. A.; Esmail, A. M. S.; O'Shea, J. N.; Beton, P. H.; Anderson, H. L. Supramolecular Nesting of Cyclic Polymers. *Nat. Chem.* **2015**, *7*, 317–322.

[72] Hogben, H. J.; Sprafke, J. K.; Hoffmann, M.; Pawlicki, M.; Anderson, H. L. Stepwise Effective Molarities in Porphyrin Oligomer Complexes: Preorganization Results in Exceptionally Strong Chelate Cooperativity. *J. Am. Chem. Soc.* **2011**, *133*, 20962–20969.

[73] Sprafke, J. K.; Kondratuk, D. V.; Wykes, M.; Thompson, A. L.; Hoffmann, M.; Drevinskas, R.; Chen, W.-H.; Yong, C. K.; Kärnbratt, J.; Bullock, J. E.; Malfois, M.; Wasielewski, M. R.; Albinsson, B.; Herz, L. M.; Zigmantas, D. et al. Belt-Shaped π-Systems: Relating Geometry to Electronic Structure in a Six-Porphyrin Nanoring. *J. Am. Chem. Soc.* **2011**, *133*, 17262–17273.

[74] HyperChem(TM) Professional 9.0, Hypercube Inc., 1115 NW 4th Street, Gainesville, Florida 32601, USA.

[75] Marques, H. M.; Cukrowski, I. Molecular Mechanics Parameters for the Modelling of Four-Coordinate Zn(II) Porphyrins. *Phys. Chem. Chem. Phys.* **2003**, *5*, 5499–5506.

[76] Marques, H. M.; Cukrowski, I. Molecular Mechanics Modelling of Porphyrins. Using Artificial Neural Networks to Develop Metal Parameters for Four-Coordinate Metalloporphyrins. *Phys. Chem. Chem. Phys.* **2002**, *4*, 5878–5887.

[77] Goldstein, E.; Ma, B.; Lii, J.-H.; Allinger, N. L. Molecular Mechanics Calculations (MM3) on Nitriles and Alkynes. *J. Phys. Org. Chem.* **1996**, *9*, 191–202.

[78] Jarowski, P. D.; Diederich, F.; Houk, K. N. Structures and Stabilities of Diacetylene-Expanded Polyhedranes by Quantum Mechanics and Molecular Mechanics. *J. Org. Chem.* **2005**, *70*, 1671–1678.

[79] Zimmer, B.; Hutin, M.; Bulach, V.; Wais Hosseini, M.; De Cian, A.; Kyritsakas, N. Coordination Polymers Based on Porphyrin and Copper: The Influence of the Crystallization Solvents on the Dimensionality of the Network. *New J. Chem.* **2002**, *26*, 1532–1535.

[80] Lipstman, S.; Goldberg, I. Versatile Molecular Recognition Features of Tetra(3-pyridyl)porphyrin in Crystal Engineering. *Cryst. Growth Des.* **2010**, *10*, 4596–4606.

[81] Yang, Z.; Becker, J.; Saxena, S. On Cu(II)-Cu(II) Distance Measurements using Pulsed Electron Electron Double Resonance. *J. Magn. Reson.* **2007**, *188*, 337–343.

[82] Bode, B. E.; Plackmeyer, J.; Prisner, T. F.; Schiemann, O. PELDOR Measurements on a Nitroxide-Labeled Cu(II) Porphyrin: Orientation Selection, Spin-Density Distribution, and Conformational Flexibility. *J. Phys. Chem. A* **2008**, *112*, 5064–5073.

[83] Marko, A.; Margraf, D.; Yu, H.; Mu, Y.; Stock, G.; Prisner, T. Molecular Orientation Studies by Pulsed Electron-Electron Double Resonance Experiments. *J. Chem. Phys.* **2009**, *130*, 064102/1–9.

[84] Abdullin, D.; Hagelueken, G.; Hunter, R. I.; Smith, G. M.; Schiemann, O. Geometric Model-Based Fitting Algorithm for Orientation-Selective PELDOR Data. *Mol. Phys.* **2015**, *113*, 544–560.

[85] Gong, J. Q.; Parkinson, P.; Kondratuk, D. V.; Gil-Ramírez, G.; Anderson, H. L.; Herz, L. M. Structure-Directed Exciton Dynamics in Templated Molecular Nanorings. *J. Phys. Chem. C* **2015**, *119*, 6414–6420.

[86] Reuter, M. G.; Seideman, T.; Ratner, M. A. Molecular Conduction through Adlayers: Cooperative Effects Can Help or Hamper Electron Transport. *Nano Lett.* **2011**, *11*, 4693–4696.

[87] Yaliraki, S. N.; Ratner, M. A. Molecule-Interface Coupling Effects on Electronic Transport in Molecular Wires. *J. Chem. Phys.* **1998**, *109*, 5036–5043.

[88] Magoga, M.; Joachim, C. Conductance of Molecular Wires Connected or Bonded in Parallel. *Phys. Rev. B* **1999**, *59*, 16011–16021.

[89] Kirk, M. L.; Shultz, D. A.; Stasiw, D. E.; Habel-Rodriguez, D.; Stein, B.; Boyle, P. D. Electronic and Exchange Coupling in a Cross-Conjugated D−B−A Biradical: Mechanistic Implications for Quantum Interference Effects. *J. Am. Chem. Soc.* **2013**, *135*, 14713–14725.

[90] Lambert, C. J. Basic Concepts of Quantum Interference and Electron Transport in Single-Molecule Electronics. *Chem. Soc. Rev.* **2015**, *44*, 875–888.

[91] Vazquez, H.; Skouta, R.; Schneebeli, S.; Kamenetska, M.; Breslow, R.; Venkataraman, L.; Hybertsen, M. S. Probing the Conductance Superposition Law in Single-Molecule Circuits with Parallel Paths. *Nat. Nanotech.* **2012**, *7*, 663–667.

[92] Zhu, P.; Cruz-Silva, E.; Meunier, V. Electronic Transport Properties in Graphene Oxide Frameworks. *Phys. Rev. B* **2014**, *89*, 085427/1–8.

[93] Li, Z.; Smeu, M.; Rives, A.; Maraval, V.; Chauvin, R.; Ratner, M. A.; Borguet, E. Towards Graphyne Molecular Electronics. *Nat. Commun.* **2015**, *6*, 6321/1–9.

[94] Zhou, Y.-H.; Chen, C.-Y.; Li, B.-L.; Chen, K.-Q. Characteristics of Classical Kirchhoff's Superposition Law in Carbon Atomic Wires Connected in Parallel. *Carbon* **2015**, *95*, 503–510.

[95] Margraf, D.; Cekan, P.; Prisner, T. F.; Sigurdsson, S. T.; Schiemann, O. Ferro- and Antiferromagnetic Exchange Coupling Constants in PELDOR Spectra. *Phys. Chem. Chem. Phys.* **2009**, *11*, 6708–6714.

[96] Weber, A.; Schiemann, O.; Bode, B.; Prisner, T. F. PELDOR at S- and X-Band Frequencies and the Separation of Exchange Coupling from Dipolar Coupling. *J. Magn. Reson.* **2002**, *157*, 277–285.

[97] Reginsson, G. W.; Hunter, R. I.; Cruickshank, P. A. S.; Bolton, D. R.; Sigurdsson, S. T.; Smith, G. M.; Schiemann, O. W-band PELDOR with 1 kW Microwave Power: Molecular Geometry, Flexibility and Exchange Coupling. *J. Magn. Reson.* **2012**, *216*, 175–182.

[98] Huber, M.; Doubinskii, A. A.; Kay, C. W. M.; Möbius, K. ENDOR on the Triplet State of the Primary Electron Donor in the Photosynthetic Bacterium *Rhodobacter sphaeroides* – One Step Forward in a Still Unfinished Story. *Appl. Magn. Reson.* **1997**, *13*, 473–485.

[99] Lendzian, F.; Bittl, R.; Lubitz, W. Pulsed ENDOR of the Photoexcited Triplet States of Bacteriochlorophyll a and of the Primary Donor P865 in Reaction Centers of Rhodobacter Sphaeroides R-26. *Photosynth. Res.* **1998**, *55*, 189–197.

[100] Budil, D. E.; Thurnauer, M. C. The Chlorophyll Triplet State as a Probe of Structure and Function in Photosynthesis. *Biochem. Biophys. Acta* **1991**, *1057*, 1–41.

[101] De Groot, A.; Evelo, R.; Hoff, A. J.; De Beer, R.; Scheer, H. Electron Spin Echo Envelope Modulation (ESEEM) Spectroscopy of the Triplet State of the Primary Donor of ^{14}N and ^{15}N Bacterial Photosynthetic Reaction Centers and of ^{14}N and ^{15}N Bacteriochlorophyll a. *Chem. Phys. Lett.* **1985**, *118*, 48–54.

[102] Lendzian, F.; Bittl, R.; Telfer, A.; Lubitz, W. Hyperfine Structure of the Photoexcited Triplet State ^{3}P680 in Plant PS II Reaction Centres as Determined by Pulse ENDOR Spectroscopy. *Biochim. Biophys. Acta* **2003**, *1605*, 35–46.

[103] Hasharoni, K.; Levanon, H.; Greenfield, D. J., S. R. Gosztola; Svec, W. A.; Wasielewski, M. R. Radical Pair and Triplet State Dynamics of a Photosynthetic Reaction-Center Model Embedded in Isotropic Media and Liquid Crystals. *J. Am. Chem. Soc.* **1996**, *118*, 10228–10235.

[104] Di Valentin, M.; Bisol, A.; Agostini, G.; Fuhs, M.; Liddell, P. A.; Moore, A. L.; Moore, T. A.; Gust, D.; Carbonera, D. Photochemistry of Artificial Photosynthetic Reaction Centers in Liquid Crystals Probed by Multifrequency EPR (9.5 and 95 GHz). *J. Am. Chem. Soc.* **2004**, *126*, 17074–17086.

[105] Levanon, H.; Norris, J. R. The Photoexcited Triplet State and Photosynthesis. *Chem. Rev.* **1978**, *78*, 185–198.

[106] Wasielewski, M. R. Energy, Charge, and Spin Transport in Molecules and Self-Assembled Nanostructures Inspired by Photosynthesis. *J. Org. Chem.* **2006**, *71*, 5051–5066.

[107] Angiolillo, P. J.; Rawson, J.; Frail, P. R.; Therien, M. J. The Evolution of Spin Distribution in the Photoexcited Triplet State of Ethyne-Elaborated Porphyrins. *Chem. Commun.* **2013**, *49*, 9722–9724.

[108] Angiolillo, P. J.; Susumu, K.; Uyeda, H. T.; Lin, V. S.-Y.; Shediac, R.; Therien, M. J. Trends in Triplet Excitation Delocalization in Highly Conjugated (Porphinato)zinc(II) Arrays Probed by EPR Spectroscopy. *Synth. Met.* **2001**, *116*, 247–253.

[109] Tait, C. E.; Neuhaus, P.; Peeks, M. D.; Anderson, H. L.; Timmel, C. R. Transient EPR Reveals Triplet State Delocalization in a Series of Cyclic and Linear pi-Conjugated Porphyrin Oligomers. *J. Am. Chem. Soc.* **2015**, *137*, 8284–8293.

[110] Ratner, M. A Brief History of Molecular Electronics. *Nat. Nanotech.* **2013**, *8*, 378–381.

[111] Bakulin, A. A.; Rao, A.; Pavelyev, V. G.; van Loosdrecht, P. H. M.; Pshenichnikov, M. S.; Niedzialek, D.; Cornil, J.; Beljonne, D.; Friend, R. H. The Role of Driving Energy and Delocalized States for Charge Separation in Organic Semiconductors. *Science* **2012**, *335*, 1340–1344.

[112] Angiolillo, P. J.; Lin, V. S.-Y.; Vanderkooi, J. M.; Therien, M. J. EPR Spectroscopy and Photophysics of the Lowest Photoactivated Triplet State of a Series of Highly Conjugated (Porphinato) Zn Arrays. *J. Am. Chem. Soc.* **1995**, *117*, 12514–12527.

[113] Lin, V. S.-Y.; DiMagno, S. G.; Therien, M. J. Highly Conjugated, Acetylenyl Bridged Porphyrins: New Models for Light-Harvesting Antenna Systems. *Science* **1994**, *264*, 1105–1111.

[114] Angiolillo, P. J.; Uyeda, H. T.; Duncan, T. V.; Therien, M. J. Impact of Electronic Asymmetry on Photoexcited Triplet-State Spin Distributions in Conjugated Porphyrin Oligomers Probed via EPR Spectroscopy. *J. Phys. Chem. B* **2004**, *108*, 11893–11903.

[115] Anderson, H. L. Building Molecular Wires from the Colours of Life: Conjugated Porphyrin Oligomers. *Chem. Commun.* **1999**, 2323–2330.

[116] Tanaka, T.; Osuka, A. Conjugated Porphyrin Arrays: Synthesis, Properties and Applications for Functional Materials. *Chem. Soc. Rev.* **2015**, *44*, 943–969.

[117] Senge, M. O.; Fazekas, M.; Notaras, E. G. A.; Blau, W. J.; Zawadzka, M.; Locos, O. B.; Mhuircheartaigh, E. M. N. Nonlinear Optical Properties of Porphyrins. *Adv. Mater.* **2007**, *19*, 2737–2774.

[118] Screen, T. E. O.; Thorne, J. R. G.; Denning, R. G.; Bucknall, D. G.; Anderson, H. L. Two Methods for Amplifying the Optical Nonlinearity of a Conjugated Porphyrin Polymer: Transmetallation and Self-Assembly. *J. Mater. Chem.* **2003**, *13*, 2796–2808.

[119] Kocherzhenko, A. A.; Whaley, K. B.; Sforazzini, G.; Anderson, H. L.; Wykes, M.; Beljonne, D.; Grozema, F. C.; Siebbeles, L. D. A. Effects of the Environment on Charge Transport in Molecular Wires. *J. Phys. Chem. C* **2012**, *116*, 25213–25225.

[120] Thurnauer, M. C.; Norris, J. R. Magnetophotoselection Applied to the Triplet State Observed by EPR in Photosynthetic Bacteria. *Biochem. Biophys. Res. Commun.* **1976**, *73*, 501–506.

[121] Thurnauer, M. C.; Norris, J. R. The Ordering of the Zero Field Triplet Spin Sublevels in the Chlorophylls. A Magnetophotoselection Study. *Chem. Phys. Lett.* **1977**, *47*, 100–105.

[122] Tait, C. E.; Neuhaus, P.; Anderson, H. L.; Timmel, C. R. Triplet State Delocalization in a Conjugated Porphyrin Dimer Probed by Transient Electron Paramagnetic Resonance Techniques. *J. Am. Chem. Soc.* **2015**, *137*, 6670–6679.

[123] Thurnauer, M. C.; Katz, J. J.; Norris, J. R. The Triplet State in Bacterial Photosynthesis: Possible Mechanisms of the Primary Photo-Act. *Proc. Natl. Acad. Sci. USA* **1975**, *72*, 3270–3274.

[124] Weil, J. A.; Bolton, J. R. *Electron Paramagnetic Resonance*, 2nd ed.; John Wiley & Sons, Inc., 2007.

[125] McConnell, H. M. Electron Densities in Semiquinones by Paramagnetic Resonance. *J. Chem. Phys.* **1956**, *24*, 632.

[126] Anderson, H. L. Conjugated Porphyrin Ladders. *Inorg. Chem.* **1994**, *33*, 972–981.

[127] Taylor, P. N.; Anderson, H. L. Cooperative Self-Assembly of Double-Stranded Conjugated Porphyrin Ladders. *J. Am. Chem. Soc.* **1999**, *121*, 11538–11545.

[128] Oliveri, C. G.; Gianneschi, N. C.; Nguyen, S. T.; Mirkin, C. A.; Stern, C. L.; Wawrzak, Z.; Pink, M. Supramolecular Allosteric Cofacial Porphyrin Complexes. *J. Am. Chem. Soc.* **2006**, *128*, 16286–16296.

[129] Tait, C. E.; Neuhaus, P.; Peeks, M. D.; Anderson, H. L.; Timmel, C. R. Excitation Wavelength-Dependent EPR Study on the Influence of the Conformation of Multiporphyrin Arrays on Triplet State Delocalization. *Phys. Chem. Chem. Phys.* **2016**, *18*, 5275–5280.

[130] Screen, T. E. O.; Thorne, J. R. G.; Denning, R. G.; Bucknall, D. G.; Anderson, H. L. Amplified Optical Nonlinearity in a Self-Assembled Double-Strand Conjugated Porphyrin Polymer Ladder. *J. Am. Chem. Soc.* **2002**, *124*, 9712–9713.

[131] Drobizhev, M.; Stepanenko, Y.; Rebane, A.; Wilson, C. J.; Screen, T. E. O.; Anderson, H. L. Strong Cooperative Enhancement of Two-Photon Absorption in Double-Strand Conjugated Porphyrin Ladder Arrays. *J. Am. Chem. Soc.* **2006**, *128*, 12432–12433.

[132] Grozema, F. C.; Houarner-Rassin, C.; Prins, P.; Siebbeles, L. D. A.; Anderson, H. L. Supramolecular Control of Charge Transport in Molecular Wires. *J. Am. Chem. Soc.* **2007**, *129*, 13370–13371.

[133] Winters, M. U.; Kärnbratt, J.; Eng, M.; Wilson, C. J.; Anderson, H. L.; Albinsson, B. Photophysics of a Butadiyne-Linked Porphyrin Dimer: Influence of Conformational Flexibility in the Ground and First Singlet Excited State. *J. Phys. Chem. C* **2007**, *111*, 7192–7199.

[134] Hutin, M.; Sprafke, J. K.; Odell, B.; Anderson, H. L.; Claridge, T. D. W. A Discrete Three-Layer Stack Aggregate of a Linear Porphyrin Tetramer: Solution-Phase Structure Elucidation by NMR and X-ray Scattering. *J. Am. Chem. Soc.* **2013**, *135*, 12798–12807.

[135] Kärnbratt, J.; Gilbert, M.; Sprafke, J. K.; Anderson, H. L.; Albinsson, B. Self-Assembly of Linear Porphyrin Oligomers into Well-Defined Aggregates. *J. Phys. Chem. C* **2012**, *116*, 19630–19635.

[136] Stephen, M. J.; Straley, J. P. Physics of Liquid Crystals. *Rev. Mod. Phys.* **1974**, *46*, 617–704.

[137] De Gennes, P. G., Prost, J., Eds. *The Physics of Liquid Crystals*; Oxford University Press: Oxford, 1993.

[138] Pestov, S. Physical and Thermodynamic Properties of Liquid Crystalline Substances. In *Landolt-Börnstein, New Series*; Vill, V., Ed.; Springer: Berlin, 2003.

[139] Rosso, R. Orientational Order Parameters in Biaxial Nematics: Polymorphic Notation. *Liquid Crystals* **2007**, *34*, 737–748.

[140] Low, R. J. Measuring Order and Biaxiality. *Eur. J. Phys.* **2002**, *23*, 111–117.

[141] Saupe, A. Recent Results in the Field of Liquid Crystals. *Angew. Chem. Int. Ed.* **1968**, *7*, 97–112.

[142] Gonen, O.; Levanon, H. Line-Shape Analysis of Transient Triplet Electron Paramagnetic Resonance Spectra. Application to Porphyrins and Chlorophylls in Nematic Uniaxial Liquid Crystals. *J. Phys. Chem.* **1984**, *88*, 4223–4228.

[143] Wiederrecht, G. P.; Yoon, B. A.; Svec, W. A.; Wasielewski, M. R. Photorefractivity in Nematic Liquid Crystals Containing Electron Donor-Acceptor Molecules That Undergo Intramolecular Charge Separation. *J. Am. Chem. Soc.* **1997**, *119*, 3358–3364.

[144] Wohlfarth, C.; Wohlfarth, B. Refractive Indices of Organic Liquids. In *Landolt-Börnstein, New Series*; Lechner, M. D., Ed.; Springer: Berlin, 1996.

[145] Wohlfarth, C. Static Dielectric Constants of Pure Liquids and Binary Liquid Mixtures. In *Landolt-Börnstein, New Series*; Lechner, M. D., Ed.; Springer: Berlin, 2008.

[146] Closs, G. Mechanism Explaining Nuclear Spin Polarizations in Radical Combination Reactions. *J. Am. Chem. Soc.* **1969**, *91*, 4552–4554.

[147] Kaptein, R.; Oosterhoff, J. L. Chemically Induced Dynamic Nuclear Polarization II (Relation with Anomalous ESR Spectra). *Chem. Phys. Lett.* **1969**, *4*, 195–197.

[148] Salikhov, K. M., Molin, Y. N., Sagdeev, R. Z., Buchachenko, A. L., Eds. *Spin Polarization and Magnetic Effects in Radical Reactions*; Elsevier: Amsterdam, 1984.

[149] Weller, A.; Staerk, H.; Treichel, R. Magnetic-Field Effects on Geminate Radical-Pair Recombination. *Faraday Discuss. Chem. Soc.* **1984**, *78*, 271–278.

[150] Hayashi, H., Ed. *Introduction to Dynamic Spin Chemistry*; World Scientific Publishing: New Jersey, 2004.

[151] Steiner, U. E.; Ulrich, T. Magnetic Field Effects in Chemical Kinetics and Related Phenomena. *Chem. Rev.* **1989**, *89*, 51–147.

[152] Mouritsen, H.; Ritz, T. Magnetoreception and its Use in Bird Navigation. *Curr. Opin. Neurobiol.* **2005**, *15*, 406–414.

[153] Wiltschko, W.; Wiltschko, R. Magnetoreception in Birds: Two Receptors for Two Different Tasks. *J. Ornithol.* **2007**, *148*, S61–S76.

[154] Wiltschko, R.; Wiltschko, W. Magnetoreception. *BioEssays* **2006**, *28*, 157–168.

[155] Wiltschko, R.; Wiltschko, W. Sensing Magnetic Directions in Birds: Radical Pair Processes Involving Cryptochrome. *Biosensors* **2014**, *4*, 221–242.

[156] Beason, R. C.; Nichols, J. E. Magnetic Orientation and Magnetically Sensitive Material in a Transequatorial Migratory Bird. *Nature* **1984**, *309*, 151–153.

[157] Beason, R. C.; Dussourd, N.; Deutschlander, M. E. Behavioural Evidence for the Use of Magnetic Material in Magnetoreception by a Migratory Bird. *J. Exp. Biol.* **1995**, *198*, 141–146.

[158] Diebel, C. E.; Proksch, R.; Green, C. R.; Neilson, P.; Walker, M. M. Magnetite Defines a Vertebrate Magnetoreceptor. *Nature* **2000**, *406*, 299–302.

[159] Kirschvink, J. L.; Gould, J. L. Biogenic Magnetite as a Basis for Magnetic Field Detection in Animals. *BioSystems* **1981**, *13*, 181–201.

[160] Munro, U.; Munro, J. A.; Phillips, J. B. Evidence for a Magnetite-Based Navigational "Map" in Birds. *Naturwissenschaften* **1997**, *84*, 26–28.

[161] Walker, M. M.; Diebel, C. E.; Haugh, C. V.; Pankhurst, P. M.; Montgomery, J. C.; Green, C. R. Structure and Function of the Vertebrate Magnetic Sense. *Nature* **1997**, *390*, 371–376.

[162] Fleissner, G.; Holtkamp-Rötzler, E.; Hanzlik, M.; Winklhofer, M.; Fleissner, G.; Petersen, N.; Wiltschko, W. Ultrastructural Analysis of a Putative Magnetoreceptor in the Beak of Homing Pigeons. *J. Comp. Neurol.* **2003**, *458*, 350–360.

[163] Schulten, K.; Swenberg, C. E.; Weller, A. A Biomagnetic Sensory Mechanism Based on Magnetic Field Modulated Coherent Electron Spin Motion. *Z. Phys. Chem.* **1978**, *111*, 1–5.

[164] Ritz, T.; Adem, S.; Schulten, K. A Model for Photoreceptor-Based Magnetoreception in Birds. *Biophys. J.* **2000**, *78*, 707–718.

[165] Rodgers, C. T.; Hore, P. J. Chemical Magnetoreception in Birds: The Radical Pair Mechanism. *Proc. Natl. Acad. Sci. USA* **2009**, *106*, 353–360.

[166] Wiltschko, W.; Wiltschko, R. Migratory Orientation of European Robins is Affected by the Wavelength of Light as well as by a Magnetic Pulse. *J. Comp. Physiol. A* **1995**, *177*, 363–369.

[167] Davila, A. F.; Winklhofer, M.; Shcherbakov, V. P.; Petersen, N. Magnetic Pulse Affects a Putative Magnetoreceptor Mechanism. *Biophys. J.* **2005**, *89*, 56–63.

[168] Wiltschko, W.; Munro, U.; Beason, R. C.; Ford, H.; Wiltschko, R. A Magnetic Pulse Leads to a Temporary Deflection in the Orientation of Migratory Birds. *Experientia* **1994**, *50*, 697–700.

[169] Wiltschko, W.; Munro, U.; Ford, H.; Wiltschko, R. Effect of a Magnetic Pulse on the Orientation of Silvereyes, *Zosterops L. Lateralis*, During Spring Migration. *J. Exp. Biol.* **1998**, *201*, 3257–3261.

[170] Treiber, C. D.; Salzer, M. C.; Riegler, J.; Edelman, N.; Sugar, C.; Breuss, M.; Pichler, P.; Cadiou, H.; Saunders, M.; Lythgoe, M.; Shaw, J.; Keays, D. A. Clusters of Iron-rich Cells in the Upper Beak of Pigeons are Macrophages not Magnetosensitive Neurons. *Nature* **2012**, *484*, 367–371.

[171] Brocklehurst, B.; McLauchlan, K. A. Free Radical Mechanism for the Effects of Environmental Electromagnetic Fields on Biological Systems. *Int. J. Radiat. Biol.* **1996**, *69*, 3–24.

[172] Timmel, C. R.; Till, U.; Brocklehurst, B.; McLauchlan, K. A.; Hore, P. J. Effects of Weak Magnetic Fields on Free Radical Recombination Reactions. *Mol. Phys.* **1998**, *95*, 71–89.

[173] Brocklehurst, B. Magnetic Fields and Radical Reactions: Recent Developments and Their Role in Nature. *Chem. Soc. Rev.* **2002**, *31*, 301–311.

[174] Timmel, C. R.; Henbest, K. B. A Study of Spin Chemistry in Weak Magnetic Fields. *Phil. Trans. R. Soc. Lond. A* **2004**, *362*, 2573–2589.

[175] Möller, A.; Sagasser, S.; Wiltschko, W.; Schierwater, B. Retinal Cryptochrome in a Migratory Passerine Bird: A Possible Transducer for the Avian Magnetic Compass. *Naturwissenschaften* **2004**, *91*, 585–588.

[176] Liedvogel, M.; Maeda, K.; Henbest, K.; Schleicher, E.; Simon, T.; Timmel, C. R.; Hore, P. J.; Mouritsen, H. Chemical Magnetoreception: Bird Cryptochrome 1a is Excited by Blue Light and Forms Long-Lived Radical-Pairs. *PLoS ONE* **2007**, *10*, e1106/1–7.

[177] Liedvogel, M.; Mouritsen, H. Cryptochromes – A Potential Magnetoreceptor: What Do We Know and What Do We Want to Know? *J. R. Soc. Interface* **2010**, *7*, S147–S162.

[178] Sancar, A. Structure and Function of DNA Photolyase and Cryptochrome Blue-Light Photoreceptors. *Chem. Rev.* **2003**, *103*, 2203–2237.

[179] Mouritsen, H.; Janssen-Bienhold, U.; Liedvogel, M.; Feenders, G.; Stalleicken, J.; Dirks, P.; Weiler, R. Cryptochromes and Neuronal-Activity Markers Colocalize in the Retina of Migratory Birds During Magnetic Orientation. *Proc. Natl. Acad. Sci. USA* **2004**, *101*, 14294–14299.

[180] Nießner, C.; Denzau, S.; Stapput, K.; Ahmad, M.; Peichl, L.; Wiltschko, W.; Wiltschko, R. Magnetoreception: Activated Cryptochrome 1a concurs with Magnetic Orientation in Birds. *J. R. Soc. Interface* **2013**, *10*, 20130638.

[181] Solov'yov, I. A.; Chandler, D. E.; Schulten, K. Magnetic Field Effects in *Arabidopsis thaliana* Chryptochrome-1. *Biophys. J.* **2007**, *92*, 2711–2726.

[182] Maeda, K.; Robinson, A. J.; Henbest, K. B.; Hogben, H. J.; Biskup, T.; Ahmad, M.; Schleicher, E.; Weber, S.; Timmel, C. R.; Hore, P. J. Magnetically Sensitive Light-induced Reactions in Cryptochrome are Consistent with its Proposed Role as a Magnetoreceptor. *Proc. Natl. Acad. Sci. USA* **2012**, *109*, 4774–4779.

[183] Lee, A. A.; Lau, J. C. S.; Hogben, H. J.; Biskup, T.; Kattnig, D. R.; Hore, P. J. Alternative Radical Pairs for Cryptochrome-Based Magnetoreception. *J. R. Soc. Interface* **2013**, *11*, 20131063.

[184] Cintolesi, F.; Ritz, T.; Kay, C. W. M.; Timmel, C. R.; Hore, P. J. Anisotropic Recombination of an Immobilized Photoinduced Radical Pair in a 50 μT Magnetic Field: A Model Avian Photomagnetoreceptor. *Chem. Phys.* **2003**, *294*, 385–399.

[185] Mouritsen, H.; Feenders, G.; Liedvogel, M.; Wada, K.; Jarvis, E. D. Night-vision Brain Area in Migratory Songbirds. *Proc. Natl. Acad. Sci. USA* **2005**, *102*, 8339–8344.

[186] Zapka, M.; Heyers, D.; Hein, C. M.; Engels, S.; Schneider, N.-L.; Hans, J.; Weiler, S.; Dreyer, D.; Kishkinev, D.; Wild, J. M.; Mouritsen, H. Visual but not Trigeminal Mediation of Magnetic Compass Information in a Migratory Bird. *Nature* **2009**, *461*, 1274–1278.

[187] Zapka, M.; Heyers, D.; Liedvogel, M.; Jarvis, E. D.; Mouritsen, H. Night-time Neuronal Activation of Cluster N in a Day- and Night-migrating Songbird. *Eurp. J. Neurosci.* **2010**, *32*, 619–624.

[188] Emlen, S. T.; Emlen, J. T. A Technique for Recording Migratory Orientation of Captive Birds. *Auk* **1966**, *83*, 361–367.

[189] Emlen, S. T.; Wiltschko, W.; Demong, N. J.; Wiltschko, R.; Bergman, S. Magnetic Direction Finding: Evidence for Its Use in Migratory Indigo Buntings. *Science* **1976**, *193*, 505–508.

[190] Wiltschko, W.; Wiltschko, R. Magnetic Compass of European Robins. *Science* **1972**, *176*, 62–64.

[191] Phillips, J. B.; Borland, S. C. Behavioral Evidence for Use of a Light-Dependent Magnetoreception Mechanism by a Vertebrate. *Nature* **1992**, *359*, 142–144.

[192] Wiltschko, W.; Munro, U.; Ford, H.; Wiltschko, R. Red Light Disrupts Magnetic Orientation of Migratory Birds. *Nature* **1993**, *364*, 525–527.

[193] Wiltschko, W.; Wiltschko, R. Light-dependent Magnetoreception in Birds: The Behaviour of European Robins, *Erithacus rubecula*, under Monochromatic Light of Various Wavelengths and Intensities. *J. Exp. Biol.* **2001**, *204*, 3295–3302.

[194] Muheim, R.; Bäckman, J.; Akesson, S. Magnetic Compass Orientation in European Robins is Dependent on Both Wavelength and Intensity of Light. *J. Exp. Biol.* **2002**, *205*, 3845–3856.

[195] Wiltschko, R.; Stapput, K.; Thalau, P.; Wiltschko, W. Directional Orientation of Birds by the Magnetic Field under Different Light Conditions. *J. R. Soc. Interface* **2010**, *7*, S163–S177.

[196] Wiltschko, W.; Traudt, J.; Güntürkün, O.; Prior, H.; Wiltschko, R. Lateralization of Magnetic Compass Orientation in a Migratory Bird. *Nature* **2002**, *419*, 467–470.

[197] Ritz, T.; Thalau, P.; Phillips, J. B.; Wiltschko, R.; Wiltschko, W. Resonance Effects Indicate a Radical-Pair Mechanism for Avian Magnetic Compass. *Nature* **2004**, *429*, 177–180.

[198] Henbest, K. B.; Kukura, P.; Rodgers, C. T.; Hore, P. J.; Timmel, C. R. Radio Frequency Magnetic Field Effects on a Radical Recombination Reaction: A Diagnostic Test for the Radical Pair Mechanism. *J. Am. Chem. Soc.* **2004**, *126*, 8102–8103.

[199] Thalau, P.; Ritz, T.; Stapput, K.; Wiltschko, R.; Wiltschko, W. Magnetic Compass Orientation of Migratory Birds in the Presence of a 1.315 MHz Oscillating Field. *Naturwissenschaften* **2005**, *92*, 86–90.

[200] Grissom, C. B. Magnetic Field Effects in Biology: A Survey of Possible Mechanisms with Emphasis on Radical-Pair Recombination. *Chem. Rev.* **1995**, *95*, 3–24.

[201] Beason, R. C.; Semm, P. Does the Avian Ophthalmic Nerve Carry Magnetic Navigational Information? *J. Exp. Biol.* **1996**, *199*, 1241–1244.

[202] Wiltschko, W.; Wiltschko, R. Magnetic Orientation in Birds. *J. Exp. Biol.* **1996**, *199*, 29–38.

[203] Wiltschko, W.; Wiltschko, R. Magnetic Compass Orientation in Birds and its Physiological Basis. *Naturwissenschaften* **2002**, *89*, 445–452.

[204] Beason, R. C. Mechanisms of Magnetic Orientation in Birds. *Integr. Comp. Biol.* **2005**, *45*, 565–573.

[205] Johnsen, S.; Lohmann, K. J. The Physics and Neurobiology of Magnetoreception. *Nat. Rev. Neurosci.* **2005**, *9*, 703–712.

[206] Wiltschko, W.; Wiltschko, R. Magnetic Orientation and Magnetoreception in Birds and Other Animals. *J. Comp. Physiol. A* **2005**, *191*, 675–693.

[207] Ritz, T.; Ahmad, M.; Mouritsen, H.; Wiltschko, R.; Wiltschko, W. Photoreceptor-based Magnetoreception: Optimal Design of Receptor Molecules, Cells, and Neuronal Processing. *J. R. Soc. Interface* **2010**, *7*, S135–S146.

[208] Ritz, T. Quantum Effects in Biology: Bird Navigation. *Procedia Chem.* **2011**, *3*, 262–275.

[209] Maeda, K.; Henbest, K. B.; Cintolesi, F.; Kuprov, I.; Rodgers, C. T.; Liddell, P. A.; Gust, D.; Timmel, C. R.; Hore, P. J. Chemical Compass Model of Avian Magnetoreception. *Nature* **2008**, *453*, 387–391.

[210] Efimova, O.; Hore, P. J. Role of Exchange and Dipolar Interactions in the Radical Pair Model of the Avian Magnetic Compass. *Biophys. J.* **2008**, *94*, 1565–1574.

[211] O'Dea, A. R.; Curtis, A. F.; Green, N. J. B.; Timmel, C. R.; Hore, P. J. Influence of Dipolar Interactions on Radical Pair Recombination Reactions Subject to Weak Magnetic Fields. *J. Phys. Chem. A* **2005**, *109*, 869–873.

[212] Furutsuka, T.; Imura, T.; Kojima, T.; Kawabe, K. Dielectric Constant of 2-Methyltetrahydrofuran. *Technol. Rep. Osaka Univ.* **1974**, *24*, 367–369.

[213] Richert, S.; Rosspeintner, A.; Landgraf, S.; Grampp, G.; Vauthey, E.; Kattnig, D. R. Time-Resolved Magnetic Field Effects Distinguish Loose Ion Pairs from Exciplexes. *J. Am. Chem. Soc.* **2013**, *135*, 15144–15152.

[214] Werner, U.; Staerk, H. Magnetic Field Effect in the Recombination Reaction of Radical Ion Pairs: Dependence on Solvent Dielectric Constant. *J. Phys. Chem.* **1995**, *99*, 248–254.

[215] Marcus, R. A. On the Theory of Oxidation-Reduction Reactions Involving Electron Transfer. I. *J. Chem. Phys.* **1956**, *24*, 966–978.

[216] Marcus, R. A. On the Theory of Oxidation-Reduction Reactions Involving Electron Transfer. II. Applications to Data on the Rates of Isotopic Exchange Reactions. *J. Chem. Phys.* **1957**, *26*, 867–871.

[217] Marcus, R. A. Chemical and Electrochemical Electron-Transfer Theory. *Annu. Rev. Phys. Chem.* **1964**, *15*, 155–196.

[218] Siders, P.; Marcus, R. A. Quantum Effects for Electron-Transfer Reactions in the 'Inverted Region'. *J. Am. Chem. Soc.* **1981**, *103*, 748–752.

[219] Marcus, R.; Sutin, N. Electron Transfers in Chemistry and Biology. *Biochim. Biophys. Acta* **1985**, *811*, 265–322.

[220] Yoshihara, K.; Tominaga, K.; Nagasawa, Y. Effects of the Solvent Dynamics and Vibrational Motions in Electron Transfer. *Bull. Chem. Soc. Jpn.* **1995**, *68*, 696–712.

[221] Bolton, J. R.; Archer, M. D. Basic Electron-Transfer Theory. In *Electron Transfer in Inorganic, Organic, and Biological Systems*; Bolton, J. R., Mataga, N., McLendon, G., Eds.; Advances in Chemistry; American Chemical Society: Washington DC, 1991; Vol. 228; Chapter 2, pp 7–23.

[222] Weller, A. Photoinduced Electron Transfer in Solution: Exciplex and Radical Ion Pair Formation Free Enthalpies and their Solvent Dependence. *Z. Physik. Chem. N. F.* **1982**, *133*, 93–98.

[223] Wasielewski, M. R.; Niemczyk, M. P.; Svec, W. A.; Pewitt, E. B. Dependence of Rate Constants for Photoinduced Charge Separation and Dark Charge Recombination on the Free Energy of Reaction in Restricted-Distance Porphyrin-Quinone Molecules. *J. Am. Chem. Soc.* **1985**, *107*, 1080–1082.

[224] Gould, I. R.; Ege, D.; Mattes, S. L.; Farid, S. Return Electron Transfer within Geminate Radical Ion Pairs. Observation of the Marcus Inverted Region. *J. Am. Chem. Soc.* **1987**, *109*, 3794–3796.

[225] Mataga, N.; Asahi, T.; Kanda, Y.; Okada, T. The Bell-Shaped Energy Gap Dependence of the Charge Recombination Reaction of Geminate Radical Ion Pairs Produced by Fluorescence Quenching Reaction in Acetonitrile Solution. *Chem. Phys.* **1988**, *127*, 249–261.

[226] Vauthey, E. Direct Measurements of the Charge-Recombination Dynamics of Geminate Ion Pairs Formed upon Electron-Transfer Quenching at High Donor Concentration. *J. Phys. Chem. A* **2001**, *105*, 340–348.

[227] Storey, J. Magnetic Field Effects on Electron-Hole Recombination Reactions – Theoretical and Experimental Developments. Dissertation, University of Oxford, 2014.

[228] Thurnauer, M. C.; Norris, J. R. An Electron Spin Echo Phase Shift Observed in Photosynthetic Algae. Possible Evidence for Dynamic Radical Pair Interactions. *Chem. Phys. Lett.* **1980**, *76*, 557–561.

[229] Salikhov, K. M.; Dzuba, S. A.; Raitsimring, A. M. The Theory of Electron Spin-Echo Signal Decay Resulting from Dipole-Dipole Interactions between Paramagnetic Centers in Solids. *J. Magn. Reson.* **1981**, *42*, 255–276.

[230] Dzuba, S. A.; Gast, P.; Hoff, A. J. ESEEM Study of Spin-Spin Interactions in Spin-Polarised $P^+Q_A^-$ Pairs in the Photosynthetic Purple Bacterium *Rhodobacter Sphaeroides* R26. *Chem. Phys. Lett.* **1995**, *236*, 595–602.

[231] Bittl, R.; Zech, S. G. Pulsed EPR Spectroscopy on Short-Lived Intermediates in Photosystem I. *Biochim. Biophys. Acta* **2001**, *1507*, 194–211.

[232] Carmieli, R.; Mi, Q.; Butler Ricks, A.; Giacobbe, E. M.; Mickley, S. M.; Wasielewski, M. R. Direct Measurement of Photoinduced Charge Separation Distances in Donor-Acceptor Systems for Artificial Photosynthesis Using OOP-ESEEM. *J. Am. Chem. Soc.* **2009**, *131*, 8372–8373.

[233] Zwanenburg, G.; Hore, P. J. Analytical Theory of Electron-Spin-Echo Modulations in Correlated Radical Pairs. *J. Magn. Reson.* **1995**, *144*, 139–146.

[234] Hoff, A. J.; Gast, P.; Dzuba, S. A.; Timmel, C. R.; Fursman, C. E.; Hore, P. J. The Nuts and Bolds of Distance Determination and Zero- and Double-Quantum Coherence in Photoinduced Radical Pairs. *Spectrochim. Acta A* **1998**, *54*, 2283–2293.

[235] Fursman, C. E.; Hore, P. J. Distance Determination in Spin-Correlated Radical Pairs in Photosynthetic Reaction Centres by Electron Spin Echo Envelope Modulation. *Chem. Phys. Lett.* **1999**, *303*, 593–600.

[236] Santabarbara, S.; Kuprov, I.; Fairclough, W. V.; Purton, S.; Hore, P. J.; Heathcote, P.; Evans, M. C. W. Bidirectional Electron Transfer in Photosystem I: Determination of Two Distances between P_{700}^+ and A_1^- in Spin-Correlated Radical Pairs. *Biochemistry* **2005**, *44*, 2119–2128.

[237] Santabarbara, S.; Kuprov, I.; Hore, P. J.; Casal, A.; Heathcote, P.; Evans, M. C. W. Analysis of the Spin-Polarized Electron Spin Echo of the $[P_{700}^+A_1^-]$ Radical Pair of Photosystem I Indicates that both Reaction Center Subunits Are Competent in Electron Transfer in Cyanobacteria, Green Algae, and Higher Plants. *Biochemistry* **2006**, *45*, 7389–7403.

[238] Tero-Kubota, S. Singlet and Triplet Energy Splitting in the Radical Ion Pairs Generated by Photoinduced Electron-Transfer Reactions. *Pure Appl. Chem.* **2001**, *73*, 519–523.

[239] Sekiguchi, S.; Kobori, Y.; Akiyama, K.; Tero-Kubota, S. Marcus Free Energy Dependence of the Sign of Exchange Interactions in Radical Ion Pairs Generated by Photoinduced Electron Transfer Reactions. *J. Am. Chem. Soc.* **1998**, *120*, 1325–1326.

[240] Kobori, Y.; Sekiguchi, S.; Akiyama, K.; Tero-Kubota, S. Chemically Induced Dynamic Electron Polarization Study on the Mechanism of Exchange Interaction in Radical Ion Pairs Generated by Photoinduced Electron Transfer Reactions. *J. Phys. Chem. A* **1999**, *103*, 5416–5424.

[241] Maeda, K.; Wedge, C. J.; Storey, J. G.; Henbest, K. B.; Liddell, P. A.; Kodis, G.; Gust, D.; Hore, P. J.; Timmel, C. R. Spin-Selective Recombination Kinetics of a Model Chemical Magnetoreceptor. *Chem. Commun.* **2011**, *47*, 6563–6565.

[242] Liddell, P. A.; Kuciauskas, D.; Sumida, J. P.; Nash, B.; Nguyen, D.; Moore, A. L.; Moore, T. A.; Gust, D. Photoinduced Charge Separation and Charge Recombination to a Triplet State in a Carotene−Porphyrin−Fullerene Triad. *J. Am. Chem. Soc.* **1997**, *119*, 1400–1405.

[243] Gust, D.; Moore, T. A.; Moore, A. L.; Kuciauskas, D.; Liddell, P. A.; Halbert, B. D. Mimicry of Carotenoid Photoprotection in Artificial Photosynthetic Reaction Centers: Triplet-Triplet Energy Transfer by a Relay Mechanism. *J. Photochem. Photobiol. B* **1998**, *43*, 209–216.

[244] Kuciauskas, D.; Liddell, P. A.; Lin, S.; Stone, S. G.; Moore, A. L.; Moore, T. A.; Gust, D. Photoinduced Electron Transfer in Carotenoporphyrin−Fullerene Triads: Temperature and Solvent Effects. *J. Phys. Chem. B* **2000**, *104*, 4307–4321.

[245] Carbonera, D.; Di Valentin, M.; Corvaja, C.; Agostini, G.; Giacometti, G.; Liddell, P. A.; Kuciauskas, D.; Moore, A. L.; Moore, T. A.; Gust, D. EPR Investigation of Photoinduced Radical Pair Formation and Decay to a Triplet State in a Carotene−Porphyrin−Fullerene Triad. *J. Am. Chem. Soc.* **1998**, *120*, 4398–4405.

[246] Kodis, G.; Liddell, P. A.; Moore, A. L.; Moore, T. A.; Gust, D. Synthesis and Photochemistry of a Carotene-Porphyrin-Fullerene Model Photosynthetic Reaction Center. *J. Phys. Org. Chem.* **2004**, *17*, 724–734.

[247] Di Valentin, M.; Bisol, A.; Giacometti, G.; Carbonera, D.; Agostini, G.; Liddell, P. A.; Moore, A. L.; Moore, T. A.; Gust, D. Reaction Center Models in Liquid Crystals: Identification of Paramagnetic Intermediates. *Mol. Cryst. Liq. Cryst.* **2003**, *394*, 19–30.

[248] Gemperle, C.; Aebli, G.; Schweiger, A.; Ernst, R. R. Phase Cycling in Pulse EPR. *J. Magn. Reson.* **1990**, *88*, 241–256.

[249] Ahlrichs, R.; Bär, M.; Häser, M.; Horn, H.; Kölmel, C. Electronic Structure Calculations on Workstation Computers: The Program System TURBOMOLE. *Chem. Phys. Lett.* **1989**, *162*, 165–169.

[250] TURBOMOLE V6.1 2009, a development of University of Karlsruhe and Forschungszentrum Karlsruhe GmbH, 1989-2007, TURBOMOLE GmbH, since 2007; available from `http://www.turbomole.com`.

[251] Schäfer, A.; Huber, C.; Ahlrichs, R. Fully Optimized Contracted Gaussian Basis Sets of Triple Zeta Valence Quality for Atoms Li to Kr. *J. Chem. Phys.* **1994**, *100*, 5829–5835.

[252] Eichkorn, K.; Weigend, F.; Treutler, O.; Ahlrichs, R. Auxiliary Basis Sets for Main Row Atoms and Transition Metals and their Use to Approximate Coulomb Potentials. *Theor. Chem. Acc.* **1997**, *97*, 119–124.

[253] Neese, F. The ORCA Program System. *Wiley Interdiscip. Rev.: Comput. Mol. Sci.* **2012**, *2*, 73–78.

[254] Barone, V. Structure, Magnetic Properties and Reactivities of Open-Shell Species from Density Functional and Self-Consistent Hybrid Methods. In *Recent Advances in Density Functional Methods, Part I*; Chong, D. P., Ed.; World Scientific: Singapore, 1996.

[255] Pettersen, E. F.; Goddard, T. D.; Huang, C. C.; Couch, G. S.; Greenblatt, D. M.; Meng, E. C.; Ferrin, T. E. UCSF Chimera – A Visualization System for Exploratory Research and Analysis. *J. Comput. Chem.* **2004**, *25*, 1605–1612.

[256] Wachters, A. J. H. Gaussian Basis Set for Molecular Wavefunctions Containing Third-Row Atoms. *J. Chem. Phys.* **1970**, *52*, 1033–1036.

[257] Neese, F. Theoretical Study of Ligand Superhyperfine Structure. Application to Cu(II) Complexes. *J. Phys. Chem. A* **2001**, *105*, 4290–4299.

[258] Neese, F. Metal and Ligand Hyperfine Couplings in Transition Metal Complexes: The Effect of Spin-Orbit Coupling as Studied by Coupled Perturbed Kohn-Sham Theory. *J. Chem. Phys.* **2003**, *118*, 3939–3948.

[259] Neese, F. Sum-over-states based Multireference *ab initio* Calculation of EPR Spin Hamiltonian Parameters for Transition Metal Complexes. A Case Study. *Magn. Reson. Chem.* **2004**, *42*, S187–S198.

[260] Lovett, J. E.; Hoffmann, M.; Cnossen, A.; Shutter, A. T. J.; Hogben, H. J.; Warren, J. E.; Pascu, S. I.; Kay, C. W. M.; Timmel, C. R.; Anderson, H. L. Probing Flexibility in Porphyrin-Based Molecular Wired Using Double Electron Electron Resonance. *J. Am. Chem. Soc.* **2009**, *131*, 13852–13859.

[261] Giannoulis, A.; Ward, R.; Branigan, E.; Naismith, J. H.; Bode, B. E. PELDOR in Rotationally Symmetric Homo-Oligomers. *Mol. Phys.* **2013**, *111*, 2845–2854.

[262] Jeschke, G.; Sajid, M.; Schulte, M.; Godt, A. Three-Spin Correlations in Double Electron-Electron Resonance. *Phys. Chem. Chem. Phys.* **2009**, *11*, 6580–6591.

[263] Kuprov, I.; Wagner-Rundell, N.; Hore, P. J. Polynomially Scaling Spin Dynamics Simulation Algorithm based on Adaptive State-Space Restriction. *J. Magn. Reson.* **2007**, *189*, 241–250.

[264] Karabanov, A.; Kuprov, I.; Charnock, G. T. P.; van der Drift, A.; Edwards, L. J.; Köckenberger, W. On the Accuracy of the State Space Restriction Approximation for Spin Dynamics Simulations. *J. Chem. Phys.* **2011**, *135*, 084106.

[265] Hogben, H. J.; Hore, P. J.; Kuprov, I. Strategies for State Space Restriction in Densely Coupled Spin Systems with Applications to Spin Chemistry. *J. Chem. Phys.* **2010**, *132*, 174101.

[266] Kuprov, I. Polynomially Scaling Spin Dynamics II: Further State-Space Compression using Krylov Subspace Techniques and Zero Track Elimination. *J. Magn. Reson.* **2008**, *195*, 45–51.

[267] Bak, M.; Nielsen, N. C. REPULSION – A Novel Approach to Efficient Powder Averaging in Solid-State NMR. *J. Magn. Reson.* **1997**, *125*, 132–139.

[268] Segawa, T. F.; Doll, A.; Pribitzer, S.; Jeschke, G. Copper ESEEM and HYSCORE through Ultra-Wideband Chirp EPR Spectroscopy. *J. Chem. Phys.* **2015**, *143*, 044201/1–8.

[269] Bowen, A. M.; Jones, M. W.; Lovett, J. E.; Gaule, T. G.; McPherson, M. J.; Dilworth, J. R.; Timmel, C. R.; Harmer, J. R. Exploiting Orientation-Selective DEER: Determining Molecular Structure in Systems Containing Cu(II) Centres. *Phys. Chem. Chem. Phys.* **2016**, *18*, 5981–5994.